

A Detailed Description of the CamSpec Likelihood Pipeline and a Reanalysis of the Planck High Frequency Maps

G. Efstathiou¹ and S. Gratton

Kavli Institute for Cosmology Cambridge
Madingley Road
Cambridge CB3 0HA
UK

E-mail: gpe@ast.cam.ac.uk, stg20@cam.ac.uk

Abstract. This paper presents a detailed description of the CamSpec likelihood which has been used to analyse *Planck* temperature and polarization maps of the cosmic microwave background since the first *Planck* data release. The goal of the CamSpec pipeline has been to extract an accurate likelihood based on the TT, TE and EE spectra from Planck which can be used to test cosmological models. *Planck* is an important legacy dataset which is likely to be reanalysed by many researchers for many years to come. Our aim in this paper is to present, in a single source, a comprehensive analysis of our methodology including what we have learned about: (a) the CMB sky and associated foregrounds at the *Planck* high frequencies ($\nu \geq 100$ GHz); (b) the consistency of the *Planck* data in temperature and polarization; (c) experimental systematics in the *Planck* data which need to be corrected when building a likelihood. For this paper we have created a number of temperature and polarization likelihoods using a range of Galactic sky masks and different methods of temperature foreground cleaning. Our most powerful likelihood uses 80% of the sky in temperature and polarization. Our results show that the base six-parameter Λ CDM cosmology provides an excellent fit to the *Planck* data. There is no evidence for statistically significant internal tensions in the *Planck* TT, TE and EE spectra computed for different frequency combinations. The cosmological parameters of the base Λ CDM model are entirely consistent with those reported by the *Planck* collaboration in [96] and earlier *Planck* papers, though our most powerful likelihood tightens up the statistical uncertainties and reduces the residuals of the TT, TE and EE spectra relative to the best fit model. We present evidence that the tendencies for the *Planck* temperature power spectra to favour a lensing amplitude $A_L > 1$ and positive spatial curvature $\Omega_k < 0$ reported in [96] are caused by statistical fluctuations in the temperature power spectra in the multipole range $800 \lesssim \ell \lesssim 1600$, which are repeatable between detectors and frequencies. Using our statistically most powerful likelihood, combined with the 2018 *Planck* low multipole likelihoods for $\ell < 30$, we find that the A_L parameter determined from the *Planck* power spectra alone differs from unity at no more than the 2.2σ level. We find no

¹Corresponding author.

evidence for anomalous shifts in cosmological parameters with multipole range. In fact, we show that the combined TTTEEE **CamSpec** likelihood over the restricted multipole range $2 \leq \ell \leq 800$ gives cosmological parameters for the base Λ CDM cosmology that are very close to those derived from the full multipole range $2 \leq \ell \leq 2500$. We present revised constraints on a few extensions of the base Λ CDM cosmology, focussing on the sum of neutrino masses, the number of relativistic species and the tensor-scalar ratio. The results presented here show that the *Planck* data are remarkably consistent between detector-sets, frequencies and sky area. We find no evidence in our analysis that cosmological parameters determined from the **CamSpec** likelihood are affected to any significant degree by systematic errors in the *Planck* data.

Contents

1	Introduction	2
2	Spectra and covariance matrices	4
2.1	Pseudo-cross spectra	4
2.2	Covariance Matrices	6
2.3	Data compression	8
3	Foreground masks	9
3.1	Temperature masks	9
3.2	Polarization masks	10
4	Input maps and multipole ranges	11
4.1	Detector set and half mission maps	11
4.2	Multipole ranges	12
5	Estimating noise	13
5.1	Noise power spectra	13
5.2	Correlated noise	16
6	Beams, calibrations and polarization efficiencies	18
6.1	Planck effective beams	18
6.2	Intra-frequency residuals in temperature	20
6.3	Relative calibrations of polarization spectra: effective polarization efficiencies	23
6.4	Tests of the temperature-polarization leakage model	27
7	Galactic dust emission in temperature	29
7.1	Map-based cleaning coefficients	30
7.2	Power spectrum of Galactic dust emission	32
7.3	Spectrum-based cleaning coefficients	37
7.4	Universality of Galactic dust emission	42
8	Galactic dust emission in polarization	44
8.1	Spectrum-based cleaning coefficients	45
8.2	Cleaning EE, TE, ET spectra	48
9	Nuisance parameters	52
9.1	Instrumental nuisance parameters	52
9.1.1	Inter-frequency relative calibrations in temperature	52
9.1.2	Polarization calibrations	54
9.1.3	Absolute calibration	54
9.1.4	Beam errors	54
9.2	Galactic dust in temperature	54
9.3	Extragalactic foregrounds	54
9.3.1	Poisson point sources	54
9.3.2	Clustered CIB	55

9.3.3	Thermal and kinetic Sunyaev-Zeldovich effects	56
9.3.4	tSZ/CIB cross-correlation	57
9.3.5	Priors on A^{tSZ} , A^{kSZ} , and $\xi^{\text{tSZ}\times\text{CIB}}$	57
9.4	Cleaned likelihoods	57
9.5	Summary	58
10	Combined temperature and polarization likelihood	58
10.1	The CamSpec likelihoods	58
10.2	Low multipole likelihoods	60
10.3	Notation	61
10.4	The fiducial base Λ CDM cosmology	61
10.5	Conditional spectra	66
11	Inter-frequency consistency in temperature	67
11.1	Consistency of TT spectra in the 12.1HM half mission likelihood	67
11.2	Cleaned temperature spectra	72
11.3	Residuals as a function of sky coverage	74
11.4	Comparison with full mission spectra	75
11.5	Summary	77
12	Inter-frequency consistency in polarization	78
12.1	The 12.1HM likelihood	78
12.2	Comparison with full mission detset spectra	82
12.3	Variation of TE and EE with sky area	84
13	The base ΛCDM model	84
13.1	Supplementary Likelihoods	84
13.2	Acoustic scale parameters	86
13.3	Consistency between temperature and polarization	87
13.4	Best-fit models	90
13.5	Comparison with Baryon Acoustic Oscillations and <i>Planck</i> lensing	91
13.6	Dependence on multipole range	94
13.7	Tensions with other astrophysical data	100
14	Extensions to ΛCDM	101
14.1	The A_L parameter	101
14.2	Spatial Curvature	103
14.3	Relativistic species and massive neutrinos	103
14.4	Tensor amplitude	105
14.5	Summary	106
15	Conclusions	106
A	Mathematical Details	111
A.1	Coupling Matrices	111
A.2	Covariance matrices	111
B	Comparison with ACTpol and SPTpol	113

1 Introduction

Since the discovery of the cosmic microwave background radiation (CMB) in 1965 [74], observations of the CMB have provided a wealth of new information on the early and late time Universe. The *Planck* satellite¹ [78, 82] is the third space mission dedicated to measuring anisotropies in the CMB, following COBE [116] and WMAP [10, 11]. The first cosmological results from the *Planck* nominal mission temperature data were presented in [88] and results for the full mission², including polarization data, have been reported in [76] and [96]. To extract cosmological information from CMB data requires the construction of a likelihood. The likelihoods used in the *Planck* analysis are described in abbreviated form in [87, 97, 101]³.

The main purpose of this paper is to present a detailed description of the **CamSpec** likelihood that we developed and applied to *Planck* in PCP13, PCP15 and PCP18. The **CamSpec** likelihood has been described in short form in the *Planck* collaboration likelihood papers PPL13, PPL15 and PPL18 and has been compared with the alternative **Plik** likelihood developed by the Paris group (which was chosen as the baseline for cosmological parameter analysis in the 2015 and 2018 data releases) in PCP15 and PCP18 and the corresponding *Planck* likelihood papers. *Planck* is an important legacy dataset and is likely to be analysed by other researchers in the future. We believe that it will be useful to present, in a single source, a detailed description of exactly what we have done in constructing likelihoods for the *Planck* collaboration. A second motivation for this paper has been to address the consistency and fidelity of the *Planck* data. The *Planck* data are consistent with the CMB fluctuations predicted for a spatially flat Universe with a power-law spectrum of scalar Gaussian adiabatic fluctuations. This model, which we will refer to as the base- Λ CDM cosmology is described by six parameters. The values of some of these parameters are not in perfect agreement with some other data, for example direct measurements of the Hubble constant (as will be discussed in Sect. 13.7). It is therefore important to demonstrate the consistency of the *Planck* results. In developing **CamSpec** we focussed extensively on the fidelity of the *Planck* power spectra, testing for consistency between power spectra determined from individual detector-sets and frequency combinations. Such consistency checks are more direct than tests based on consistency of cosmological parameters. The third motivation for this paper is to investigate a number of peculiar results reported in PCP18. These include the tendency of the *Planck* temperature power spectra to favour a lensing amplitude A_L greater than unity⁴ and to favour closed universes. Neither of these results has been reported at a high statistical significance (at $\lesssim 3\sigma$), but since they could be signs of new physics or internal tensions within the *Planck* data, we felt that a closer investigation was merited. We have therefore created statistically more powerful **CamSpec** likelihoods than those used in PPL18 and PCP18, primarily by extending sky coverage.

¹*Planck* (<http://www.esa.int/Planck>) is a project of the European Space Agency (ESA) with instruments provided by two scientific consortia funded by ESA member states (in particular the lead countries France and Italy), with contributions from NASA (USA), and telescope reflectors provided by a collaboration between ESA and a scientific consortium led and funded by Denmark

²The nominal mission comprises the first 15.5 months of data from *Planck*. The full mission uses 29 months of data for the *Planck* High Frequency Instrument (HFI) and 48 months for the Low Frequency Instrument (LFI).

³This paper will refer extensively to the *Planck* 2013, 2015 and 2018 cosmological parameters papers [76, 88, 96], which will henceforth be referred to as PCP13, PCP15 and PCP18. The corresponding likelihood papers will be referred to as PPL13, PPL15 and PPL18.

⁴See PCP18 for a definition of this parameter.

A short summary of the mathematical framework underlying **CamSpec** for both temperature and polarization is presented in Sect. 2, with details relegated to an Appendix. The application of this theoretical framework to real CMB data requires: (a) an accurate model of unresolved foregrounds, including Galactic contamination; (b) accurate models of beams and instrumental noise; (c) control of instrumental systematics. Since (a)-(c) can lead to biases in the cosmology, a large part of this paper is devoted to these aspects of the analysis. Various choices need to be made to construct a likelihood, for example, the choices of sky cuts, multipole ranges and methods of foreground removal. We present the rationale behind these choices and investigate the robustness of the **CamSpec** results to these choices.

The rest of this paper is divided into four distinct blocks:

[1] *Sections 3 - 6: Preliminaries and instrumental effects.*

Section 3 summarizes the Galactic temperature and polarization masks used in this paper. Section 4 discusses the maps that we have used to estimate cross-spectra. PCP13 used nominal mission detector-set maps whereas the likelihoods used in PCP15 and PCP18 used half mission cross spectra. In this paper, we compare half mission spectra with spectra constructed from the full mission detector-set maps. Section 5 discusses ways of estimating detector noise and analyses correlated noise between detectors. Beam corrections and polarization efficiencies are described in Sect. 6. This section presents a detailed intercomparison of the temperature spectra power spectra measured by different detectors and presents a cross-check of the temperature to polarization leakage corrections applied to the polarization spectra.

[2] *Sections 7 - 9: Galactic dust emission in temperature and polarization, extragalactic foregrounds and nuisance parameters.*

Section 7 presents an analysis of Galactic dust emission in temperature. In early versions of **CamSpec** (see PCP13) we corrected for Galactic dust emission in temperature by constructing and fitting dust power spectrum templates together with template power spectra for extragalactic foregrounds. The construction of such templates is discussed in Sect. 7 together with an analysis of the universality of the dust power spectrum as a function of frequency and sky coverage. We analyse CMB-dust correlations, which introduce substantial additional scatter to the power spectrum estimates, especially at 217 GHz, limiting the sky area that can be used reliably at this frequency. This motivates an alternative method of removing Galactic dust by subtracting high frequency maps (as described by [65, 117] and PPL15). We demonstrate that ‘cleaning’ the 143×143 , 143×217 and 217×217 spectra⁵ with higher *Planck* frequencies removes Galactic dust very accurately leaving residual power-spectrum contributions from extragalactic foregrounds that are well described by power-laws. We therefore form likelihoods using the standard template based foreground model, as described in previous *Planck* papers, and ‘cleaned’ likelihoods using a much simpler foreground model. Comparison of these likelihoods gives an indication of residual uncertainties associated with temperature foreground modelling on the cosmological results. Cleaning allows us to extend the sky coverage at 143 and 217 GHz reliably to 80% of the sky. Extragalactic foregrounds in polarization are well below the sensitivity level of *Planck*. All of our likelihoods use 353 GHz maps to subtract polarized dust emission, as discussed in Sect. 8. Instrumental nuisance parameters and the extragalactic foreground templates are discussed in Sect. 9, together with the priors adopted in the likelihood analysis. We have made minor changes to

⁵The notation 143×143 denotes the cross spectrum of two 143 GHz maps. In later sections we will use more specific notation, for example $143\text{HM1} \times 143\text{HM2}$ denotes the cross spectrum of a first half mission 143 GHz map with a second half mission 143 GHz map.

the foreground/nuisance model used in PCP18. Here we fix the relative calibrations of the cross-spectra, rather than carrying them as nuisance parameters, since they can be determined to high accuracy as described in Sect. 9.1.1; we also allow the amplitude of the Cosmic Infrared Background (CIB) contribution to the 143×217 spectrum to vary independently of the amplitude in the 217×217 spectrum. These changes have relatively little impact on cosmological parameters.

[3] *Sections 10 - 12: Likelihoods and inter-frequency comparisons of power spectra.*

Comparison of power spectra at different frequencies requires a likelihood analysis to determine the foreground parameters. In this part of the paper, we adopt the six parameter base Λ CDM model. Section 11 compares the consistency of the temperature spectra in the half mission, cleaned and full mission likelihoods and analyses spectrum residuals as a function of sky coverage. Section 12 presents a similar analysis for the TE and EE spectra cleaned with 353 GHz. We also compare our spectra with the spectra used to form the low multipole ($\ell < 30$) temperature and polarization likelihoods.

[4] *Sections 13 - 14: Science results.*

Section 13 discusses cosmological parameters for the base Λ CDM model. We demonstrate the consistency of the cosmological parameters determined from various likelihoods, sky areas, temperature and polarization combinations and also with different methods of temperature foreground cleaning. We also revisit the consistency of cosmological parameters determined from different multipole ranges. Possible tensions with other astrophysical data are discussed briefly in this section. One-parameter extensions to the base Λ CDM model are discussed in Sect. 14. We do not present a comprehensive analysis of extended models, but instead focus on the parameters A_L and Ω_K for which there were hints of anomalies in PCP15 and PCP18. We also present results on the sum of neutrino masses $\sum m_\nu$, the number of relativistic species N_ν and the tensor-to-scalar ratio r , using our statistically most powerful likelihood, combined with results from other experiments. A comparison of our best fit Λ CDM cosmology with the power spectra measured from ground based polarization experiments [43, 64] is presented in Appendix B.

Since most of this paper is technical in nature, readers interested only in the cosmological results can skip to Sect. 13. Our conclusions are summarized in Sect. 15. Throughout this paper, we use the same notation and definitions of cosmological parameters as in PCP18.

2 Spectra and covariance matrices

This section presents a summary of the mathematical framework developed for the `CamSpec` pipeline. Analytic expressions for the covariance matrices have been presented in [21, 30, 31, 41] and are summarized in Appendix A.2. These are based on a number of idealised assumptions which do not apply exactly to the real *Planck* data. We discuss the mismatch between the theoretical framework and the real data in this section.

2.1 Pseudo-cross spectra

The `CamSpec` likelihood uses pseudo-cross spectra computed on masked skies. Since the masks are apodised (see Sect. 3), they are described by weight functions w_p^T for temperature and w_p^P for Q and U polarization maps at each map pixel p . (Note that we always apply identical weight functions to Q and U maps).

For a particular weighting scheme we compute the following pseudo-spectra from maps i and j expressed as a vector:

$$\bar{\mathbf{C}}^{ij} = (\bar{C}_\ell^{T_i T_j}, \bar{C}_\ell^{T_i E_j}, \bar{C}_\ell^{E_i T_j}, \bar{C}_\ell^{E_i E_j}, \bar{C}_\ell^{B_i B_j}, \bar{C}_\ell^{E_i B_j}, \bar{C}_\ell^{B_i E_j}, \bar{C}_\ell^{T_i B_j}, \bar{C}_\ell^{B_i T_j})^T. \quad (2.1)$$

The pseudo-spectra of equation (2.1) are constructed from the following transforms:

$$\bar{a}_{\ell m}^{T_i} = \sum_p (T_i)_p w_p^{T_i} \Omega_p Y_{\ell m}^*(\boldsymbol{\theta}_p), \quad (2.2a)$$

$$\bar{a}_{\ell m}^{E_i} = -\frac{1}{2} \sum_p (Q_i + iU_i)_p w_p^{P_i} \Omega_p {}_2Y_{\ell m}^*(\boldsymbol{\theta}_p) + (Q_i - iU_i)_p w_p^{P_i} \Omega_p {}_{-2}Y_{\ell m}^*(\boldsymbol{\theta}_p), \quad (2.2b)$$

$$\bar{a}_{\ell m}^{B_i} = -\frac{1}{2} \sum_p (U_i - iQ_i)_p w_p^{P_i} \Omega_p {}_2Y_{\ell m}^*(\boldsymbol{\theta}_p) + (U_i + iQ_i)_p w_p^{P_i} \Omega_p {}_{-2}Y_{\ell m}^*(\boldsymbol{\theta}_p), \quad (2.2c)$$

where the sums extend over the number of map pixels each of solid angle Ω_p . The pseudo-power spectra are then computed in the usual way, for example,

$$\bar{C}_\ell^{T_i T_j} = \frac{1}{(2\ell + 1)} \sum_m \bar{a}_{\ell m}^{T_i} \bar{a}_{\ell m}^{*T_j}. \quad (2.3)$$

For the majority of this paper, we use the *Planck* 2018 HFI half-mission frequency maps in Healpix format [40] at a resolution NSIDE=2048 available from the *Planck* Legacy Archive⁶ (hereafter PLA). The only preprocessing applied to these maps before applying the transforms 2.2a-2.2c is to remove the means within the unmasked area of sky. For example, for map T_i we subtract the mean

$$(T^i)_{\text{mean}} = \sum_p w_p^{T_i} (T_i)_p / \sum_p w_p^{T_i}, \quad (2.4)$$

(and similarly for the Q_i and U_i maps). We make no other corrections to the maps prior to transformation.

The expectation values of the pseudo-spectral estimates are related to the beam convolved theoretical spectra $\bar{\mathbf{C}}^{ij}$ via a coupling matrix \mathbf{K}^{ij} [48, 56]. The components of the coupling matrix are given in Sect. A.1. At this stage, for clarity we recap on the notation used for various power spectra:

- $\bar{\bar{C}}_\ell$ is the beam convolved spectrum computed on the incomplete sky.
- \tilde{C}_ℓ is a beam corrected spectrum computed on incomplete sky.
- \hat{C}_ℓ is a beam corrected spectrum deconvolved for the sky mask.
- \bar{C}_ℓ is a beam convolved theoretical spectrum
- C_ℓ is the theoretical spectrum.

The power spectrum estimates need to be deconvolved for the effects of the sky mask (described by the coupling matrix \mathbf{K}^{ij}), the *Planck* instrumental beams and the effects of the finite size of the sky pixels, which we assume are described by functions that depend only on multipole ℓ . To simplify the discussion, we will discuss estimates of the temperature power

⁶<https://pla.esac.int>.

spectrum. The power spectra measured on the incomplete sky are related to the theoretical power spectrum as

$$\langle \bar{C}_\ell^{TT} \rangle = \sum_{\ell'} K_{\ell\ell'}^{TT} \bar{C}_{\ell'}^{TT}, \quad (2.5a)$$

$$= \sum_{\ell'} K_{\ell\ell'}^{TT} C_{\ell'}^{TT} W_{\ell'}^{TTTT} \pi_{\ell'}^2, \quad (2.5b)$$

where W_ℓ^{TTTT} is the TTTT beam transfer function for the particular pair of maps (i, j) used to compute \bar{C}_ℓ^{TT} and π_ℓ is the correction for finite pixel size returned by the `HEALpix` routine `pixel_window` (which we have verified, by simulation, accurately describes the effects of the finite pixel size for the sky masks used in this paper). The beam transfer functions vary slightly depending on how much sky is excluded by the masks; in our analysis we use beam transfer functions computed for similar (but not strictly identical) sky cuts to those used to estimate the power spectra. We then form the spectra \tilde{C}_ℓ^{TT} and \hat{C}_ℓ^{TT} :

$$\tilde{C}_\ell^{TT} = \bar{C}_\ell^{TT} / (W_\ell^{TTTT} \pi_\ell^2), \quad (2.6a)$$

$$\hat{C}_\ell^{TT} = \left(\sum_{\ell'} (K_{\ell\ell'}^{TT})^{-1} \bar{C}_{\ell'}^{TT} \right) / (W_\ell^{TTTT} \pi_\ell^2). \quad (2.6b)$$

and take \hat{C}_ℓ as our estimate of the theory spectrum C_ℓ . Note that Eq. 2.6b assumes that the product $W_\ell^{TTTT} \pi_\ell^2$ is much broader than the width of the mask coupling matrix $(K_{\ell\ell'}^{TT})^{-1}$. The generalization of these equations to polarized beams is discussed in Sect. 6.1.

In almost all of this paper, we show plots of the mask-deconvolved, beam- and pixel-window corrected spectra

$$\hat{D}_\ell \equiv \frac{\ell(\ell+1)}{2\pi} \hat{C}_\ell, \quad (2.7)$$

usually omitting the circumflex accent. We will, however, apply accents rigorously if we display other spectra.

2.2 Covariance Matrices

`CamSpec` uses analytic approximations to the covariance matrices of the pseudo-spectra derived under the assumptions of narrow window functions and uncorrelated, but anisotropic, pixel noise $((\sigma_i^T)^2, (\sigma_i^Q)^2, (\sigma_i^U)^2)$ [21, 30, 31, 41]. The components of the covariance matrix \mathbf{M} are given in Sect. A.2. Idealised simulations [30, 31] show that these expressions are accurate to typically percent level precision at high multipoles for typical Galactic sky masks for TT, TE and EE spectra, but are only accurate at the $\sim 10\%$ level for spectra involving B-modes.

In `CamSpec`, we compute all of the spectra in Eq. 2.1 and all of the mask coupling matrices for all detector combinations. In the absence of parity violating physics in the early universe, the primordial C^{TB} and C^{EB} spectra should be identically zero. In the absence of tensor modes, the BB spectra should also be zero apart from a small contribution from gravitational lensing. Although we compute these spectra, they are used primarily as diagnostic tools to test for systematics in the data. The current version of the `CamSpec` temperature-polarization likelihood uses *only* the TT, TE, ET and EE spectra and associated covariance matrices.

The `CamSpec` covariance matrices are based on a number of approximations:

[1] For realistic experiments such as *Planck* the noise is non-white. As described in PPL13, in `CamSpec` we adopt a heuristic prescription for dealing with non-white noise by multiplying

noise weight functions (see Eqs. A.6b-A.6d) with ℓ -dependent functions, ψ_ℓ , fitted to the noise power spectra (see Sect. A.2). In Sect. 5, we discuss ways of estimating noise directly from the maps. Inaccuracies in the noise model are the main source of error in the **CamSpec** polarization covariance matrices. Correlated noise between maps is demonstrably small (see Sect. 5.2) and is ignored in the covariance matrices.

[2] Foregrounds can make a significant contribution to the spectra and are included in the covariance matrices by adding a best-fit foreground model to the fiducial primordial CMB model. This assumes that the foregrounds are well approximated as isotropic Gaussian random fields. This is a good approximation at high multipoles, where the dominant foreground contributions are extragalactic, but clearly fails at multipoles $\ell \lesssim 500$ where Galactic dust emission, which is anisotropic on the sky, becomes the dominant foreground contribution. A technique for incorporating anisotropic dust emission into the covariance matrices is described in [67], but since Galactic dust emission in temperature is small compared to the primordial CMB in the frequency range 100 – 217 GHz we do not implement the prescription of reference [67] in the **CamSpec** covariance matrices. For ‘uncleaned’ temperature likelihoods, designed for the standard temperature foreground model, the covariance matrices include a dust contribution under the assumption of Gaussianity and isotropy, and so underestimate the amplitude of CMB-dust correlations. For high frequency ‘cleaned’ temperature likelihoods, CMB-dust correlations are strongly suppressed (see Sect. 7.3) so dust is ignored in computing the the covariance matrices. All of the **CamSpec** polarization spectra are cleaned for polarized Galactic dust emission at low multipoles using 353 GHz polarization maps, as described in Sect. 8.

[3] Point source holes and missing pixels increase the effective widths of the window functions introducing ‘leakage’ of large-scale power to smaller scales. This leakage can introduce errors in the analytic covariance matrices. However, experimentation with numerical simulations and high pass filtered maps have shown that these errors have negligible effect on cosmological parameters and so they are ignored.

The covariance matrices require a fiducial theoretical power spectrum. In this paper, we use the **CamSpec** TT base Λ CDM best fit power spectrum from PCP18. The number of covariance matrices required to form a likelihood scales as N_{map}^4 and becomes prohibitively expensive as the number of spectra becomes large. To reduce the number of operations, we (usually) adopt the same polarization mask at all frequencies, though this may differ from the masks applied to the temperature maps. The *Planck* maps contain ‘missing’ pixels, defined as pixels which are either not scanned by *Planck*, or for which the map-making algorithm cannot return a reliable solution for T,Q and U (see [99]). The number of missing pixels is small for half mission and full mission coadded frequency maps, but can become significant for individual detector set (hereafter detset) maps (see Sect. 4.1). In **CamSpec**, we therefore compute coupling matrices \mathbf{K} for each spectrum and map combination including missing pixels, but ignore differences in missing pixels when we compute the covariance matrices. This dramatically reduces the computational cost of computing covariance matrices for all detector combinations for very little loss in computational accuracy.

Following these computations, we end up with covariance matrices for the TT, TE, ET and EE components of the data vectors $\tilde{\mathbf{C}}_\ell^{\text{ij}}$, $\hat{\mathbf{C}}_\ell^{\text{ij}}$ and also all cross-covariances. We can then easily compute covariance matrices for any linear combination of these spectra.

2.3 Data compression

Since we have a relatively large number of maps (especially if we are analysing detset maps), the full cross-spectrum data vector and associated covariance matrix would be very large. To make the computation of a high- ℓ likelihood fast enough for parameter estimation without any band-averaging of the spectra, we compress the the data vector. We therefore discard all of the spectra involving B modes, retaining only the TT, TE, ET and EE spectra.

In principle all of the mask/beam deconvolved temperature cross-spectra *within* a given frequency combination should be identical to within the levels set by instrument noise. These can then be compressed into a single power spectrum estimate with little loss of information. However, we do not average across frequency combinations since the unresolved foregrounds depend on frequency. Further compression can be accomplished only after unresolved foreground parameters have been determined via likelihood analysis.⁷

In temperature, we form a linear combination of individual cross-spectra,

$$\hat{C}_\ell^{kT} = \sum_{ij \subset k, i \neq j} \alpha_\ell^{TTij} c_i c_j \hat{C}_\ell^{Tij}. \quad (2.8)$$

Here the index k denotes each distinct frequency cross-spectrum combination retained in the likelihood (*e.g.* 100×100 , 143×217 , ...) and the coefficients c_i denote the relative calibration factors for each map. The coefficients α_{ij} are normalized so that

$$\sum_{ij \subset k, i \neq j} \alpha_\ell^{TTij} = 1, \quad \alpha_\ell^{TTii} = 0. \quad (2.9)$$

To determine the coefficients α_{ij} we adopt another simplifying assumption. An optimal linear combination, \hat{X}_ℓ^k , is given by solving

$$\sum_{pq \subset k, p \neq q} \hat{\mathcal{M}}_{pq}^{-1} \hat{X}_\ell^k = \sum_{pq \subset k, p \neq q} \hat{\mathcal{M}}_{pq}^{-1} \hat{X}_\ell^{pq}, \quad (2.10)$$

where $\hat{\mathcal{M}}_{pq}^{-1}$ is the block of the inverse covariance matrix appropriate to the spectrum combination k . If the covariance matrix $\hat{\mathcal{M}}$ accurately describes the data, the solution of Eq. (2.10) properly accounts for the correlations between the cross-spectra. However, solving Eq. (2.10) requires the inversion of a very large matrix, and so we adopt a simpler solution by weighting each cross spectrum estimate by the diagonal component of the relevant covariance matrix, *i.e.*

$$\alpha_\ell^{TTij} \propto 1/\text{Cov}(\hat{C}_\ell^{Tij} \hat{C}_\ell^{Tij}). \quad (2.11)$$

This has the effect of assigning each cross-spectrum equal weight in the signal dominated regime and inverse variance weighting in the noise dominated regime. Thus, in temperature, we compress all cross-spectra within a particular frequency combination into a single cross-spectrum. This means that it is straightforward to compare, for example, coadded full mission with half mission cross spectra. It is, however, important to test the consistency of spectra within each frequency combination prior to coaddition (see Sect. 6.2).

For TE and EE spectra, we adopt a different approach. For TE and EE, the only frequency dependent foreground contribution detected in the Planck spectra is polarized Galactic dust emission. This affects the polarization spectra at multipoles $\lesssim 500$ (see Sect. 8).

⁷For example, as has been done to create the `plik_lite` likelihoods described in PPL15 and PPL18.

There is no evidence for a frequency dependent contribution from polarized point sources at high multipoles at the *Planck* sensitivity levels, consistent with the results of high resolution ground-based CMB experiments [43, 64]. We therefore ‘clean’ each of the TE and EE spectra using 353 GHz maps as dust templates as described in Sect. 8. With Galactic dust emission cleaned at low multipoles, we coadd all frequency combinations of TE and EE spectra using inverse diagonal weighting, analogous to Eq. 2.11, to form a single coadded TE and a single coadded EE spectrum *with no further free parameters to model polarized foregrounds*.

The compressed data vector in the standard version of **CamSpec** consists of four TT spectra involving the frequency combinations 100×100 , 143×143 , 143×217 and 217×217 spectra, together with TE and EE spectra coadded over all polarized HFI frequencies with the exception of 353 GHz, which is used as a Galactic dust template. We do not retain the 100×143 and 100×217 TT spectra since they add very little new information on the primordial CMB, but would require carrying additional foreground nuisance parameters. We also produce ‘cleaned’ likelihoods, in which we subtract Galactic dust emission in temperature using 545 GHz maps. For these cleaned likelihoods, in temperature we retain only the 143×143 , 143×217 and 217×217 TT spectra.

3 Foreground masks

3.1 Temperature masks

In this paper, we use the same family of temperature masks as used in PCP15 and PCP18. These masks are described in PPL15 and form a sequence with unapodised sky fractions increasing in increments of 5% in sky area. The masks are apodised with a Gaussian window function of width $\sigma = 2^\circ$. Examples of the temperature masks used frequently in this paper are shown in Fig. 3.1. We will use the simple nomenclature *mask25*, *mask60*, *mask70* *etc.* to delineate these masks, where the numbers refer to the unapodised sky areas retained after applying the masks.

The sky fraction over which an unapodised mask is non-zero is denoted f_{sky} . Apodisation (and any additional masking, for example, point source holes, CO masks) reduces the effective sky area. We therefore define a weighted sky fraction f_{sky}^W

$$f_{\text{sky}}^W = \frac{1}{4\pi} \sum_i w_i^2 \Omega_i. \quad (3.1)$$

Values for f_{sky} and f_{sky}^W are given in Table 1.

In addition to the diffuse masks, we mask point sources, extended objects (such as the Large Magellanic Cloud) and for 100 and 217 GHz maps we also mask out areas of sky with strong CO line emission. These masks are identical to those used in PCP18 and are described in PPL15. The point source+CO+extended object masks are shown in Fig. 3.1. To avoid cumbersome nomenclature, we loosely refer to these masks as ‘point source’ masks in the rest of this paper.

For this paper we have produced a series of likelihoods labelled 12.1-12.5 that use a range of different sky masks. These likelihoods are described in Sect. 10. The temperature masks shown in Fig. 3.1 have been used to form the 12.1HM likelihood. This is a half mission likelihood that is similar (differing in minor ways that will be discussed in Sect. 13) to the **CamSpec** likelihood used in PCP18.

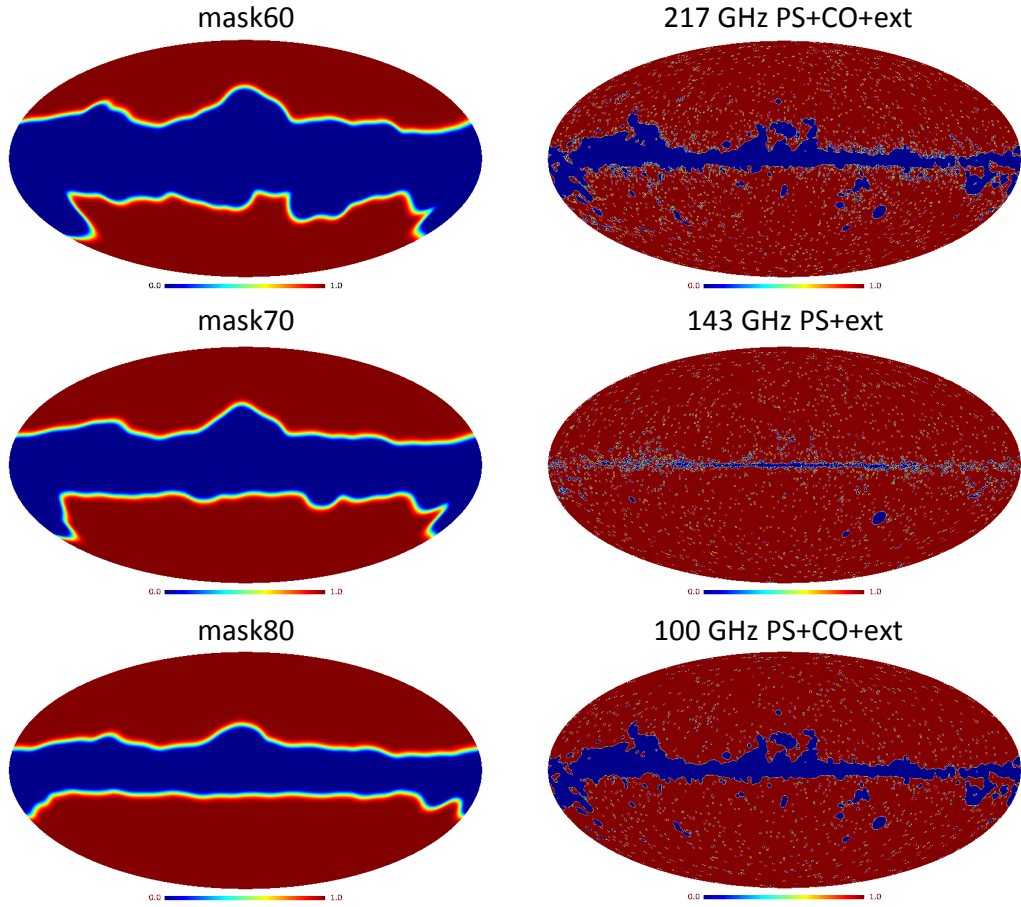


Figure 3.1. Figures to the left show the sequence of apodised diffuse foreground temperature masks (from top to bottom) applied to the 217, 143 and 100 GHz maps used to form our 12.1HM likelihood. Figures to the right show the point source+CO+extended object masks that we apply to the 217, 143 and 100 GHz maps.

Table 1. Sky fractions retained by the diffuse temperature and polarization masks

Temperature Mask	f_{sky} (%)	f_{sky}^W (%)	Polarization Mask	f_{sky} (%)	f_{sky}^W (%)
mask25	24.68	18.55	–	–	–
mask50	49.27	41.07	maskpol50	50.26	38.94
mask60	59.10	50.01	maskpol60	59.57	48.81
mask70	69.40	60.19	–	–	–
mask80	79.13	70.15	–	–	–

3.2 Polarization masks

The large-scale features in *Planck* Q and U maps are dominated by Galactic dust emission at all HFI frequencies (see Fig. 8.1 of Sect. 8). When we first started analysis of *Planck* polarization, we created diffuse polarization masks from the 353 GHz Q and U maps. We

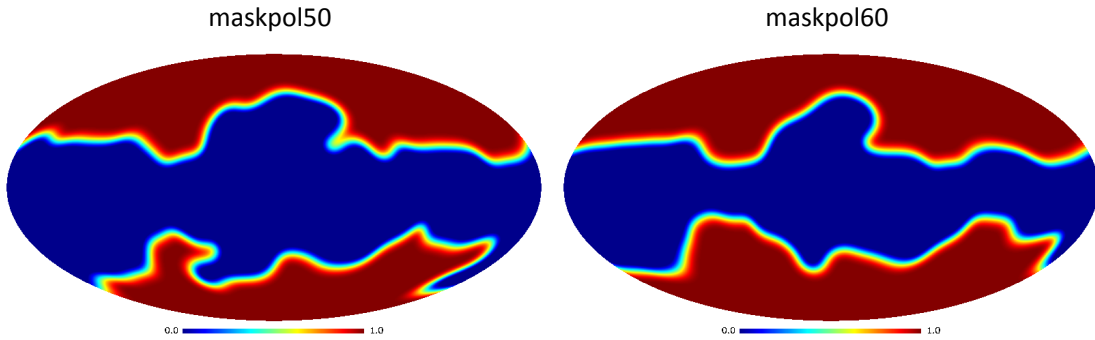


Figure 3.2. Polarization masks constructed from a degraded resolution full mission 353 GHz $P = (Q^2 + U^2)^{1/2}$ map.

first subtracted 143 GHz Q and U maps to remove the primordial CMB signal and then smoothed the maps with a Gaussian of FWHM of 10° . We then applied a threshold in $P = (Q^2 + U^2)^{1/2}$. The thresholded mask was then apodised by smoothing with a Gaussian of FWHM of 5° . To avoid isolated ‘islands’ in the resulting polarization masks, we iterated the thresholding and smoothing operations four times. Two examples of the polarized masks constructed in this way are shown in Fig. 3.2. In fact, since we decided to clean dust emission from the polarization spectra using 353 GHz maps, the precise shape of the polarization mask is unimportant, and so for some of the likelihoods we have applied the temperature masks of Fig. 3.1 to the Q and U maps.

Although we have found no strong evidence to suggest that bright polarized point sources (e.g. bright AGN) influence the TE and EE polarization spectra, for some likelihoods we have applied the 143 GHz point source mask shown in Fig. 3.1. Our statistically most powerful likelihood (12.5HMcl, see Sect. 10) uses mask80 together with the point source masks shown in Fig. 3.1 for temperature and mask80 with the 143 GHz point source mask from Fig. 3.1 applied to all polarization maps.

4 Input maps and multipole ranges

4.1 Detector set and half mission maps

The Planck focal plane contains a mixture of spider web bolometers (SWB) and polarization sensitive bolometers (PSB). The SWBs can be processed individually to produce temperature maps and the PSBs can be processed in pairs (i.e. 4 bolometers) to produce T, Q and U Stokes parameter polarization maps. We refer to ‘detset’ maps⁸ as the set of 13 maps constructed from the detector combinations listed in Table 2. A detset cross-spectrum analysis involves cross-correlation analysis of all 13 detsets. Excluding auto spectra, this leads to 78 TT, 72 TE/ET and 15 EE detset cross spectra. This large number of spectra allows cross-checks of potential instrumental systematics, as will be described in subsequent sections.

⁸The 2018 detset maps are not available on the PLA. We are indebted to the *Planck* collaboration for permission to present results based on these maps in this paper. Apart from slightly increased noise levels (caused by the omission of some data at the end of mission survey 5), the 2018 detset maps at high multipoles ($\ell \gtrsim 30$) are almost identical to the 2015 detset maps, which are available on the PLA. The 2018 HFI DPC paper [99] uses the detset maps for several internal consistency tests of the noise and calibration characteristics of these maps.

We use the 2018 HFI maps available from the PLA which are described in [99]. Note that the 2018 HFI maps do not include scanning rings 26050 to 27005 (which were included in the 2015 HFI maps). This selection removes data from the end of the HFI cryogenic phase of the *Planck* mission which showed increased thermal fluctuations in the HFI focal plane. As a consequence, the noise levels of the 2018 HFI maps are slightly higher than those of the 2015 maps. We note, however, that the removal of these rings has no noticeable impact on the power spectra at high multipoles. In addition to the full mission dataset maps, we analyse frequency averaged half mission (HM) maps. The first half mission (HM1) maps are constructed from scanning rings 240 to 13471 and the second half mission (HM2) maps are constructed from scanning rings 13472 to 26050 (as summarized in the PLA).

Table 2. Detector combinations used in this analysis

freq. (GHz)	detector	type	\bar{N}^T	\bar{N}^Q	\bar{N}^U
100	1+4 (ds1)	PSB	1.708E-4	2.763E-4	2.575E-4
100	2+3 (ds2)	PSB	7.340E-5	1.164E-4	1.172E-4
143	5	SWB	6.464E-5	–	–
143	6	SWB	7.171E-5	–	–
143	7	SWB	5.307E-5	–	–
143	1+3 (ds1)	PSB	3.230E-5	6.941E-5	6.989E-5
143	2+4 (ds2)	PSB	2.922E-5	5.687E-5	5.689E-5
217	1	SWB	9.815E-5	–	–
217	2	SWB	1.179E-4	–	–
217	3	SWB	1.038E-4	–	–
217	4	SWB	9.422E-5	–	–
217	5+7 (ds1)	PSB	5.985E-5	1.306E-4	1.292E-4
217	6+8 (ds2)	PSB	7.337E-5	1.616E-4	1.652E-4

The last three columns in Table 2 give the effective white-noise power level computed from Eq. 5.1 below over the default temperature+point source masks shown in Fig. 3.1 (i.e. mask60 for 217 GHz, mask70 for 143 GHz and mask80 for 217 GHz) and maskpol60 in polarization. One can see from these entries that there are some significant differences in the noise levels of datasets within a frequency band. For example, 100ds1 maps are considerably noisier than 100ds2 maps. The weighting that we apply to form coadded cross spectra for a given frequency combination (Eq. 2.11) downweights the noisier spectrum at high multipoles where the spectra are noise dominated.

4.2 Multipole ranges

We impose lower (ℓ_{\min}) and upper (ℓ_{\max}) multipole cuts for each spectrum. At low multipoles, the pseudo-power spectra are statistically sub-optimal [30]. The *Planck* likelihoods are therefore hybrids [30, 31], using more optimal likelihoods over the multipole range $2 \leq \ell \leq 29$ (see Sect. 10.2) patched to the *Planck* high multipole likelihoods. The default values of the multipole ranges used in CamSpec are listed in Table 3. The rationale for these choices is as follows:

- For each spectrum, ℓ_{\max} is chosen so that we do not use spectra at multipoles well into the inner beams where the beam transfer functions become small (and issues such as beam errors

Table 3. Multipole ranges used in the 12.1HM `CamSpec` likelihood

	TT		TE		EE	
spectrum	ℓ_{\min}	ℓ_{\max}	ℓ_{\min}	ℓ_{\max}	ℓ_{\min}	ℓ_{\max}
100×100	30	1400	30	1200	200	1200
100×143	–	–	30	1500	30	1500
100×217	–	–	200	1500	200	1200
143×143	30	2000	30	2000	200	2000
143×217	500	2500	200	2000	300	2000
217×217	500	2500	500	2000	500	2000

and correlated noise between detsets become significant). At such high multipoles, the noise in the beam corrected power spectra increases exponentially and so little information is lost by truncating the spectra.

- As discussed in the previous section, we do not include the 100×143 and 100×217 temperature spectra in the likelihood, since they add little cosmological information compared to the 100×100 and 143×143 spectra.
- We impose ℓ_{\min} cuts on the 143×217 and 217×217 temperature spectra for which Galactic dust has a higher amplitude than in the 100×100 and 143×143 spectra. Since instrumental noise is negligible in temperature at multipoles $\ell \lesssim 500$, no significant cosmological information is lost by truncating these spectra. However, by eliminating the low multipoles in the 143×217 and 217×217 spectra, we reduce the sensitivity of the temperature likelihood to inaccurate dust subtraction and also suppress the impact of CMB-dust correlations on the likelihood (see Sect. 7).
- For TE and EE, the Planck spectra are noisy and so we coadd all frequency combinations including the 100×143 and 100×217 spectra to improve the signal-to-noise of the coadded spectra.
- EE spectra involving 217 GHz maps are strongly contaminated by dust at low multipoles (see Sect. 8). To avoid biases associated with inaccurate dust subtraction we impose lower multipole cuts at the expense of a reduction of signal-to-noise in the coadded spectra. In addition, at multipoles $\ell \lesssim 50$ we find clear evidence of systematics in EE spectra involving 217 GHz (see Fig. 12.4). Therefore, we include only the 100×143 EE spectra at $\ell \leq 200$ which gives consistency with the low multipole EE likelihood at $\ell < 30$. If we include the 100×217 , 143×217 and 217×217 EE at $\ell < 200$ in the `CamSpec` likelihoods, we find negligible impact on cosmological parameters for Λ CDM-like cosmologies. However, we then see inconsistencies between the TT and EE solutions for models with low frequency oscillatory features in the primordial power spectrum [61].

5 Estimating noise

5.1 Noise power spectra

Accurate covariance matrices for a cross spectrum likelihood require accurate noise estimates. The map making stage returns an estimate of the noise at each pixel, $(\sigma^T)_i^2$, for unpolarized maps and a 3×3 noise matrix with diagonal components, $(\sigma^T)_i^2$, $(\sigma^Q)_i^2$, $(\sigma^U)_i^2$ for polarized

maps. If the noise is uncorrelated between pixels, the noise power spectra of maps computed with weighting w_i^X is

$$\bar{N}^X = \frac{1}{4\pi} \sum_i (\sigma^X)_i^2 (w_i^X)^2 \Omega_i^2, \quad (5.1)$$

where $X = (T, Q, U)$. These are independent of multipole (i.e. the noise power spectra are white). However, the *Planck* noise differs significantly from white noise. In the time-ordered-data (TOI), the *Planck* noise from each bolometer can be decomposed (roughly) into three components: a white noise component at high frequencies; a $1/f^\alpha$ component with $\alpha \sim 1$ at intermediate frequencies (defining an effective ‘knee’ frequency) coming from the bolometer electronics; a $1/f^\beta$ component with $\beta \sim 2$ at low frequencies from thermal noise (see [99]). Low frequency noise at the map level is substantially suppressed (but cannot be completely removed) by destriping during the map making stage. In addition, as will be discussed in Sect. 5.2, aspects of the TOI processing (such as deglitching thermal fluctuations caused by cosmic ray hits and removal of 4K cooler/bolometer interference lines) introduce correlated noise at high multipoles in cotemporal cross spectra.

The noise power spectra of *Planck* maps are therefore complex and strongly dependent on the details of the TOI data processing, bolometer time constant corrections, and map-making. The question then arises as to how to accurately determine noise spectra. Ever since our first analyses of the *Planck* data, we have preferred to use empirical noise estimates rather than to rely on simulations (which even in the elaborate end-to-end form described in DPC18, do not include deglitching, direct injection of 4K lines and a number of other key aspects of the data processing, as described in their Appendix A4). To determine the noise, we use differences of maps constructed from each detector, or combination of detectors:

Half-ring differences (HRD): Half-ring (HR) maps are created from the first and second half of each **HEALpix** pointing ring. Noise estimates can then be formed by differencing these maps. We call these half-ring difference (HRD) maps.

Odd-even differences (OED): Maps can be created from the odd and even **HEALpix** pointing rings. The differences of these (OE) maps are called odd-even difference (OED) maps.

Before showing results, it is extremely important to comment on corrections for ‘missing’ pixels. As a result of the *Planck* scanning strategy, the sky coverage is highly inhomogeneous. Regions close to the ecliptic poles are well sampled, but the coverage becomes sparser towards the ecliptic plane. In addition, to construct polarization maps, a threshold is applied to the 3×3 pixel noise covariance matrices returned by the map-making algorithm. If the condition number of the 3×3 matrix is high at a particular pixel, then the pixel is flagged as ‘missing’. For combined frequency maps, e.g. half mission maps, the number of missing pixels is small. However, the number of missing pixels is higher for detset maps, since these are created either from a single SWB or a PSB detset. The number of missing pixels is even greater in HR and OE maps. In particular, in odd or even maps, several million pixels (or several percent of sky) can be classified as ‘missing’. Furthermore, there is very little overlap between the missing pixels in odd and even splits. Simply ignoring missing pixels leads to very large (up to 30%) biases in the OED noise power spectra for individual SWB maps.

Consider two maps M_1 and M_2 (we drop the superscripts denoting T,Q or U, and ignore noise correlations between these quantities) with noise variances given by the relevant diagonal components of the 3×3 covariance matrices σ_1^2 and σ_2^2 . The minimum variance combined

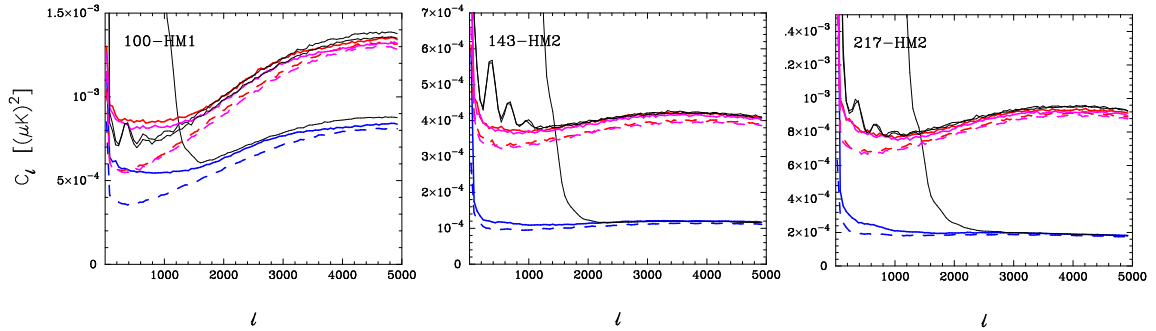


Figure 5.1. Estimates of undeconvolved (i.e. uncorrected for missing sky and beam transfer functions) noise spectra for three half mission maps: 100 GHz HM1, 143 GHz HM2, 217 GHz HM2 computed for the masks used in the 12.1HM likelihood. The solid lines show noise estimates derived from OED maps and the dotted lines show noise estimates derived from HRD maps. T, Q, and U noise spectra are shown by the blue, red and purple lines respectively. The solid black lines show the auto-spectra of the T, Q and U maps.

map is

$$M = \frac{\sigma_1^2 \sigma_2^2}{(\sigma_1^2 + \sigma_2^2)} \left(\frac{M_1}{\sigma_1^2} + \frac{M_2}{\sigma_2^2} \right), \quad (5.2a)$$

with noise level

$$\sigma^2 = \frac{\sigma_1^2 \sigma_2^2}{(\sigma_1^2 + \sigma_2^2)}. \quad (5.2b)$$

To match this noise level, we need to weight the difference map as follows:

$$D = \frac{\sigma_1 \sigma_2}{(\sigma_1^2 + \sigma_2^2)} (M_1 - M_2). \quad (5.3)$$

However, in our application σ_1 and σ_2 are not determined for missing pixels. We therefore ‘infill’ the missing pixels in each of the maps M_1 and M_2 by replacing the missing pixel and its noise estimate with that of a pixel drawn at random from the nearest 100 pixels within a disc centred on the missing pixel.

Typical noise estimates derived from OED and HRD maps are shown in Fig. 5.1. The noise power spectra are clearly non-white and this needs to be accounted for in computing the power spectrum covariance matrices (via the heuristic ψ_ℓ factors discussed in Sect. A.2). The noise spectra can be well fitted by the following functional form:

$$N_\ell = A \left(\frac{100}{\ell} \right)^\alpha + B \frac{(\ell/1000)^\beta}{(1 + (\ell/\ell_c)^\gamma)^\delta}, \quad (5.4)$$

with A , α , B , β , ℓ_c , γ and δ as free parameters. However, an important result from this analysis is the systematic *underestimate* of the noise power from the HRD maps compared to the OED maps. Similar results are reported in PPL18 and in Section 5.4 of [99] and are caused by the fact that deglitching is performed on the full set of HEALpix pointing rings leading to correlated errors in half-rings which cancel in the HRD maps. In addition, the OED spectra fall off less steeply than the HRD spectra at low multipoles. This is particularly noticeable in the 100 GHz noise spectra. The black lines in Fig. 5.1 show the (undeconvolved) auto spectra of each map (with Q and U maps treated as scalar maps). One can see here that

the temperature auto spectra are signal dominated over most of the multipole range used for cosmology, and so errors in the noise spectra are not particularly critical for cosmology. However, this is not true for the polarization spectra which are noise dominated over most of the multipole range. At 100 GHz, for example, the *Planck* EE spectra contain very limited information at multipoles $\ell \sim 1000$ and are completely noise dominated at higher multipoles. Errors in the noise modelling can therefore have a very significant effect on statistics (for example, χ^2) involving EE power spectra. One can see from Fig. 5.1 that the auto spectra in both temperature and polarization match well with the OED spectra at high multipoles for both temperature and polarization. For 100 GHz, the OED polarization spectra sit high compared to the auto spectra at multipoles $\lesssim 1000$ which suggests that the OED spectra have some correlated component in addition to instrument noise.

In the *Planck* 2013 and 2015 analyses, we used HRD maps to estimate noise in forming the **CamSpec** likelihoods and so the noise was underestimated. This is the main reason for high χ^2 values for the **CamSpec** EE spectra used in PPL15 and PCP15, rather than systematics in the polarization data⁹. In this paper, we use the OED noise estimates (as illustrated in Fig. 5.1) though our analysis suggests that they overestimate the noise contribution to the 100 GHz and possibly the 143 GHz EE spectra.

As pointed out in PCP13, the larger the data vector, the more accurately one needs to know the noise levels to avoid a significant bias in χ^2 . As a rough rule of thumb, for a data vector of length N the noise estimates need to satisfy

$$\frac{\Delta\sigma^2}{\sigma^2} \lesssim \sqrt{\frac{2}{N}}, \quad (5.5)$$

to give an accurate χ^2 . For the full **CamSpec** TTTEEE likelihoods, $N \sim 12000$, so we require covariance matrices accurate to $\sim 1\%$ if the value of χ^2 is to be used as a simple ‘goodness-of-fit’ criterion. In reality, the covariance matrices are accurate to only a few percent and this needs to be borne in mind when interpreting χ^2 values for the full likelihood. As we show in Table 13, by adopting the OED noise estimates, the full TTTEEE likelihood fitted to a base Λ CDM cosmology gives an acceptable χ^2 (to within $\sim 2.2\sigma$), though the χ^2 values for individual EE spectra are consistently low (see Table 15).

5.2 Correlated noise

As pointed out by Spergel et. al. [117], there is clear evidence for correlated noise between cotemporal HFI temperature maps. For this reason, in the 2015 and 2018 *Planck* analyses the *Planck* collaboration used half mission cross spectra to form *Planck* likelihoods rather than using full mission detset spectra, sacrificing signal-to-noise in favour of reducing systematics from correlated noise¹⁰. There are two simple ways of testing for correlated noise: (i) we can compute the differences between full mission coadded detset (DS) spectra and half mission (HM) cross spectra; (ii) we can cross-correlate the OED detset maps. The DS and HM cross

⁹These papers suggested that temperature-polarization leakage may have been responsible for the high EE χ^2 values for both the **CamSpec** and **Planck** likelihoods. In fact, temperature-to-polarization leakage is a small effect for EE and the high χ^2 values were caused primarily by underestimated noise and inaccurate polarization efficiencies (see Sect. 6.3).

¹⁰PCP13 used nominal mission detset spectra. The coadded 217×217 detset spectrum showed a ‘dip’ at $\ell \sim 1800$, which was traced to incomplete removal of 4 K lines in the TOD data, which primarily affected survey 1. The systematic origin of this feature was demonstrated convincingly in [117]. Fortunately, the 217×217 feature was not strong enough to significantly affect cosmological parameters.

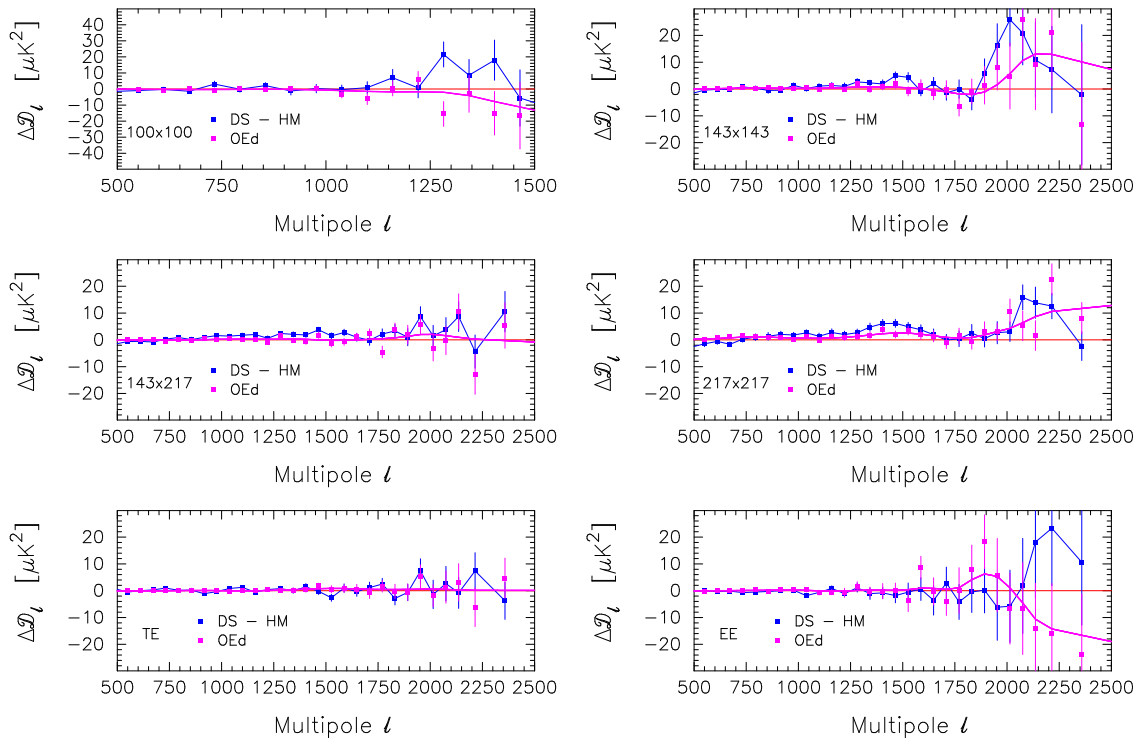


Figure 5.2. Top four figures show 100×100 , 143×143 , 143×217 and 217×217 TT spectra. The blue points show the differences between coadded DS TT spectra and HM spectra in bands of width $\Delta\ell = 61$. The purple points show the DS OED cross spectra, coadded using the same weights (Eq. 2.11) as those for the TT spectra. The lines show fits to the OED spectra. The error bars show the 1σ scatter of points within each bandpower. The lower two figures show the equivalent plots for coadded TE and EE spectra.

spectra may differ because of correlated noise, errors in the effective beams etc. The OED DS cross spectra therefore give a direct measure of correlated noise, though we use both tests in the results presented below.

Results are shown in Fig. 5.2. The blue points show the differences between coadded DS and HM spectra together with error bars reflecting variance caused by instrumental noise. The purple points show coadded DS OED spectra using the DS TT weights (Eq. 2.11). The purple lines show fits to the OED spectra computed by applying a three-point filter to the purple points. From these plots we conclude the following:

- There is evidence of correlated noise in the 143×143 and 217×217 OED TT spectra at high multipoles that matches reasonably well with the differences between DS and HM cross spectra. The level of correlated noise is comparable to the $\pm 1\sigma$ errors from noise.
- The OED spectra show no evidence for correlated noise in the 100×100 and 143×217 TT spectra or in the coadded TE OED spectra at a level that could bias cosmological parameters in the high multipole likelihoods.
- The EE OED spectra are very noisy at multipoles $\ell \gtrsim 2000$. At lower multipoles, there is no evidence for correlated noise in either the OED spectra or the (DS-HM) difference spectra at a level that could bias cosmological parameters in the high multipole likelihoods.
- There is an indication of a small excess in the DS-HM 217×217 TT spectrum compared to the OED spectrum in the multipole range $\ell \sim 1450$, which is qualitatively reproduced in

the OED spectrum.

- Although we have presented results in Fig. 5.2 for OED detset spectra, we find similar results for OED HM cross spectra.

With the choices of ℓ_{\max} in Table 3, correlated noise will have little impact on the DS spectra except for the 217×217 DS spectrum at $\ell \gtrsim 2000$, where correlated noise appears to bias the DS spectrum high by about 1σ . In forming a DS likelihood, we therefore subtract the fits to the OED spectra (purple lines) from the coadded DS TT spectra.

6 Beams, calibrations and polarization efficiencies

6.1 Planck effective beams

As discussed in [99], the absolute calibration of Planck HFI maps is based on the orbital dipole over the frequency range 100 – 353 GHz and on Uranus and Neptune at 545 and 857 GHz. As far as this paper is concerned, the absolute calibration of the 100 – 217 GHz DS or HM maps at $\ell = 1$ is assumed to be exact, and any differences between TT cross spectra is ascribed to errors in the effective beam transfer functions. Analysis of the Solar dipole at 545 GHz reported in DPC18 shows that the absolute calibration at 545 GHz agrees to within 0.2% of the calibrations at lower frequencies. Since we use 353, 545 and 857 GHz only as Galactic dust templates in this paper, any calibration errors relative to lower frequencies are absorbed in the cleaning coefficients (see Sects. 7 and 8).

In simplified form, the power absorbed by a detector at time t on the sky is

$$P(t) = G[I + \rho(Q \cos 2(\psi(t) + \psi_0) + U \sin(2(\psi(t) + \psi_0)))] + n(t), \quad (6.1)$$

where I , Q , U are the beam convolved Stokes parameters seen by the detector at time t , G is the effective gain (setting the absolute calibration), ρ is the detector polarization efficiency, $\psi(t)$ is the roll angle of the satellite, ψ_0 is the detector polarization angle and $n(t)$ is the noise. For a perfect PSB, $\rho = 1$, while for a perfect SWB, $\rho = 0$. The polarization efficiencies and polarization angles for the HFI bolometers were measured on the ground and are reported by Rosset et al. [113]. For PSB detectors, the ground based measurements of polarization angles were measured to an accuracy of $\sim 1^\circ$ and the polarization efficiencies to an accuracy of $\sim 0.1 - 0.3\%$. The SRoll map making algorithm used to produce the 2018 HFI maps (described in [99]) assumes the ground based measurements of polarization angles and efficiencies. Within the SRoll formalism, polarization angles and efficiencies are degenerate and cannot be disentangled from each other. Errors in the polarization angles induce leakage from E to B modes while errors in the polarization efficiencies induce leakage from temperature to polarization. As discussed in [99], analysis of the Planck TB and EB spectra (which should be zero in the absence of parity violating physics) suggest errors in the polarization angles of $\lesssim 0.5^\circ$, within the errors reported by Rosset et al. However, by inter-comparing spectra, [99] concluded that systematic errors in the polarization efficiencies are significantly larger than the statistical errors reported by Rosset et al. (perhaps at the 1% level). This conclusion is supported by the results presented in this paper. As we will show in Sect. 6.3, the polarization efficiencies and temperature-to-polarization leakage can be constrained accurately by comparing different frequency combinations of TE and EE spectra. In this paper, we ignore errors in the polarization angles and determine polarization efficiencies empirically.

We use the definitions of [85], distinguishing between scanning and effective beams. The scanning beam is defined as the coupled response of the optical system, deconvolved

time response function and software low pass filter applied to the TOD. The effective beam describes the beam in the map domain, after combining the TOD in the map making process. The effective beam will vary from pixel to pixel in any given map. For some applications, *e.g.* analysis of individual sources, it is useful to have estimates of the effective beams at each pixel, as provided by the **FEBecoP**¹¹ software [71]. However, for power spectrum estimation it is more useful to have an ‘isotropised’ beam transfer function which can be used to correct the power spectra as in Eqs. 2.6a and 2.6b. Such isotropized beam transfer functions are provided by the **QuickPol** software [49], which can be tuned to return beam transfer functions for the exact masks used in a cosmological analysis. (In practice, we use beams computed on *almost* the same sky maps used to compute spectra, differing in point-source holes, missing pixels, CO masks etc.) Discrete sampling of the sky can lead to a small additive (rather than multiplicative) sub-pixel contribution to the beam convolved power spectra with an amplitude that depends on the temperature gradient within each pixel. These sub-pixel effects can be computed in **QuickPol** assuming fiducial spectra (including any foreground contributions). Sub-pixel effects have been quantified in detail in PPL15 and PPL18, and have been shown to be small. We have therefore neglected sub-pixel effects in creating **CamSpec** likelihoods.

The determination of Planck HFI beams is complex and is described in detail in [85]. We summarize some of the main details here. The ‘main beam’ is defined as the scanning beam out to 100’ from the beam axis. Smearing of the main beam (caused by the time dependent response of a bolometer to a signal) is reduced by deconvolving the TOD. This deconvolution amplifies the noise at high frequencies, which is why the noise power spectra are non-white at high multipoles (cf. Fig. 5.1). The main beams of the 100 – 353 GHz detectors are determined by calibrating against scans of Saturn and Jupiter; at 545 and 857 GHz, Mars observations are used to calibrate the peak of the main beam since Saturn and Jupiter saturate the detectors in the inner parts of the main beam. At beam radii that are larger than those set by the noise levels of the Jupiter scans, the main beam is patched to a power law ($\propto \theta^{-3}$, where θ is the angular distance from the main beam axis) where the exponent is derived from GRASP¹² physical optics models. The main beam calibrations do not correct for the filtering of the sky from far side-lobes (FSL) arising from reflector and baffle spillover. The FSL for each detector is defined as the beam response at $\theta > 5^\circ$ and is computed from GRASP models. These computations are used to generate FSL convolutions of the dipole and Galaxy, which are removed from the TOD during the **SRoll** map making stage. Since the FSL contributions project onto the sky in different ways for odd and even sky surveys, odd-even survey null tests can be used to test for residual effects arising from FSL (and also Zodiacal emission) as described in Section 3 of [99].

The polarization maps are constructed from pairs of PSB detectors. Mismatch of the beams for individual bolometers within each PSB pair will introduce couplings between the temperature and polarization maps. The **QuickPol** formalism computes a beam matrix relating the expectation values of the beam convolved spectra measured on the sky (\bar{C}_ℓ^{TT} , \bar{C}_ℓ^{TE} , \bar{C}_ℓ^{EE} , \bar{C}_ℓ^{BB}) to the beam uncorrected spectra (\tilde{C}_ℓ^{TT} , \tilde{C}_ℓ^{TE} , \tilde{C}_ℓ^{EE} , \tilde{C}_ℓ^{BB}):

$$\begin{pmatrix} \bar{C}_\ell^{TT} \\ \bar{C}_\ell^{TE} \\ \bar{C}_\ell^{EE} \\ \bar{C}_\ell^{BB} \end{pmatrix} = \begin{pmatrix} W_\ell^{TTTT} & W_\ell^{TTTE} & W_\ell^{TTTE} & W_\ell^{TTBB} \\ W_\ell^{TETT} & W_\ell^{TETE} & W_\ell^{TEEE} & W_\ell^{TEBB} \\ W_\ell^{EETT} & W_\ell^{EETE} & W_\ell^{EEEE} & W_\ell^{EEBB} \\ W_\ell^{BBTT} & W_\ell^{BBTE} & W_\ell^{BBEE} & W_\ell^{BBBB} \end{pmatrix} \begin{pmatrix} \tilde{C}_\ell^{TT} \\ \tilde{C}_\ell^{TE} \\ \tilde{C}_\ell^{EE} \\ \tilde{C}_\ell^{BB} \end{pmatrix}. \quad (6.2)$$

¹¹Fast Effective Beam Convolution in Pixel Space.

¹²See <https://www.ticra.com/software/grasp>.

This generalises the discussion given in Sect. 2.1 to polarized beams. The diagonal components of this matrix are the dominant terms, and we (loosely) refer to these diagonal components as ‘scalar beams’.

In `CamSpec`, we ignore the off-diagonal terms in the full beam matrix for the TT spectra. However, for the TE and EE spectra we retain the most important off-diagonal terms

$$\bar{C}_\ell^{TE} = W_\ell^{TETE} \tilde{C}_\ell^{TE} + W_\ell^{TETT} \tilde{C}_\ell^{TT}, \quad (6.3a)$$

$$\bar{C}_\ell^{EE} = W_\ell^{EEEE} \tilde{C}_\ell^{EE} + W_\ell^{EETT} \tilde{C}_\ell^{TT}, \quad (6.3b)$$

describing beam-induced temperature-to-polarization (TP) leakage. For these, we make corrections to the measured spectra assuming the best fit base Λ CDM theoretical TT spectrum. These corrections have a small impact on the *Planck* TE spectra and are negligible for the EE spectra. Section 6.4 presents tests of the TP leakage model of Eqs. 6.3a and 6.3b.

A useful model for TP leakage has been proposed by Hivon et al. [47]. Here it is assumed that TP leakage modifies the measured $a_{\ell m}$ coefficients and power spectra as follows:

$$a_{\ell m}^T \rightarrow a_{\ell m}^T, \quad (6.4a)$$

$$a_{\ell m}^E \rightarrow a_{\ell m}^E + \epsilon_\ell a_{\ell m}^T, \quad (6.4b)$$

causing perturbations to the power spectra of

$$\Delta C_\ell^{TT} = 0, \quad (6.5a)$$

$$\Delta C_\ell^{TE} = \epsilon_\ell C_\ell^{TT}, \quad (6.5b)$$

$$\Delta C_\ell^{EE} = \epsilon_\ell^2 C_\ell^{TT} + 2\epsilon_\ell C_\ell^{TE}. \quad (6.5c)$$

If it is assumed that the main effect of beam mismatch arises from $m = 2$ and $m = 4$ beam modes describing beam ellipticity (note that beam modes with odd values of m are small as a result of the *Planck* scanning strategy), then the coefficients ϵ_ℓ should vary approximately as powers ℓ^m . In this highly simplified model,

$$\epsilon_\ell \approx \epsilon_2 \ell^2 + \epsilon_4 \ell^4, \quad (6.6)$$

and so the coefficients ϵ_2 and ϵ_4 , together with Eqs. 6.5b-6.5c describe TP leakage. In the *Planck* 2015 analyses, we did not at that time have estimates of the full polarized beam matrices of Eq. 6.2 and so we used this simplified model to roughly characterise TP leakage. We will revisit this model in Sect. 6.4.

6.2 Intra-frequency residuals in temperature

The detset spectra provide a good test of the accuracy of beams, calibrations and other instrumental systematics. As discussed in Sect. 4.4 of [99] based on the consistency of the Solar dipole solutions, errors in the absolute calibration of *Planck* over the 100–217 GHz frequency range are extremely small ($\lesssim 3 \times 10^{-4}$) and have negligible impact on the power spectra. The formal errors on the main beam calibrations are also small (see Fig. 21 of PPL15) and are neglected in this paper. However errors in characterising the beams beyond the main beams (at $\theta \gtrsim 100'$) introduce beam transfer function errors at multipoles $\ell \lesssim 100$. At the power spectrum level, such errors will appear to be nearly degenerate with multiplicative (i.e. effective calibration) errors in the power spectra. To test for such errors, we investigate intra-frequency residuals using the detsets. Excluding auto spectra, the detsets provide $N_s = 10\,143 \times 143$

cross spectra, 15 217×217 and 30 143×217 cross spectra. Since the foregrounds are the same in each of these frequency groups, the cross spectra within each group should be identical provided beam, calibration, band-pass mismatch and other systematics are negligible.

To test this, we minimise

$$\chi^2 = \sum_{ij \subset k} \sum_{\ell_{\min}}^{\ell_{\max}} \left(\psi_{ij} \hat{D}_\ell^{ij} - 1/N_s \sum_{pq \subset k} \psi_{pq} \hat{D}_\ell^{pq} \right)^2, \quad (6.7)$$

with respect to the coefficients ψ_{ij} for all N_s TT detset cross spectra within frequency group k . We impose the constraint that $\psi_{ij} = 1$ for the first cross spectrum within the frequency group (with detsets ordered as in Table 2) computed using our default masks. (For example, we fix $\psi_{56} = 1$ for the $143-5 \times 143-6$ cross spectrum). The χ^2 in Eq. 6.7 is unnormalised, since the dominant source of variance at multipoles $\ell \lesssim 1000$ comes from systematic errors in the far-field beams. Note that this differs from our analysis of intra-frequency residuals in PLP13, where we minimised to fit detset calibration coefficients, c_i , at the map level. At that stage in the Planck analysis, the beam transfer functions beyond the main beams had not been characterised accurately, which led to relatively large 1–2% effective calibration differences which were easily detectable in the power spectra.

Results are shown in Fig. 6.1. The upper panel in each figure shows the residuals of the beam corrected cross spectra as measured from the detset maps relative to the mean spectrum $\langle D_\ell \rangle$ within each frequency group¹³. The middle and lower plots in each panel show the corrected spectra $\psi_{ij} \hat{D}_\ell^{ij}$ minimising Eq. 6.7 over the multipole ranges $50 \leq \ell \leq 500$ and $500 \leq \ell \leq 1000$ respectively. We draw the following conclusions:

- For the 143×143 and 143×217 spectra, small calibration changes significantly reduce the scatter between the detset spectra with no systematic difference between SWB×SWB, SWB×PSB and PSB×PSB spectra. The corrections, ψ_{ij} , are stable with respect to multipole range and are almost identical for the two multipole ranges shown.
- For the 217×217 cross spectra, we see a systematic separation between the SWB×SWB, SWB×PSB and PSB×PSB spectra that remains after minimisation of Eq. 6.7. The figures to the right show what happens if we subtract the odd-even difference spectra (see Sect. 5.2) detset-by-detset as a proxy for correlated noise. As can be seen, subtracting these corrections increases the noise levels at high multipoles. Nevertheless, most of the difference between SWB×SWB and SWB×PSB in the 217×217 spectra is removed with this correction. The remaining differences between the spectra are largely removed after minimisation of Eq. 6.7.
- Correlated noise has no detectable effect on the 143×143 and 143×217 cross spectra.

The multiplicative factors ψ_{ij} determined from Eq. 6.7 are all extremely close to unity. The means and standard deviations about the mean are as follows: $\overline{\psi_{ij}} = 1.0014$, $\sigma_\psi = 7.77 \times 10^{-4}$ for 143×143 ; $\overline{\psi_{ij}} = 1.00057$, $\sigma_\psi = 7.59 \times 10^{-4}$ for 217×217 ; $\overline{\psi_{ij}} = 1.00074$, $\sigma_\psi = 8.1 \times 10^{-4}$ for 143×217 . These numbers are for minimising Eq. 6.7 over the multipole range $50 \leq \ell \leq 500$ with no corrections of the spectra for correlated noise (and are very similar for all of the fits shown in Fig. 6.1).

These results show that in temperature the QuickPol beam transfer functions have small residual errors at low multipoles which are largely absorbed by multiplicative calibration factors of order 0.1% in the power spectra. Correlated noise is responsible for part of the

¹³We show residuals relative to the mean spectrum rather than to a theoretical model to eliminate residuals from cosmic variance and foregrounds.

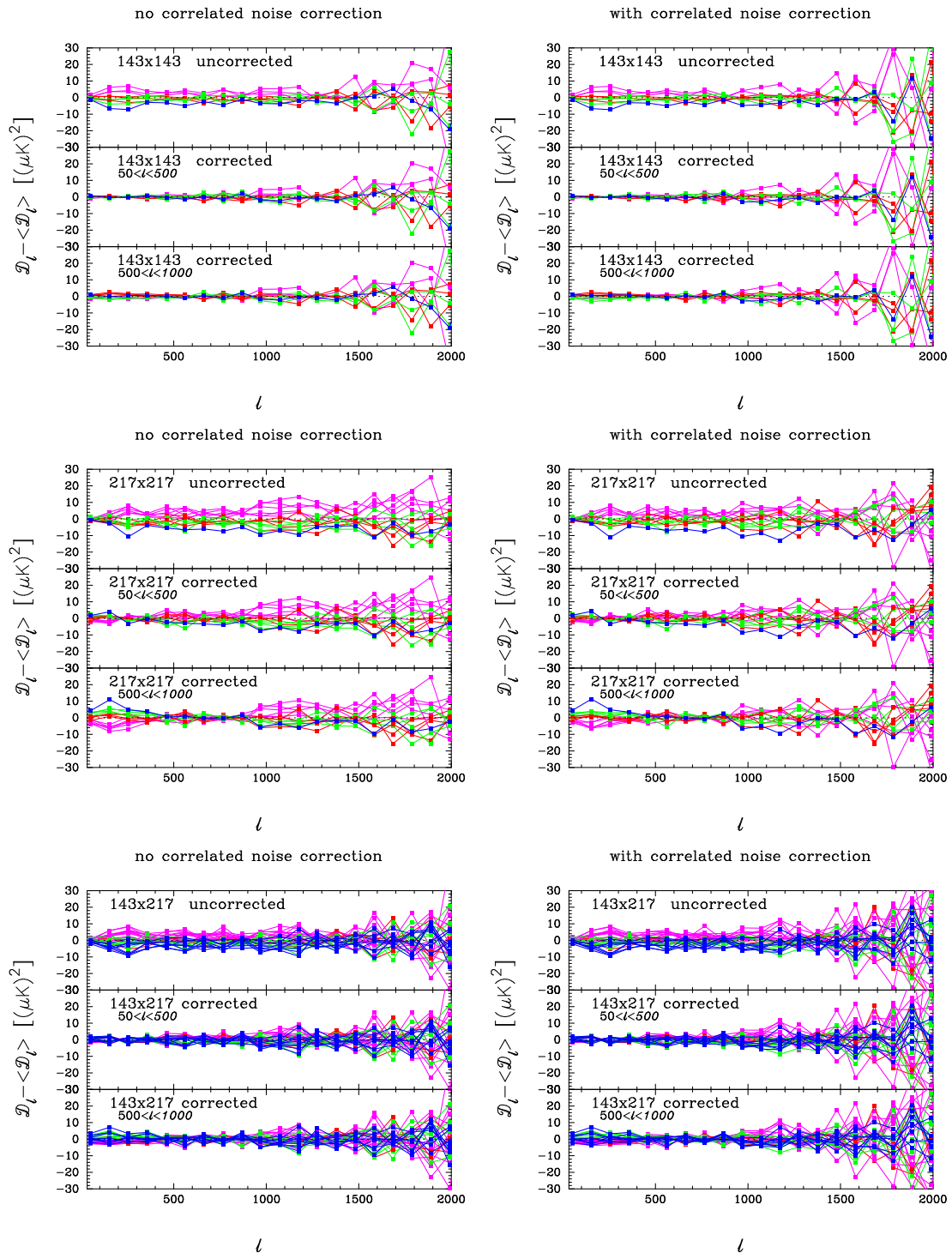


Figure 6.1. Intra-frequency residuals for the detset 143×143 , 217×217 and 143×217 TT spectra. The spectra are colour coded as follows, SWB \times SWB spectra are in purple, SWB \times PSB in green and PSB \times PSB in blue. $\langle D_\ell \rangle$ is the mean of the spectra within each frequency group. In each panel, the top figure shows the raw spectra, the middle figure shows the corrected spectra with multiplicative corrections ψ_{ij} determined by minimising Eq. 6.7 over the multipole range $50 \leq \ell \leq 500$, the lower figure shows results of minimisation over the multipole range $500 \leq \ell \leq 1000$. The panels to the left show the cross spectra as measured from the maps with no correction for correlated noise. The panels to the right show what happens if we subtract the odd-even difference spectra detset-by-detset as an indicator of correlated noise.

mismatch in the 217×217 spectra shown in Fig. 6.1. After correction for correlated noise and multiplicative corrections, there is perhaps a hint of a transfer function difference between the 217×217 PSB \times PSB spectrum and the other detset spectra, but any difference is small and unimportant for cosmology. These results demonstrate that the intra-frequency spectra are consistent to extremely high accuracy.

6.3 Relative calibrations of polarization spectra: effective polarization efficiencies

Since there is a degeneracy between polarization efficiencies and polarization angles (cf. Eq. 6.1), the SRoll mapmaking algorithm assumes the ground based calibrations of [113]. The combined systematic and statistical errors in the polarization efficiencies are uncertain and may be as high as a few percent. Errors in the polarization efficiencies will show up as multiplicative calibration factors in the TE and EE spectra. However, by intercomparing power spectra, we measure *effective polarization efficiencies*, because of the degeneracy between polarization angles and polarization efficiencies in the map making stage and because of transfer functions caused by errors in modelling the beams beyond the main beam. The relative calibrations discussed here should be interpreted in this light and should not be interpreted as bolometer polarization efficiencies.

Our analysis of polarization efficiencies differs from the TT calibration analysis described in the previous section. Since we have many fewer detset EE spectra than TT spectra within a frequency combination (one only for each of 100×100 , 143×143 and 217×217), we cannot minimise intra-frequency residuals between detset spectra to fix calibration coefficients. However, apart from Galactic dust emission, there are no other foreground contributions detectable in the *Planck* TE and EE spectra. We can therefore perform *inter-frequency* comparisons of TE and EE spectra to determine effective polarization efficiencies with polarized dust emission removed using 353 GHz maps as templates. The dust subtraction is discussed in detail in Sect. 8. In addition, the TE and EE spectra are corrected for TP leakage using Eqs 6.3a-6.3b with the QuickPol polarized beams assuming the best fit base Λ CDM TT, TE and EE spectra for the 12.1HM TT likelihood (which we will henceforth refer to as the fiducial theoretical model). Tests of the TP leakage model are discussed in Sect. 6.4. The analysis described in this section has been done for both half mission and detset spectra, though for reasons of economy we present only the half mission results.

Since the TE and EE spectra are noisy, we determine calibration factors c_k^{TE} and c_k^{EE} for each TE and EE spectrum by minimising the residuals with respect to the theoretical TE and EE spectra of the fiducial cosmology. For either TE or EE we therefore minimise

$$\chi^2 = \sum_{\ell_1 \ell_2} (\hat{C}_{\ell_1}^k - c_k C_{\ell_1}^{\text{theory}})(M^k)^{-1}_{\ell_1 \ell_2} (\hat{C}_{\ell_2}^k - c_k C_{\ell_2}^{\text{theory}}), \quad (6.8)$$

with respect to c_k , where the index k identifies the spectrum, M^k is the covariance matrix for spectrum k and C_{ℓ}^{theory} is the relevant theoretical spectrum. This gives:

$$c_k = \sum_{\ell_1 \ell_2} C_{\ell_1}^{\text{theory}} (M^k)^{-1}_{\ell_1 \ell_2} \hat{C}_{\ell_2}^k / \sum_{\ell_1 \ell_2} C_{\ell_1}^{\text{theory}} (M^k)^{-1}_{\ell_1 \ell_2} C_{\ell_2}^{\text{theory}}. \quad (6.9)$$

The sums in Eqs. 6.8 and 6.9 extend over the multipole ranges $\ell_{\min} \leq \ell_1 \leq \ell_{\max}$, $\ell_{\min} \leq \ell_2 \leq \ell_{\max}$. Note that with this definition of c_k , only theory terms enter in the denominator in Eq. 6.9 giving reasonably stable estimates of c_k from the noisy *Planck* polarization spectra. Since

the χ^2 in Eq. 6.8 is correctly normalized, we can calculate error estimates on the coefficients c_k .

We apply this scheme first to the half mission EE spectra. The HM maps are labelled (1)-(6) in the order 100HM1, 100HM2, 143HM1, 143HM2, 217HM1, 217HM2, where HM1 refers to maps from the first half mission and HM2 to the second half mission. We exclude auto spectra and any other cotemporal spectra (e.g. 100HM1 \times 143HM1, 100HM2 \times 143HM2). This leaves nine EE spectra with map indices as given in the first column of Table 4. The next three columns give the best fit calibration factors and 1σ errors for fits over three multipole ranges. The numbers are stable with respect to multipole ranges and differ from unity by up to a few percent. In two cases, the best fit calibrations exceed unity (which is possible given that `SRoll` assumes the polarization efficiencies of reference [113]). Our results are consistent with the conclusions of [99] and PPL18, namely that systematic errors in the HFI effective polarization calibrations are at the level of 1% or more, i.e. several times larger than the statistical errors on the detector polarization efficiencies quoted in [113]¹⁴.

Table 4. Relative calibrations of half mission EE spectra

Spectrum	EE index	200 – 1000	200 – 1500	500 – 1000
100HM1x100HM2	(1,2)	0.978 ± 0.010	0.979 ± 0.011	0.978 ± 0.019
100HM1x143HM2	(1,4)	1.010 ± 0.008	1.010 ± 0.008	1.013 ± 0.014
100HM1x217HM2	(1,6)	0.958 ± 0.010	0.960 ± 0.010	0.949 ± 0.016
100HM2x143HM1	(2,3)	0.998 ± 0.008	0.998 ± 0.008	1.011 ± 0.013
100HM2x217HM1	(2,5)	0.956 ± 0.010	0.954 ± 0.010	0.960 ± 0.016
143HM1x143HM2	(3,4)	1.034 ± 0.006	1.037 ± 0.006	1.043 ± 0.010
143HM1x217HM2	(3,6)	0.982 ± 0.008	0.985 ± 0.008	0.966 ± 0.011
143HM2x217HM1	(4,5)	0.985 ± 0.008	0.985 ± 0.008	0.984 ± 0.012
217HM1x217HM2	(5,6)	0.959 ± 0.010	0.960 ± 0.009	0.930 ± 0.014

Table 5 summarizes results on the effective calibrations of the half mission TE spectra. As with the EE spectra, the calibration coefficients are close to unity to within 2–3% and are relatively insensitive to the multipole ranges used in the fits. There is, however, a tendency for smaller effective calibrations if multipoles $\ell < 500$ are excluded from the fits. This suggests that treating the TE efficiency factors as purely multiplicative may be an oversimplification. (The 143HM1 \times 143HM2 TE spectrum is the worst offender, though most of the spectra show a similar trend.)

We now ask whether we can relate the numbers in Tables 4 and 5. Section 6.2 demonstrates that any effective calibration errors in the TT maps are negligible compared to the polarization calibrations given in Tables 4 and 5. We can therefore assume that the temperature maps are perfect and that any deviations from unity in the TE calibrations listed in Table 5 are caused by effective polarization efficiencies, ρ_i . With this assumption, we can group the TE spectra into triplets giving an effective polarization efficiency for each map. The results are summarized in Table 6 (for which we use the calibrations from Table 5 computed over the multipole range $200 \leq \ell \leq 1000$).

Notice the good agreement between the numbers within each triplet, which are consistent to $\lesssim 0.005$ (i.e. significantly better than the errors of 0.010 – 0.013 given in Table 5). The

¹⁴Note that at the power spectrum level, the errors are doubled relative to the map level.

Table 5. Relative calibrations of half mission TE spectra

Spectrum	TE index	200 – 1000	200 – 1500	500 – 1000
100HM1x100HM2	(1,2)	0.990 ± 0.013	0.986 ± 0.012	0.984 ± 0.022
100HM1x143HM2	(1,4)	1.005 ± 0.010	1.004 ± 0.010	0.980 ± 0.015
100HM1x217HM2	(1,6)	0.987 ± 0.012	0.988 ± 0.011	0.971 ± 0.015
100HM2x143HM1	(2,3)	1.010 ± 0.011	1.010 ± 0.010	1.010 ± 0.016
100HM2x217HM1	(2,5)	0.969 ± 0.013	0.974 ± 0.012	0.967 ± 0.020
143HM1x143HM2	(3,4)	1.002 ± 0.010	1.002 ± 0.009	0.977 ± 0.015
143HM1x217HM2	(3,6)	0.991 ± 0.012	0.988 ± 0.011	0.980 ± 0.018
143HM2x217HM1	(4,5)	0.971 ± 0.013	0.972 ± 0.012	0.968 ± 0.019
217HM1x217HM2	(5,6)	0.995 ± 0.012	0.992 ± 0.012	0.990 ± 0.019
100HM1x100HM2	(2,1)	0.982 ± 0.014	0.984 ± 0.013	0.966 ± 0.023
100HM1x143HM2	(4,1)	0.978 ± 0.014	0.980 ± 0.013	0.957 ± 0.023
100HM1x217HM2	(6,1)	0.980 ± 0.014	0.982 ± 0.014	0.964 ± 0.024
100HM2x143HM1	(3,2)	0.979 ± 0.013	0.983 ± 0.013	0.966 ± 0.022
100HM2x217HM1	(5,2)	0.985 ± 0.014	0.989 ± 0.013	0.966 ± 0.023
143HM1x143HM2	(4,3)	1.012 ± 0.011	1.013 ± 0.010	1.012 ± 0.016
143HM1x217HM2	(6,3)	1.008 ± 0.011	1.010 ± 0.010	1.007 ± 0.017
143HM2x217HM1	(5,4)	1.007 ± 0.011	1.008 ± 0.009	0.981 ± 0.016
217HM1x217HM2	(6,5)	0.973 ± 0.014	0.974 ± 0.012	0.970 ± 0.020

Table 6. Effective polarization efficiencies

Map	k	$\bar{\rho}_k$					
100HM1	1	(2,1) 0.982	(4,1) 0.978	(6,1) 0.980	0.980		
100HM2	2	(1,2) 0.990	(3,2) 0.979	(5,2) 0.985	0.984		
143HM1	3	(2,3) 1.010	(4,3) 1.012	(6,3) 1.008	1.007		
143HM2	4	(1,4) 1.005	(3,4) 1.002	(5,4) 1.007	1.005		
217HM1	5	(2,5) 0.969	(4,5) 0.971	(6,5) 0.973	0.971		
217HM2	6	(1,6) 0.987	(3,6) 0.991	(5,6) 0.995	0.991		

last column in Table 6 gives the average value of the calibrations for each triplet, $\bar{\rho}_k$, which we take as our estimate of the effective polarization efficiency for each half mission map. Note also that these polarization efficiencies pair up by frequency. The ground based polarization efficiencies measured by [113] are strongly correlated within a frequency band, and so our results suggest that systematic biases in the ground based calibrations are similar for all detectors within a frequency band.

From these effective polarization efficiencies, we can try to predict the calibrations c_{ij} for each EE spectrum listed in Table 4:

$$c_{ij}^{\text{pred}} = \bar{\rho}_i \bar{\rho}_j. \quad (6.10)$$

The results are summarized in Fig. 6.2.

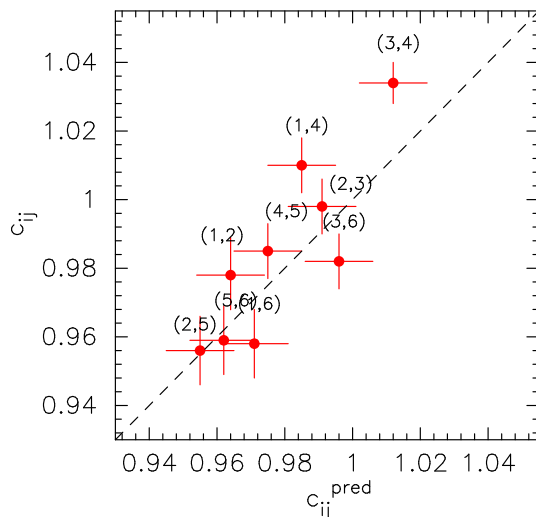


Figure 6.2. Calibrations of the EE spectra from Table 4 with 1σ errors plotted against the predicted coefficients from Eq. 6.10. We have assigned a nominal 1σ error of ± 0.01 on c_{ij}^{pred} . Each point is labelled with the map indices i, j as in Table 4.

There is a strong correlation between the measured calibration coefficients c_{ij} for the EE spectra and those predicted from Eq. 6.10. This is consistent with the idea that the effective calibrations measured from the EE and TE spectra come mainly from systematic errors in the ground based polarization efficiency calibrations. The correlation in Fig. 6.2 is not perfect, however, and is not expected to be perfect since errors in polarization efficiencies are strongly coupled to errors in polarization angles and far-field polarized beams.

In the `CamSpec` half mission likelihoods, we apply the calibration factors from Tables 4 and 5 to the EE and TE half mission spectra prior to coaddition. For the full mission detset likelihoods, we apply corrections determined from a similar analysis using all detset polarization spectra. Since these calibrations are computed with respect to a theoretical model determined from the TT likelihood, amplitude parameters determined from the TE and EE likelihoods are not strictly independent of those determined from TT. Furthermore, as can be seen from Tables 4, 5 and Fig. 6.2, the calibration factors applied are accurate to no better than about a percent. We therefore include calibration factors c^{EE} and c^{TE} for the coadded EE and TE spectra which are treated as nuisance parameters in the likelihood, with priors as given in Table 10.

The scheme discussed above for estimating polarization efficiencies in `CamSpec` differs from that used in the `Planck` likelihood (described in PPL18). The publically distributed `Planck` likelihood code with its default settings uses effective polarization efficiencies determined from the EE spectra which are then applied to the TE spectra¹⁵ on the assumption that the efficiencies are ‘map based’. With this procedure, TE spectra involving 143 GHz receive a large (and uncertain) polarization efficiency correction (see Table 4 and Fig. 6.2) which is not wanted by the TE spectra. In producing a TTTEEE likelihood it is essential that polarization efficiencies are corrected accurately in the TE spectra; errors in EE polarization efficiency corrections are of less importance, since the EE spectra are noisy and carry little statistical weight in a TTTEEE likelihood. In producing `CamSpec` we therefore corrected

¹⁵Which in `Planck` are symmetrized, i.e. $T^i E^j$ and $E^i T^j$ are averaged.

each TE/ET spectrum with the polarization efficiency corrections given in the third column of Table 5. We can also see from Table 6 that these efficiency corrections are consistent with map based coefficients $\bar{\rho}_k$. In fact, for each frequency we have six estimates of a map based effective polarization efficiency which are consistent to typically ± 0.005 . For **CamSpec** it would therefore make no difference to the TE likelihood had we adopted ‘map based’ polarization efficiencies rather than ‘spectrum based’ efficiencies. The results of this section show that our procedure for determining and correcting polarization efficiencies is strongly supported by the data. The differences in correcting polarization efficiencies are largely responsible for the differences between the **CamSpec** and **Planck** TTTEEE likelihoods for some cosmologies, in particular when the parameters A_L and Ω_K are allowed as extensions to the base Λ CDM cosmology (see Sect. 14 for further discussion). For these cosmologies, the **CamSpec** TTTEEE likelihood is more reliable than the **Planck** likelihood with its default settings.

6.4 Tests of the temperature-polarization leakage model

Beam mismatch introduces temperature-to-polarization (TP) leakage in the *Planck* maps, which can be characterised by the polarized beam matrix of Eq. 6.2. For the TE spectra, TP leakage has a small but non-negligible effect on cosmology. For the EE spectra, TP leakage is small compared to the EE noise and can be safely neglected. In this section, we test the *Planck* polarized beam model for the TE spectra. As in the previous section, we assume that the temperature maps are perfect. We can then arrange the TE HM spectra, uncorrected for beam leakage, into triplets as in Table 6 and search for correlated residuals. These residuals should be caused by temperature leakage into the (Q,U) maps, which are identical within each triplet. We therefore expect that these residuals should match up with the residuals computed from the polarized beam matrix.

This test is illustrated in Fig. 6.3. The TE spectra shown in this figure are divided by the calibration coefficients given in Table 5. In each panel, we show the residuals of the TE spectra in each triplet relative to the mean TE spectrum computed from all 18 cross spectra (weighted by the diagonals of the covariance matrices as in Eq. 2.11). Subtracting the mean TE spectrum reduces scatter from cosmic variance in these plots. The residuals within each panel match up extremely well. Furthermore, the patterns of these residuals are very similar for polarization maps with the same frequency, as expected from the **QuickPol** polarized beam matrix. The dotted lines in Fig. 6.3 show the residuals computed from the polarized beams assuming the fiducial base Λ CDM cosmology. (These dotted lines are the TP corrections applied to the TE spectra in the **CamSpec** half mission likelihoods used in this paper.) The TP corrections computed from the polarized beams provide a good match to the TE residuals and have nearly identical shapes within each triplet. The solid lines show fits of the model of Eqs. 6.5b and 6.6 to the data points with ϵ_2 and ϵ_4 as free parameters. This simple model provides a good match to the polarized beam TP leakage model, except at high multipoles where the TE spectra become noise dominated.

The tests shown in Fig. 6.3 provide strong evidence that the polarized beams accurately account for TP leakage in the TE spectra. If we coadd the 18 half mission TE spectra, the TP leakage corrections partially cancel so that the net effect of TP leakage is relatively small. If we ignore TP leakage entirely in the **CamSpec** TTTEEE likelihoods we find shifts of up to 1σ in base Λ CDM parameters in agreement with the **Planck** results reported in PCP18 and PPL18. Given the tests shown in Fig. 6.3 we can be confident that the TP corrections applied to the **CamSpec** spectra are reasonably accurate and that any errors in these corrections have

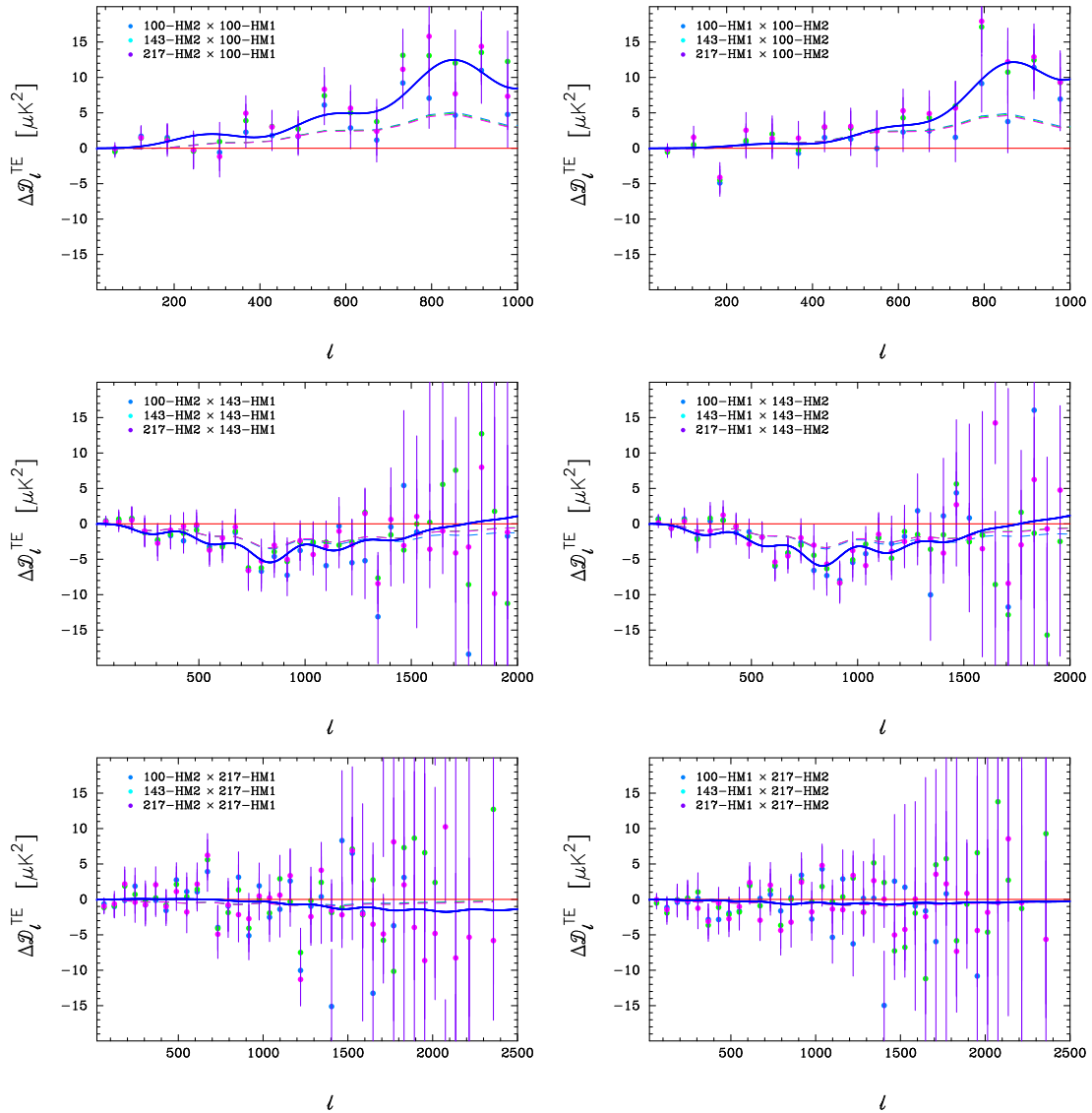


Figure 6.3. TE half mission spectrum residuals (mask and beam deconvolved and corrected for effective polarization efficiencies) organized into triplets. Each triplet corresponds to a distinct polarization half mission map (e.g. top left is 100HM1 and bottom right is 217HM2). The dotted lines show the TP leakage computed from the polarized beams as described in the text. The solid lines show a fit to the leakage based on Eqs. 6.5b and 6.6. The error bars show $\pm 1\sigma$ errors computed from the CamSpec covariance matrices.

significantly less than 1σ impact on cosmological parameters. The beam-derived TP leakage corrections for the EE spectra are negligible and have no impact on cosmology.

In summary, the results of this section show that the main systematic in the *Planck* polarization spectra is caused by errors in the polarization efficiencies assumed in SRoll and errors in the far-field *Planck* beams. These effects can be accurately modelled by multiplicative calibration factors (effective polarization efficiencies) applied to each of the TE and EE spectra. TP leakage is a subdominant effect and we have demonstrated via internal consistency tests that TP leakage is described accurately by the QuickPol polarized beam matrices.

7 Galactic dust emission in temperature

To extract cosmology from CMB experiments, Galactic and extragalactic foregrounds need to be removed to high accuracy to reveal the primary CMB anisotropies. There is a large literature on foreground cleaning methods which will not be reviewed here. Various techniques have been applied to the *Planck* data, and are described in [79, 86, 106] (to which we refer the reader for details, including references to earlier work). Broadly speaking, the methods can be divided into two classes: methods such as Commander [35, 36], which fit a parametric model of foreground spectral energy distributions to a set of maps at different frequencies, and template fitting methods which are based on linear combinations of pixelised maps (or ‘needlets’ in the multipole domain) at different frequencies (e.g. ILC, SMICA, SEVEM, NILC)¹⁶. In contrast to these techniques, in the CamSpec likelihood we remove foregrounds by fitting parametric foreground models to the power spectra over a range of frequencies. By using power spectra, it is possible to fit foreground components such as the cosmic infrared background (CIB) which decorrelate with frequency (see [91]). Such foregrounds cannot be cleaned by conventional map based techniques. In addition, we can make use of the fact that Galactic dust emission is anisotropic on the sky, whereas extragalactic foregrounds are isotropically distributed. It is then straightforward to use power spectra computed on different areas of sky to separate Galactic dust emission from the CIB (see [67]). A further advantage is that a parametric foreground model is ‘controllable’, in the sense that we can investigate power spectrum residuals for each frequency combination to assess whether a physically reasonable foreground model (compatible with external data) provides an acceptable fit to the measured power spectra.

At all HFI frequencies, Galactic dust emission is the dominant foreground at low multipoles ($\ell \lesssim 500$). In this section, which focusses on temperature (polarized foregrounds are discussed in Sect. 8), we investigate the properties of Galactic dust emission in more detail to assess: (a) the ‘universality’ of dust emission, i.e. the accuracy with which a *Planck* high frequency map can be used as a template with a single ‘cleaning’ coefficient to remove Galactic dust emission at a lower frequency; (b) the amplitude of dust emission at 100, 143 and 217 GHz; (c) the sensitivity of Galactic dust emission to point source masking; (d) the creation of power spectrum templates for Galactic dust emission; (e) impact of template cleaning on the 100, 143 and 217 GHz spectra.

¹⁶ILC: Internal Linear Combination [10]; SMICA: Spectral Matching Independent Component Analysis [20]; NILC: Needlet Internal Linear Combination [25]; SEVEM: Spectral Estimation Via Expectation Maximisation [37, 60].

7.1 Map-based cleaning coefficients

The simplest way of removing Galactic dust from the 100-217 GHz maps is to use one of the higher frequency maps as a dust template. The goal then is to determine an appropriate template cleaning coefficient. We have experimented with various different ways of determining cleaning coefficients. Two of these methods are based on minimising map residuals:

$$\sigma^2 = \sum_i ((1 + \alpha_m^{T\nu})M_i^\nu - \alpha_m^{T\nu}(M_i^T + c))^2, \quad (7.1a)$$

$$\sigma'^2 = \sum_i ((M_i^\nu - M_i^{\text{SMICA}}) - \alpha_{m'}^{T\nu}(M_i^T - M_i^{\text{SMICA}} + c'))^2, \quad (7.1b)$$

where the sums extend over all unmasked pixels. Here M_i^ν is the low frequency map, M_i^T is the high frequency ‘template’ map and M_i^{SMICA} is an estimate of the primordial CMB from the SMICA component separation algorithm. The masks used in these summations are the unapodised sequence of masks defined in Sect. 3.1, except that we *always exclude* the high Galactic latitude regions of sky defined by mask25¹⁷. In other words, the summations in Eqs. 7.1a and 7.1b are over *annuli* on the sky. This is done to reduce the impact of the CIB anisotropies on the scaling coefficients $\alpha_m^{T\nu}$ and $\alpha_{m'}^{T\nu}$. (The relative importance of CIB anisotropies compared to Galactic dust emission is discussed in Sect. 11.2.) We remove bright point sources, extended objects and CO emission by multiplying the three ‘point source’ masks at 100, 143 and 217 GHz shown in Fig. 3.1. By using a concatenated point source mask, the masks are identical for all frequencies. Note that the point source masks have a small effect on the shapes of the dust power spectra, as discussed in Sect. 7.2, but have little effect on the template coefficients derived from Eqs. 7.1a and 7.1b. The constants c and c' are included in Eqs. 7.1a and 7.1b to model the uncertainties in the absolute zero levels of the high frequency maps. Note further that the Planck 857 and 545 GHz maps are calibrated in MJy sr⁻¹. Throughout this paper, we convert these high frequency maps into units of thermodynamic temperature in μK by dividing the 857 and 545 GHz maps by factors of 2.269 and 57.98 respectively as described in [91].

In Eq. 7.1a, the maps are uncorrected for CMB anisotropies. In Eq. 7.1b we subtract the *Planck* SMICA component separated CMB map [79] from the low frequency maps to remove primordial CMB anisotropies¹⁸. To reduce sensitivity to noise and foreground contributions at high multipoles, we first smooth all of the (unmasked) maps to a common resolution with a Gaussian of FWHM of one degree. This smoothing has almost no effect on the cleaning coefficients determined using 545 and 857 GHz as templates (since these maps are effectively noise-free), but gives more stable results if 353 GHz is used as a template. The form of Eq. 7.1a is chosen to reduce the sensitivity of the CMB component on the recovered cleaning coefficients. However, Eq. 7.1a will lead to biased coefficients. If we write

$$M^\nu = S + \beta F, \quad (7.2a)$$

$$M^{\nu T} = S + F, \quad (7.2b)$$

where S is the CMB signal and F is the foreground, then it is straightforward to show that if CMB-foreground cross-correlations are negligible, then minimising Eq. 7.1a leads to a biased

¹⁷Interestingly, mask25 roughly delineates the ‘shore line’ where the CIB dominates over Galactic dust emission at 217 GHz.

¹⁸For the purposes of this section, it makes no difference whether we use the SMICA component separated map, or any of the other component separated maps discussed in [79].

Table 7. Template cleaning coefficients: The first column gives the sky area used to compute the cleaning coefficients. The map residuals are minimised within ‘annuli’ in which the high Galactic latitude sky defined by mask25 is excluded. The second and third columns list map-based cleaning coefficients computed by minimising Eqs. 7.1a and 7.1b. The fourth column lists the spectrum-based cleaning coefficients computed by minimising Eq. 7.8 over the multipole range $100 \leq \ell \leq 500$, where Galactic dust emission dominates over the CIB. The coefficients listed in boldface were used to generate the ‘fake’ maps shown in Fig. 7.3.

217 cleaned with 857	$\alpha_m^T/(1 + \alpha_m^T)$	$\alpha_{m'}^T$		$\alpha_s^T/(1 + \alpha_s^T)$
mask50-mask25	9.45×10^{-5}	9.46×10^{-5}	mask50	1.02×10^{-4}
mask60-mask25	9.85×10^{-5}	9.64×10^{-5}	mask60	1.02×10^{-4}
mask70-mask25	1.06×10^{-4}	1.00×10^{-4}	mask70	1.03×10^{-4}
mask80-mask25	1.04×10^{-4}	1.02×10^{-4}	mask80	1.03×10^{-4}
217 cleaned with 545	$\alpha_m^T/(1 + \alpha_m^T)$	$\alpha_{m'}^T$		$\alpha_s^T/(1 + \alpha_s^T)$
mask50-mask25	7.33×10^{-3}	7.47×10^{-3}	mask50	7.83×10^{-3}
mask60-mask25	7.67×10^{-3}	7.55×10^{-3}	mask60	7.86×10^{-3}
mask70-mask25	8.15×10^{-3}	7.67×10^{-3}	mask70	7.91×10^{-3}
mask80-mask25	7.95×10^{-3}	7.81×10^{-3}	mask80	7.77×10^{-3}
217 cleaned with 353	$\alpha_m^T/(1 + \alpha_m^T)$	$\alpha_{m'}^T$		$\alpha_s^T/(1 + \alpha_s^T)$
mask50-mask25	1.27×10^{-1}	1.30×10^{-1}	mask50	1.32×10^{-1}
mask60-mask25	1.31×10^{-1}	1.30×10^{-1}	mask60	1.32×10^{-1}
mask70-mask25	1.38×10^{-1}	1.31×10^{-1}	mask70	1.32×10^{-1}
mask80-mask25	1.36×10^{-1}	1.33×10^{-1}	mask80	1.32×10^{-1}
143 cleaned with 857	$\alpha_m^T/(1 + \alpha_m^T)$	$\alpha_{m'}^T$		$\alpha_s^T/(1 + \alpha_s^T)$
mask50-mask25	2.83×10^{-5}	2.68×10^{-5}	mask50	2.55×10^{-5}
mask60-mask25	3.09×10^{-5}	2.77×10^{-5}	mask60	2.27×10^{-5}
mask70-mask25	3.41×10^{-5}	2.91×10^{-5}	mask70	2.52×10^{-5}
mask80-mask25	3.07×10^{-5}	3.02×10^{-5}	mask80	2.83×10^{-5}
143 cleaned with 545	$\alpha_m^T/(1 + \alpha_m^T)$	$\alpha_{m'}^T$		$\alpha_s^T/(1 + \alpha_s^T)$
mask50-mask25	2.11×10^{-3}	2.12×10^{-3}	mask50	1.97×10^{-3}
mask60-mask25	2.39×10^{-3}	2.18×10^{-3}	mask60	1.76×10^{-3}
mask70-mask25	2.60×10^{-3}	2.23×10^{-3}	mask70	1.92×10^{-3}
mask80-mask25	2.35×10^{-3}	2.30×10^{-3}	mask80	2.11×10^{-3}
143 cleaned with 353	$\alpha_m^T/(1 + \alpha_m^T)$	$\alpha_{m'}^T$		$\alpha_s^T/(1 + \alpha_s^T)$
mask50-mask25	3.57×10^{-2}	3.71×10^{-2}	mask50	3.36×10^{-2}
mask60-mask25	4.05×10^{-2}	3.78×10^{-2}	mask60	3.01×10^{-2}
mask70-mask25	4.40×10^{-2}	3.81×10^{-2}	mask70	3.26×10^{-2}
mask80-mask25	3.98×10^{-2}	3.91×10^{-2}	mask80	3.54×10^{-2}
100 cleaned with 857	$\alpha_m^T/(1 + \alpha_m^T)$	$\alpha_{m'}^T$		$\alpha_s^T/(1 + \alpha_s^T)$
mask50-mask25	1.78×10^{-5}	1.61×10^{-5}	mask50	1.79×10^{-5}
mask60-mask25	1.91×10^{-5}	1.59×10^{-5}	mask60	1.60×10^{-5}
mask70-mask25	2.30×10^{-5}	1.80×10^{-5}	mask70	1.67×10^{-5}
mask80-mask25	2.21×10^{-5}	2.17×10^{-5}	mask80	1.88×10^{-5}
100 cleaned with 545	$\alpha_m^T/(1 + \alpha_m^T)$	$\alpha_{m'}^T$		$\alpha_s^T/(1 + \alpha_s^T)$
mask50-mask25	1.26×10^{-3}	1.26×10^{-3}	mask50	1.33×10^{-3}
mask60-mask25	1.45×10^{-3}	1.25×10^{-3}	mask60	1.20×10^{-3}
mask70-mask25	1.76×10^{-3}	1.38×10^{-3}	mask70	1.26×10^{-3}
mask80-mask25	1.68×10^{-3}	1.64×10^{-3}	mask80	1.40×10^{-3}
100 cleaned with 353	$\alpha_m^T/(1 + \alpha_m^T)$	$\alpha_{m'}^T$		$\alpha_s^T/(1 + \alpha_s^T)$
mask50-mask25	2.05×10^{-2}	2.21×10^{-2}	mask50	2.23×10^{-2}
mask60-mask25	2.43×10^{-2}	2.16×10^{-2}	mask60	2.00×10^{-2}
mask70-mask25	2.96×10^{-2}	2.37×10^{-2}	mask70	2.11×10^{-2}
mask80-mask25	2.86×10^{-2}	2.79×10^{-2}	mask80	2.35×10^{-2}

cleaning coefficient with

$$\alpha_m^{T_\nu} = \frac{\beta}{(1 - \beta)}. \quad (7.3)$$

Since an estimate of the CMB is subtracted from the maps in Eq. 7.1b, the cleaning coefficients $\alpha_{m'}^{T_\nu}$ give an unbiased estimate of β . We therefore compare $\alpha_{m'}^{T_\nu}$ with $\alpha_m^{T_\nu}/(1 + \alpha_m^{T_\nu})$.

Results are listed in Table 7 for various masks. For all frequencies and templates we see a trend for the cleaning coefficients to increase with increasing sky area. We postpone a discussion of whether this trend indicates a departure of the dust properties from universality until Sect. 7.4. For 217 GHz, which is the most heavily dust-contaminated channel in the CamSpec likelihood, the cleaning coefficients vary by a few percent as the sky used changes from (mask50 – mask25) to (mask80 – mask25). At 100 GHz, the level of dust contamination is so low that it is difficult to derive an accurate cleaning coefficient using any of the high frequency templates. The cleaning coefficients derived from Eqs. 7.1a and 7.1b agree reasonably well, but we expect 7.1b to be more reliable since the cleaning coefficients are not biased by the CMB and CMB-foreground correlations.

7.2 Power spectrum of Galactic dust emission

We can eliminate all isotropic components, including the CMB, CIB, and extragalactic point sources by differencing the power spectra computed on different masks. Fig. 7.1 is similar to Fig. 3 of PPL13. This figure shows the mask-differenced HM1×HM2 spectra at 857, 545 and 353 GHz scaled to the amplitude of the foreground emission at 217 GHz using the coefficients listed in boldface in Table 7. We use the concatenated 100 – 217 GHz point source mask for the spectra in Fig. 7.1, consistent with the cleaning coefficients listed in Table 7. Since we are plotting mask-differenced spectra, the points plotted in Fig. 7.1 reflect the properties of *Galactic dust emission alone*. As can be seen, the rescaled 857, 545 and 353 GHz spectra match to high accuracy and are barely distinguishable in Fig. 7.1.

The solid line in Fig. 7.1 shows a fit of the 545 GHz points to a simple analytic fitting function. We use the same parametric form, Eq. 5.4, that was used to fit the *Planck* noise spectra. The second term in Eq. 5.4 fits the small ‘bump’ in the 545 GHz spectrum at multipoles $\ell \sim 300$. However, the dominant term is the power-law component $D_\ell^D = A(100/\ell)^\alpha$. The best fit parameters are $A = 90.661 (\mu\text{K})^2$, $\alpha = 0.6873$, $B = 14.402 (\mu\text{K})^2$, $\beta = 1.646$, $\ell_c = 100.73$, $\gamma = 3.283$, $\delta = 33.26$. Note that at high multipoles, the dust power spectrum falls off with a slope of $C_\ell \propto \ell^{-2.69}$, consistent with the power-law slope of approximately -2.7 to -2.8 inferred from a very different analysis [91] of the *Planck* data.

The pink points in Fig. 7.1 show the double-differenced $217 \times 217 - 143 \times 143$ power spectrum. The reason for plotting the double-difference is to suppress the large cosmic variance fluctuations in the primordial CMB contribution, which dominate over foreground fluctuations at frequencies ≤ 217 GHz. The double-differenced spectrum is corrected by a scaling factor to account for the small amplitude of dust emission in the 143×143 mask-differenced spectrum. As with the higher frequency spectra, the mask-differencing isolates Galactic dust emission from isotropic foregrounds. Evidently, Galactic dust emission at low frequencies is extremely well approximated by the model of Eq. 5.4. Over the same sky region, therefore, we have demonstrated that the power spectrum of Galactic dust emission has the same shape, to very high accuracy, over the wide frequency range 217 – 857 GHz.

We now investigate variations of the shape of the dust power spectra with changes in the sky area and point source mask. Fig. 7.2 shows mask-differenced power spectra for the 545 GHz half mission maps as a function of sky area for the 217, 143 and 100 point source

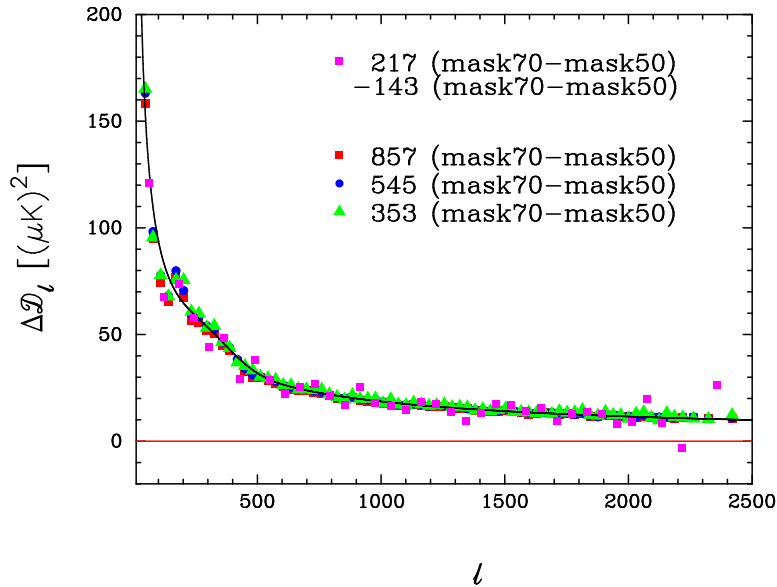


Figure 7.1. Differences of power spectra computed on mask70 and mask50 at 857, 545 and 353 GHz scaled to match the foreground emission at 217 GHz using the cleaning coefficients given by the bold-faced entries in Table 7. The pink points show the ‘double-differenced’ $217 \times 217 - 143 \times 143$ spectrum (renormalized to the dust amplitude of the 217×217 spectrum). The solid line shows a fit of the 545 GHz spectrum to the expression given in Eq. 5.4.

masks used in the cosmological analysis. The amplitudes of the spectra have been matched to the amplitude of the mask50-mask25 spectrum over the multipole range $500 \leq \ell \leq 1000$. The blue lines show the best-fit dust spectrum from Fig. 7.1. The 217 GHz point source mask is very similar to the concatenated point source mask used in Fig. 7.1, thus the fit provides a very good match to the 217 GHz spectra for sky areas up to mask70. There are, however, small differences in the shape of the dust spectrum computed on mask80 at lower frequencies. However, it would be incorrect to conclude that this is caused by variations in diffuse Galactic dust emission over the sky. One can see that the 545 GHz spectra using the 143 and 100 points source masks are nearly identical over 50-80% of sky. The 217 GHz point sources are distributed anisotropically over the sky (see Fig. 3.1) with a surface density that increases strongly at low Galactic latitudes. At low Galactic latitudes, where the dust emission is high and the background level varies strongly, dust knots become identified as point sources. The point source masks remove some of the dust emission from the unmasked sky causing the estimated dust spectra to steepen if one uses sky areas extending to low Galactic latitudes. This effect is less important for the 143 and 100 point source masks, because at these frequencies there is less contamination of the point source catalogues by knots of dust emission. However, the dust spectra computed using these point source masks are slightly shallower than the spectra measured using the 217 GHz point source masks. For this reason, we tailor the Galactic dust template spectra used in the CamSpec likelihoods to the identical point source masks used to compute the spectra (see Sect. 9.2).

The plot at the top left in Fig. 7.2 shows what happens if we apply no point source mask. These spectra show a dramatic departure from universality for mask70 and mask80. The excesses seen in these spectra arise from a small number ($\lesssim 100$) of extremely bright sources

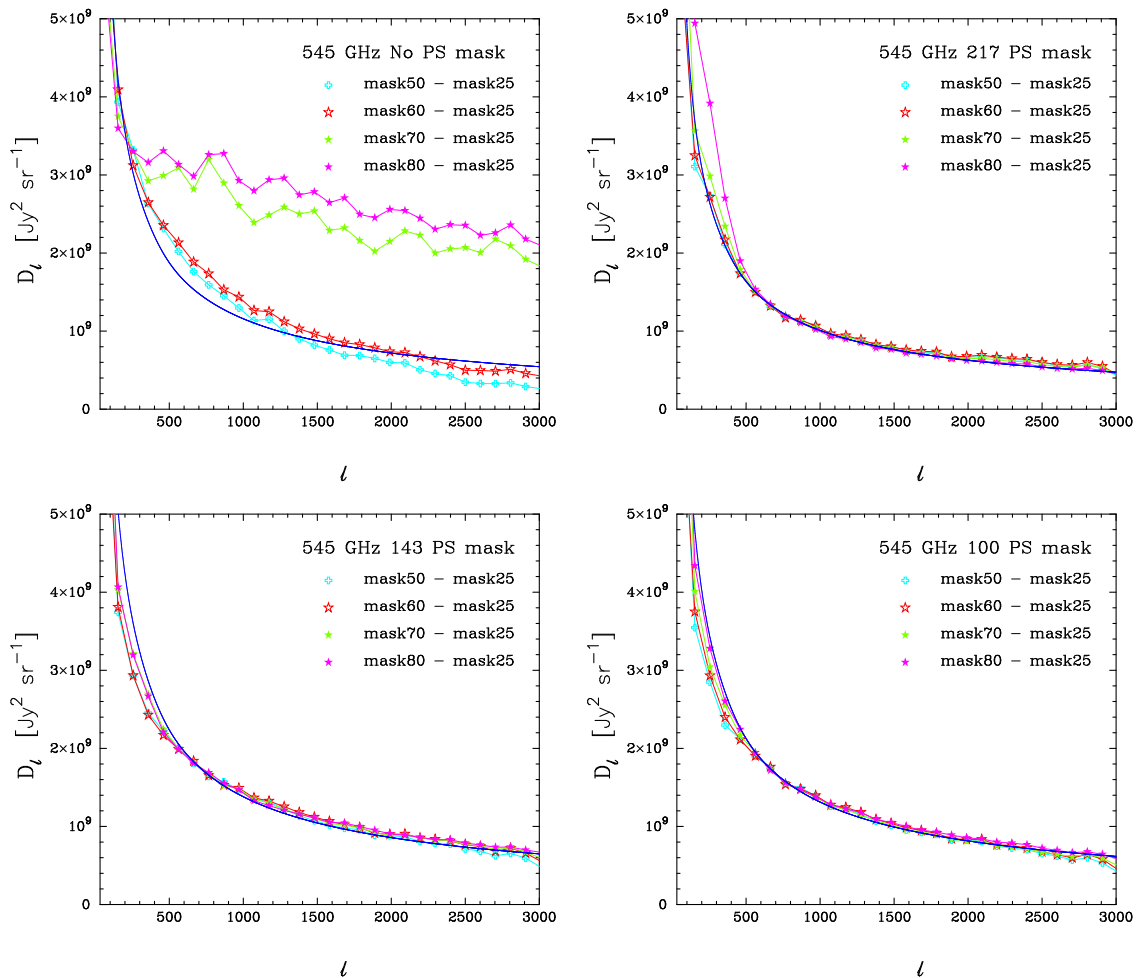


Figure 7.2. Differenced 545 GHz half mission spectra for various sky masks. For the figure at the top left no point source mask was applied. The other figures show spectra for the 217, 143 and 100 GHz point source masks as shown in Fig. 3.1. The blue-lines show the best-fit dust spectrum from Fig. 7.1.

(such as Centaurus A and compact knots of dust emission). These bright sources contaminate the *Planck* temperature power spectra over the entire HFI frequency range 100 – 857 GHz and must be removed for any meaningful science analysis.

Even though we have plotted a double-differenced spectrum at low frequencies in Fig. 7.1, the pink points show scatter that is much higher than the scatter of the higher frequency spectra. This scatter is also much higher than that expected from instrument noise. The excess scatter is caused by ‘chance’ CMB-foreground cross-correlations. Consider the simple model where the signal at frequency 1 is a sum of primordial CMB (denoted S) plus a contribution from a foreground F . We assume that frequency 2 is dominated by the foreground F :

$$M_1 = S + \alpha F, \quad (7.4a)$$

$$M_2 = F. \quad (7.4b)$$

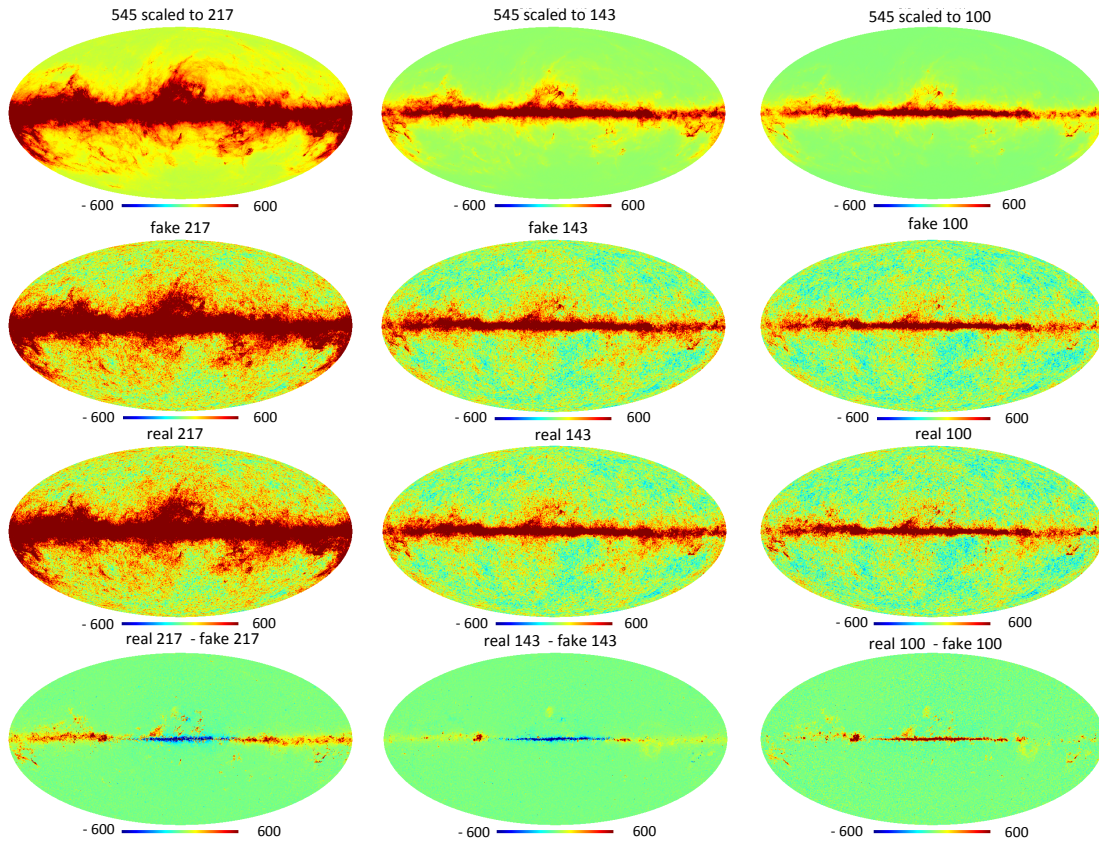


Figure 7.3. The top row shows the 545 GHz maps scaled to match the dust emission at 217, 143 and 100 GHz (left to right) using the boldface dust cleaning coefficients listed in Table 7. The second row shows the addition of the SMICA component separated CMB map to the scaled 545 GHz maps creating ‘fake’ maps at 217, 143 and 100 GHz. The third row shows the real maps at these frequencies. The bottom row shows the difference between the real and fake maps. The color scales are in units of μK .

Schematically, the power spectra of these two maps are

$$C_1 = S * S + 2\alpha S * F + \alpha^2 F * F, \quad (7.5a)$$

$$C_2 = F * F, \quad (7.5b)$$

and so the power spectrum of the low frequency map will contain a CMB-foreground cross-term. The excess scatter in the $217 \times 217 - 143 \times 143$ spectrum shown in Fig. 7.1 compared to the spectra at higher frequencies is caused by the CMB-foreground cross-terms, not by any intrinsic variation of the dust emission between low and high frequencies. We can demonstrate this conclusively by analysing ‘fake’ maps at 217, 143 and 100 GHz constructed by adding appropriately scaled 545 GHz maps to the SMICA half-mission CMB maps.

The top row of Fig. 7.3 shows the 545 GHz maps scaled to 217, 143 and 100 GHz respectively (with the best fit constant, c' , subtracted from each map). The second row shows the scaled 545 maps added to the SMICA component separated map to produce ‘fake’ 217, 143 and 100 GHz maps. The real maps are shown in the third row. The fourth row shows the differences between the real and the fake maps. The broad *Planck* frequency bands centred at 100 GHz and 217 GHz are contaminated by CO rotational transitions [83]

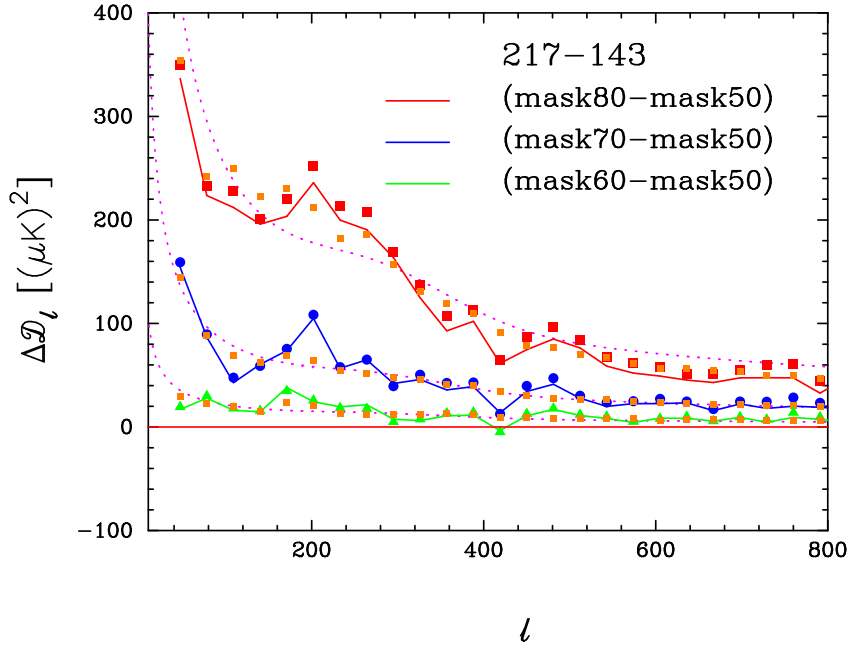


Figure 7.4. The filled green, blue and red points show the double-differenced $217 \times 217 - 143 \times 143$ half mission power spectra for various masks. These double-differences cancel the CMB and isotropic foreground components leaving only Galactic dust components. The orange points show the half mission power spectra computed from the 545 GHz maps, scaled to match the amplitudes of the $217 \times 217 - 143 \times 143$ spectra. The green, blue and red solid lines show the double-differenced power spectra computed from the ‘fake’ 217 and 143 GHz maps shown in Fig. 7.3. The dotted lines show the best-fit dust templates from Eq. 5.4 with amplitudes scaled to match the $217 \times 217 - 143 \times 143$ double-differenced spectra.

($J = 1 \rightarrow 0$ at 115 GHz and $J = 2 \rightarrow 1$ at 230 GHz). CO emission contaminates the 100 and 217 GHz maps at low Galactic latitudes and accounts for much of the residual emission seen in Fig. 7.3 at these frequencies. It is for this reason that we apply CO masks at 100 and 217 GHz in the cosmological analysis (see Fig. 3.1). At 143 GHz, the residuals are at low levels except within a few degrees of the Galactic plane. There is some excess emission at 100 – 217 GHz in the Ophiucus region, which has a higher dust temperature than the bulk of the Galactic dust [77].

The green, blue and red points in Fig. 7.4 show the 217-143 double-differenced power spectra for the real maps. The solid lines show the double-differenced power spectra computed from the fake 545 GHz + SMICA maps described above. One can see that the spectra for the fake maps are in very good agreement with those for the real data, tracking the fluctuations to high accuracy. The orange points in the figure show the mask differenced power spectra for the 545 GHz half mission maps, scaled to the lower frequencies. The dotted line shows the best fitting model of Eq. 5.4 scaled to match the various mask sizes. Evidently, the increased scatter in the $217 \times 217 - 143 \times 143$ spectra compared to the 545×545 spectra comes from chance CMB-dust cross correlations and the spectra are almost perfectly matched by the ‘fake’ 545 GHz + SMICA maps.

The additional variance arising from chance CMB-dust correlations should be included in the covariance matrices if the 217 GHz spectra are to be used at low multipoles in forming

a likelihood. In the **CamSpec** likelihoods, we add the best fit foreground power spectrum (which varies with frequency and sky-coverage) to the fiducial theoretical model. In other words, we treat the foregrounds as an additional statistically isotropic contribution to the primordial CMB signal when we compute covariance matrices. This is a good approximation for the extragalactic foreground contributions, but as mentioned in Sect. 2.2 it is a poor approximation for Galactic dust, which is statistically anisotropic on the sky. This issue is discussed in detail in [67], which presents a more accurate model based on the assumption that Galactic dust can be approximated as a small-scale isotropic component superimposed on a smooth field with large-scale gradients. In the **CamSpec** likelihood, we simply exclude the 217×217 and 143×217 spectra at low multipoles and so we have not adopted the prescription of [67].

7.3 Spectrum-based cleaning coefficients

Another way to determine cleaning coefficients, explicitly tuning to a selected range of multipoles, is to minimise power spectrum residuals [65, 117]. Consider the ‘cleaned’ maps,

$$M^{T_\nu \text{clean}} = (1 + \alpha_s^{T_\nu})M^{T_\nu} - \alpha_s^{T_\nu} M^{T_{\nu T}}, \quad (7.6)$$

where ν_T is the frequency of the template map¹⁹. The cross power spectrum of cleaned maps at frequencies ν_1 and ν_2 is:

$$\begin{aligned} \hat{C}^{T_{\nu_1 T_{\nu_2} \text{clean}}} &= (1 + \alpha_s^{T_{\nu_1}})(1 + \alpha_s^{T_{\nu_2}})\hat{C}^{T_{\nu_1 T_{\nu_2}}} - (1 + \alpha_s^{T_{\nu_1}})\alpha_s^{T_{\nu_2}}\hat{C}^{T_{\nu_1 T_{\nu T}}} \\ &\quad - (1 + \alpha_s^{T_{\nu_2}})\alpha_s^{T_{\nu_1}}\hat{C}^{T_{\nu_2 T_{\nu T}}} + \alpha_s^{T_{\nu_1}}\alpha_s^{T_{\nu_2}}\hat{C}^{T_{\nu T T_{\nu T}}}, \end{aligned} \quad (7.7)$$

where $\hat{C}^{T_{\nu_1 T_{\nu_2}}$ etc. are the mask-deconvolved beam corrected power spectra. An advantage of working with power spectra rather than maps is that it is straightforward to correct for differences in the beams of the low frequency and high frequency template maps. The coefficients $\alpha_s^{T_{\nu_1}}$ are determined by minimising

$$\Psi_{TT} = \sum_{\ell_{\min}}^{\ell_{\max}} \hat{C}_\ell^{T_{\nu_1 T_{\nu_1} \text{clean}}}. \quad (7.8)$$

We minimise Eq. 7.8 instead of the usual χ^2 , which leads to biased cleaning coefficients when $\hat{C}^{T_{\nu_1 T_{\nu_2} \text{clean}}$ becomes noise dominated.

As in the discussion of map based template fitting based on Eq. 7.1a, minimisation of Eq. 7.8 leads to biased cleaning coefficients. If we adopt the simplified model of Eqs. 7.2a and 7.2b, then Eq. 7.8 is minimized for

$$\alpha_s^{T_\nu} = \frac{\beta}{(1 - \beta)} \left[1 + \frac{S * F}{F * F} \right] \approx \frac{\beta}{(1 - \beta)}, \quad (7.9)$$

(assuming $S * F \ll F * F$) and so gives a biased estimate of the true cleaning coefficient β , though the ‘cleaned’ power spectrum from Eq. 7.7 is unbiased, i.e.

$$\langle \hat{C}^{T_{\nu_1 T_{\nu_2} \text{clean}}} \rangle = S * S. \quad (7.10)$$

¹⁹To avoid cumbersome notation, we write the cleaning coefficients as $\alpha_s^{T_\nu}$ rather than $\alpha_s^{T_\nu T_{\nu T}}$.

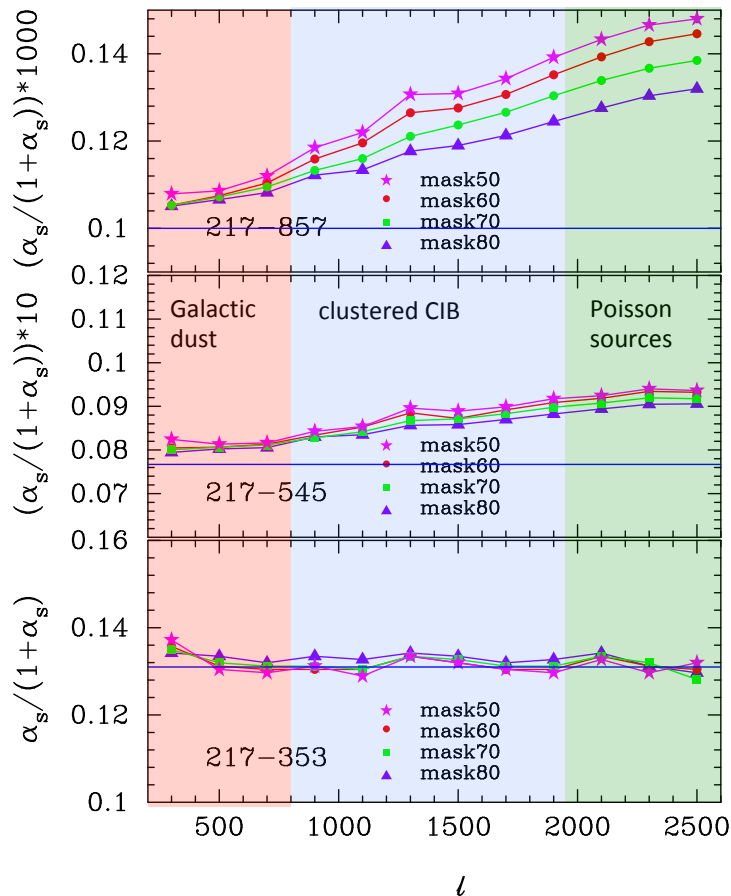


Figure 7.5. Cleaning coefficients derived by minimising Eq. 7.8 in bands of multipole of width $\Delta\ell = 200$ for 217 GHz cleaned with 857 GHz (top), 545 GHz (middle) and 353 GHz (bottom). Results are shown for four different masks. The horizontal lines show the map-based cleaning coefficients $\alpha_{m'}^T$, listed in bold face in Table 7. The shaded areas delineate the multipole ranges where on mask60 the 217×217 spectrum is dominated by Galactic dust emission, clustered CIB and Poisson point sources (determined from the Monte-Carlo Markov Chain fits to the 12.1HM CamSpec likelihood).

Evidently, for values of $\alpha_s^{T_\nu} \ll 1$, the bias is negligible, but for larger values, e.g. the coefficient appropriate for cleaning 217 GHz with 353 GHz, the bias can become significant. We therefore list values of $\alpha_s^T/(1 + \alpha_s^T)$ in the final column of Table 7, determined by minimising Eq. 7.8 over the multipole range $100 \leq \ell \leq 500$. Over this multipole range, Galactic dust emission dominates over the CIB. The spectrum-based cleaning coefficients listed in Table 7 are generally in very good agreement with the map-based coefficients determined by minimising Eq. 7.1b (i.e. with an estimate of the CMB removed from the maps). However, we find less good agreement with the map based coefficients based on Eq. 7.1a at low frequencies and for small sky fractions where Galactic dust emission does not dominate strongly compared to the CMB. For those cases, the CMB can strongly bias the cleaning coefficients. The cleaning coefficients listed in columns 3 and 5 of Table 7 provide our best estimates of the contribution of Galactic dust emission over the frequency range 100 – 217 GHz.

Fig. 7.5 shows the 217 GHz cleaning coefficients computed by minimising Eq. 7.8 in multipole bands of width $\Delta\ell = 200$ for four different masks using 353, 545 and 857 GHz

maps as templates. The shaded areas in Fig. 7.5 show the multipole ranges over which various foreground components dominate on mask60: Galactic dust emission ($\ell \lesssim 500$), clustered CIB ($500 \lesssim \ell \lesssim 2000$) and Poisson point sources ($\ell \gtrsim 2000$). (These ranges are computed from the fits of the combined CMB + foreground model to the 12.1HM likelihood described in Sect. 10.) The horizontal lines show the map-based cleaning coefficients listed in bold face in Table 7. Using 353 GHz as a template, we find cleaning coefficients that are remarkably flat and insensitive to the sky mask. Using 545 GHz as a template, we see a gradual drift in α_S from $\approx 7.9 \times 10^{-3}$ at multipoles $\ell \lesssim 500$ to 9.3×10^{-3} at $\ell \sim 2500$. This drift is a consequence of the CIB having a slightly different spectral energy distribution (SED) compared to Galactic dust. We see a stronger drift if we use 857 GHz as a template. The differences in the SEDs of Galactic dust emission and the CIB can be exploited to construct 857 and 545 GHz difference maps that are dominated by the CIB and so can be used as a tracer of large-scale structure and lensing of the CMB [59].

In fact, we can use the cleaning coefficients in the last column of Table 7 to estimate the SED of Galactic dust emission. We use the central frequencies and conversions from temperature to units of MJy sr $^{-1}$ for a dust-like spectrum from [84]. We estimate a rough error on each cleaning coefficient from the scatter in the cleaning coefficients measured for the four masks listed in Table 7 and we add a 7% absolute calibration error for the 545 and 857 GHz maps [80]. We normalize the SED to unity at the 217 GHz channel and fit the points to a modified black-body (MBB):

$$I_\nu = \tau_{\text{obs}} \left(\frac{\nu}{\nu_0} \right)^{\beta_{\text{obs}}} \frac{B_\nu(T_{\text{obs}})}{B_{\nu_0}(T_{\text{obs}})}, \quad (7.11a)$$

where $B_\nu(T)$ is the Planck function

$$B_\nu(T) \propto \frac{\nu^3}{[\exp(h\nu/kT) - 1]}. \quad (7.11b)$$

The SED is plotted in Fig. 7.6. The inset in this figures shows the marginalized posteriors of β_{obs} and T_{obs} determined from an MCMC fit to the data points. We find $\beta_{\text{obs}} = 1.49 \pm 0.05$, $T_{\text{obs}} = 22.7 \pm 2.8$ K, in reasonable agreement with the map-based analysis of [77], which finds $\beta_{\text{obs}} = 1.59 \pm 0.12$, $T_{\text{obs}} = 20.3 \pm 1.3$ K by fitting to the *Planck* 353, 545, 857 GHz and IRAS 100 μm data over the sky at $|b| > 15^\circ$. This single component MBB is an acceptable fit to the observed dust spectrum over the *Planck* frequency range. The question of whether the Galactic dust spectrum is better fitted by a two component model (see e.g. [38, 70]) is beyond the scope of this paper.

Note that Eq. 7.8 has a very broad minimum. If we make an error in the cleaning coefficient of $\alpha_s^{T_\nu} = \beta/(1 - \beta) + \delta\alpha_s^{T_\nu}$, then assuming our simplified model of a perfect foreground match between frequencies (Eqs. 7.2a and 7.2b), the leading contribution to the cleaned spectrum varies as

$$\hat{C}^{T_{\nu_1} T_{\nu_2} \text{clean}} \approx S * S + (\delta\alpha_s^{T_\nu})^2 (1 - \beta)^2 F * F, \quad (7.12)$$

i.e. the bias varies as the square of the error in the cleaning coefficient. In practice, the biases in the cleaned spectra are dominated by template mismatch, which cannot be removed via a single cleaning coefficient.

The degree of template mismatch is shown clearly in Fig. 7.7. The filled points show the residuals of the 217×217 half mission cross spectrum with respect to the base ΛCDM

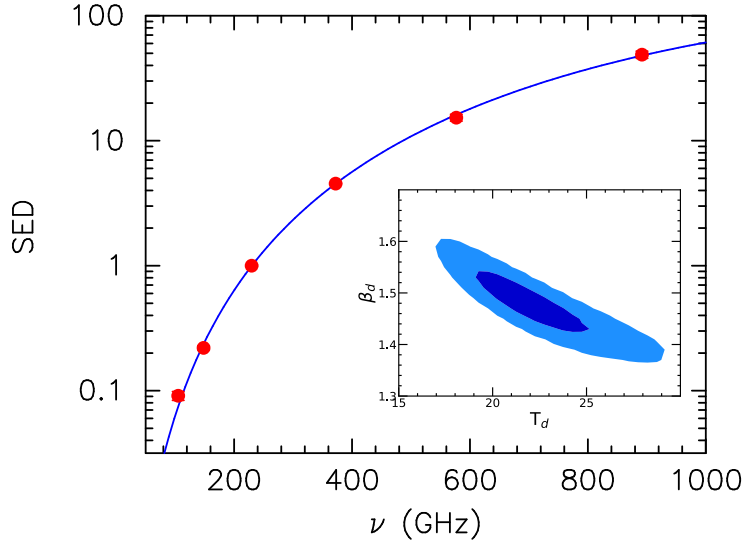


Figure 7.6. Spectral energy distribution of dust emission based on the spectrum-based cleaning coefficients listed in column 5 of Table 7. The SED is normalized to unity at 229 GHz (the effective central frequency for a dust-like SED in the 217 GHz band). The solid line shows the best-fit modified black body distribution of Eqs. 7.11a and 7.11b. 68% and 95% confidence contours for the parameters β_{obs} and T_{obs} are plotted in the inset.

fiducial spectrum, $\Delta D_\ell = \hat{D}_\ell^{T_{217}T_{217}} - D_\ell^{\text{fid}}$ for four masks. (These points are therefore the same in each panel.) The dashed lines show $\beta_{\nu_T}^2 (\hat{D}_\ell^{T_{\nu_T}T_{\nu_T}} - D_\ell^{\text{fid}})$ for each of the three template frequencies. One can see that these lines match the filled points quite well at low multipoles for each of the templates, but for 545 and 857 GHz they fail to match at multipoles $\gtrsim 500$. This is consistent with the results shown in Fig. 7.6 and occurs because the CIB decorrelates between 217 and 857 GHz [91]. One can see from the constancy of the cleaning coefficients for 353 GHz in Fig. 7.5 that Galactic dust emission *and most of the CIB* can be removed from 217 GHz using 353 GHz. However, since the CIB at 217 GHz progressively decorrelates with the CIB at 545 and 857 GHz, template cleaning with these frequencies removes Galactic dust emission accurately at low multipoles (even for large sky masks), but leaves residual CIB excesses at high multipoles, which cannot be removed by template cleaning for any value of the cleaning coefficient. The solid lines in Fig. 7.7 show:

$$\Delta D_\ell = (1 - \beta_{\nu_T}^2) [2\alpha^{T_{\nu_T}} (1 + \alpha^{T_{\nu_T}}) (\hat{D}_\ell^{T_{217}T_{\nu_T}} + \hat{D}_\ell^{T_{\nu_T}T_{217}}) - (\alpha^{T_{\nu_T}})^2 \hat{D}_\ell^{T_{\nu_T}T_{\nu_T}} + 2\alpha^{T_{\nu_T}} (2 + \alpha^{T_{\nu_T}}) D_\ell^{\text{fid}}], \quad (7.13)$$

which accounts for signal-foreground correlations and partially compensates for template mismatch. The differences between the filled points and the solid lines give an accurate indication of the remaining foreground residuals in the template cleaned spectra (Eq. 7.7). Notice that the solid lines show quite large fluctuations from chance CMB-foreground correlations, even at relatively high multipoles. We draw attention to the ‘dip’ at $\ell \approx 1500$, which is particularly prominent using 353 and 545 GHz as templates. This feature has a bearing on the parameters A_L and Ω_K , as will be discussed in Sects. 11 and 14.

In PCP15 and PCP18, we formed ‘cleaned’ CamSpec likelihoods by cleaning the 217×217 , 143×217 and 143×143 TT spectra using 545 GHz as a template. As will be discussed in

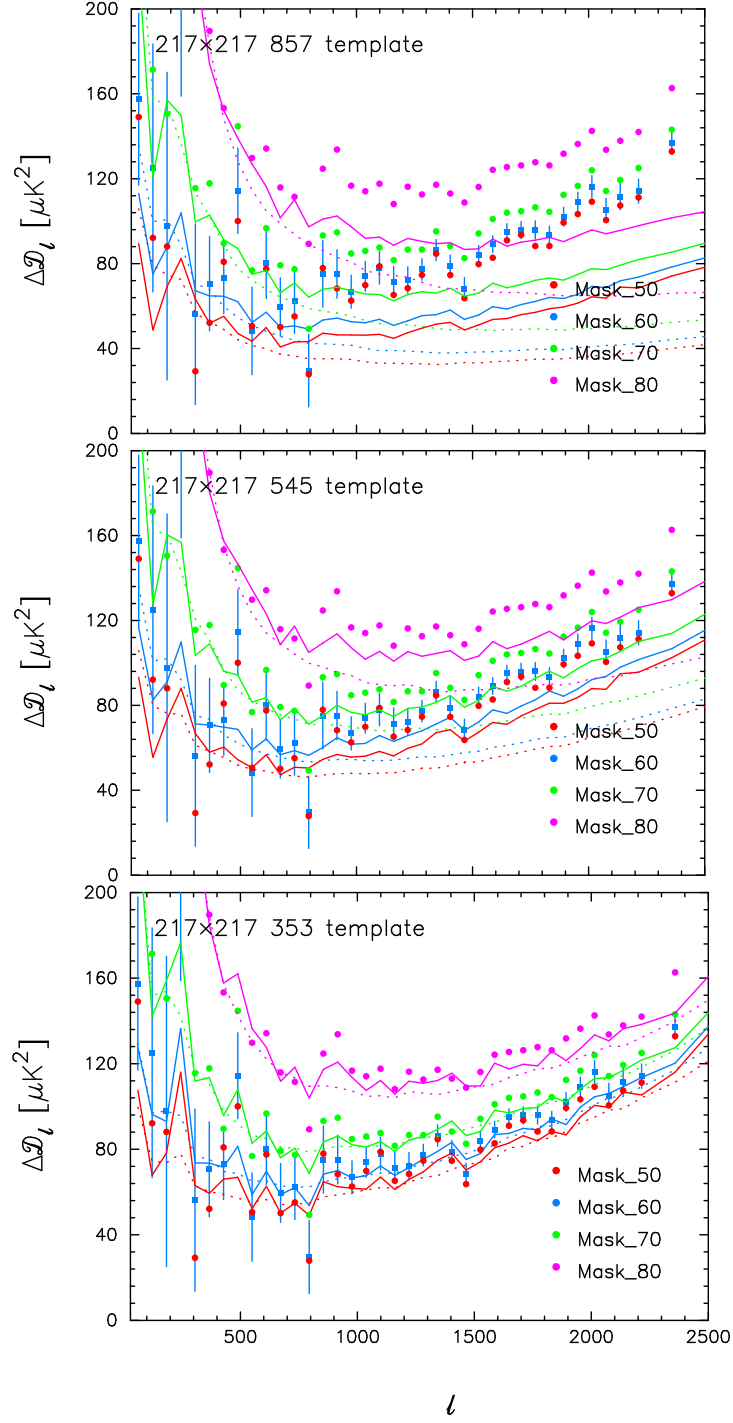


Figure 7.7. The filled points show band averages of the 217×217 half mission cross spectra, $\hat{D}_\ell^{T_{217}T_{217}}$ minus the fiducial base ΛCDM spectrum, D_ℓ^{fid} , for various masks. We plot the errors on the mask60 spectrum, computed from the covariance matrix used in the 12.1HM *CamSpec* likelihood. The dashed lines show $\beta_{\nu_T}^2(\hat{D}_\ell^{T_{\nu_T}T_{\nu_T}} - D_\ell^{\text{fid}})$ for the three template frequencies, illustrating the degree of template mismatch. The solid lines show $(1 - \beta_{\nu_T}^2)[2\alpha^{T_{\nu_T}}(1 + \alpha^{T_{\nu_T}})(\hat{D}_\ell^{T_{217}T_{\nu_T}} + \hat{D}_\ell^{T_{\nu_T}T_{217}}) - (\alpha^{T_{\nu_T}})^2\hat{D}_\ell^{T_{\nu_T}T_{\nu_T}} + 2\alpha^{T_{\nu_T}}(2 + \alpha^{T_{\nu_T}})D_\ell^{\text{fid}}]$, which includes signal-foreground correlations and partially compensates for template mismatch.

the next section, any of 353, 545 or 857 GHz could be used as an accurate tracer of Galactic dust emission. However, the 545 GHz maps are effectively noise free and remove more of the CIB compared to using 857 GHz as a template. Since the 353 GHz maps are noisy (and the cleaning coefficient relative to 217 GHz is large), one pays a significant signal-to-noise penalty if 353 GHz is used as a template. For these reasons, in this paper we use 545 GHz as a template to form cleaned temperature likelihoods.

7.4 Universality of Galactic dust emission

The results presented so far suggest that Galactic dust emission is remarkably universal over most of the sky, i.e. a dust template rescaled with a single template coefficient describes dust emission to high accuracy over the entire *Planck* frequency range of 100 – 857 GHz. This is illustrated by Fig. 7.8, which shows the 217, 143 and 100 GHz maps cleaned with 353, 545 and 857 GHz maps. The differences between the cleaned 143 GHz maps and the SMICA CMB map are shown in the bottom row of this figure on an expanded scale. The large scale features visible in these plots reflect the inhomogeneous noise levels in the *Planck* maps. We do, however, see residuals above the Galactic plane that are clearly physical. As in Fig. 7.3 we see a prominent residual coincident with the Ophiuchus molecular cloud complex, which has a higher temperature than the diffuse Galactic dust emission. We also see residuals in the 100 GHz and 217 GHz maps in the region of the Aquila Rift, Perseus and the Gum Nebula. These residuals correlate strongly with the *Planck* Galactic CO emission maps [83]. Evidently at low Galactic latitudes, CO emission makes a significant contribution to the residuals in the 100 and 217 GHz maps. The universality of Galactic dust emission over most of the sky leads to the following (and somewhat unorthodox) conclusions concerning foregrounds at low multipoles:

- The ‘cleanest’ *Planck* channel is at 143 GHz. Even though the net amplitude of foreground emission is lower at 100 and 70 GHz, the dominant foreground at 143 GHz is Galactic dust emission which can be subtracted to high accuracy even at low Galactic latitudes using the higher frequency *Planck* channels.
- At 100 GHz, CO emission is a significant contaminant (and there is a small contribution from synchrotron emission which will not be discussed here). Regions of intense CO emission (which coincide with molecular clouds) can be masked without paying a significant penalty in loss of sky area.
- Apart from a narrow region centered on the Galactic plane, the template subtracted 143 GHz maps are almost indistinguishable from the *Planck* component separated maps. (We compare with the SMICA maps in Fig. 7.8, but the results are almost identical if we compare with the *Planck* NILC or SEVEM maps.) In fact, applying various statistical tests (see, for example, Fig. 7.9), we find that differences between the cleaned 143 GHz maps and the SMICA maps are of the same order as the differences between the various *Planck* component separated maps. Over at least 80% of sky, sophisticated component separation methods are not required to produce science quality maps of the CMB free of Galactic dust emission; simple template subtraction of higher frequency maps is perfectly adequate.
- The foregrounds at lower frequencies are more complicated than at the HFI frequencies. At frequencies $\lesssim 100$ GHz, synchrotron, free-free and anomalous microwave emission become the dominant foregrounds and vary significantly over the sky (see [106]). To produce an accurate foreground-cleaned CMB map, one needs to make a trade-off between the net amplitude of the foregrounds and the complexity of the foregrounds. This trade-off depends critically on the universality of the foregrounds. The results shown in Fig. 7.8 show that dust cleaning of

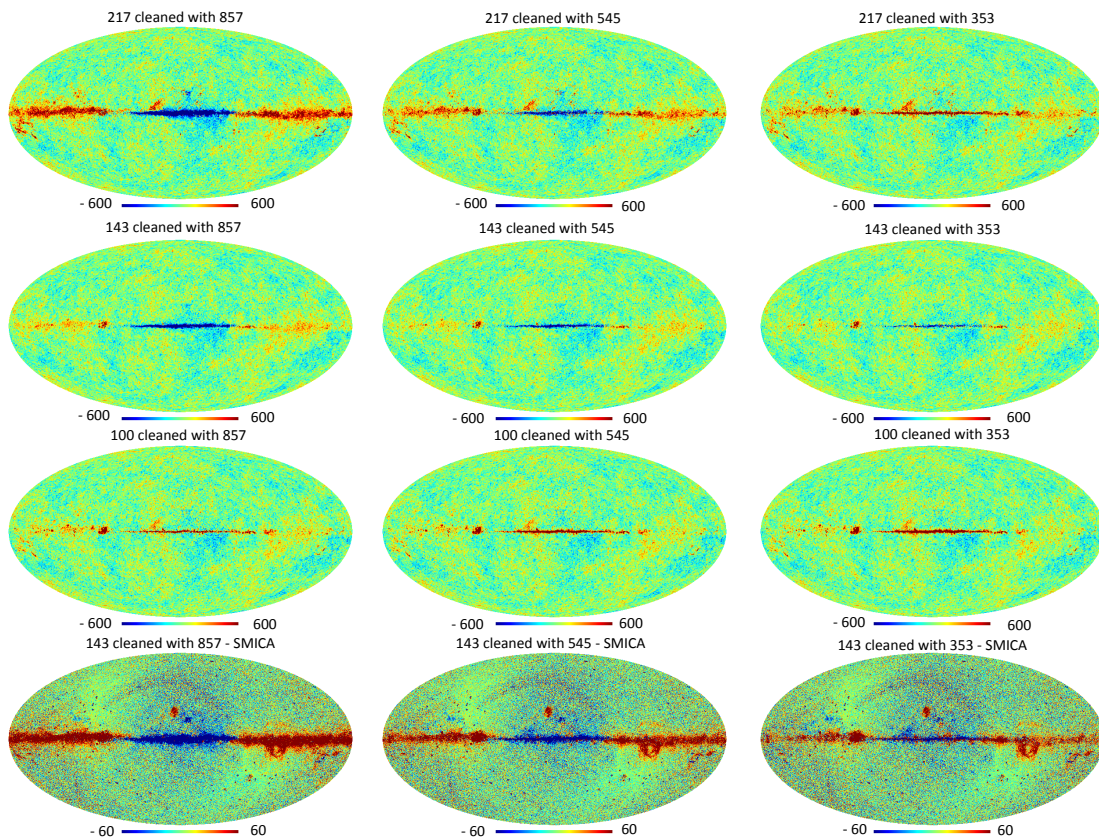


Figure 7.8. The top three rows show 217, 143 and 100 GHz full mission maps cleaned with 857, 545 and 353 GHz full mission maps (left to right) using the bold-faced cleaning coefficients listed in Table 7. The differences between the cleaned 143 GHz maps and the SMICA map are shown in the bottom row on an expanded temperature scale. The color scales are in units of μK .

the 143 GHz *Planck* maps produces accurate maps of the CMB over almost all of the sky. Adding information from low frequencies produces little additional gain in the fidelity of the cleaned CMB maps and could, potentially, introduce errors if the model adopted for the low frequency foregrounds differs from reality. At very low Galactic latitudes (within about $\pm 5^\circ$ of the Galactic plane) Galactic emission becomes so complicated that all component separation methods fail²⁰. Our main conclusion (applicable even more strongly to polarization, for which polarized Galactic emission is a major problem in the search for B-modes) is that it is a better strategy to concentrate science measurements at frequencies where the foregrounds are *simplest*. These may differ from the frequencies at which the foregrounds have their lowest amplitude.

The power spectra of half mission template cleaned temperature maps are plotted in Fig. 7.9 and compared to those of half mission SMICA maps for various Galactic masks. According to the discussion of the previous subsection, at multipoles $\lesssim 500$, the template cleaned spectra should look almost identical and in close agreement with the SMICA spectra,

²⁰To give some perspective, at 143 GHz, the Galactic emission in the Galactic plane has a typical amplitude of $\sim 1 \times 10^5 \mu\text{K}$, requiring foreground removal to an accuracy $\lesssim 0.1\%$ to achieve an accuracy of $\sim 100 \mu\text{K}$ on the primordial CMB.

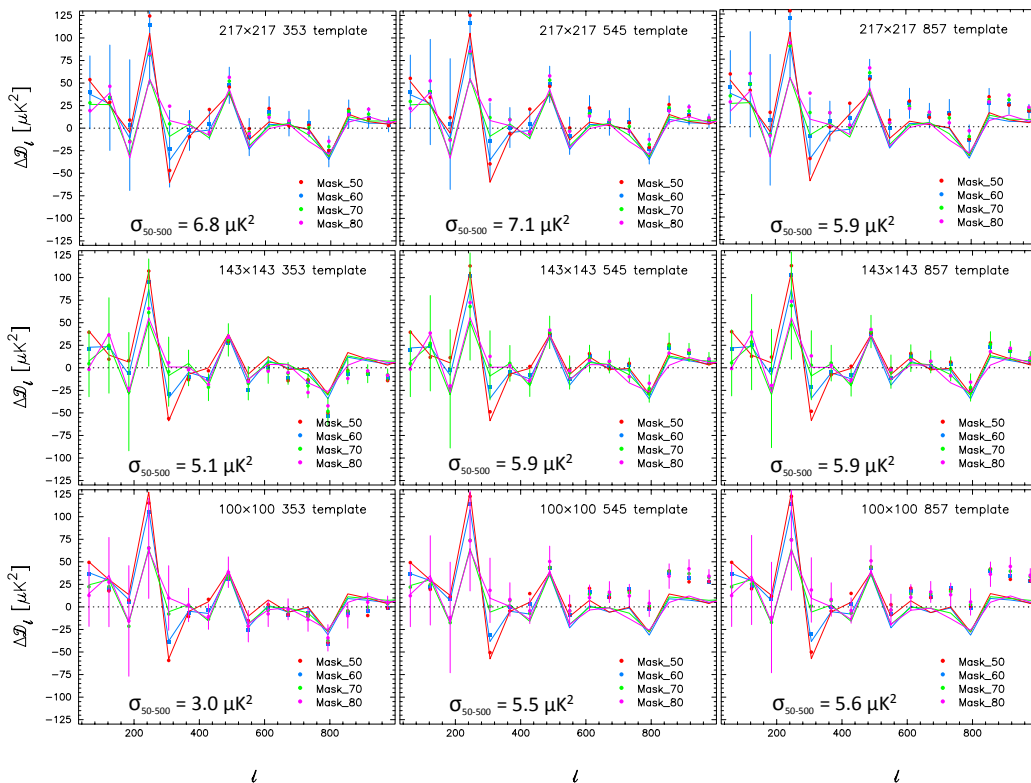


Figure 7.9. Cross-power spectra of template cleaned half mission maps using the same cleaning coefficients as the full mission maps shown in Fig. 7.8. The filled points show the residuals of the power spectra with respect to the fiducial base Λ CDM power spectrum for four Galactic masks. The masks include the point source, extended object and (for 100 and 217 GHz) CO masks appropriate to each frequency (as plotted in Fig. 3.1). We show the *CamSpec* errors on the set of points corresponding to the masks used in the 12.1HM *CamSpec* likelihood (mask80 for 100 GHz, mask70 for 143 GHz and mask60 for 217 GHz). The solid lines show the power spectrum residuals for half mission SMICA maps. The numbers give the dispersion in the differences between the template cleaned and SMICA band-averaged power spectra over the multipole range $50 \leq \ell \leq 500$ for the 12.1HM masks.

reflecting the universality of Galactic dust emission. At higher multipoles, we should see excesses that are independent of the sky area caused by extragalactic foregrounds (primarily point sources at 100 GHz and CIB at 217 GHz). This is what is observed in Fig. 7.9. The numbers in each panel give the dispersion in the differences between the template-cleaned and SMICA band-averaged power spectra over the multipole range $50 \leq \ell \leq 500$ for the temperature masks used in the 12.1HM *CamSpec* likelihood. These are all within a few $(\mu\text{K})^2$. This figure also shows that the 12.1HM masks are conservative and that it is possible to use larger areas of sky in forming temperature likelihood. This is explored further in Sect. 11.

8 Galactic dust emission in polarization

The results of the previous section show that Galactic dust emission in temperature can be subtracted to high accuracy from the *Planck* spectra. However, dust subtraction leaves residuals at high multipoles in temperature which arise from frequency dependent extragalac-

Table 8. Cleaning coefficients using 353 GHz half mission T,Q,U maps as templates. The cleaning coefficients α_s^E and α_s^B are determined by separately minimising cleaning residuals in the E - and B -mode spectra over the multipole range $30 \leq \ell \leq 300$, using the 12.1HM **CamSpec** polarization mask. For reference, we also list the temperature cleaning coefficient for the 12.1HM **CamSpec** temperature masks, computed over the same multipole range.

	α_s^E	α_s^B	α_s^T
217×217	0.141	0.146	0.143
143×143	0.0392	0.0381	0.0341
100×100	0.0192	0.0171	0.0208

tic foregrounds. This necessarily requires that we fit for frequency dependent extragalactic foregrounds described by ‘nuisance’ parameters. For polarization, the situation is different since extragalactic foregrounds are expected to be very weakly polarized. The high multipole polarization measurements from ACTpol and SPTpol [43, 64] provide strong evidence that extragalactic infrared sources should be undetectable in the *Planck* polarization power spectra (consistent with what we see from the *Planck* data). In polarization, Galactic dust emission is the only foreground that needs to be removed from the *Planck* maps.

8.1 Spectrum-based cleaning coefficients

Since the 545 and 857 GHz bands are unpolarized, *Planck* has a limited frequency range over which to monitor polarized Galactic dust emission (100 – 353 GHz). In addition, the polarization maps are noisy and strongly ‘contaminated’ by the primordial E-mode signal, even at 353 GHz. We therefore do not use map-based cleaning coefficients in polarization but instead use spectrum-based cleaning coefficients, determined by minimising residual functions Ψ_{EE} and Ψ_{BB} and generalising Eqs. 7.7 and 7.8 to the polarization spectra.

Table 8 lists cleaning coefficients, using 353 GHz maps as templates determined by minimising Ψ_{EE} and Ψ_{BB} for the 217×217 , 143×143 and 100×100 EE and BB half mission spectra over the multipole range $30 \leq \ell \leq 300$ using the 12.1HM **CamSpec** polarization mask. For completeness, we also list the TT cleaning coefficient computed over this multipole range, which can be compared with the entries in Table 7. We recover almost identical polarization cleaning coefficients using the EE and BB spectra. In addition, we find that these coefficients are insensitive to the size of the polarization mask. As discussed in Sect. 7.3, the statistics Ψ_{TT} , Ψ_{EE} , Ψ_{BB} have broad minima and so the cleaned polarization spectra are insensitive to the precise values of the cleaning coefficients. We adopt the α_s^T and α_s^E cleaning coefficients listed in Table 8 to clean the TE, ET and EE polarization spectra used in the **CamSpec** likelihoods at low multipoles. Note that the polarization cleaning coefficients are quite close to the temperature cleaning coefficients. Over the limited range of frequencies probed by *Planck*, the SED of polarized Galactic emission is very close to the SED in intensity (see Fig. 7.6), in agreement with the results of [94].

We can get a visual feel for polarized dust emission from Fig. 8.1. In this figure, we have smoothed the full mission HFI *Planck* polarization maps with a Gaussian of FWHM of 2 degrees. The plots to the left show the smoothed Q and U maps at 100, 143 and 217 GHz with a temperature scale based on the α_s^E template coefficients given in Table 8 such that polarized Galactic dust emission should look identical in each plot. The plots in the middle panel show the 353 GHz Q and U maps rescaled using the α_s^E coefficients of Table

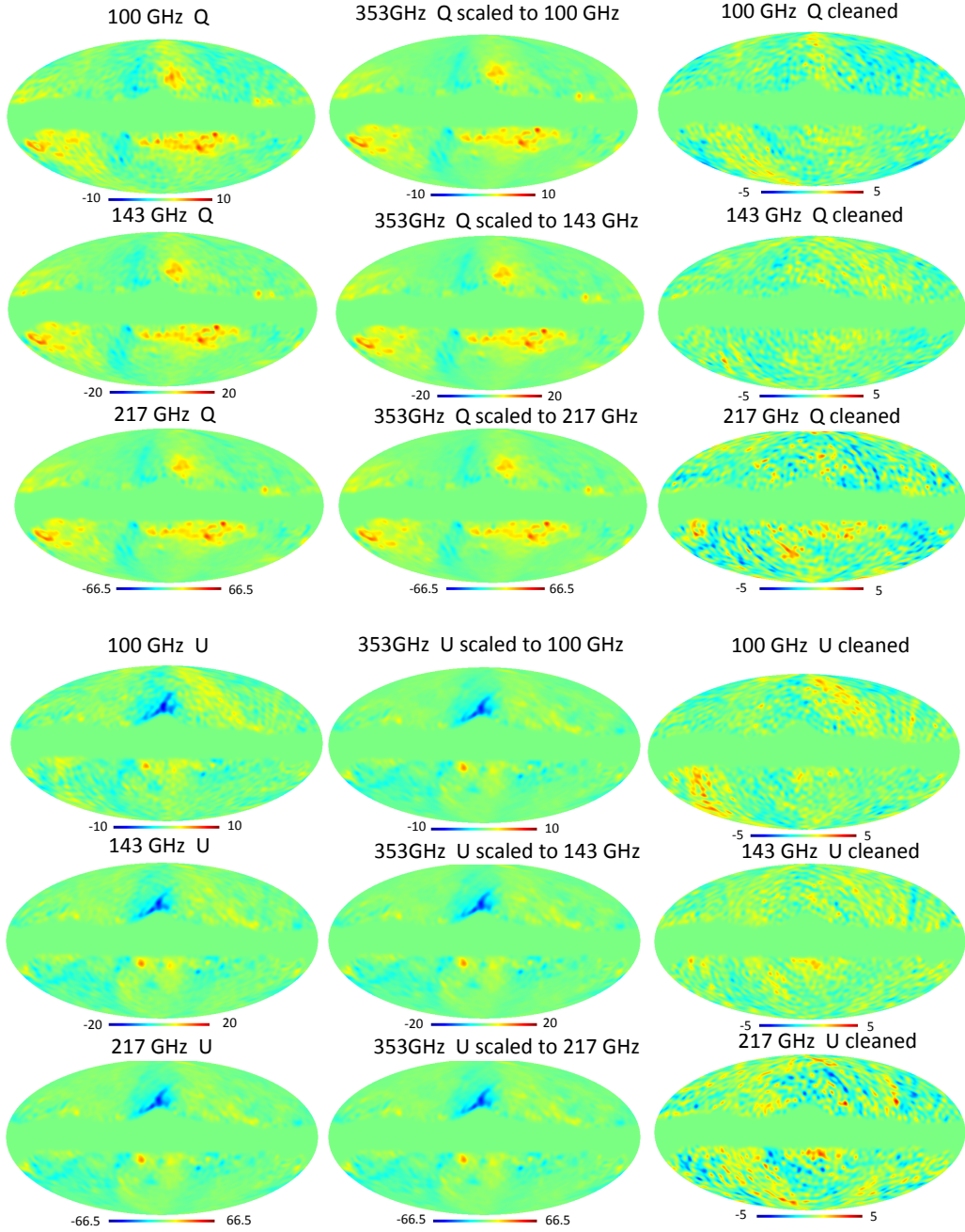


Figure 8.1. Q and U polarization maps smoothed with a Gaussian beam of FWHM of 2 degrees. The temperature mask80 has been applied to these maps. The top three rows show Q maps and the bottom three rows show U maps. In each row, the left-most map shows the polarization maps at each frequency on a scale such that Galactic dust emission is expected to have the same amplitude. The maps in the centre show 353 GHz Q and U maps scaled to the dust amplitude for the appropriate frequency using the α_s^E template coefficients given in Table 8. The figures on the right show the 353 GHz subtracted polarization maps at each frequency (i.e. the differences between the left-most and middle figures in each row). The temperature scales are in units of μK .

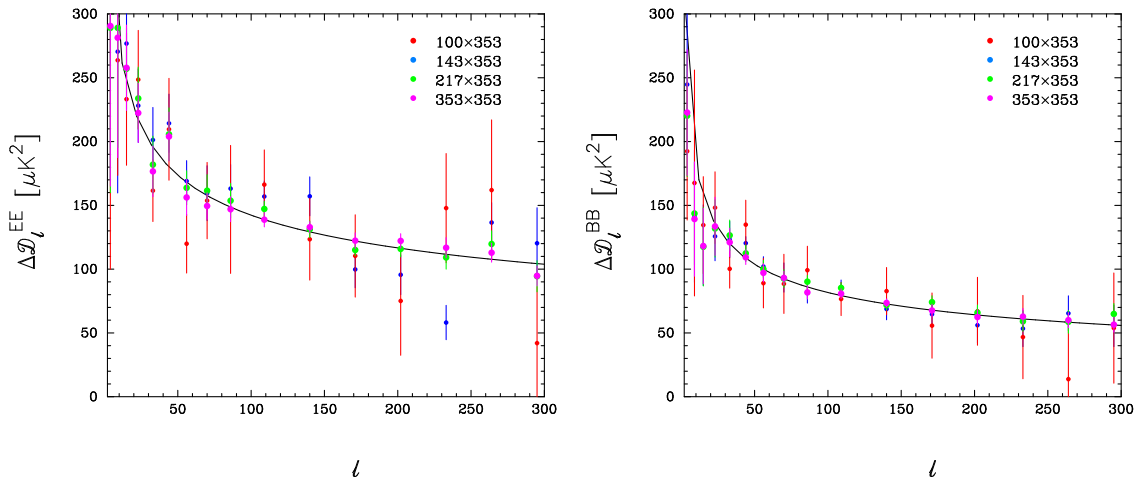


Figure 8.2. Band averaged EE and BB cross-spectra involving 353 GHz computed for the 12.1HM CamSpec polarization mask. We have subtracted the fiducial base Λ CDM E-mode spectrum from the EE spectra. The 100×353 , 143×353 and 217×353 spectra have been renormalized to the amplitude of the 353×353 spectra by dividing by $\alpha_s^E/(1 + \alpha_s^E)$, using the cleaning coefficients listed in Table 8. (We use the same coefficients for the EE and BB spectra.) The solid lines show power-law fits to the 353×353 spectrum (Eq. 8.1) as described in the text.

8 to match the respective lower frequency Q and U maps. The plots to the right show the differences between the scaled 353 GHz and the lower frequency maps on an expanded colour scale that is the same for all frequencies. As can be seen, the scaled 353 GHz maps match extremely well with the lower frequency maps, showing that polarized Galactic dust emission is the dominant source of the large scale features in all of the HFI polarized maps (dominating over the CMB at multipoles $\ell \lesssim 50$ at 100 GHz and $\ell \lesssim 250$ at 217 GHz, see Fig. 8.3). The cleaned polarization maps are noise dominated, so it is not possible to see the primordial CMB fluctuations in this figure. Large scale systematic features are visible in the cleaned maps and are largely caused by the distortion of the Solar dipole caused by non-linearities in the analogue-to-digital conversion electronics, which are not corrected accurately by SRo11 (see Appendix B.4.2 of [102]).

Figure 8.2 shows the half mission 353×353 , 217×353 , 143×353 and 100×353 EE and BB spectra. Since there are no detectable extragalactic foreground components in polarization, these spectra can be used to estimate the power spectrum of Galactic polarized dust emission. The CMB E-modes contribute to the EE spectra, so we have subtracted the E-mode spectrum of the fiducial base Λ CDM model. Each of the spectra has been renormalized to match the 353×353 spectrum using the cleaning coefficients α_s^E from Table 8. The error bars on the points are computed from the internal scatter of the power spectra within each multipole band. The solid lines show power-laws

$$\hat{D}_\ell = A \left(\frac{\ell}{200} \right)^\epsilon, \quad (8.1)$$

fitted over the multipole range $30 \leq \ell \leq 500$ to the 353×353 EE and BB spectra. We find:

$$A^{EE} = 116.5 \pm 1.9 (\mu\text{K})^2, \quad \epsilon^{EE} = -0.29 \pm 0.03, \quad (8.2a)$$

$$A^{BB} = 64.2 \pm 1.6 (\mu\text{K})^2, \quad \epsilon^{BB} = -0.35 \pm 0.03. \quad (8.2b)$$

We see that $A^{BB}/A^{EE} \approx 0.55$, which is typical for polarized Galactic dust emission measured by *Planck* over large areas of the sky [e.g. 81]. However, we find shallower spectral indices than [81], who concluded $\epsilon^{EE} = \epsilon^{BB} = -0.42 \pm 0.02$. The reason for this small difference is not understood, but may be related to the very different error model adopted in [81]²¹. The amplitudes of the rescaled frequency spectra in Fig. 8 match reasonably well for both EE and BB. However, the spectra are noisy and so do not provide a high precision test of the accuracy of the cleaning coefficients. The effectiveness of template cleaning at lower frequencies provides a more stringent test, as described in the next subsection.

Applying a similar analysis to half mission 353×353 TE and ET spectra (using mask60 for the temperature maps) we find:

$$A^{TE} = 195.3 \pm 8.0 (\mu\text{K})^2, \quad \epsilon^{TE} = -0.30 \pm 0.06, \quad (8.3a)$$

$$A^{ET} = 189.0 \pm 8.0 (\mu\text{K})^2, \quad \epsilon^{ET} = -0.27 \pm 0.06, \quad (8.3b)$$

and these two estimates are consistent with each other. Thus for all of the polarization spectra, we find shallower slopes than for the Galactic dust temperature power spectrum (for which $\epsilon^{TT} = -0.67$ as shown in Sect. 7.2).

8.2 Cleaning EE, TE, ET spectra

Figs. 8.3 - 8.5 show the impact of 353 GHz cleaning on the EE, TE and ET spectra for the 12.1HM CamSpec masks. The blue points in each figure show the deconvolved half mission cross spectra (including corrections for temperature-to-polarization leakage and polarization efficiencies described in Sect. 6). The pink points with errors show the 353 GHz cleaned spectra and the red solid lines show the theoretical spectra for the 12.1HM TT fiducial base Λ CDM cosmology. The red points show the differences between the uncleaned and cleaned spectra, which quantify the polarized Galactic dust contamination and CMB-dust cross-correlations in each spectrum. The green lines show power-laws (Eq. 8.1) fitted to the red points over the multipole range $50 \leq \ell \leq 500$ with parameters listed in Table 9. Since these dust spectra are noisy, we have imposed Gaussian priors on the spectral indices ϵ^{EE} , ϵ^{TE} and ϵ^{ET} of $\epsilon = -0.30 \pm 0.05$ based on the fits to the 353×353 spectra (Eqs. 8.2a, 8.3a and 8.3b). From Table 9 one can see that there is some sensitivity to ϵ in the 217×217 and 143×217 EE spectra, but for the rest ϵ is fixed by the prior. These power law fits are shown by the green lines in Figs 8.3 - 8.5.

For the EE spectra, polarized Galactic dust emission is a major contaminant at low multipoles. However, polarized dust emission is very accurately removed by 353 GHz cleaning, even when the foreground contamination exceeds the CMB signal by an order of magnitude or more. *We see no evidence for any decorrelation of polarized Galactic dust emission over the frequency range 100 – 353 GHz* [see also 105]. The excess in the cleaned 217×217 spectrum at $\ell \lesssim 50$ visible in Fig. 8.3 is caused primarily by systematic errors in the 217 GHz Q and U maps (see Fig. 8.1), not by errors in dust subtraction. Additional evidence of systematic errors in the SRoll maps at low multipoles is presented in Sect. 12.

The approach that we adopt in the CamSpec likelihood is to apply conservative multipole cuts, as listed in Table 3. This avoids using polarization data at multipoles where the spectra are heavily dominated by Galactic dust emission. We use the 353 GHz cleaned spectra up to a multipole $\ell_{\text{clean}} = 150$ and subtract the power-law fits of Table 9 from the uncleaned spectra at higher multipoles. We chose $\ell_{\text{clean}} = 150$ to limit the impact of 353 GHz noise

²¹Which attempts to remove sample variance and so gives high weight to points at low multipoles.

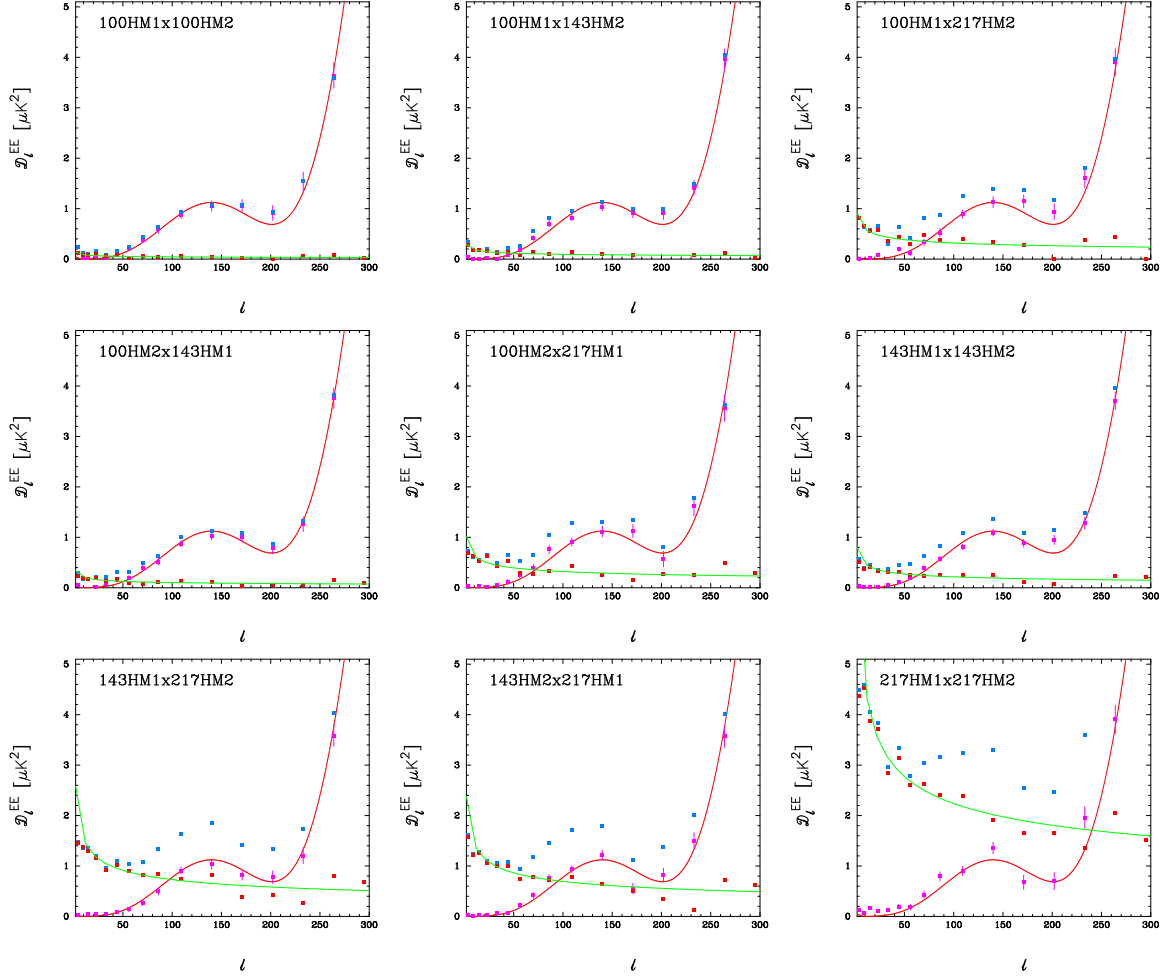


Figure 8.3. The nine EE spectra used to form the frequency averaged EE power spectrum in the 12.1HM CamSpec likelihood plotted at low multipoles. The blue points show the uncleaned EE spectra. The red points show the difference between the 353 cleaned and uncleaned spectra. The green lines show the power law fits to the red points, with the parameters listed in Table 9. The pink points show the dust cleaned spectra. These are computed from the analogue of Eq. 7.7 for $\ell \leq 150$; at higher multipoles we subtract the power-law fit from the blue points. The error bars are computed from the 12.1HM CamSpec covariance matrix. The red lines show the EE spectrum for the fiducial base Λ CDM model.

Table 9. Power-law fits (Eq. 8.1) to the polarized dust spectra plotted as the red points in Figs. 8.3 - 8.5. The fits are performed over the multipole range $50 \leq \ell \leq 500$.

spectrum	$A^{EE} [\mu\text{K}^2]$	ϵ^{EE}	$A^{TE} [\mu\text{K}^2]$	ϵ^{TE}	$A^{ET} [\mu\text{K}^2]$	ϵ^{ET}
217HM1x217HM2	1.806 ± 0.067	-0.31 ± 0.03	4.18 ± 0.61	-0.31 ± 0.05	3.41 ± 0.61	-0.31 ± 0.05
143HM2x217HM1	0.557 ± 0.033	-0.31 ± 0.04	1.14 ± 0.46	-0.30 ± 0.05	1.52 ± 0.22	-0.31 ± 0.05
143HM1x217HM2	0.582 ± 0.030	-0.32 ± 0.04	1.71 ± 0.52	-0.30 ± 0.05	1.00 ± 0.24	-0.30 ± 0.05
143HM1x143HM2	0.172 ± 0.010	-0.33 ± 0.04	0.56 ± 0.12	-0.30 ± 0.05	0.34 ± 0.15	-0.30 ± 0.05
100HM2x217HM1	0.263 ± 0.026	-0.29 ± 0.05	0.79 ± 0.31	-0.30 ± 0.05	0.50 ± 0.18	-0.30 ± 0.05
100HM2x143HM1	0.084 ± 0.008	-0.30 ± 0.05	0.24 ± 0.12	-0.30 ± 0.05	0.29 ± 0.08	-0.30 ± 0.05
100HM1x217HM2	0.265 ± 0.026	-0.27 ± 0.05	1.35 ± 0.22	-0.30 ± 0.05	0.73 ± 0.20	-0.30 ± 0.05
100HM1x143HM2	0.078 ± 0.008	-0.29 ± 0.05	0.40 ± 0.13	-0.31 ± 0.05	0.27 ± 0.08	-0.30 ± 0.05
100HM1x100HM2	0.036 ± 0.005	-0.28 ± 0.05	0.20 ± 0.06	-0.30 ± 0.05	0.13 ± 0.05	-0.30 ± 0.05

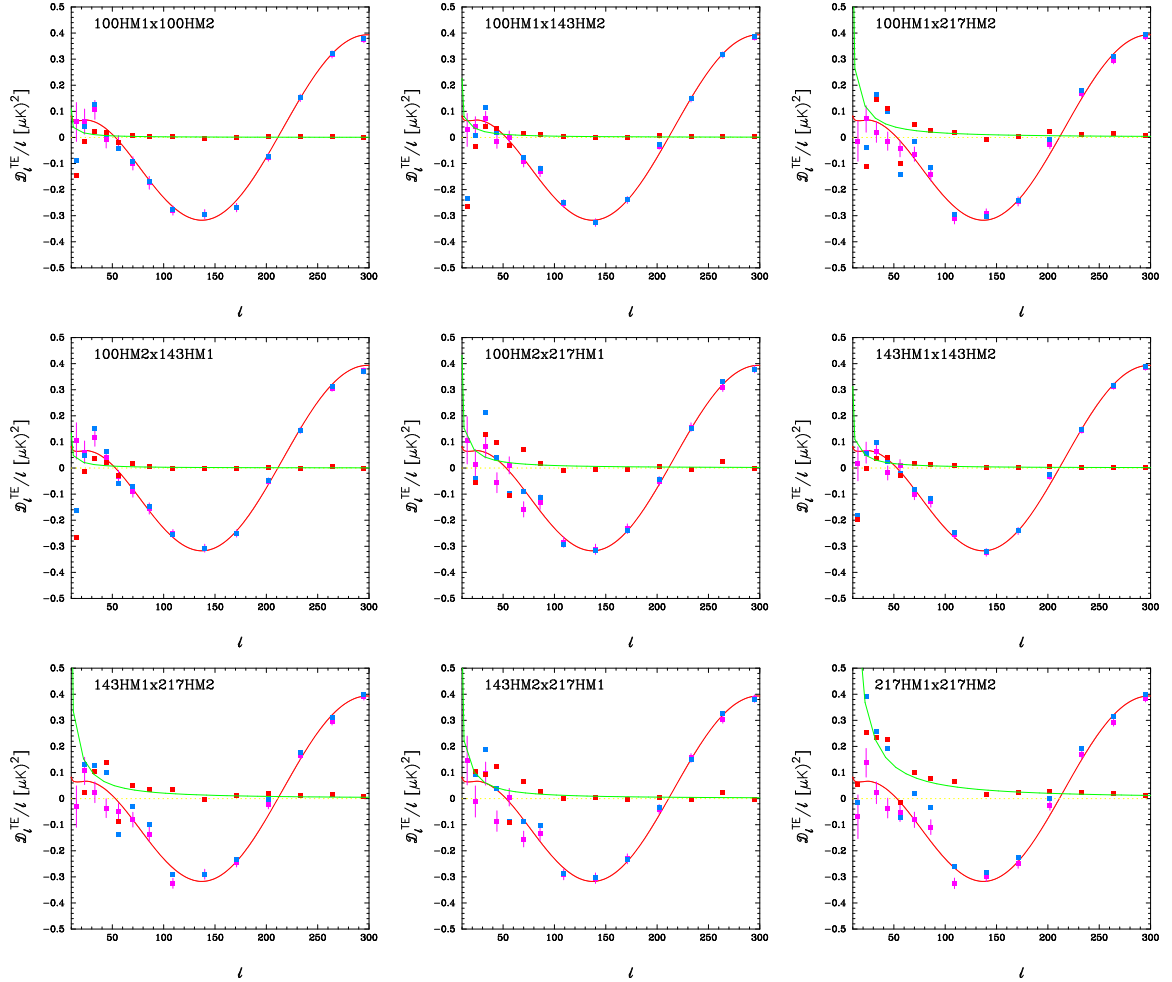


Figure 8.4. As for Fig. 8.3 illustrating the effects of 353 GHz cleaning but for the TE spectra using the 12.1HM CamSpec temperature and polarization masks. The red lines show the TE spectrum for the fiducial base Λ CDM model. Note that we plot $\hat{\mathcal{D}}^{TE}/\ell$.

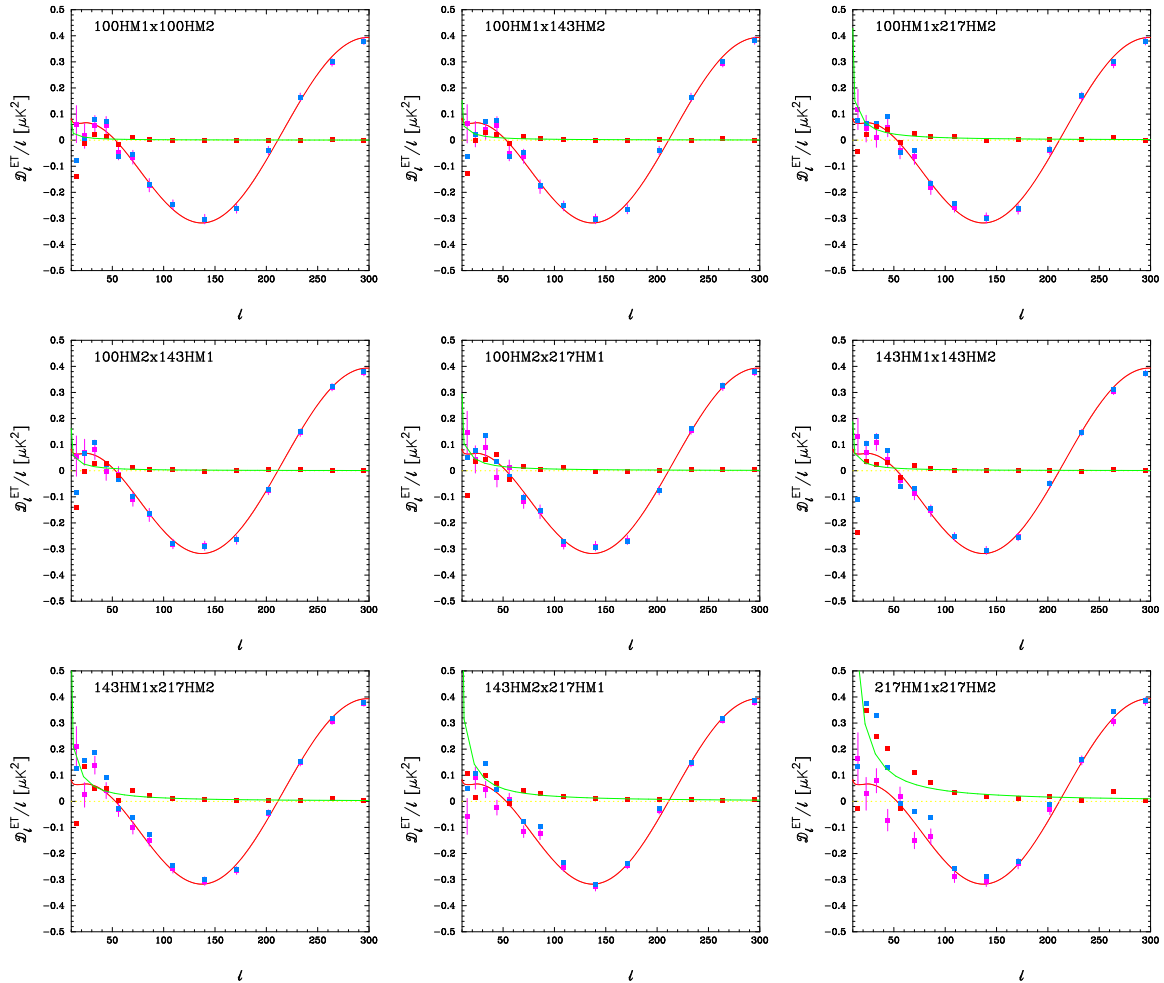


Figure 8.5. As for Fig. 8.4 but for the ET spectra.

on the cleaned spectra. With these choices, polarized Galactic dust emission and dust-CMB cross-correlations are removed accurately from the polarization spectra.

Figs. 8.4 and 8.5 show that Galactic dust emission makes a very small contribution to the TE/ET spectra at $\ell \gtrsim 150$. At lower multipoles, CMB-dust cross-correlations become important and the dust corrections can be positive or negative. At these low multipoles, assuming a power-law dust spectrum (as is done in the Planck likelihood) is a very poor approximation and could potentially lead to biases in the TE likelihood.

In summary, by cleaning the polarization spectra at lower frequencies using 353 GHz maps, we produce spectra free of polarized dust emission. Since there are no other frequency dependent foregrounds in the cleaned polarization spectra, these are then coadded (after correction for effective polarization efficiencies and small corrections for temperature-to-polarization leakage) to produce a single EE and a single TE spectrum which are used in the CamSpec likelihoods. Thus no nuisance parameters are required in the CamSpec likelihoods to describe foreground emission, though we include overall relative calibration parameters c^{TE} and c^{EE} , mainly as a consistency check of the likelihood, as described in Sect. 9. Comparisons of cosmological parameters determined separately from the TT, TE and EE likelihood blocks

therefore provide an important additional consistency check of systematics in the *Planck* data and errors in the TT foreground model.

9 Nuisance parameters

The *Planck* likelihoods fit parameters describing foreground power spectrum templates and instrumental nuisance parameters at the Monte-Carlo Markov Chain (MCMC) sampling stage²². This approach has been adopted by ground-based experiments [e.g. 29, 107]. The foreground/nuisance model used for the *Planck* likelihoods has been described in previous *Planck* papers PPL13, PPL15 and PPL18. For completeness, in this section we summarize the model adopted in this paper, detailing changes that we have made to the model since PCP18.

9.1 Instrumental nuisance parameters

9.1.1 Inter-frequency relative calibrations in temperature

The discussion presented in Sect. 6.2 shows that the relative calibrations of detset temperature spectra at fixed frequency are consistent to better than about 0.1%. As described in [99], the absolute calibrations of the 100 – 217 GHz frequency maps, based on the orbital dipole, are much more accurate than this. Our interpretation of these small residual ‘calibration’ differences is that they reflect small transfer function errors arising from the modelling of the beams beyond 100’ of the beam axis. These errors can be absorbed to high accuracy by a single multiplicative factor (i.e. an effective calibration factor). Given that we see such effects between detectors within a frequency band, we would expect to find small effective calibration differences between frequencies. As demonstrated in Sect. 6.2, it is relatively straightforward to measure small intra-frequency calibration factors accurately, since each detector within a frequency band sees the same sky (apart from small band-pass differences). It is more difficult to test effective calibrations between frequency bands because the foregrounds are strongly frequency dependent.

In previous versions of *CamSpec* we have determined relative calibrations between frequencies jointly with the foreground and cosmological parameters. We (arbitrarily) chose the 143×143 spectrum as the reference and solved for two relative calibration factors c_{100} , c_{217} , setting $c_{143 \times 217} = \sqrt{c_{100} c_{217}}$. These calibration factors multiply the data spectra (though as discussed in PPL13, in the likelihood we divide the theory power spectra by these factors when comparing to the *Planck* spectra).

However, since PCP18, we have developed a method to measure inter-frequency relative calibrations to high accuracy. Fig. 9.1 shows the differences between recalibrated 100×100 , 143×217 and 217×217 545 GHz cleaned half mission cross spectra and the 143×143 545 GHz cleaned cross spectra. We use mask30 together with the 217 GHz point source mask (and also eliminating missing pixels from all frequencies). Subtraction of 143×143 eliminates cosmic variance and by using mask30 and 545 cleaning, we eliminate contamination by Galactic dust and suppress frequency-dependent variations caused by foregrounds and CMB/foreground cross correlations. We recalibrate the spectra by minimising

$$\chi^2 = \sum_k \frac{(c_{xy} \hat{D}_k^{xy} - \hat{D}_k^{143 \times 143})^2}{\sigma_{xy}^2}, \quad (9.1)$$

²²Throughout this paper we use the *CosmoMC* sampler [63] developed and maintained by Antony Lewis (<https://cosmologist.info/cosmomc>). The version of *CosmoMC* is almost identical to that used in PCP18.

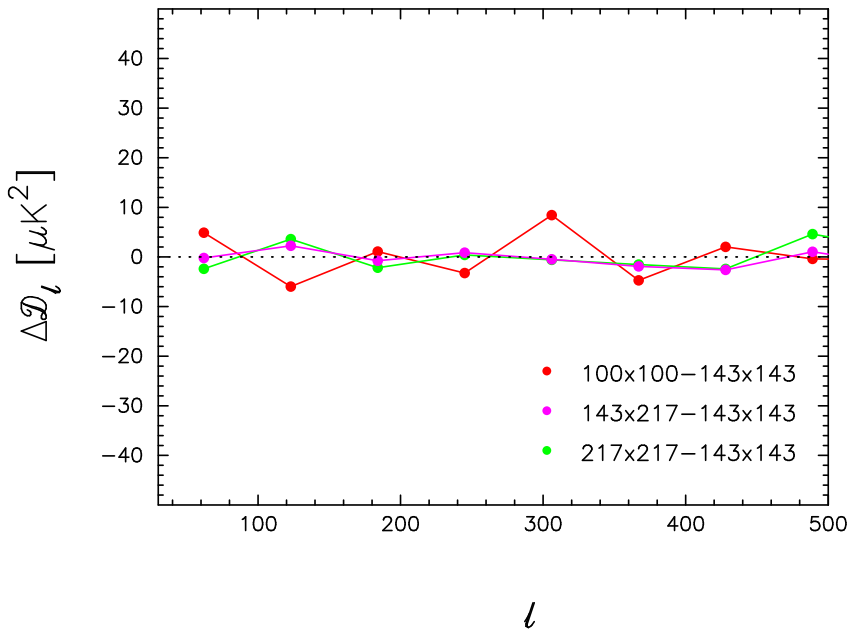


Figure 9.1. Differences between recalibrated 545 GHz cleaned half mission temperature cross spectra and the 143×143 545 GHz cleaned spectrum. The relative calibration coefficients are given in Eqs. 9.2a- 9.2c.

for each spectrum \hat{D}^{xy} over bandpowers k within the range $50 \leq l \leq 500$. (For the 100×100 spectrum we also make a small correction for point sources and the thermal Sunyaev-Zeldovich effect, which are not removed by 545 GHz cleaning, using parameters from the base Λ CDM fits to the 12.1HM TT likelihood). In Eq. 9.1, σ_{xy} is the scatter of the bandpowers shown in Fig. 9.1 over the fitted multipole range. The results of recalibration give

$$c_{100 \times 100} = 1.0022 \pm 0.0009, \quad \sigma_{100 \times 100} = 4.5 (\mu\text{K})^2, \quad (9.2a)$$

$$c_{143 \times 217} = 0.9989 \pm 0.0003, \quad \sigma_{143 \times 217} = 1.5 (\mu\text{K})^2, \quad (9.2b)$$

$$c_{217 \times 217} = 0.9972 \pm 0.0005, \quad \sigma_{217 \times 217} = 2.6 (\mu\text{K})^2. \quad (9.2c)$$

These relative calibration coefficients are determined very precisely and show that the inter-frequency effective calibrations display small $\sim 0.1 - 0.3\%$ variations from unity (consistent with our analysis of intra-frequency relative calibrations). These relative calibrations are insensitive to multipole range and, provided one restricts to high latitude areas of the sky, are insensitive to dust cleaning²³. Note that at the position of the first acoustic peak ($l \approx 220$), the four temperature spectra in the CamSpec likelihoods are consistent with each other to within $\sim 0.08\%$ after recalibration.

In the current version of CamSpec we simply recalibrate the temperature spectra using the coefficients of 9.2a - 9.2c (or equivalents for the full mission dataset likelihood) and no longer include relative calibrations as nuisance parameters. This reduces degeneracies with other foreground components (principally dust amplitudes) but has little impact on cosmological parameters.

²³However, if instead of cleaning with 545 GHz, we remove dust using the smooth power spectrum dust templates discussed in Sect. 7.2, the errors on the calibration coefficients are increased because of the additional scatter from CMB-foreground correlations.

9.1.2 Polarization calibrations

Section 6.3 described our procedure for recalibrating the individual polarization spectra, accounting for errors in polarization efficiencies and far-field beams. These effective calibrations have typical accuracies of about 1% (see Tables 4 and 5). The corrections for effective polarization efficiencies are applied to the **CamSpec** TE, ET and EE spectra prior to coaddition. To account for possible residual calibration differences with respect to the TT spectra, we include two nuisance parameters, c_{TE} and c_{EE} , which multiply the coadded TE and EE spectra. We adopt Gaussian priors centred on unity with a standard deviation of 0.01.

9.1.3 Absolute calibration

To account for possible errors in the absolute calibration of the *Planck* HFI spectra, we include an overall map-based calibration parameter y_{cal} . All of the spectra are multiplied by y_{cal}^2 . As a result, this parameter has very little impact on cosmology, but adds an additional contribution to the errors on parameters related to the amplitude of the fluctuation spectrum. We adopt a Gaussian prior on y_{cal} centred on unity with a (very conservative) standard deviation of 0.25%. We emphasise that this calibration parameter describes an effective calibration error at high multipoles, and should not be confused with the absolute calibration error on the orbital dipole. In reality, the dominant uncertainty in the *absolute* amplitude of the primordial fluctuation spectrum comes from systematic errors in the EE likelihood at $\ell < 30$, which is used to fix the optical depth to reionization. Systematic errors in the HFI EE spectrum at low multipoles have been discussed at length [26, 102] and will not be revisited here.

9.1.4 Beam errors

In PCP13, we modelled beam errors via a set of nuisance parameters multiplying beam error eigenmodes. For subsequent *Planck* data releases, the errors on the 100 – 217 HFI *Planck* main beams are so small that they have negligible impact on cosmology. We therefore no longer include nuisance parameters describing beam errors. Errors in the beams beyond the main beams are largely absorbed by the effective calibration factors.

9.2 Galactic dust in temperature

As described in Sect. 7, the power spectrum of Galactic dust emission can be measured accurately, free from extragalactic foregrounds, by differencing the high frequency power spectra measured on different masks (see Fig. 7.1). We therefore constructed a set of template dust spectra from fits to the 545 GHz spectra using the identical point source masks used in the **CamSpec** likelihoods. This accounts for the small differences in the shapes of the dust spectra caused by differences in the point source holes (as discussed in Sect. 7.2 and illustrated in Fig. 7.2). The template dust spectra for the 12.1HM **CamSpec** masks are plotted in Fig. 9.2. The amplitudes of these templates depend on the cleaning coefficients listed in bold face in Table 7 and so are not known precisely. For our ‘standard’ likelihoods, we therefore sample over four dust amplitude parameters, $A_{100 \times 100}^{\text{dust}}$, $A_{143 \times 143}^{\text{dust}}$, $A_{143 \times 217}^{\text{dust}}$, and $A_{217 \times 217}^{\text{dust}}$, with Gaussian priors centred on unity and with a standard deviation of 0.2.

9.3 Extragalactic foregrounds

9.3.1 Poisson point sources

The Poisson point source contributions are described by amplitude parameters

$$\hat{D}_{\ell=3000}^{PS} = A^{PS}. \quad (9.3)$$

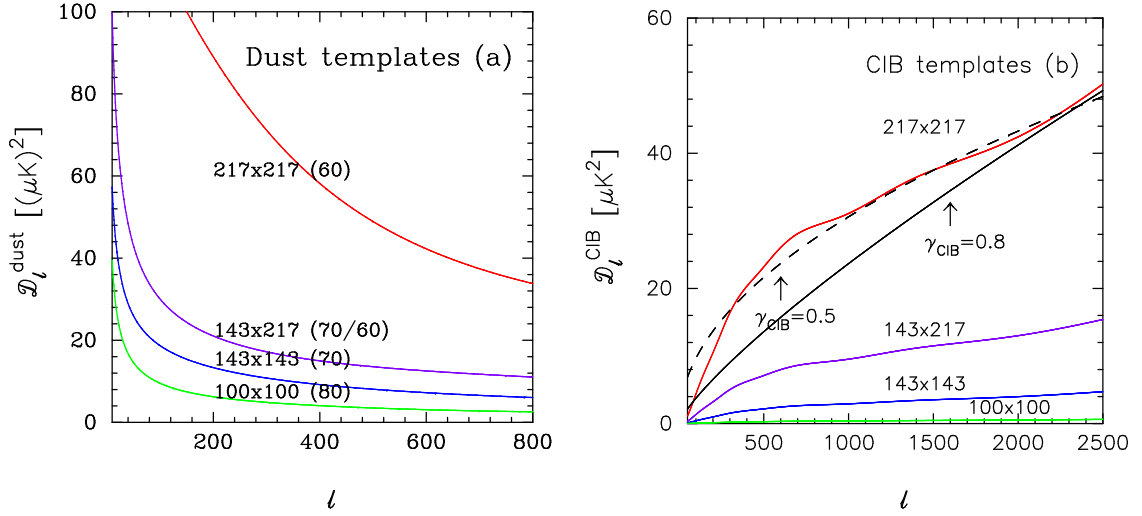


Figure 9.2. The figure to the left shows the 217×217 , 143×217 , 143×143 and 100×100 Galactic dust templates used in the 12.1HM likelihood (the sizes of the masks are given in brackets). The figure to the right shows the clustered CIB templates from the models of [91]. The 217×217 CIB spectrum is normalized to the best fit value determined from the 12.1HM TT likelihood. The relative amplitudes of the other spectra are as given by the model of [91] (though we allow the amplitude of the 143×217 spectrum to float in the likelihood). The dashed and solid black lines show power laws, $\hat{D}_\ell^{\text{CIB}} \propto \ell^{\gamma_{\text{CIB}}}$ with $\gamma_{\text{CIB}} = 0.5$ and $\gamma_{\text{CIB}} = 0.8$ respectively.

A_{100}^{PS} , A_{143}^{PS} and A_{217}^{PS} are the point source amplitudes of the 100×100 , 143×143 and 217×217 spectra respectively. The point source amplitude of the 143×217 spectrum is described by a correlation parameter $r_{143 \times 217}^{\text{PS}}$, so that $A_{143 \times 217}^{\text{PS}} = r_{143 \times 217}^{\text{PS}} \sqrt{A_{143}^{\text{PS}} A_{217}^{\text{PS}}}$. We adopt uniform priors for these parameters with ranges as given in Table 10.

9.3.2 Clustered CIB

As in PCP15, we adopt the clustered CIB templates for 217×217 , 143×217 and 143×143 from the halo model of [91]. These templates are plotted in Fig. 9.2. Mak et al. [67] showed that at multipoles $\ell \gtrsim 3000$, these templates become much steeper than the power spectra of the CIB measured at $350 \mu\text{m}$ and $500 \mu\text{m}$ from Herschel [122]. However, over the multipole range accessible to *Planck*, $\ell \lesssim 2500$, the templates of reference [91] are reasonably well approximated by a power law $D_\ell^{\text{CIB}} \propto \ell^{\gamma_{\text{CIB}}}$ with $\gamma_{\text{CIB}} \approx 0.5$ (see Fig. 9.2 and Fig. 2 of [67]). This is consistent with the results presented in PCP13, where we found values of $\gamma_{\text{CIB}} \approx 0.5$ from *Planck*, with evidence of steepening to $\gamma_{\text{CIB}} \approx 0.8$ when we combined *Planck* with high multipole ground-based CMB measurements. Nevertheless, uncertainties in the shapes of the CIB templates, particularly for the 217×217 spectrum, are a potential source of systematic error in the foreground model.

In PCP18, we varied a single amplitude

$$\hat{D}_{\ell=3000}^{\text{CIB}} = A_{217}^{\text{CIB}}, \quad (9.4)$$

measuring the clustered CIB contribution to the 217×217 spectrum. The CIB contributions to the 143×217 , 143×143 and 100×100 spectra were then fixed according to the model of [91]. Given the uncertainties in the model of [91], we considered this to be too restrictive

Table 10. Nuisance parameters: For parameters with Gaussian priors we list the mean and standard deviation. For parameters with uniform priors, we give the range of the prior.

Parameter	Description	Prior	
y_{cal}	absolute calibration	Gaussian	$\mu = 1, \sigma = 0.0025$
c_{TE}	relative calibration of TE spectrum	Gaussian	$\mu = 1, \sigma = 0.01$
c_{EE}	relative calibration of EE spectrum	Gaussian	$\mu = 1, \sigma = 0.01$
$A_{100 \times 100}^{\text{dust}}$	dust amplitude 100×100	Gaussian	$\mu = 1, \sigma = 0.02$
$A_{143 \times 143}^{\text{dust}}$	dust amplitude 143×143	Gaussian	$\mu = 1, \sigma = 0.02$
$A_{143 \times 217}^{\text{dust}}$	dust amplitude 143×217	Gaussian	$\mu = 1, \sigma = 0.02$
$A_{217 \times 217}^{\text{dust}}$	dust amplitude 217×217	Gaussian	$\mu = 1, \sigma = 0.02$
A_{100}^{PS}	point source amplitude 100×100	uniform	$0 - 360 (\mu\text{K})^2$
A_{143}^{PS}	point source amplitude 143×143	uniform	$0 - 270 (\mu\text{K})^2$
A_{217}^{PS}	point source amplitude 217×217	uniform	$0 - 450 (\mu\text{K})^2$
$r_{143 \times 217}^{\text{PS}}$	point source correlation coeff. 143×217	uniform	$0 - 1$
A_{217}^{CIB}	CIB amplitude 217×217	uniform	$0 - 80 (\mu\text{K})^2$
$r_{143 \times 217}^{\text{CIB}}$	CIB correlation coeff. 143×217	uniform	$0 - 1$
A_{143}^{tSZ}	thermal SZ amplitude 143×143	see Sect. 9.3.5	
A^{kSZ}	kinetic amplitude	see Sect. 9.3.5	
$\xi^{\text{tSZ} \times \text{CIB}}$	tSZ-CIB correlation parameter	uniform	$0 - 1$

and so have added a parameter $r_{143 \times 217}^{\text{CIB}}$ to adjust the amplitude of the CIB in the 143×217 spectrum, $A_{143 \times 217}^{\text{CIB}} = r_{143 \times 217}^{\text{CIB}} \sqrt{A_{143}^{\text{CIB}} A_{217}^{\text{CIB}}}$. Since the CIB makes a very small contribution to the 143×143 and 100×100 spectra, we keep these amplitudes pinned to the amplitude of the 217×217 spectrum according to the model of [91].

9.3.3 Thermal and kinetic Sunyaev-Zeldovich effects

As in PCP13 and later *Planck* papers, we use the $\epsilon = 0.5$ thermal Sunyaev-Zeldovich (tSZ) template from [33] normalized to a frequency of 143 GHz. For cross-spectra between frequencies ν_i and ν_j , the tSZ template is normalized as

$$\mathcal{D}_\ell^{\text{tSZ}_{\nu_i \times \nu_j}} = A_{143}^{\text{tSZ}} \frac{f(\nu_i) f(\nu_j)}{f^2(\nu_0)} \frac{\mathcal{D}_\ell^{\text{tSZ template}}}{\mathcal{D}_{3000}^{\text{tSZ template}}}, \quad (9.5)$$

where ν_0 is the reference frequency of 143 GHz, $\mathcal{D}_\ell^{\text{tSZ template}}$ is the template spectrum at 143 GHz, and

$$f(\nu) = \left(x \frac{e^x + 1}{e^x - 1} - 4 \right), \quad \text{with } x = \frac{h\nu}{k_{\text{B}} T_{\text{CMB}}}. \quad (9.6)$$

We neglect the tSZ contribution for any spectra involving the *Planck* 217 GHz channels. The tSZ contribution is therefore characterized by the single amplitude parameter A_{143}^{tSZ} .

Over the multipole range probed by *Planck*, the tSZ template is a good match to the tSZ power spectra measured from numerical simulations e.g. [9, 69], though the amplitude and shape of the tSZ spectrum at multipoles $\ell \gtrsim 2000$ is sensitive to the details of energy injection by active galactic nuclei into the intra-cluster medium.

We adopt the kSZ template from [120] and solve for the amplitude A^{kSZ} :

$$\mathcal{D}_\ell^{\text{kSZ}} = A^{\text{kSZ}} \frac{\mathcal{D}_\ell^{\text{kSZ template}}}{\mathcal{D}_{3000}^{\text{kSZ template}}}. \quad (9.7)$$

9.3.4 tSZ/CIB cross-correlation

The cross-correlation between dust emission from CIB galaxies and SZ emission from clusters (tSZ×CIB) is expected to be non-zero. However, it is difficult to model this correlation reliably, but fortunately over the multipole ranges probed by *Planck* it only makes a small contribution to the foregrounds (as confirmed by high resolution ground-based experiments, e.g. [107]). We adopt the template spectrum computed by [2] in this paper and model the frequency dependence of the power spectrum according to:

$$\mathcal{D}_\ell^{\text{tSZ}\times\text{CIB}\nu_i\times\nu_j} = -\xi^{\text{tSZ}\times\text{CIB}} \mathcal{D}_\ell^{\text{tSZ}\times\text{CIB template}} \times \left(\sqrt{\mathcal{D}_{3000}^{\text{CIB}\nu_i\times\nu_i} \mathcal{D}_{3000}^{\text{tSZ}\nu_j\times\nu_j}} + \sqrt{\mathcal{D}_{3000}^{\text{CIB}\nu_j\times\nu_j} \mathcal{D}_{3000}^{\text{tSZ}\nu_i\times\nu_i}} \right), \quad (9.8)$$

where $\mathcal{D}_\ell^{\text{tSZ}\times\text{CIB template}}$ is the template spectrum from [2] normalized to unity at $\ell = 3000$ and $\mathcal{D}_\ell^{\text{CIB}\nu_i\times\nu_i}$ and $\mathcal{D}_\ell^{\text{tSZ}\nu_i\times\nu_i}$ are given by Eqs. 9.5 and 9.7. The tSZ×CIB contribution is therefore characterized by the dimensionless cross-correlation coefficient $\xi^{\text{tSZ}\times\text{CIB}}$. With the definition of Eq. 9.8, a positive value of $\xi^{\text{tSZ}\times\text{CIB}}$ corresponds to an anti-correlation between the CIB and the tSZ signals.

9.3.5 Priors on A^{tSZ} , A^{kSZ} , and $\xi^{\text{tSZ}\times\text{CIB}}$

The three parameters A^{tSZ} , A^{kSZ} , and $\xi^{\text{tSZ}\times\text{CIB}}$ are highly correlated with each other and not well constrained by *Planck* alone. Using high multipole data from SPT, Reichardt et al. [107] find strong constraints on the linear combination

$$A^{\text{kSZ}} + 1.55 A^{\text{tSZ}} = (9.2 \pm 1.3) \mu\text{K}^2, \quad (9.9)$$

after marginalizing over $\xi^{\text{tSZ}\times\text{CIB}}$ (where we have corrected the [107] constraints to the effective frequencies used to define the *Planck* amplitudes A^{kSZ} and A^{tSZ}).

As in PCP15, in this paper we impose a conservative Gaussian prior on A^{SZ} , as defined by

$$A^{\text{SZ}} = A^{\text{kSZ}} + 1.6 A^{\text{tSZ}} = (9.5 \pm 3.0) \mu\text{K}^2, \quad (9.10)$$

based on the PCP13 *Planck*+highL solutions (i.e., somewhat broader than the dispersion reported in [107]). This condition prevents the individual SZ amplitudes from wandering too far into unphysical regions of parameter space. We apply a uniform prior of [0,1] on $\xi^{\text{tSZ}\times\text{CIB}}$. Results from the complete 2540 deg² SPT-SZ survey area [39] are consistent with Eq. 9.9 and, in addition, constrain the correlation parameter to low values, $\xi^{\text{tSZ}\times\text{CIB}} = 0.113_{-0.054}^{+0.057}$. The parameter $\xi^{\text{tSZ}\times\text{CIB}}$ is not well constrained by the *Planck* data and so values are sampled by the CamSpec likelihood that are excluded by [39].

9.4 Cleaned likelihoods

We have also produced a set of ‘cleaned’ likelihoods in which the 143×143 , 143×217 and 217×217 TT spectra are cleaned with 545 GHz as described in Sect. 7.3. The TE and EE polarization spectra in these likelihoods are cleaned using the 353 GHz maps, as described in Sect. 8.2. In the TT blocks of the cleaned likelihoods, we discard the 100×100 spectra so that we do not need to propagate foreground nuisance parameters for this frequency. (Although 545 GHz cleaning removes Galactic dust emission, it does very little to reduce the extragalactic foregrounds, mainly point sources and tSZ, at high multipoles in the 100×100

spectrum.) We adopt a heuristic model for the foreground contributions to the remaining TT spectra. For each of the 143×143 , 143×217 and 217×217 spectra, we adopt a power law foreground model:

$$D_\ell^{\text{for}} = A^{\text{for}} \left(\frac{\ell}{1500} \right)^{\epsilon^{\text{for}}}, \quad (9.11)$$

to capture the high multipole excesses seen in Fig. 11.4. The temperature foreground model in the cleaned likelihoods is therefore described by six parameters, instead of the twelve parameters of the standard foreground model. We adopt uniform priors within the ranges $0 - 50$ (μK)² for the amplitudes A^{for} and $0 - 5$ for the exponents ϵ^{for} .

The foreground corrected cleaned TT spectra are compared with those of the standard foreground model in Sect. 11.2 using exactly the same sky masks. Furthermore, because Galactic dust emission is subtracted accurately with 545 GHz cleaning, we have been able to create a statistically powerful cleaned likelihood using mask80 in both temperature and polarization at 143 and 217 GHz. Results from this likelihood (12.5HMcl) are presented in Sects. 13 and 14.

9.5 Summary

Extensive tests described in PPL13 and PPL15 show that cosmological parameters for the base ΛCDM and many simple extensions to the base ΛCDM model are remarkably insensitive to the nuisance parameters. We can gain further confidence in the cosmological results by comparing TE results with TT (since there are no nuisance parameters in the TE likelihood apart from an overall calibration) and by comparing with results from the ‘cleaned’ TT likelihoods which use a completely different parameterization of the residual extragalactic foregrounds involving fewer parameters. Such tests are described in Sects. 11 and 13.

10 Combined temperature and polarization likelihood

Since the extragalactic temperature foregrounds depend strongly on frequency, it is necessary to apply the likelihoods to solve for nuisance and cosmological parameters in a full likelihood analysis *before* one can perform a detailed analysis of inter-frequency residuals in the TT spectra. The **CamSpec** temperature-polarization likelihoods used in this paper are discussed in Sect. 10.1. Section 10.2 provides a short summary of the TT and EE likelihoods used at $\ell < 30$. Section 10.4 discusses fits to the base ΛCDM cosmology using the 12.1HM **CamSpec** half mission likelihood (which is similar to the **CamSpec** likelihood used in PCP18) and presents a number of consistency tests of the spectra and likelihood. A detailed analysis of inter-frequency residuals is given in Sects. 11 and 12.

10.1 The **CamSpec** likelihoods

The data vector of the combined temperature-polarization **CamSpec** likelihoods consists of a set of spectra:

$$\hat{\mathbf{C}} = (\hat{\mathbf{C}}_1^{\text{TT}}, \hat{\mathbf{C}}_2^{\text{TT}}, \dots, \hat{\mathbf{C}}_N^{\text{TT}}, \hat{\mathbf{C}}^{\text{TE}}, \hat{\mathbf{C}}^{\text{EE}})^T, \quad (10.1)$$

with covariance matrix:

$$\mathbf{M} = \begin{pmatrix} \langle \Delta \hat{\mathbf{C}}_1^{\text{TT}} \Delta \hat{\mathbf{C}}_1^{\text{TT}} \rangle, \langle \Delta \hat{\mathbf{C}}_1^{\text{TT}} \Delta \hat{\mathbf{C}}_2^{\text{TT}} \rangle, \dots, \langle \Delta \hat{\mathbf{C}}_1^{\text{TT}} \Delta \hat{\mathbf{C}}^{\text{TE}} \rangle, \langle \Delta \hat{\mathbf{C}}_1^{\text{TT}} \Delta \hat{\mathbf{C}}^{\text{EE}} \rangle \\ \vdots \\ \langle \Delta \hat{\mathbf{C}}^{\text{TE}} \Delta \hat{\mathbf{C}}_1^{\text{TT}} \rangle, \langle \Delta \hat{\mathbf{C}}^{\text{TE}} \Delta \hat{\mathbf{C}}_2^{\text{TT}} \rangle, \dots, \langle \Delta \hat{\mathbf{C}}^{\text{TE}} \Delta \hat{\mathbf{C}}^{\text{TE}} \rangle, \langle \Delta \hat{\mathbf{C}}^{\text{TE}} \Delta \hat{\mathbf{C}}^{\text{EE}} \rangle \\ \langle \Delta \hat{\mathbf{C}}^{\text{EE}} \Delta \hat{\mathbf{C}}_1^{\text{TT}} \rangle, \langle \Delta \hat{\mathbf{C}}^{\text{EE}} \Delta \hat{\mathbf{C}}_2^{\text{TT}} \rangle, \dots, \langle \Delta \hat{\mathbf{C}}^{\text{EE}} \Delta \hat{\mathbf{C}}^{\text{TE}} \rangle, \langle \Delta \hat{\mathbf{C}}^{\text{EE}} \Delta \hat{\mathbf{C}}^{\text{EE}} \rangle \end{pmatrix}, \quad (10.2)$$

Table 11. The likelihoods constructed for this paper. The 12.1HM likelihoods are the most similar to the `CamSpec` likelihoods used in PCP18. These likelihoods use the default choice of masks at each frequency in temperature as illustrated in Fig. 3.1. HM denotes half mission cross spectra and F denotes full mission detset cross spectra with corrections for correlated TT noise as described in Sect. 5.2. The likelihoods use either the the standard temperature foreground model described in Sect. 9 or 545 GHz cleaned spectra with the much simpler foreground model of Sect. 9.4. All of the HM likelihoods use 353 GHz cleaned TE and EE spectra as described in Sect. 8.2.

Likelihood	TT foreground	Type	TT masks	Q/U masks
12.1HM	standard	half mission frequency maps	default	maskpol60
12.1HMcl	cleaned	half mission frequency maps	default	maskpol60
12.1F	standard	full mission detset maps	default	maskpol60
12.2HM	standard	half mission frequency maps	default	mask60
12.3HM	standard	half mission frequency maps	default	mask70
12.4HM	standard	half mission frequency maps	default	mask80
12.5HMcl	cleaned	half mission frequency maps	mask80	mask80

which we can write as

$$\mathbf{M} = \begin{pmatrix} \mathbf{M}_T & \mathbf{M}_{TP} \\ \mathbf{M}_{TP}^T & \mathbf{M}_P \end{pmatrix}, \quad (10.3)$$

where \mathbf{M}_P is the polarization block:

$$\mathbf{M}_P = \begin{pmatrix} \langle \Delta \hat{\mathbf{C}}^{TE} \Delta \hat{\mathbf{C}}^{TE} \rangle & \langle \Delta \hat{\mathbf{C}}^{TE} \Delta \hat{\mathbf{C}}^{EE} \rangle \\ \langle \Delta \hat{\mathbf{C}}^{EE} \Delta \hat{\mathbf{C}}^{TE} \rangle & \langle \Delta \hat{\mathbf{C}}^{EE} \Delta \hat{\mathbf{C}}^{EE} \rangle \end{pmatrix}. \quad (10.4)$$

In Eq. 10.1, $N = 4$ for the ‘uncleaned’ `CamSpec` temperature likelihoods, corresponding to the 100×100 , 143×143 , 143×217 and 217×217 coadded TT spectra. For 545 GHz temperature cleaned likelihoods, $N = 3$ since we discard the 100×100 TT spectrum. The polarization cross spectra $\hat{\mathbf{C}}^{TE}$, $\hat{\mathbf{C}}^{EE}$, are coadded over all frequency combinations, though some multipoles are excluded as discussed in Sect. 4.2.

We use a Gaussian approximation to the likelihood at multipoles $\ell \geq 30$:

$$-2 \ln \mathcal{L} = (\hat{\mathbf{C}} - \hat{\mathbf{C}}^{\text{model}})^T \hat{\mathbf{M}}^{-1} (\hat{\mathbf{C}} - \hat{\mathbf{C}}^{\text{model}}), \quad (10.5)$$

where $\hat{\mathbf{C}}^{\text{model}}$ is the model prediction, including foreground and calibration parameters. The covariance matrix is computed as described in Sect. A.2, assuming a fiducial theoretical model, which is held fixed during MCMC sampling of the likelihood.

We have found it convenient to compute the inverse of \mathbf{M} as

$$\hat{\mathbf{M}}^{-1} = \begin{pmatrix} \mathbf{M}_T^{-1} + \mathbf{M}_T^{-1} \mathbf{M}_{TP} \mathbf{M}'_P^{-1} \mathbf{M}_{TP}^T \mathbf{M}_T^{-1}, & -\mathbf{M}_T^{-1} \mathbf{M}_{TP} \mathbf{M}'_P^{-1} \\ -\mathbf{M}'_P^{-1} \mathbf{M}_{TP}^T \mathbf{M}_T^{-1}, & \mathbf{M}'_P^{-1} \end{pmatrix}, \quad (10.6)$$

where $\mathbf{M}'_P = (\mathbf{M}_P - \mathbf{M}_{TP}^T \mathbf{M}_T^{-1} \mathbf{M}_{TP})$. (This form is useful for computing the temperature-polarization conditional spectra discussed in Sect. 10.5.)

The high-multipole likelihoods constructed for this paper are summarized in Table 11. These likelihoods fall into three classes:

- 12.1: The 12.1HM likelihoods are similar to the `CamSpec` likelihoods used in PCP18 in that they use the same temperature and polarization masks. The main differences with the PCP18 likelihoods are as follows: (a) in this paper we fix the temperature inter-frequency calibrations as described in Section 9.1.1, rather than carrying them as nuisance parameters; (b) we discard the 100×100 spectrum from the 12.1HMcl likelihood, (c) we have reduced the multipole range over which we clean the polarization spectra using 353 GHz template cleaning. The 12.1HM pair of likelihoods use revised calibrations of effective polarization efficiencies as described in Sect. 6.3. A comparison of results from the 12.1HM (which uses the standard temperature foreground model of Sect. 9) with those of the 12.1HMcl likelihood (which uses 545 GHz cleaned temperature spectra) is described in Sect. 7.3. This comparison tests the stability of the cosmological parameters to the temperature foreground model. The 12.1F likelihood uses the same temperature and polarization masks as in the 12.1HM likelihood but uses full mission detset spectra rather than half mission spectra. The temperature full mission detset spectra are corrected for correlated noise as described in 5.2. In the 12.1F likelihood, polarized dust emission is subtracted from the TE and EE spectra using the power-law fits from Table 9 at all multipoles. The 12.1F likelihood has higher signal-to-noise at high multipoles in TT and EE compared to the 12.1HM likelihoods. Note that because we use all non-cotemporal TE spectra in the half mission likelihoods, there is very little improvement in the signal-to-noise of the 12.1F TE spectrum compared to the 12.1HM TE spectrum.
- 12.2HM-12.4HM: The TT component of these likelihoods is the same as in 12.1HM. The sequence 12.2-12.4 explores changes in the TE and EE components of the likelihood with variations in the Q/U sky masks. Instead of using `maskpol60`, we apply the temperature masks (together with the 143 GHz point-source mask) to the Q and U maps at each frequency. For 12.2HM, 12.3HM and 12.4HM we apply `mask60`, `mask70` and `mask80` respectively to all polarization maps. All of the polarization spectra in the HM likelihoods are cleaned using 353 GHz. It is worth noting here that we have found no evidence for any point source contribution using `maskpol60`. However, we found some (albeit weak) evidence that a small number of bright highly polarized point sources such as Centaurus A contribute to the polarization spectra computed on extended polarization masks. To eliminate any possibility of bias, we decided to apply the 143 GHz point source mask to the Q and U maps in the 12.2-12.5HM likelihoods.
- 12.5HMcl: This is the most powerful likelihood that we have produced, increasing the signal-to-noise over 12.1HM by using `mask80` in both temperature and polarization²⁴. The 143 and 217 GHz temperature maps are cleaned using 545 GHz maps as described in Sect. 7.3. As discussed above, we discard 100 GHz maps. The TE and EE components of the 12.5HMcl likelihood are identical to those of the 12.4HM likelihood.

10.2 Low multipole likelihoods

The `CamSpec` likelihoods at $\ell \geq 30$ are patched on to low multipole TT and EE likelihoods covering the multipole range 2–29. These low multipole likelihoods are identical to those used in PCP18. In temperature we use the TT `Commander` likelihood, which is a Gibbs-sample-based Blackwell-Rao likelihood based on the `Commander` component separation algorithm. The `Commander` likelihood is described in [106] and PPL18 and accounts accurately for the non-Gaussian shape of the power spectrum posteriors at low multipoles. To constrain the

²⁴Applying the 143 GHz point source mask to 143 GHz temperature maps, 143 and 217 GHz Q and U maps, and the 217 GHz point source mask to 217 GHz temperature maps.

optical depth to reionization, τ , we use the **SimAll** EE likelihood, based on a which is a quasi-QML estimate of the *Planck* full mission 100×143 EE spectrum computed over the multipole range $2 \leq \ell \leq 29$. The **SimAll** likelihood is described in [99] and PPL18. We compare our TT and EE power spectra with the **Commander** and **SimAll** spectra in Figs. 10.3 and 12.4.

10.3 Notation

We adopt a simpler notation compared to that used in PCP18 to identify results from different likelihoods. Unless otherwise stated (for example, in Sect. 13.6) cosmological parameter results using a **CamSpec** TT likelihood include **Commander** and **SimAll** at low multipoles. The addition of **SimAll** is necessary to constrain τ . Parameter constraints from **CamSpec** TE, EE, or combined TEEE likelihoods include **SimAll** at low multipoles but not **Commander**. Thus, for example:

$$\begin{aligned} 12.1\text{HM TT} &\equiv 12.1\text{HM TT likelihood} + \text{Commander} + \text{SimAll}, \\ 12.1\text{HM TE} &\equiv 12.1\text{HM TE likelihood} + \text{SimAll}, \\ 12.1\text{HM TEEE} &\equiv 12.1\text{HM TE} + \text{EE likelihood} + \text{SimAll}, \\ 12.5\text{HMcl TTTEE} &\equiv 12.5\text{HM cleaned TT} + \text{TE} + \text{EE likelihood} + \text{Commander} + \text{SimAll}. \end{aligned}$$

10.4 The fiducial base Λ CDM cosmology

In the next two sections, we will present a detailed analysis of inter-frequency power spectrum residuals for both the temperature and polarization spectra. To do this, we need a fiducial cosmology and foreground solution. In this section, we will discuss results for the base Λ CDM cosmology derived from the 12.1HM likelihood, since this likelihood is the closest to the **CamSpec** temperature likelihood used in PCP18. We adopt the best-fit base Λ CDM cosmology derived from the 12.1HM TT likelihood as our fiducial theoretical model. Subsequent sections will then discuss differences between the power spectra estimated from different sky areas, between half mission and full mission data and between different methods of temperature foreground cleaning. Cosmological results from the likelihoods of Table 11 are presented in Sects. 13 and 14.

Parameter constraints for base Λ CDM derived from the 12.1HM half mission likelihood are listed in Table 12, which can be compared to Table 1 of PCP18 (which compared base Λ CDM parameters measured by **CamSpec** and **Planck**). Evidently, the small changes that we have made to **CamSpec** 12.1HM likelihood have minor effects on the cosmological parameters of base Λ CDM. For base Λ CDM, the **CamSpec** and **Planck** likelihoods agree well (as they should since the input data, temperature masks and methodology are similar). However, as discussed in PCP18 the agreement between **CamSpec** and **Planck** is less good for extensions to base Λ CDM, particularly when polarization is added to the TT likelihoods. This will be discussed in Sect. 14.

Once we have solved for a best-fit cosmology and foreground model with power spectrum $(C_\ell^{\text{for}})^k$ for frequency combination k we can maximise the likelihood Eq. 10.5 to produce a ‘best-fit’ foreground-corrected spectrum, \hat{C}_ℓ^{TT} , which is given by the solution of:

$$\sum_{kk'\ell'} (\hat{\mathcal{M}}_{\ell\ell'}^{-1})^{kk'} \hat{C}_\ell^{TT} = \sum_{kk'\ell'} (\hat{\mathcal{M}}_{\ell\ell'}^{-1})^{kk'} (\hat{C}_\ell^{k'} - (\hat{C}_\ell^{\text{for}})^{k'}). \quad (10.7)$$

Table 12. Marginalized base Λ CDM parameters with 68% confidence intervals for the 12.1HM CamSpec half mission likelihood.

Parameter	TT	TE	EE	TTTEEE
$\Omega_b h^2$	0.02218 ± 0.00022	0.02237 ± 0.00025	0.0235 ± 0.0012	0.02229 ± 0.00016
$\Omega_c h^2$	0.1202 ± 0.0021	0.1171 ± 0.0020	0.1177 ± 0.0048	0.1196 ± 0.0014
$100\theta_{\text{MC}}$	1.04081 ± 0.00047	1.04144 ± 0.00050	1.03945 ± 0.00087	1.04087 ± 0.00032
τ	0.0524 ± 0.0080	0.0504 ± 0.0082	0.0514 ± 0.0084	0.0529 ± 0.0078
$\ln(10^{10} A_s)$	3.043 ± 0.016	3.030 ± 0.022	3.054 ± 0.024	3.043 ± 0.016
n_s	0.9643 ± 0.0058	0.976 ± 0.011	0.974 ± 0.015	0.9664 ± 0.0044
H_0 [km s ⁻¹ Mpc ⁻¹]	67.09 ± 0.93	68.54 ± 0.92	68.6 ± 2.7	67.42 ± 0.63
Ω_Λ	0.682 ± 0.013	0.701 ± 0.012	$0.697^{+0.035}_{-0.027}$	0.6864 ± 0.0087
Ω_m	0.318 ± 0.013	0.299 ± 0.012	$0.303^{+0.027}_{-0.035}$	0.3136 ± 0.0087
$\Omega_m h^2$	0.1431 ± 0.0020	0.1402 ± 0.0020	0.1418 ± 0.0039	0.1425 ± 0.0013
$\Omega_m h^3$	0.09596 ± 0.00044	0.09606 ± 0.00053	$0.0973^{+0.0016}_{-0.0018}$	0.09607 ± 0.00031
σ_8	0.8117 ± 0.0090	0.799 ± 0.012	0.803 ± 0.018	0.8097 ± 0.0076
$\sigma_8 (\Omega_m/0.3)^{0.5}$	0.836 ± 0.024	0.798 ± 0.024	$0.807^{+0.053}_{-0.062}$	0.828 ± 0.017
$\sigma_8 \Omega_m^{0.25}$	0.610 ± 0.012	0.591 ± 0.013	0.595 ± 0.028	0.6059 ± 0.0086
z_{re}	$7.50^{+0.83}_{-0.75}$	$7.21^{+0.91}_{-0.77}$	$7.09^{+0.87}_{-0.73}$	$7.53^{+0.81}_{-0.73}$
$10^9 A_s$	2.097 ± 0.034	2.070 ± 0.046	2.121 ± 0.050	2.096 ± 0.033
$10^9 A_s e^{-2\tau}$	1.888 ± 0.014	1.871 ± 0.028	1.913 ± 0.032	1.885 ± 0.012
Age [Gyr]	13.821 ± 0.037	13.769 ± 0.038	13.72 ± 0.14	13.805 ± 0.025
z_*	1090.18 ± 0.41	1089.68 ± 0.42	$1088.5^{+1.5}_{-1.8}$	1089.99 ± 0.29
r_* [Mpc]	144.52 ± 0.47	145.17 ± 0.49	144.18 ± 0.71	144.61 ± 0.31
$100\theta_*$	1.04102 ± 0.00047	1.04162 ± 0.00049	1.03952 ± 0.00084	1.04106 ± 0.00031
z_{drag}	1059.51 ± 0.45	1059.73 ± 0.55	1062.2 ± 2.3	1059.72 ± 0.33
r_{drag} [Mpc]	147.24 ± 0.47	147.85 ± 0.51	146.50 ± 0.75	147.30 ± 0.31
k_D [Mpc ⁻¹]	0.14056 ± 0.00051	0.14006 ± 0.00058	0.1422 ± 0.0013	0.14059 ± 0.00034
z_{eq}	$3403 \pm 48 = 7$	3334 ± 47	3373 ± 90	3390 ± 32
k_{eq} [Mpc ⁻¹]	0.01039 ± 0.00014	0.01018 ± 0.00014	0.01030 ± 0.00028	0.010347 ± 0.000097
$100\theta_{s,\text{eq}}$	0.4492 ± 0.0046	0.4561 ± 0.0046	0.4524 ± 0.0094	0.4505 ± 0.0031
f_{2000}^{143}	29.8 ± 2.9			28.9 ± 2.7
f_{2000}^{217}	107.6 ± 2.0			107.1 ± 1.8
$f_{2000}^{143 \times 217}$	32.5 ± 2.1			31.8 ± 1.9

The covariance matrix of the estimates \hat{C}_ℓ^{TT} is given by the inverse of the Fisher matrix:

$$\langle \Delta \hat{C}_\ell^{TT} \Delta \hat{C}_{\ell'}^{TT} \rangle = \left(\sum_{kk'} (\hat{\mathcal{M}}_{\ell\ell'}^{-1})^{kk'} \right)^{-1}. \quad (10.8)$$

The spectrum \hat{C}_ℓ^{TT} is therefore simply a maximum likelihood coaddition of the individual TT spectra used in the likelihood, corrected for foregrounds.

Fig. 10.1 shows the frequency averaged temperature power spectrum determined for the 12.1HM likelihood. Fig. 10.2 shows the coadded TE and EE power spectra compared to the best fit base Λ CDM theory spectrum fitted to the TT likelihood. Note that there are no foreground parameters in TE and EE; the only ‘nuisance’ parameters in the polarization spectra are overall calibration parameters which are very close to unity. In Fig. 10.2 we have multiplied the TE and EE spectra by factors of 0.9991 and 0.9992 respectively, which are the

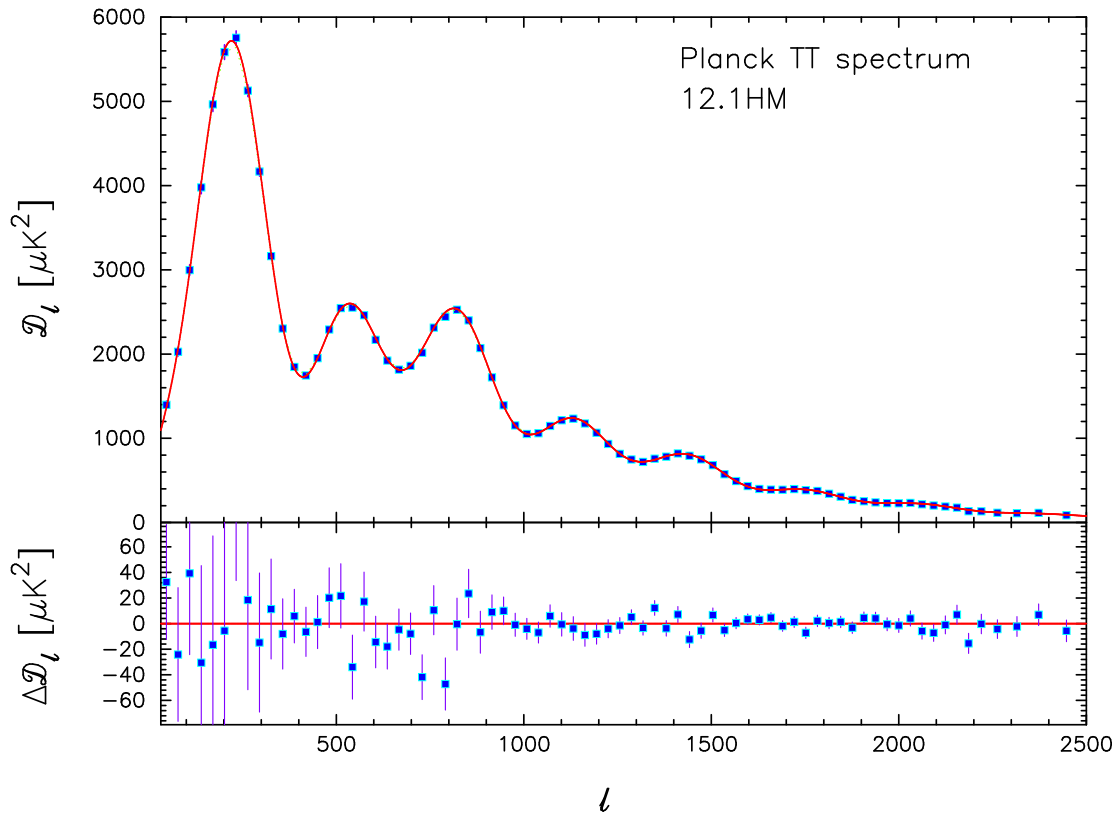


Figure 10.1. The maximum likelihood frequency averaged temperature power spectrum for the 12.1HM *CamSpec* half mission likelihood. The error bars on the band averages show $\pm 1\sigma$ ranges computed from the covariance matrix of Eq. 10.8. The lower panel shows the residuals with respect to the fiducial base Λ CDM cosmology (fitted to 12.1HM TT).

best fit values for the relative calibrations c_{TE} and c_{EE} determined from the base Λ CDM fit to the 12.1HM TTTEEE likelihood.

Values of $\hat{\chi}^2$ (where the hat denotes the reduced χ^2) for the fits plotted in Figs. 10.1 and 10.2 are listed in Table 13 for various blocks of the 12.1HM likelihood. In PCP13 we found acceptable values of $\hat{\chi}^2$ for the individual TT spectra, but excess $\hat{\chi}^2$ for the full TT likelihood. The 2015 *CamSpec* likelihood used in PCP15 had acceptable $\hat{\chi}^2$ in TT but had excess $\hat{\chi}^2$ for the TE and EE spectra. There are several reasons for the differences between the 2015 *CamSpec* likelihood and the likelihoods produced for this paper. For the TE and EE spectra, we correct for temperature-to-polarization leakage and effective calibrations as described in Sect. 6. The temperature-to-polarization leakage corrections are quite small for TE and are negligible for the EE spectra. The effective calibrations in TE and EE, on the other hand, have quite a large effect in reducing χ^2 for individual frequencies and for the coadded TE and EE spectra. The most significant change, however, is in the noise model adopted in this paper, which is now based on odd-even map differences instead of half-ring map differences. As described in Sect. 5, the odd-even differences lead to higher noise estimates than the half-ring differences, particularly for the EE spectra. We also found evidence, by comparing cross and auto spectra, that the odd-even differences actually overestimate the noise in the Q and U maps, particularly at 100 GHz. A small overestimate of the noise in polarization

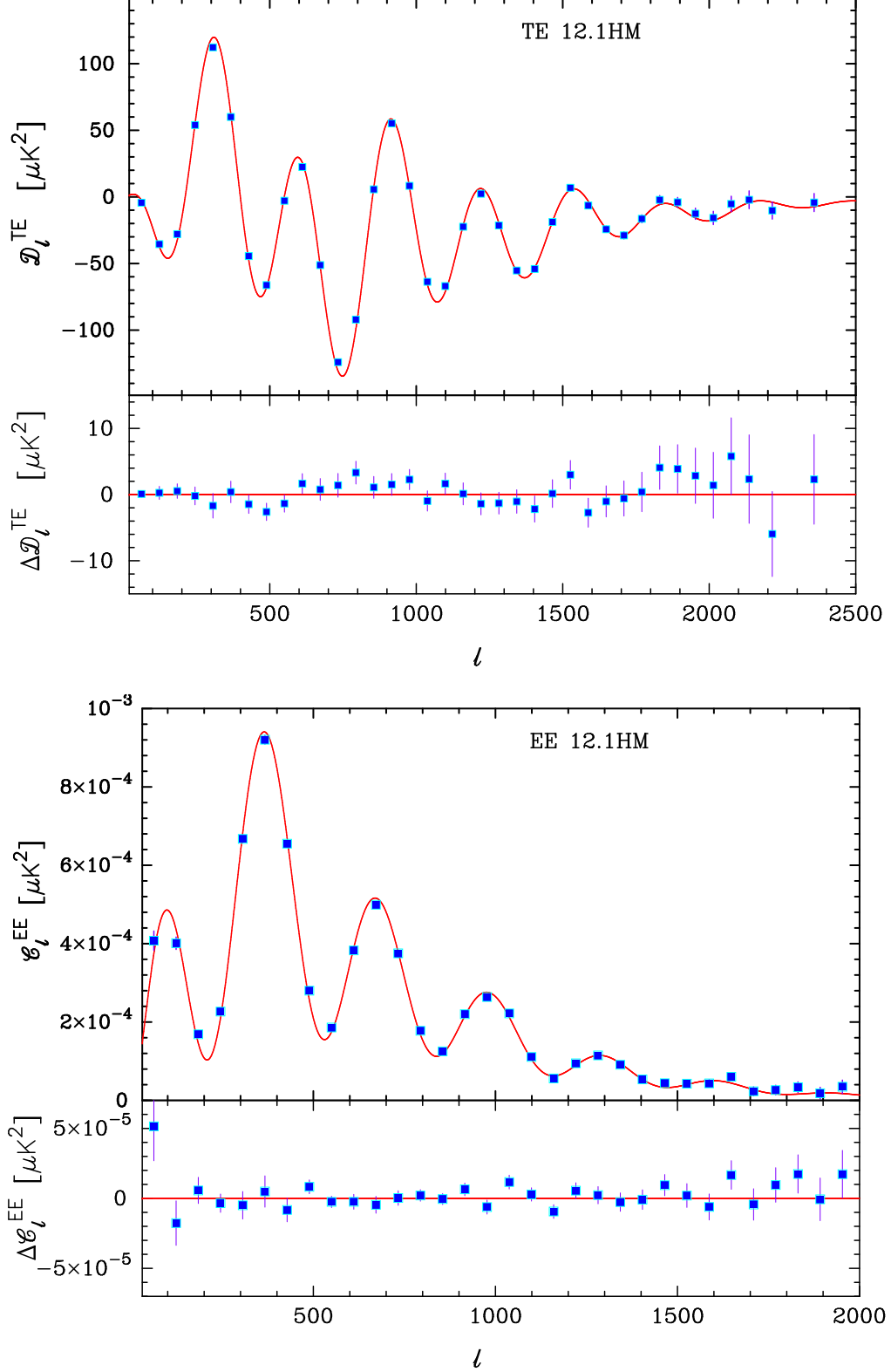


Figure 10.2. The coadded TE and EE power spectra of the 12.1HM half mission likelihood. The error bars on the band averages are computed from the `CamSpec` covariance matrices. The theoretical spectra show the fiducial base Λ CDM cosmology fitted to 12.1HM TT (i.e. they are not fits to the polarization spectra). We have applied (small) corrections to the TE and EE spectra using relative calibrations derived from fits to the 12.1HM TTTEEE likelihood. Residuals with respect to the fiducial base Λ CDM model are shown in the lower panels. Although the `CamSpec` likelihoods use TE only to $\ell_{\text{max}} = 2000$, we have plotted the TE spectra out to $\ell_{\text{max}} = 2500$.

Table 13. $\hat{\chi}^2$ values for the 12.1HM spectra and likelihood. For the first five rows, testing the TT spectra, we adopt the best fit base Λ CDM model and nuisance parameters fitted to the 12.1HM TT likelihood. For the remaining five rows, which test the components of the TTTEEE likelihood, we adopt the best fit model and nuisance parameters fitted to the 12.1HM TTTEEE likelihood. The second column gives the multipole range, N_D is the size of the data vector (equal to the multipole range for single spectra). $\hat{\chi}^2 = \chi^2/N_D$ is the reduced χ^2 . The last column lists the number of standard deviations by which $\hat{\chi}^2$ differs from unity. ‘TT coadded’ refers to the maximum likelihood frequency coadded spectrum plotted in Fig. 10.1. The next four rows give $\hat{\chi}^2$ values for the individual foreground corrected TT spectra that enter the likelihood. ‘TT all’ gives $\hat{\chi}^2$ for the complete TT likelihood and includes correlations between the frequency spectra. The next two lines give $\hat{\chi}^2$ for the TE and EE spectra plotted in Fig. 10.2. The final two lines list $\hat{\chi}^2$ for the TEEE block and for the 12.1HM TTTEEE likelihood.

spectrum	ℓ range	N_D	$\hat{\chi}^2$	$(\hat{\chi}^2 - 1)/\sqrt{2/N_D}$
TT coadded	30 – 2500	2471	1.01	0.18
TT 100 \times 100	30 – 1400	1371	1.04	0.97
TT 143 \times 143	30 – 2000	1971	1.02	0.56
TT 143 \times 217	500 – 2500	2001	0.98	–0.57
TT 217 \times 217	500 – 2500	2001	0.95	–1.58
TT All	30 – 2500	7344	0.99	–0.38
TE	30 – 2000	1971	1.01	0.32
EE	30 – 2000	1971	0.93	–2.12
TEEE	30 – 2000	3942	1.02	0.98
TTTEEE	30 – 2500	11286	0.97	–2.20

is almost certainly the explanation for the low $\hat{\chi}^2$ for the coadded EE spectrum listed in Table 13 (though it is not unreasonably low). Nevertheless, the $\hat{\chi}^2$ values are consistent with unity. Even for the full TTTEEE likelihood, which has a large data vector length of 11286, $\hat{\chi}^2$ is consistent with unity to about 2σ (cf. Eq. 5.5). In summary, the absolute values of χ^2 for the likelihoods used in this paper are acceptable, though we have evidence from the coadded (and individual) EE spectra that the Q and U noise power spectrum estimates used in this paper are too high. Estimation of noise power spectra and noise correlations to a precision of better than a percent remains a challenging problem for *Planck* analysis. End-to-end simulations have been used to characterize the noise properties of polarized HFI maps at low multipoles [102], but these fail to match the noise properties of the real data at high multipoles because some important aspects of the low-level data process (e.g. cosmic ray removal) are not included self-consistently in the simulations.

Fig. 10.3 compares the coadded foreground subtracted spectrum from Fig. 10.1 to the **Commander** spectrum. The **Commander** spectrum is computed using 86% of the sky, which is slightly larger than the (effective) $f_{\text{sky}}^W = 70.1\%$ of sky used at 100 GHz in the 12.1HM likelihood (see Table 1). The left hand figure compares the power spectra multipole-by-multipole up to the maximum of the first acoustic peak. The figure to the right shows the residuals with respect to the best-fit Λ CDM model in band powers of width $\Delta\ell = 21$. We have made no corrections for relative effective calibration differences between the **Commander** and **CamSpec** TT spectra. The **CamSpec** spectrum reproduces the features of the **Commander** spectrum multipole-by-multipole even at multipoles ≤ 30 . This demonstrates that the choice

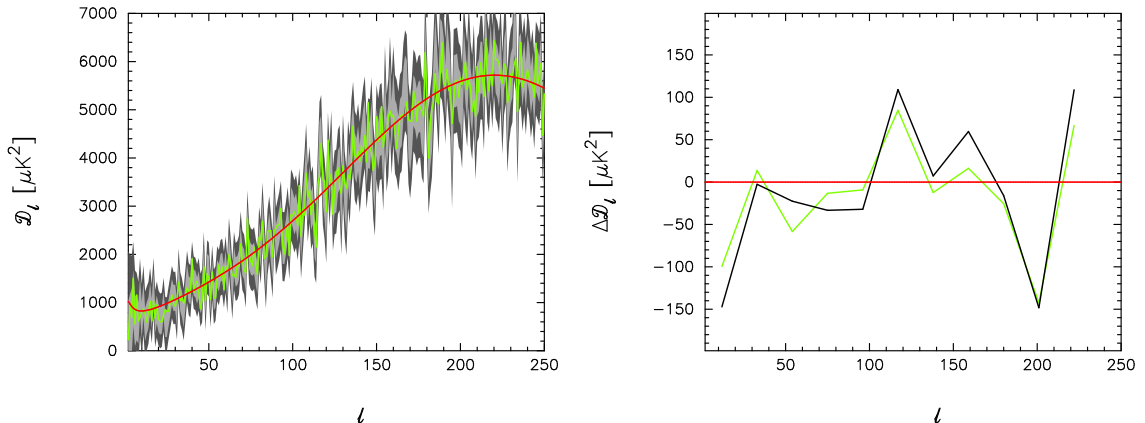


Figure 10.3. Left hand figure: The green line shows the TT power spectrum plotted multipole-by-multipole from the **Commander** component separation algorithm. The **Commander** algorithm provides samples of component separated spectra which are used to construct the TT likelihood at multipoles $\ell < 30$. The grey bands show the 1σ and 2σ ranges of the coadded foreground corrected **CamSpec** 12.1HM TT spectrum. The red line shows the fiducial base Λ CDM model, as plotted in Fig. 10.1. Right hand figure: Residuals of the power spectra with respect to the fiducial base Λ CDM model averaged in bands of width $\Delta\ell = 21$. The green line shows the **Commander** power spectrum residuals. The black line shows the **CamSpec** residuals.

of $\ell_{\min} = 30$ for the transition from the **Commander** TT likelihood to **CamSpec** is not particularly critical. The **Commander** TT estimates at low multipoles have lower variance than the PCL estimates used in **CamSpec**. The reason for using the **Commander** likelihood is not primarily to improve on foreground removal, but rather to model accurately the non-Gaussian distributions of the power spectrum estimates at low multipoles.

10.5 Conditional spectra

Having demonstrated a basic level of consistency of the TT component of the likelihood, in this subsection we present additional tests of the coadded polarization spectra. Given the best fit cosmology and foreground parameters fitted to the four temperature spectra of the 12.1HM TT likelihood, we can calculate the expected TE and EE spectra given the TT spectra. Writing the data vector of Eq. 10.1 as

$$\hat{\mathbf{C}} = (\hat{\mathbf{C}}_1^{TT}, \hat{\mathbf{C}}_2^{TT}, \dots, \hat{\mathbf{C}}_N^{TT}, \hat{\mathbf{C}}^{TE}, \hat{\mathbf{C}}^{EE})^T = (\hat{\mathbf{X}}_T, \hat{\mathbf{X}}_P)^T, \quad (10.9)$$

(where all spectra are corrected for best-fit calibration factors) the expected value of the polarization vector given the temperature vector is

$$\hat{\mathbf{X}}_P = \mathbf{X}_P^{\text{theory}} + \mathbf{M}_{TP}^T \mathbf{M}_T^{-1} (\hat{\mathbf{X}}_T - \mathbf{X}_T^{\text{theory}} - \mathbf{X}_T^{\text{for}}), \quad (10.10)$$

with covariance

$$\hat{\Sigma}_P = \mathbf{M}_P - \mathbf{M}_{TP}^T \mathbf{M}_T^{-1} \mathbf{M}_{TP}. \quad (10.11)$$

In Eq. 10.10, $\mathbf{X}_T^{\text{theory}}$ and $\mathbf{X}_P^{\text{theory}}$ are the theoretical temperature and polarization spectra deduced from minimising the TT likelihood, and $\mathbf{X}_T^{\text{for}}$ is the corresponding foreground/nuisance parameter solution.

Figure 10.4 shows the results of applying Eqs. 10.10 and 10.11. There is almost no correlation between the TT, TE and EE spectra at multipoles $\ell \gtrsim 1000$ because the polarization

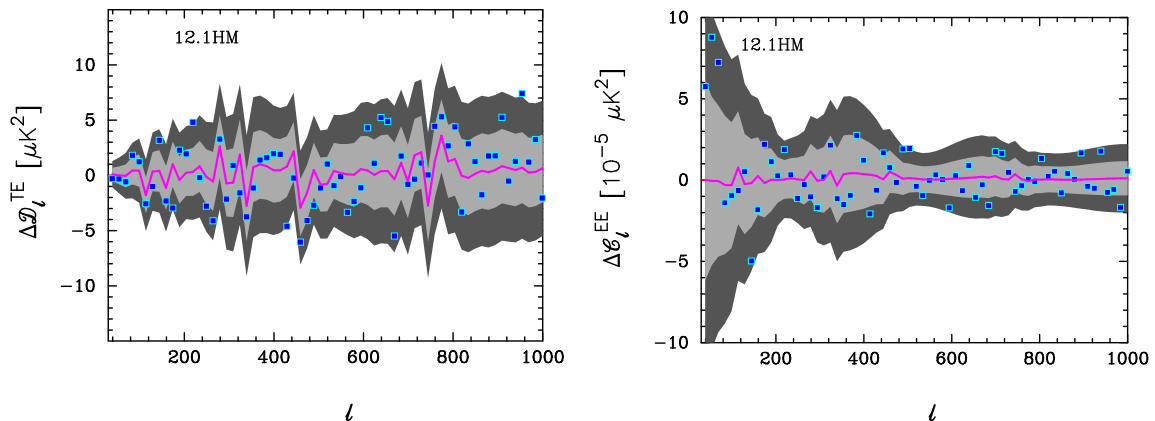


Figure 10.4. TE and EE residuals with respect to the best-fit base Λ CDM cosmology fitted to the TT likelihood. The purple lines show the expected TE and EE spectra given the TT data (Eq. 10.10). The shaded areas show the 1 and 2σ ranges computed from Eq. 10.11.

spectra are dominated by noise. We therefore plot the spectra in Fig. 10.4 only up to $\ell = 1000$. There is a correspondence between features in the TE spectrum and the predicted spectrum; evidently some of the features in the TT spectrum, for example at $\ell \approx 320$ and $\ell \approx 800$ have correlated counterparts in TE. In EE, however, the correlations with the TT spectra are extremely weak. In both cases, the data points are consistent with the error model with no obvious outliers. These tests show that the polarization spectra are statistically consistent with the TT spectra and with the base Λ CDM cosmology.

11 Inter-frequency consistency in temperature

Given the high precision of the *Planck* data, the possibility that unidentified systematics might be lurking within the dataset is an important concern. We have already demonstrated the intra-frequency consistency of the dataset spectra in Sect. 6.2. The results of the previous section showed that after solving for a parametric foreground model, the four TT spectra of the 12.1HM likelihood are compatible with the best-fit base Λ CDM cosmology as judged by χ^2 statistics. In this section, we will discuss some more detailed consistency tests of the power spectra measured for different frequency combinations. This section deals exclusively with consistency of the temperature spectra. Inter-frequency consistency of the TE and EE spectra is discussed in the next section.

11.1 Consistency of TT spectra in the 12.1HM half mission likelihood

Figure 11.1 compares the foreground corrected 100×100 and 143×143 half mission spectra used in the 12.1HM likelihood. The residuals at multipoles $\ell \lesssim 500$, where dust dominates the foreground model, are small (differing by a maximum of $26 \mu\text{K}^2$ at $\ell = 306$ for the band-powers shown in the figure, which have $\Delta\ell = 31$), demonstrating the consistency of the model for dust subtraction. These differences are similar to those seen in Fig. 10.3 comparing the *Commander* spectrum with the coadded foreground-corrected 12.1HM *CamSpec* spectrum of Fig. 10.1. Typically, the consistency of the foreground corrected *CamSpec* spectra is no better than $\sim 30 \mu\text{K}^2$ at the maximum of the first acoustic peak (i.e. consistent to $\sim 0.5\%$), though we see better consistency at these multipoles if we clean the spectra using 545 GHz and apply

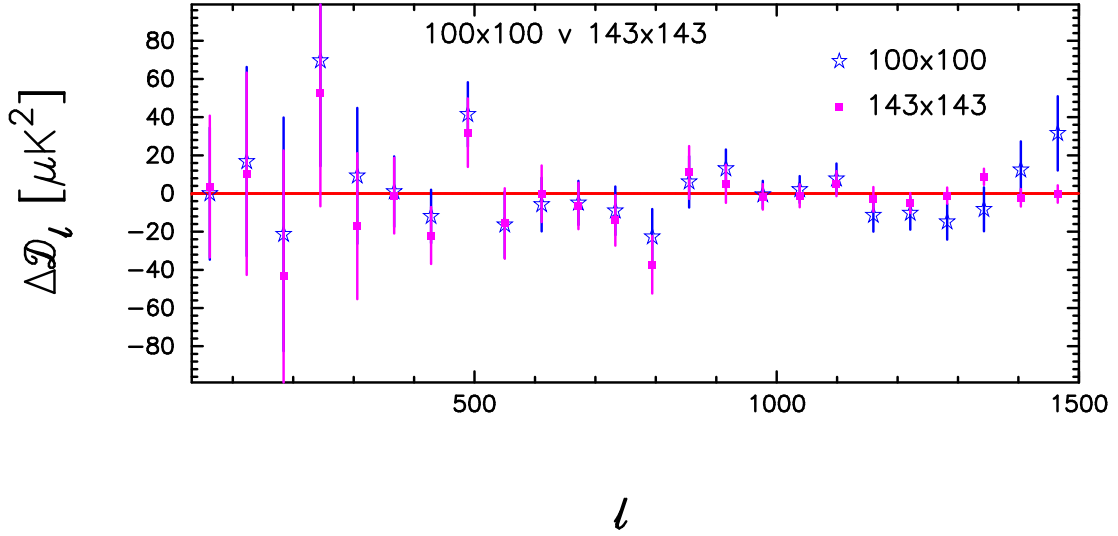


Figure 11.1. Residuals with respect to the best-fit base Λ CDM cosmology and foreground model fitted to TT for the 100×100 and 143×143 half mission cross spectra used in the 12.1HM likelihood. Note that the 100×100 and 143×143 spectra have been computed using different sky masks.

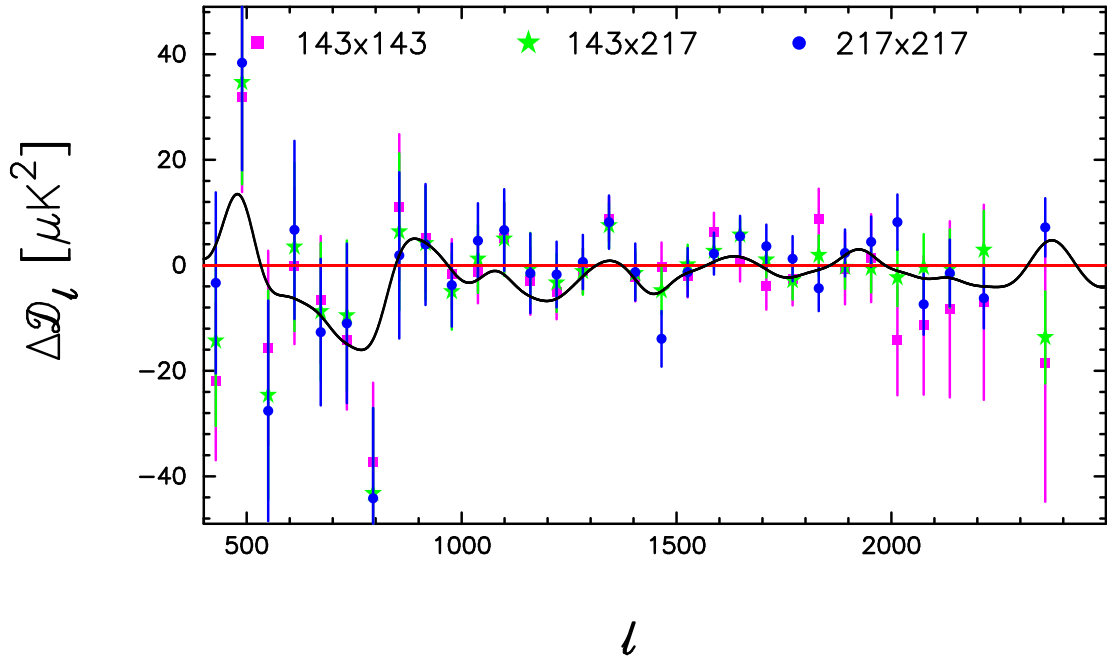


Figure 11.2. As Fig. 11.1, but comparing residuals for the 143×143 , 143×217 and 217×217 spectra used in the 12.1HM likelihood. The black line shows the residuals of the maximum likelihood coadded spectrum of Fig. 10.1 smoothed with a Gaussian of width $\sigma_\ell = 40$.

identical masks at each frequency (see Fig. 13.11). Having demonstrated the consistency of the 100×100 and 143×143 spectra, in the remainder of this section we concentrate on the consistency of the 143×143 , 143×217 and 217×217 spectra.

The residuals for the remaining three spectra are compared graphically in Fig. 11.2 and listed numerically in Table 14. Residuals that differ from zero by more than 2σ *assuming that the cosmology and foreground model are known exactly* are marked in red in Table 14. The three spectra are in very good agreement. The nearly $\sim 2\sigma$ upward fluctuation at $\ell_b \approx 489$ and $\sim 2.5\sigma$ downward fluctuation at $\ell_b = 794$ (which have been noted by some theorists e.g. [22]) are reproduced in all of the *Planck* spectra and are clearly real features of the primordial CMB spectrum. The general oscillatory patterns in the residuals, which various authors (e.g. [43]) have claimed might be related to an inconsistency in the lensing smoothing of the acoustic peaks (and related to the high value of A_L measured from *Planck* TT, see Fig. 11.5) are also reproduced across the three spectra (see also Fig. 12 of [100]). The most deviant point in Fig. 11.2 is for the 217×217 spectrum in the band centred at $\ell = 1469$ (as noted in PPL15 and PCP18). This band power deviates from zero by 2.63σ on the assumption that the cosmology and foreground model is known exactly (which is, of course, not true).

The residuals and errors in Fig. 11.2 are dominated by cosmic variance at multipoles $\ell \lesssim 1500$. A more sensitive consistency test is provided by differencing the power spectra, so reducing cosmic variance and sensitivity to the cosmological model. This is illustrated for the 12.1HM temperature spectra in the upper plot in Fig. 11.3. Note that: (a) the errors on these spectral differences are constructed by forming linear combinations of the **CamSpec** covariance matrices; (b) cosmic variance is not completely eliminated because we use different masks at 143 and 217 GHz; (c) the errors do not accurately model CMB-foreground cross-correlations, as discussed in Sect. 7.2. The agreement between the spectra is generally excellent. Nevertheless there are some outliers which might appear to be statistically unlikely. For example, in the panel showing the $143 \times 143 - 217 \times 217$ difference, there are outliers at $\ell_b = 428$ (-2.35σ) and $\ell_b = 1465$ (2.92σ). In the panel showing the $143 \times 217 - 217 \times 217$ difference, there are outliers in exactly the same bands, i.e. at $\ell_b = 428$ (-3.16σ) and $\ell_b = 1465$ (3.23σ). In the central panel, showing the $143 \times 143 - 143 \times 217$ spectrum differences, all of the bandpowers are consistent with zero to within 2σ . Our interpretation of these outliers is as follows:

- (i) None of the outliers have high statistical significance. Statistically acceptable variations in the foreground model lead to tilts in the foreground corrected spectra at high multipoles ($\ell \gtrsim 1000$) and this can alter the statistical significance of a single bandpower residual by up to $\sim 1\sigma$.
- (ii) The amplitude of the CMB-foreground correlations is highest for the 217×217 spectra and adds to the variance of this spectrum.
- (iii) At low multipoles ($\ell \lesssim 1000$), the dust correction for the 217×217 spectrum is large and inaccurate at the $\sim 10 - 30 \mu\text{K}^2$ level. The residuals in the $143 \times 143 - 217 \times 217$ and $143 \times 217 - 217 \times 217$ spectra at $\ell_b = 428$ arise from inaccurate dust subtraction in the 217×217 spectrum. This is additional motivation to exclude the 217×217 spectrum at $\ell < 500$ from the **CamSpec** likelihood.

The clearest way of demonstrating these points is to repeat these inter-frequency comparisons using a completely different model of dust cleaning and extragalactic foregrounds.

Table 14. Band-power residuals, $\Delta\hat{D}_{\ell_b}$, with respect to the fiducial base Λ CDM cosmology and foreground model for the 143×143 , 143×217 and 217×217 spectra used in the 12.1HM CamSpec likelihood. ℓ_b is the multipole at midpoint of the band. The columns labelled ‘error’ give the 1σ uncertainties on $\Delta\hat{D}_{\ell_b}$ assuming that the best-fit cosmology plus foreground model is exact. The columns labelled N_σ give the number of standard deviations by which $\Delta\hat{D}_{\ell_b}$ differs from zero. Entries which differ from zero by more than 2σ are coloured in red.

ℓ_b	143×143			143×217			217×217		
	$\Delta\hat{D}_{\ell_b}$	error	N_σ	$\Delta\hat{D}_{\ell_b}$	error	N_σ	$\Delta\hat{D}_{\ell_b}$	error	N_σ
62	3.66	37.15	0.10	1.34	40.37	0.03	36.46	43.47	0.84
123	10.34	53.01	0.20	8.97	56.86	0.16	5.49	60.12	0.09
184	-43.05	65.60	-0.66	-33.25	70.09	-0.47	-23.16	73.70	-0.31
245	52.60	59.33	0.89	85.82	63.41	1.35	109.56	66.65	1.64
306	-17.13	38.26	-0.45	-37.51	40.98	-0.92	-42.47	43.29	-0.98
367	-1.13	19.80	-0.06	-11.37	21.32	-0.53	-13.52	22.75	-0.59
428	-22.01	14.94	-1.47	-14.34	16.12	-0.89	-3.32	17.16	-0.19
489	31.84	17.96	1.77	34.68	19.33	1.79	38.41	20.40	1.88
550	-15.69	18.46	-0.85	-24.61	19.85	-1.24	-27.58	20.91	-1.32
611	-0.12	14.83	-0.01	3.48	15.96	0.22	6.71	16.89	0.40
672	-6.55	12.12	-0.54	-8.77	13.05	-0.67	-12.68	13.89	-0.91
733	-14.08	13.25	-1.06	-9.55	14.25	-0.67	-11.00	15.12	-0.73
794	-37.33	15.08	-2.48	-43.22	16.19	-2.67	-44.15	17.12	-2.58
855	11.01	13.85	0.80	6.37	14.86	0.43	1.88	15.76	0.12
916	5.09	9.97	0.51	4.14	10.70	0.39	3.95	11.48	0.34
977	-1.73	6.70	-0.26	-5.00	7.20	-0.69	-3.75	7.88	-0.48
1038	-1.19	6.01	-0.20	1.21	6.43	0.19	4.65	7.12	0.65
1099	5.16	6.59	0.78	4.99	7.03	0.71	6.69	7.75	0.86
1160	-2.98	6.41	-0.46	-0.66	6.80	-0.10	-1.49	7.54	-0.20
1221	-4.98	5.24	-0.95	-3.33	5.51	-0.60	-1.74	6.24	-0.28
1282	-1.12	4.26	-0.26	-1.17	4.42	-0.27	0.62	5.14	0.12
1343	8.76	4.23	2.07	7.53	4.32	1.74	8.17	5.07	1.61
1404	-2.24	4.60	-0.49	-1.53	4.63	-0.33	-1.28	5.42	-0.24
1465	-0.25	4.56	-0.05	-4.80	4.47	-1.07	-13.92	5.29	-2.63
1526	-2.02	4.06	-0.50	0.10	3.79	0.03	-1.32	4.60	-0.29
1587	6.27	3.69	1.70	2.66	3.19	0.83	2.22	3.99	0.56
1648	0.80	3.86	0.21	5.76	3.11	1.85	5.51	3.88	1.42
1709	-3.98	4.42	-0.90	1.04	3.36	0.31	3.62	4.11	0.88
1770	-2.52	5.07	-0.50	-2.88	3.60	-0.80	1.26	4.29	0.29
1831	8.72	5.80	1.50	1.90	3.78	0.50	-4.34	4.35	-1.00
1892	-0.59	6.82	-0.09	-0.37	4.07	-0.09	2.34	4.46	0.53
1953	1.35	8.34	0.16	-0.53	4.61	-0.11	4.46	4.78	0.93
2014	-14.22	10.42	-1.36	-2.34	5.39	-0.43	8.18	5.26	1.55
2075	-11.39	13.15	-0.87	-0.40	6.33	-0.06	-7.38	5.79	-1.27
2136	-8.35	16.70	-0.50	-0.63	7.45	-0.08	-1.48	6.35	-0.23
2215	-7.01	18.50	-0.38	2.89	7.45	0.39	-6.22	5.73	-1.09
2358	-18.44	26.38	-0.70	-13.67	8.72	-1.57	7.19	5.53	1.30

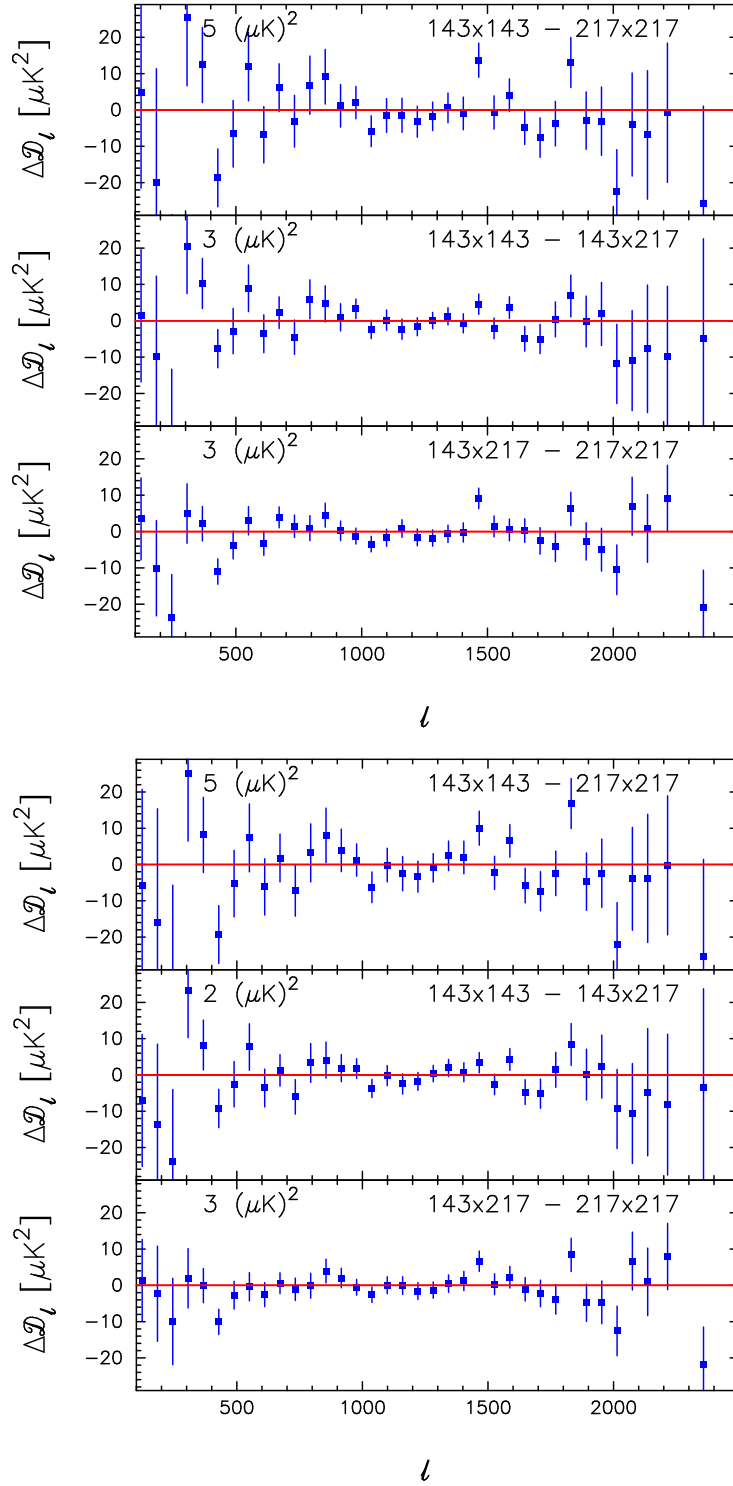


Figure 11.3. Differences in the foreground corrected temperature power spectra used in the 12.1HM likelihood (upper figure) and for the 545 GHz cleaned spectra used in the 12.1HMcl likelihood (lower figure). We use the foreground solution fitting the base Λ CDM model to the 12.1HM TT and 12.1HMcl TT likelihoods respectively. Upper panels show the difference between the 143×143 and 217×217 spectra, middle panels show the difference between the 143×217 and 143×143 spectra, and the lower panels show the difference between the 143×217 and 217×217 spectra. The error bars for the power spectrum differences are computed from linear combinations of the `CamSpec` covariance matrices. The numbers in each panel give the rms residuals of the bandpower differences over the multipole range $800 \leq \ell \leq 1500$.

11.2 Cleaned temperature spectra

Section 7.3 introduced ‘cleaned’ temperature spectra using 353, 545 and 857 GHz maps as Galactic dust templates and demonstrated that high frequency cleaning accurately removes Galactic dust and also much of the CIB. In PCP15 and PCP18, we formed ‘cleaned’ likelihoods using 545 GHz as a high frequency template. As discussed in Sect. 7.3 we focus on 545 GHz temperature cleaning in the rest of this paper, since there is a significant signal-to-noise penalty if 353 GHz is used as a template. (Note that using 353 GHz temperature cleaning leads to almost identical results to those presented here, though with additional noise at $\ell \gtrsim 2000$.)

Figure 11.4 compares the 545 GHz cleaned spectra with the 12.1HM temperature spectra. (As explained in Sect. 9.4, we exclude the 100×100 spectrum from the ‘cleaned’ likelihoods.) The upper plots in each panel of Fig. 11.4 show the difference of the spectra and the fiducial base Λ CDM model fitted to the 12.1HM TT likelihood. These panels illustrate the effectiveness of 545 GHz cleaning. For all three spectra, Galactic dust emission is accurately removed in the cleaned spectra (as discussed in Sect. 7.4). 545 GHz cleaning also removes much of the extragalactic foreground at high multipoles in the 217×217 and 143×217 spectra (which are dominated by the clustered and unclustered CIB). 545 GHz cleaning is much less effective at removing extragalactic foregrounds in the 143×143 spectrum. Nevertheless, the most striking result in Fig. 11.4 is the very close agreement between the cleaned and uncleaned residuals of the foreground corrected spectra plotted in the lower plots in each panel. (Note that for the 545 GHz cleaned spectra, we have used the foreground solution determined from the 12.1HMcl TT likelihood fitted to base Λ CDM.)

The 12.1HMcl and 12.1HM likelihoods give almost identical solutions for the base Λ CDM cosmology (see Sect. 13.3), even though the foreground models used in the two likelihoods are very different. This is perhaps the clearest demonstration that the cosmological results from *Planck* for Λ CDM-like models are insensitive to unresolved foregrounds.

Although 545 GHz temperature cleaning has no significant effect on cosmology, it does have an impact on the inter-frequency residuals. This can be seen from the lower figure in Fig. 11.3 showing the foreground cleaned spectral differences. At low multipoles, 545 GHz cleaning removes the CMB-foreground correlations and so the spectra are more consistent at $\ell \lesssim 500$. The $143 \times 217 - 217 \times 217$ difference in the band centred at $\ell_b = 1465$ deviates from zero by 2.36σ for the cleaned spectra instead of 3.23σ for the uncleaned spectra. Inter-frequency residuals are therefore sensitive to small differences in the foreground solution (and to the modelling of foreground errors in the covariance matrix). This needs to be borne in mind when comparing inter-frequency residuals. For the 545 GHz cleaned spectra, there is no evidence for unusual differences (i.e. $> 2.5\sigma$) between the three spectra over the multipole ranges used in the 12.1HMcl likelihood.

Figure 11.5 shows the inter-frequency residuals for the 12.1HMcl 545 GHz cleaned spectra. This figure can be compared with the equivalent plot (Fig. 11.2) for the uncleaned spectra. We see a similar pattern of residuals and slightly (but barely perceptible) improved consistency between the three spectra. The general pattern of the residuals in Figs. 11.2 and 11.5 is consistent between frequencies, despite the very different approaches to foreground modelling. In particular, the oscillatory features seen in these plots at multipoles $\lesssim 2000$ are reproducible in all of these spectra (and across detectors within a fixed frequency band, cf. Fig. 6.1).

One of the unusual aspects of the *Planck* TT data, evident since the 2013 data release, is the favouritism for high values of the phenomenological lensing parameter, A_L . This issue has

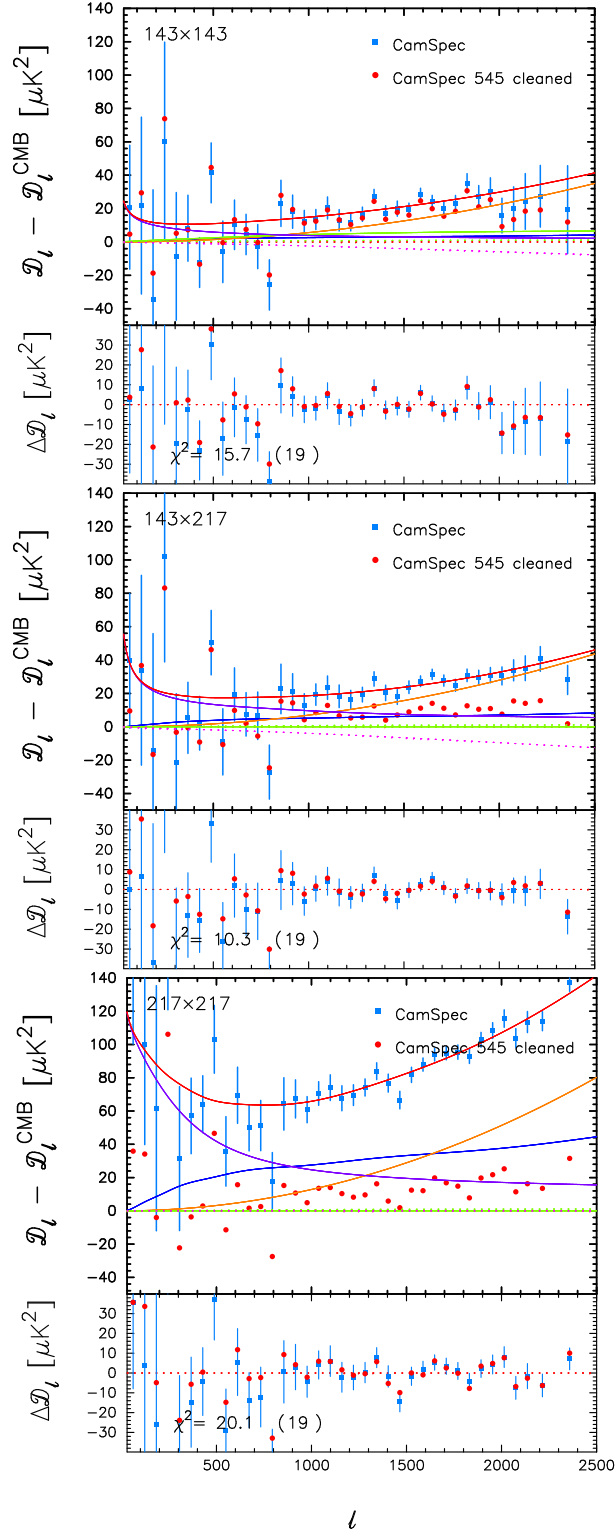


Figure 11.4. Comparison of the 12.1HM spectra (blue points) and 545 cleaned spectra (red points). The upper plot in each figure shows the residuals with respect to the fiducial base Λ CDM model. Major foregrounds are shown by the solid lines colour coded as follows: total foreground spectrum (red); Poisson point sources (orange), clustered CIB (blue); thermal SZ (green) and Galactic dust (purple). Minor foreground components are shown by the dotted lines colour coded as follows: kinetic SZ (green) and tSZxCIB (purple). The lower plots in each figure show the spectra after subtraction of the best-fit foreground model. For the cleaned spectra we adopt power-laws to model residual foregrounds, as described in Sect. 9.4. The χ^2 values of the residuals of the blue band powers over the multipole range $1000 \leq \ell \leq 2200$, and the number of band powers, are listed in the lower panels.

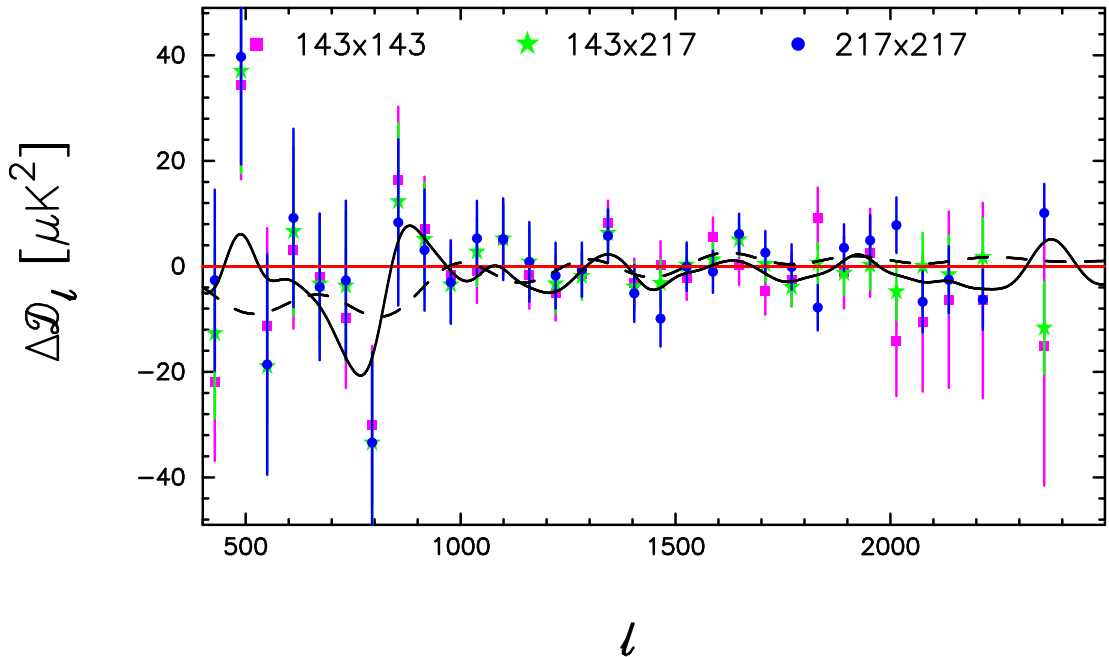


Figure 11.5. As Fig. 11.2, but for spectra cleaned with 545 GHz as used in the 12.1HMcl likelihood. The residuals here are computed with respect to the best fit base Λ CDM cosmology + foreground model derived from the 12.1HMcl TT likelihood. The black line shows the residuals of the maximum likelihood frequency coadded spectrum smoothed with a Gaussian of width $\sigma_\ell = 40$. The dashed line shows the difference between the best-fit A_L model (with $A_L = 1.14$) and the fiducial model smoothed with a Gaussian of width $\sigma_\ell = 40$.

been discussed at length in PCP15, [100] and PCP18 and will be revisited in Sect. 14.1. The dashed line in Fig. 11.5 shows the best-fit A_L model fitted to the 12.1HMcl TT likelihood, for which $A_L = 1.14$. Fig. 11.5 (which can be compared to Fig. 24 in PCP18) shows that the oscillatory residuals of the A_L model over the multipole range 800 – 1800 correlate with the residuals seen in both the cleaned and uncleaned likelihood. The tendency for *Planck* to favour high values of A_L is driven by features in this range of multipoles, which are consistent across the frequency range, and not by features exclusive to the 217×217 spectrum. As noted in PCP18, models with positive curvature show a similar pattern of residuals to A_L and so are also favoured by the TT data. As far as we can see, the favouritism for high values of A_L is a modest statistical fluctuation. We have found no evidence to suggest that this result is driven by systematic errors in the *Planck* data. Sections 14.1 and 14.2 will discuss results for A_L and Ω_K in further detail, including constraints from the TE and EE spectra. First, we will discuss the behaviour of the temperature spectra as a function of sky coverage. Our aim is to create more powerful likelihoods than the 12.1HM pair by using more sky and to quantify what happens to parameters such as A_L and Ω_K .

11.3 Residuals as a function of sky coverage

In this subsection, we analyse how the temperature spectra change with increasing sky coverage. We focus on the 217×217 and 143×217 545 GHz cleaned spectra. Figure 11.6 shows how these spectra change with increasing sky coverage. We have shown in Sect. 7.4 that 545

cleaning accurately removes Galactic dust emission leaving extragalactic residual foregrounds. The remaining foreground excesses should therefore be independent of the size of the mask.

This is what we see in Fig. 11.6. The solid lines in the upper panel shows the power-law fit to the excess foreground determined from the 12.1HMcl TT likelihood. The lower panels show the residuals of the foreground subtracted spectra as a function of mask size. The solid lines in these panels show the smoothed maximum likelihood frequency coadded spectrum as plotted in Fig. 11.5. One can see that the oscillatory residuals are present for all mask sizes and in both spectra. Furthermore, the scatter around around the black line *decreases* as more sky area is used. In fact, for the bandpowers plotted in Fig. 11.6, the rms scatter over the multipole range $1000 \leq \ell \leq 1800$ varies with mask as:

$$\left\{ \begin{array}{llll} \sigma_{217 \times 217} = 3.9 (\mu\text{K})^2, & \text{mask50}, & \sigma_{143 \times 217} = 2.9 (\mu\text{K})^2, & \text{mask50}, \\ \sigma_{217 \times 217} = 3.7 (\mu\text{K})^2, & \text{mask60}, & \sigma_{143 \times 217} = 2.3 (\mu\text{K})^2, & \text{mask60}, \\ \sigma_{143 \times 217} = 3.1 (\mu\text{K})^2, & \text{mask70}, & \sigma_{143 \times 217} = 2.3 (\mu\text{K})^2, & \text{mask70/60}, \\ \sigma_{143 \times 217} = 3.0 (\mu\text{K})^2, & \text{mask80}, & \sigma_{143 \times 217} = 2.0 (\mu\text{K})^2, & \text{mask80}, \end{array} \right. \quad (11.1)$$

where for the 143×217 spectrum the notation mask70/60 denotes mask70 for 143 GHz and mask60 for 217 GHz (as used in the 12.1HM likelihoods). In other words, by using more sky the 217×217 and 143×217 spectra move closer to the coadded spectrum (which averages all four spectra). The residual in the 217×217 spectrum for the band centred at $\ell_b = 1465$, which we have shown in the previous two subsections is slightly anomalous on mask60, becomes progressively less anomalous as the mask is extended to mask70 and mask80, as expected if the mask60 residual is a statistical fluctuation.

11.4 Comparison with full mission spectra

The noise levels in the *Planck* spectra can be reduced by forming a likelihood using the full mission detset spectra²⁵. However, as we have discussed in Sect. 5.2, the noise between detsets is correlated at high multipoles. The half mission temperature spectra are signal dominated over most of the multipole range and as we have demonstrated in PCP15 and PCP18, half mission likelihoods are sufficiently powerful to determine the parameters of the base Λ CDM model, and most simple variants, to high precision. The main motivation in constructing a full mission detset temperature likelihood is to test the consistency of the data, rather than to improve constraints on cosmology. In polarization, we use all non-cotemporal half mission cross spectra in TE and so there is almost no gain in signal-to-noise in switching from half mission to full mission TE spectra. There is, however, a gain in signal-to-noise in the full mission detset EE spectrum, since the EE spectra are noise dominated over most of the multipole range covered by *Planck*. In this section, we focus on a comparison of half mission and full mission temperature spectra. A similar comparison of polarization spectra is presented in Sect. 12.2.

Figure 11.7 is the analogue of Fig. 11.2 for the 12.1F full mission detset likelihood. In forming this likelihood, we subtracted correlated noise from each of the coadded 100×100 , 143×143 , 143×217 and 217×217 detset spectra using smooth fits to the coadded odd-even differenced noise spectra (these corrections are plotted as the red lines in Fig. 5.2). Note that these corrections have a relatively small effect on the coadded spectra over the range of

²⁵PCP13 reported results based on a nominal mission detset likelihood, though we also performed an unpublished analysis of a full mission detset likelihood at that time.

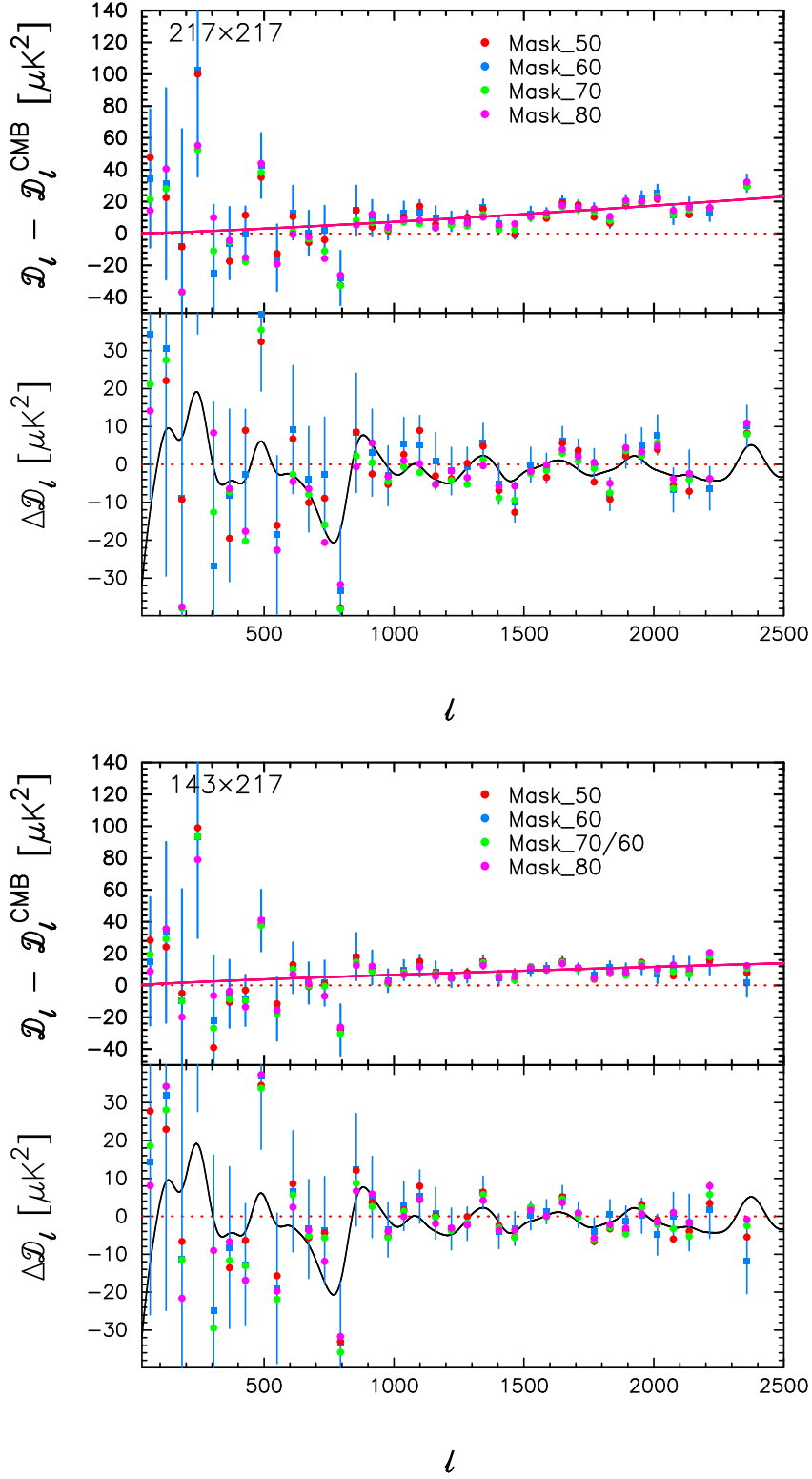


Figure 11.6. The upper panel in each plot shows the difference of the 545 cleaned half mission spectra and the 12.1HMcl TT best-fit base Λ CDM cosmology for masks of varying sizes. The upper figure shows the 217×217 spectrum and the lower figure shows the 143×217 spectrum. In the 12.1HMcl CamSpec likelihood we use mask60 for the 217 maps and mask70 for the 143 maps. Error bars are plotted on the spectra used in the 12.1HM likelihood. The solid line in the upper panel in each figure shows the best-fit power-law foreground excess (Eq. 9.11) derived from 12.1HMcl TT. The lower panel in each figure shows the residuals after subtracting the foreground excesses. The solid line in the lower panel shows the 12.1HMcl TT maximum likelihood frequency coadded residuals, smoothed with a Gaussian of width $\sigma_\ell = 40$, as plotted in Fig. 11.5.

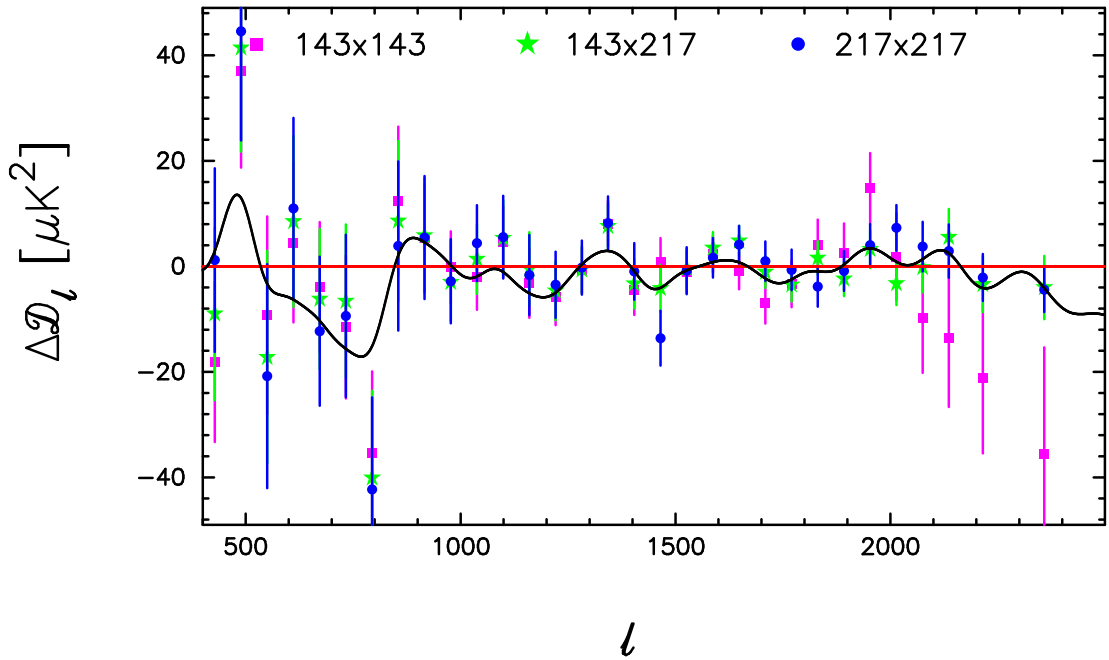


Figure 11.7. As Fig. 11.2, but for the full mission (detset) 12.1F TT likelihood. The spectra have been corrected for correlated noise between detsets, as discussed in the text, and foreground corrected using the base Λ CDM best-fit solution to the 12.1F TT likelihood. The residuals of these spectra are computed with respect to the best-fit base Λ CDM model fitted to this likelihood (which is very close to the 12.1HM TT best-fit model). The black line shows the residuals of the maximum likelihood coadded spectrum for the detset likelihood, smoothed with a Gaussian of width $\sigma_\ell = 40$.

multipoles included in the likelihood (for example, the 143×143 spectrum is not included in the 12.1F likelihood for $\ell > 2000$, where the 143×143 noise becomes large). Note also, that correlated noise is negligible in the 143×217 detset spectra over the entire range of multipoles shown in Fig. 11.7. In forming the *CamSpec* detset likelihood for PCP13, we chose to restrict the maximum multipole ranges at each frequency so that none of the spectra relied on beam calibrations at angular scales much smaller than the beam width. This choice also protected the 2013 *CamSpec* detset likelihood from biases caused by correlated noise.

As in Figs. 11.2 and 11.5, we see that the detset spectra are consistent with each other and show a similar pattern of residuals to that seen in the half mission spectra, particularly in the multipole range $800 \lesssim \ell \lesssim 1800$ which drives parameters such as A_L and Ω_K .

11.5 Summary

In summary, the characteristic oscillatory pattern of residuals in the temperature spectra at multipoles $\ell \lesssim 2000$ are: (i) consistent across frequencies; (ii) insensitive to foreground modelling; (iii) insensitive to sky coverage (and actually decrease in amplitude with increased sky coverage); (iv) are reproduced in the full mission detset spectra. For Λ CDM-like models, almost all of the statistical power from *Planck* comes from multipoles $\lesssim 1800$, so the tests described here add confidence that the cosmological results from *Planck* are robust and not driven by systematic errors.

12 Inter-frequency consistency in polarization

12.1 The 12.1HM likelihood

We process the half mission polarization spectra as follows:

- The TE/ET and EE spectra are cleaned using 353 GHz maps up to a multipole $\ell = 150$, as described in Sect. 8.2. At higher multipoles, we subtract power-law dust templates with parameters as given in Table 9.
- Each spectrum is corrected for temperature-to-polarization (TP) leakage using the beam model described in Sect. 6.1. TP leakage corrections are small but non-negligible for TE and ET (see Fig. 6.3). The TP corrections are negligible for EE. The consistency of the TP leakage model for TE/ET spectra has been tested in Sect. 6.4.
- The beam-corrected, foreground subtracted spectra are then recalibrated against a fiducial cosmology to determine effective polarization efficiencies as described in Sect. 6.3. The polarization efficiency corrections are the most significant instrumental corrections applied to the polarization spectra.

With these corrections, all of the polarization spectra should be consistent with each other in the absence of systematics. The residuals relative to the fiducial 12.1HM TT base Λ CDM cosmology for the individual polarization spectra of the 12.1HM likelihood are plotted in Figs. 12.1-12.3. Table 15 gives reduced χ^2 values for these spectra over the multipole ranges used in the 12.1HM likelihood.

One can see from both the figures and the table that there are no obvious outliers. In fact, the $\hat{\chi}^2$ values for spectra involving 100 and 143 GHz are low. This is a consequence of the difficulties discussed in Sect. 5.1 in accurately determining the noise levels of *Planck* in polarization, particularly at 100 GHz. The noise models used in this paper are based on odd-even map differences and, as discussed in Sect. 5.1, comparison with auto-spectra suggests that the odd-even map differences overestimate the noise of the 100 GHz maps (see Fig. 5.1). The $\hat{\chi}^2$ listed in Table 15 suggest that the noise levels for several of the EE spectra are overestimated by a few percent. Unfortunately, we have not been able to improve the accuracy of the noise model.

Table 15. Reduced χ^2 for the individual polarization spectra over the multipole ranges used in the 12.1HM likelihood. N_D lists the number of data points used to compute $\hat{\chi}^2$.

spectrum	ℓ range EE	N_D	$\hat{\chi}_{EE}^2$	ℓ range TE/ET	N_D	$\hat{\chi}_{TE}^2$	$\hat{\chi}_{ET}^2$
100HM1×100HM2	200 – 1200	1001	0.85	30 – 1200	1171	0.93	0.96
100HM1×143HM2	30 – 1500	1471	0.80	30 – 1500	1471	0.93	0.87
100HM1×217HM2	200 – 1200	1001	0.92	200 – 1500	1301	1.07	1.00
100HM2×143HM1	30 – 1500	1471	0.84	30 – 1500	1471	0.94	0.95
100HM2×217HM1	200 – 1200	1001	0.92	200 – 1500	1301	1.01	0.98
143HM1×143HM2	200 – 2000	1800	0.83	30 – 2000	1971	0.95	0.95
143HM1×217HM2	300 – 2000	1701	0.96	200 – 2000	1801	1.00	0.99
143HM2×217HM1	300 – 2000	1701	0.94	200 – 2000	1801	1.05	0.97
217HM1×217HM2	500 – 2000	1501	1.04	500 – 2000	1801	1.03	1.08

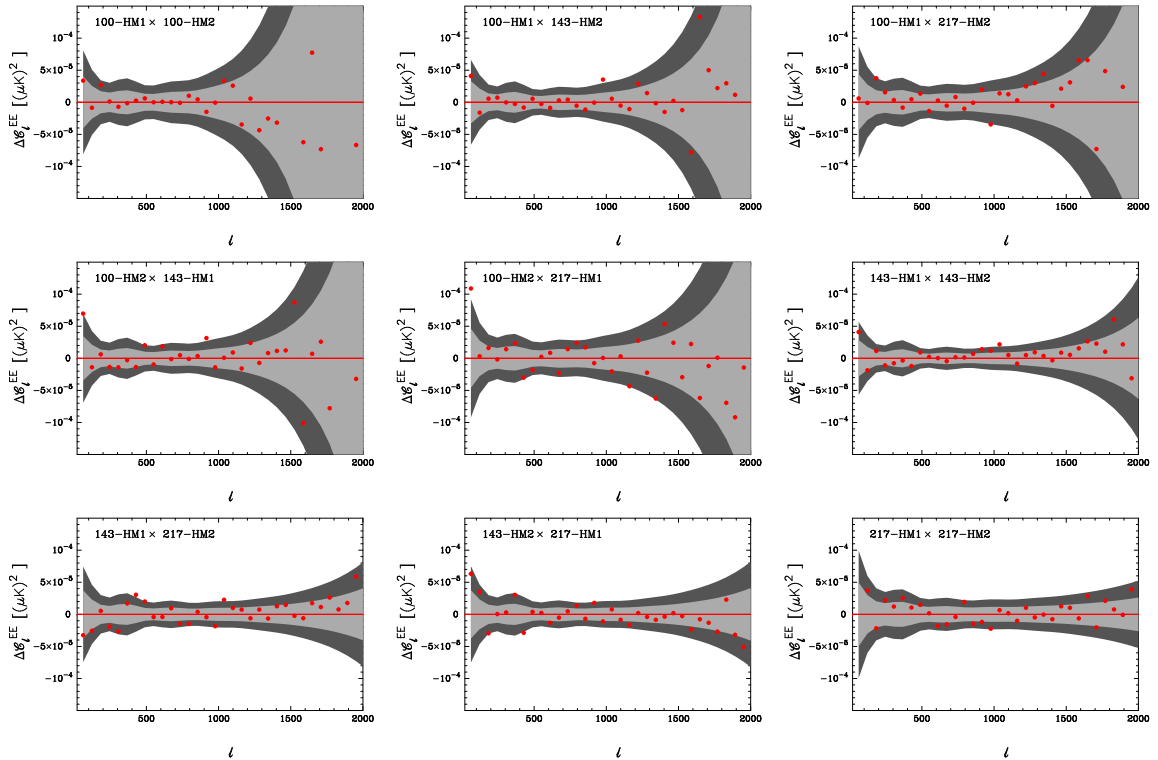


Figure 12.1. EE spectra used in the 12.1HM likelihood, corrected for dust emission, TP-leakage and effective polarization efficiencies. Residuals are computed with respect to the fiducial base Λ CDM cosmology fitted to 12.1HM TT. The grey bands show 1σ and 2σ error contours determined from the CamSpec error model.

The rationale for choosing the multipole ranges is as follows. The values of ℓ_{\max} are chosen so that we do not use the spectra when they become strongly noise dominated. The choices of ℓ_{\max} are relatively unimportant since the coadded TE and EE spectra are dominated by the highest signal-to-noise spectra. The values of ℓ_{\min} are chosen so that we do not use spectra that are heavily contaminated by dust emission. However, since we clean the polarization spectra using 353 GHz, polarized Galactic dust emission is accurately characterized and so the choices of ℓ_{\min} should be unimportant if instrumental systematics are negligible (see Figs. 8.3-8.5). This is true for the TE/ET spectra but not for EE. At very low multipoles in EE, we find clear evidence for residual systematics in the HFI maps.

The latter point is illustrated by Fig. 12.4 which shows selected half mission EE power spectra at low multipoles. The solid lines in the figures show the EE power spectrum for the fiducial base Λ CDM cosmology. The optical depth to reionization, $\tau = 0.0524 \pm 0.0080$, in this model is constrained by the SimA11 likelihood. The 100×143 EE power spectrum used in SimA11 is plotted in the upper panel. The upper figure shows the two 100×143 EE half mission power spectra. The lower figure shows the 100×100 , 143×143 and 217×217 spectra. It is clear from this figure that the 217×217 EE spectrum shows excesses at low multipoles. The 100×100 and 143×143 spectra also have excess variance, though less pronounced than in the 217×217 spectrum. The two 100×143 spectra fit well with the theoretical model. All of the half mission EE cross-spectra involving 217 GHz maps show large excesses relative to the other spectra and to the fiducial Λ CDM cosmology extending to multipoles $\ell \sim 100$.

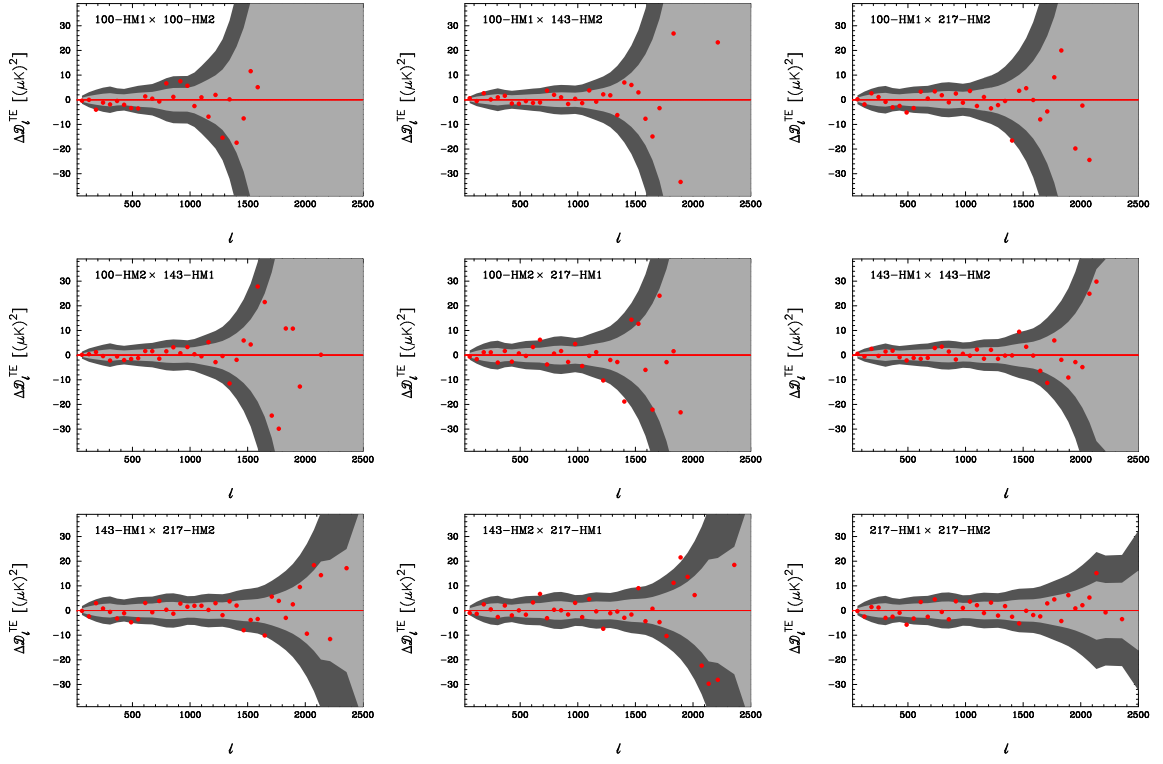


Figure 12.2. As for Fig. 12.1 but for the TE spectra.

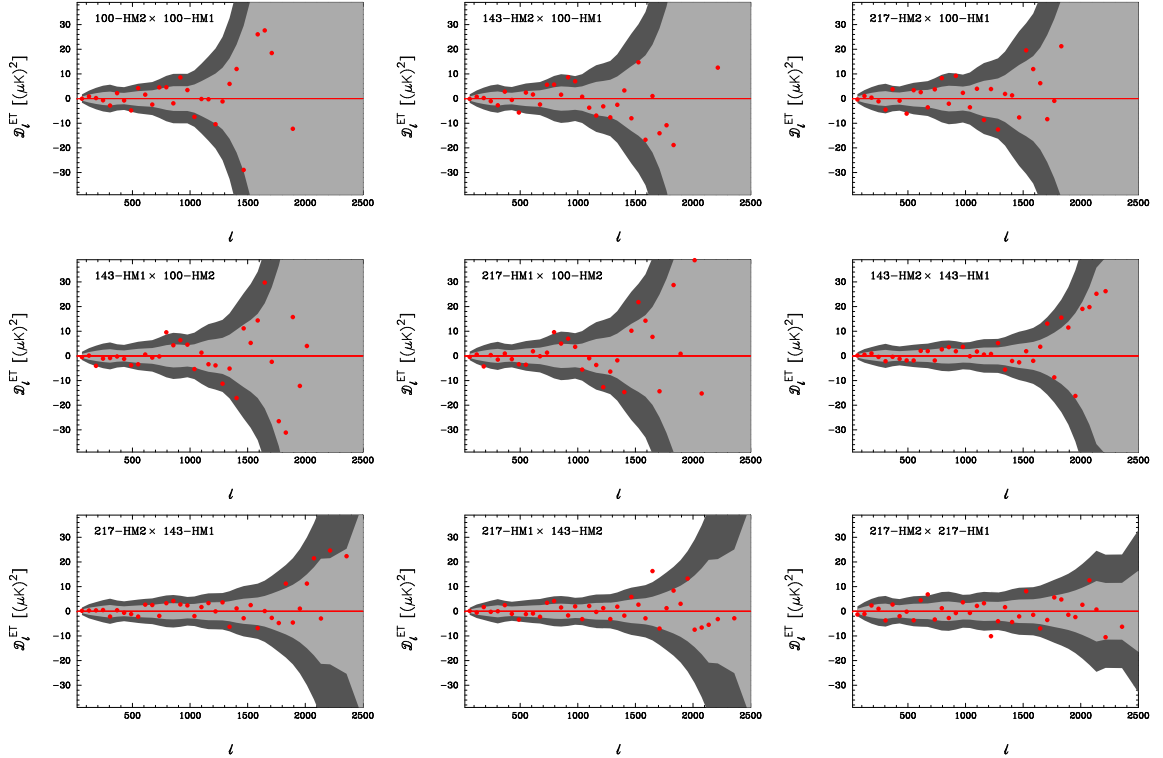


Figure 12.3. As for Fig. 12.1 but for the ET spectra.

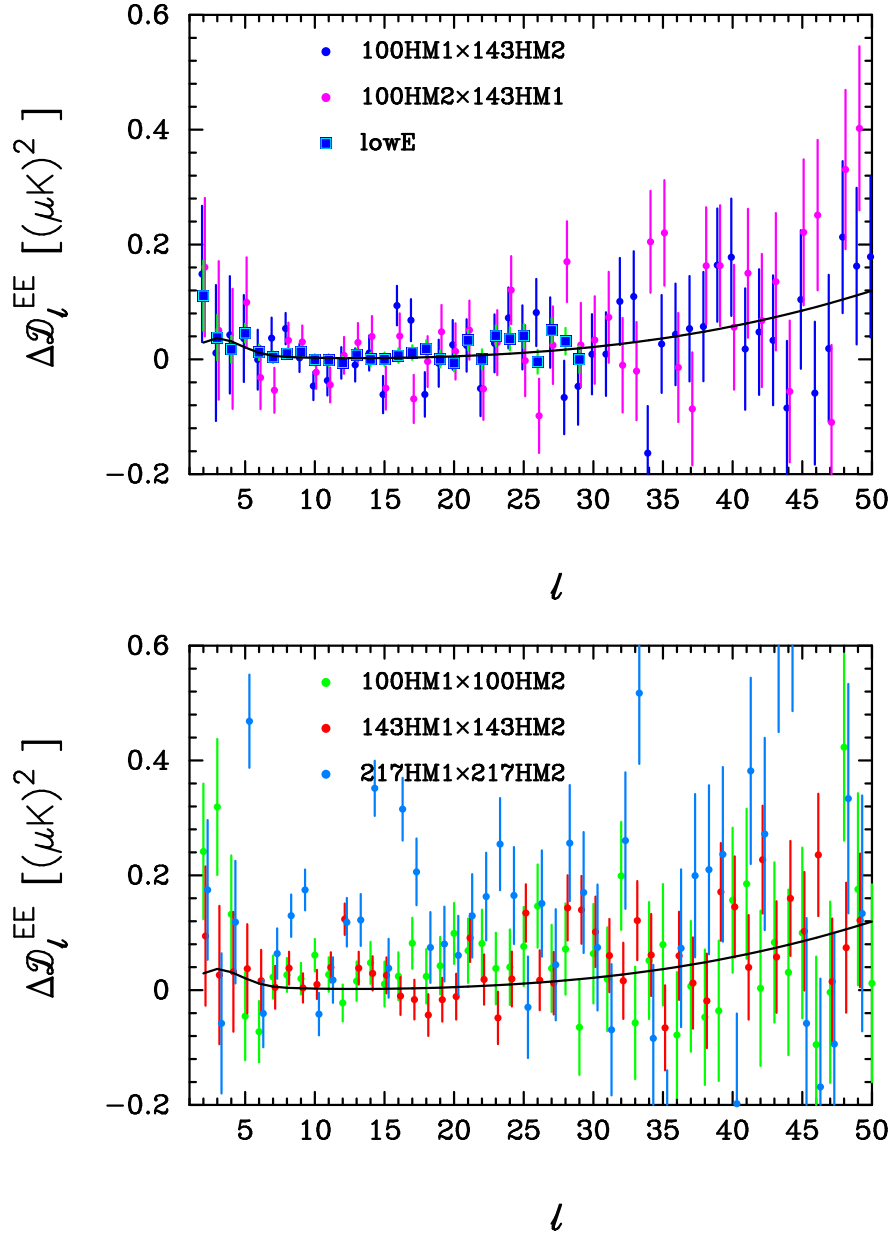


Figure 12.4. EE half mission power spectra computed using maskpol60 at low multipoles. The errors (which are highly correlated between multipoles) are computed from the diagonals of the `CamSpec` covariance matrices. The lines show the EE spectrum for the base Λ CDM cosmology fitted to the 12.1HM TT likelihood. The points labelled ‘lowE’ in the upper plot show the 100×143 EE quadratic maximum likelihood power spectrum used to form the `SimAll` likelihood used to constrain τ .

The behaviour of the EE spectra at low multipoles is discussed in detail in [103] and [99]. The main systematics (visible in Fig. 8.1) are caused by non-linearities in the bolometer analogue-to-digital converters (ADC). These non-linearities, together with other effects such as long bolometer time constants and band-pass mismatches, introduce systematic errors in the polarization maps. The main aim of the SRoll map-making algorithm used in the 2018 *Planck* data release is to correct these systematic errors at low multipoles²⁶. As discussed in [103] the ADC non-linearities can be modelled and corrected to high accuracy for 100 and 143 GHz bolometers, but the model is less accurate for 217 GHz. As a consequence, 217 GHz polarization maps are strongly affected by low multipole systematics. Even at 100 and 143 GHz, there are small biases in 100×100 and 143×143 spectra. The approach taken in [103] and [99] is to construct end-to-end simulations of the SRoll pipeline, which are used to compute and remove biases and to construct an empirical likelihood using the EE spectra. The lowE likelihood used here is discussed in [99] (and in abbreviated form in PPL18) and uses the full mission 100×143 EE cross spectrum.

The end-to-end simulations show that biases are small in the 100×143 cross spectra. We therefore use only the 100×143 half mission spectra in the EE block of the CamSpec likelihood at multipoles $\ell < 200$. One can see from the upper panel of Fig. 12.4 that the 100×143 half mission CamSpec cross-spectrum matches smoothly with the EE power spectrum used in the SimAll likelihood at $\ell < 30$. One can also see that the SimAll spectrum has much smaller errors than the 100×143 half mission spectra. There are two reasons for this: (i) the SimAll errors are based on the end-to-end simulations, whereas the CamSpec error model is heuristic and unreliable at low multipoles; (ii) CamSpec is based on pseudo- C_ℓ power spectrum estimates which are sub-optimal at low multipoles. The SimAll estimates use approximate quadratic maximum likelihood cross-spectrum estimates developed by us [32] and described in [103].

12.2 Comparison with full mission detset spectra

The analysis of full mission detset polarization spectra is almost identical to that of the half mission spectra. We use the detset beams to model TP leakage, and recalibrate each TE/ET and EE spectrum against the fiducial 12.1HM TT cosmology. However, instead of cleaning the spectra using 353 GHz, we subtract the power-law dust model with the coefficients given in Table 9²⁷. The tests described in Sect. 5.2 (see Fig. 5.2) show that correlated noise between detsets is unimportant in the polarization spectra over the multipole ranges used in the CamSpec likelihoods.

Fig. 12.5 compares the coadded full mission detset TE and EE spectra of the 12.1F likelihood to the half mission spectra used in the 12.1HM likelihood. We show the residuals with respect to the fiducial base Λ CDM cosmology fitted to 12.1HM TT²⁸. The green lines show the best fit base Λ CDM cosmology fitted to TE and EE blocks of the 12.1HM and 12.1F likelihoods. The cosmological parameters determined from the polarization spectra

²⁶The SRoll maps produced for the 2018 release give almost identical TT, TE and EE power spectra as the 2015 *Planck* maps at multipoles $\ell \gtrsim 200$. The changes in map making between the 2015 and 2018 *Planck* data releases (including the elimination of the last part of survey 5) have negligible impact on the power spectra at high multipoles.

²⁷This is done because with half mission 353 GHz it is not possible to clean the detset spectra without introducing noise correlations in the cleaned cross spectra.

²⁸The calibration parameters c_{TE} and c_{EE} determined from the 12.1HM TTTEEE and 12.1F TTTEEE likelihoods are very close to unity. We have therefore not applied relative calibration factors in Fig. 12.5.

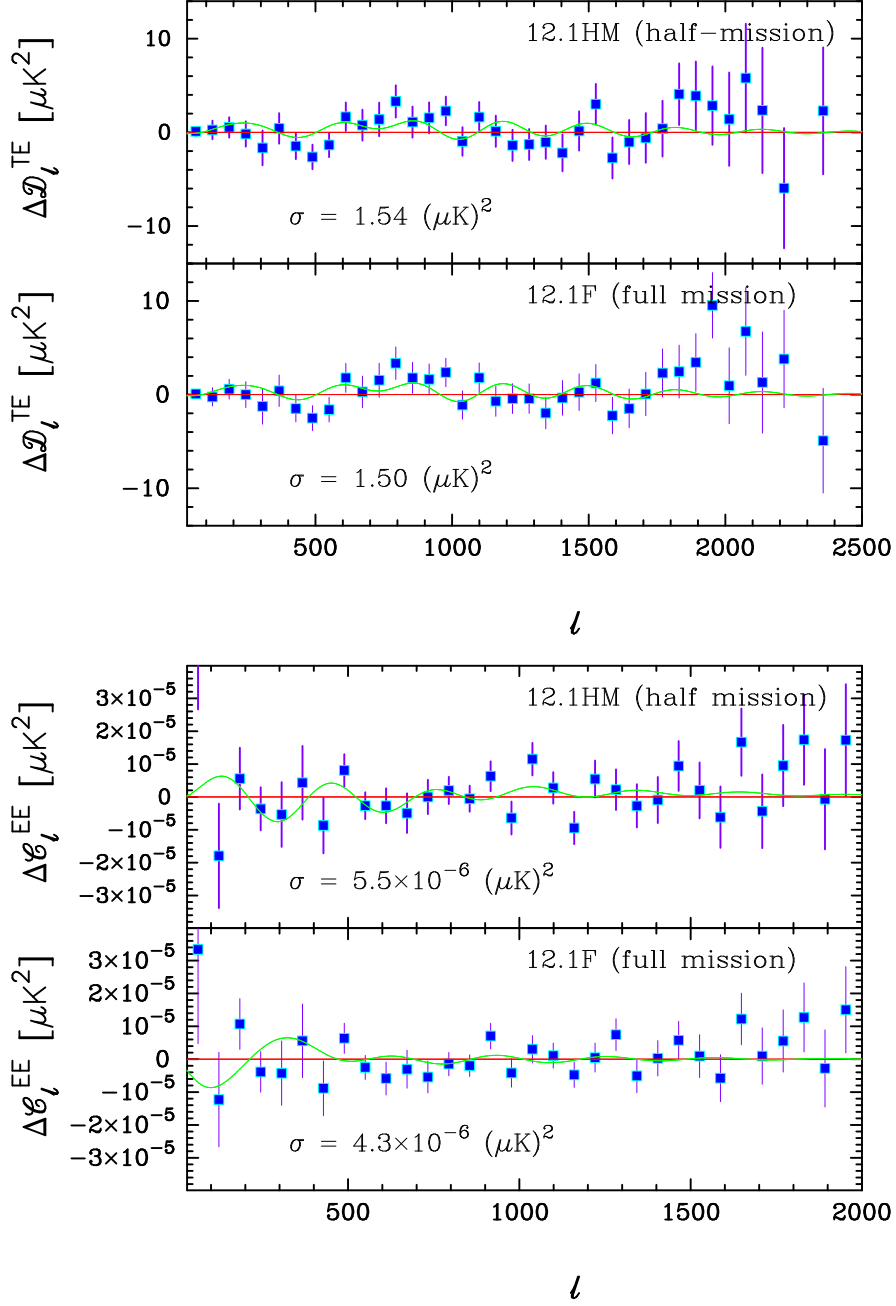


Figure 12.5. Comparison of the 12.1HM half mission and 12.1F full mission dataset TE spectra (upper figure) and EE spectra (lower figure). The residuals are computed with respect to the fiducial 12.1HM TT base Λ CDM cosmology. The numbers give the dispersion of the residuals over the multipole range $500 \leq \ell \leq 1500$. The green curves in each panel show the residuals relative to best-fit base Λ CDM cosmology fitted to 12.1HM TE (upper panel, upper figure) and 12.1F TE (lower panel, upper figure) and to 12.1HM EE (upper panel, lower figure) and 12.1F EE (lower panel, lower figure).

differ slightly from (but are consistent with) those of the fiducial base Λ CDM model (see Table 12 and Fig. 13.2).

We note the following:

- The full mission TE spectrum is almost identical to the half mission spectrum. As noted in Sect. 10.1 the increase in signal-to-noise of the full mission TE spectrum compared to the half mission spectrum is marginal (and comes primarily from slight improvements in the signal-to-noise of the temperature maps). Unsurprisingly, therefore, the 12.1HM TE and 12.1F TE likelihoods lead to almost the same cosmologies. The numbers in the figure give the dispersion in the band-powers over the multipole range $500 \leq \ell \leq 1500$ and are almost identical for the two spectra.
- The residuals of the full mission EE spectrum has noticeably lower scatter compared to those of the half mission spectrum, particularly at multipoles $\gtrsim 1000$. For EE there is a non-negligible improvement in signal-to-noise in switching from half mission to the full mission dataset spectra. The green lines in this figure show the residuals relative to the base Λ CDM cosmology fitted to 12.1HM EE and 12.1F EE. For the EE spectra, these two fits differ, with the 12.1F EE fit lying closer to the 12.1HM TT cosmology. In other words, the improved signal-to-noise of the 12.1F EE spectrum brings it closer to the TT solution.
- These results show that there is relatively little to be gained in forming a full mission dataset likelihood compared to a half mission likelihood. Although we see an improvement in the signal-to-noise of the full mission EE spectrum, the EE spectra at high multipoles are much less powerful than the TT and TE spectra in constraining Λ CDM-like models. The full mission EE spectra should therefore be more appropriately considered a consistency check of the *Planck* polarization data.

12.3 Variation of TE and EE with sky area

The only other way of improving the signal-to-noise of the polarization spectra is to increase the sky area. Fig. 12.6 shows the coadded TE and EE spectra of the 12.1HM likelihood compared to dust-subtracted coadded half mission polarization spectra using larger areas of sky. The polarization spectra computed on mask70 and mask80 show the same general features as the 12.1HM spectra, showing that these spectra are stable with respect to sky coverage. The 12.5HMcl uses mask80 in both temperature and polarization. Because of the large sky coverage, 12.5HMcl is the most powerful likelihood that we have produced from *Planck* HFI data.

13 The base Λ CDM model

13.1 Supplementary Likelihoods

The primary purpose of this paper is to explore the consistency of the *Planck* power spectra rather than to perform an exhaustive analysis of the consistency of *Planck* with other types of data. We have therefore limited the use of supplementary likelihoods to: (a) *Planck* lensing (described in detail in [98]) where we use the lensing likelihood as summarized in section 2.3 of PCP18, and (b) baryon acoustic oscillation (BAO) measurements, where we use the identical combination of BAO data as in PCP18. Most of the statistical weight in the BAO measurements comes from the ‘consensus’ constraints on $D_M(z)$ and $H(z)$ (see below for definitions) measured in three redshift bins ($z_{\text{eff}} = 0.38, 0.51$ and 0.61) from the Baryon Oscillation Spectroscopic Survey (BOSS) DR12 analysis [6]. As in PCP18, we also include the

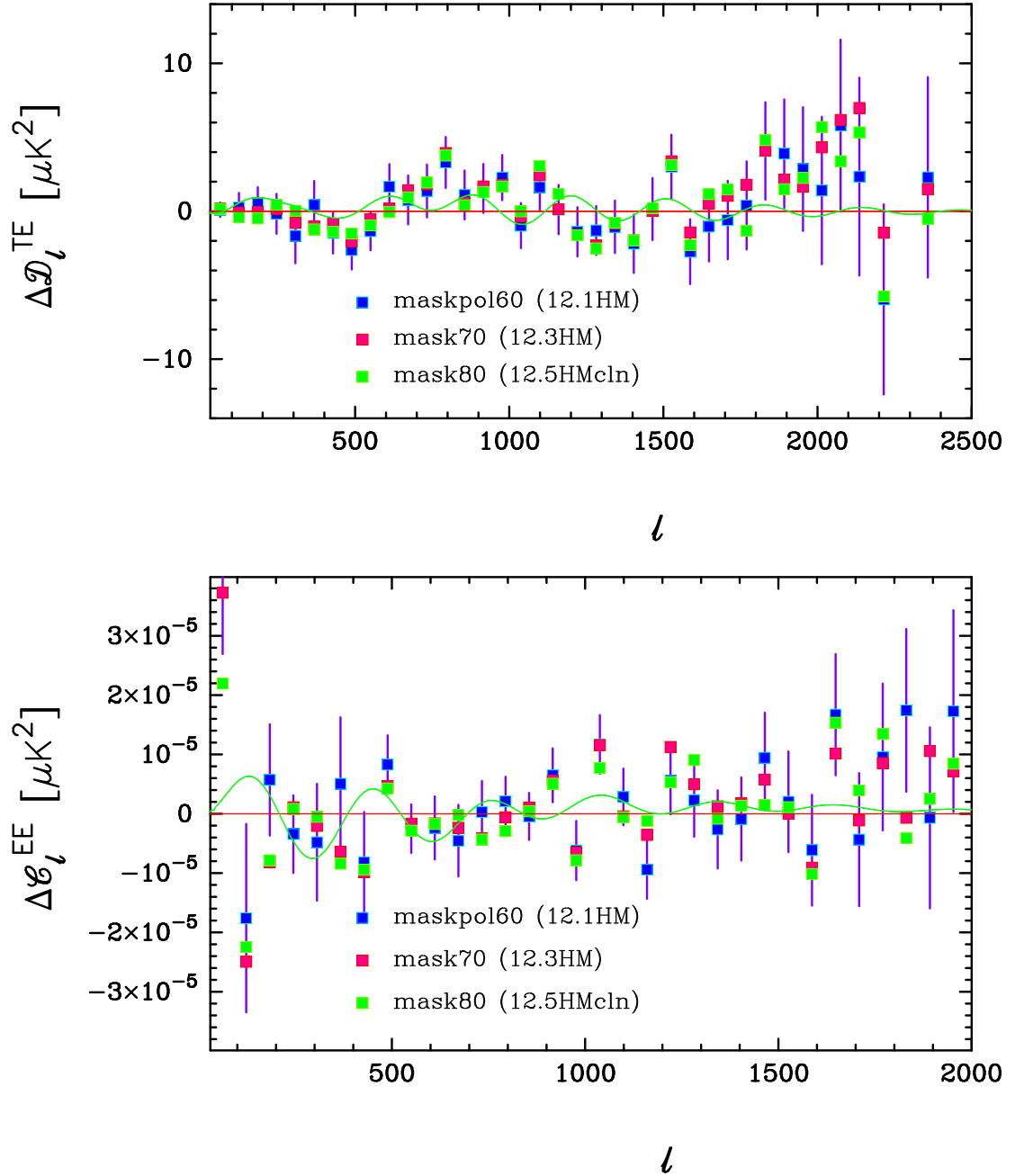


Figure 12.6. Half mission TE spectra (upper figure) and EE spectra (lower figure) computed using different polarization masks. The residuals are computed with respect to the 12.1HM TT fiducial ΛCDM base cosmology. The blue points with error bars show the TE and EE spectra used in the 12.1HM likelihood. The red and green points show the spectra using the mask70 and mask80 temperature masks in polarization (including the 143 GHz point source+extended object mask) as used in the 12.3HM and 12.5HMcln likelihoods. Polarized dust emission is subtracted from the polarization spectra using 353 GHz, as described in Sect. 8.2. The green curves in each panel show the residuals of the best-fit base ΛCDM cosmologies fitted to 12.1HM TE (upper figure) and 12.1HM EE (lower figure).

Table 16. Acoustic scale parameters in base Λ CDM

Likelihood	$100\theta_*$	Σ	$\Omega_m h^3$
12.1HM TT	1.04103 ± 0.00047	101.089 ± 0.052	0.09707 ± 0.00045
12.1HMcl TT	1.04087 ± 0.00048	101.085 ± 0.055	0.09586 ± 0.00047
12.1F TT	1.04095 ± 0.00047	101.081 ± 0.053	0.09614 ± 0.00045
12.5HMcl TT	1.04095 ± 0.00044	101.083 ± 0.052	0.09576 ± 0.00043
12.1HM TE	1.04162 ± 0.00050	101.115 ± 0.066	0.09606 ± 0.00053
12.1HMcl TE	1.04163 ± 0.00050	101.116 ± 0.067	0.09605 ± 0.00053
12.1F TE	1.04173 ± 0.00050	101.120 ± 0.066	0.09614 ± 0.00054
12.2HM TE	1.04155 ± 0.00050	101.112 ± 0.067	0.09598 ± 0.00054
12.3HM TE	1.04160 ± 0.00047	101.139 ± 0.065	0.09612 ± 0.00051
12.4HM TE	1.04166 ± 0.00048	101.140 ± 0.062	0.09612 ± 0.00049
12.5HMcl TE	1.04165 ± 0.00045	101.148 ± 0.060	0.09616 ± 0.00046
12.1HM EE	1.03952 ± 0.00085	100.67 ± 0.24	0.0973 ± 0.0017
12.1F EE	1.04031 ± 0.00077	100.58 ± 0.23	0.0987 ± 0.0016
12.2HM EE	1.04044 ± 0.00091	100.64 ± 0.28	0.0978 ± 0.0019
12.3HM EE	1.04093 ± 0.00084	100.79 ± 0.25	0.0977 ± 0.0017
12.4HM EE	1.04126 ± 0.00079	100.89 ± 0.23	0.0973 ± 0.0016
12.1HM TTTEEE	1.04106 ± 0.00032	101.072 ± 0.039	0.09607 ± 0.00031
12.1HMcl TTTEEE	1.04100 ± 0.00032	101.067 ± 0.039	0.09604 ± 0.00032
12.1F TTTEEE	1.04123 ± 0.00030	101.076 ± 0.039	0.09622 ± 0.00031
12.2HM TTTEEE	1.04111 ± 0.00033	101.075 ± 0.039	0.09611 ± 0.00032
12.3HM TTTEEE	1.04103 ± 0.00031	101.085 ± 0.038	0.09610 ± 0.00031
12.4HM TTTEEE	1.04121 ± 0.00030	101.094 ± 0.037	0.09622 ± 0.00031
12.5HMcl TTTEEE	1.04124 ± 0.00028	101.096 ± 0.036	0.09613 ± 0.00029

measurements of D_V/r_{drag} at lower redshift from the 6dFGS [13] and SDSS-MGS [112]. We follow a similar, but more compact, notation to that used in PCP18. For example: 12.5HMcl TTTEEE+lensing+BAO denotes the TT+TE+EE 12.5HMcl high multipole likelihood combined with `Commander` and `SimAll` at low multipoles together with the *Planck* lensing and BAO likelihoods.

13.2 Acoustic scale parameters

The characteristic angular scale of CMB acoustic fluctuations, θ_* , is very accurately determined by the *Planck* power spectra. In base Λ CDM, the CMB measurements of θ_* can be approximated as a tight constraint on the parameter combination

$$\Sigma = \left(\frac{r_{\text{drag}} h}{\text{Mpc}} \right) \left(\frac{\Omega_m}{0.3} \right)^{0.4}. \quad (13.1)$$

Typically, θ_* and Σ are fixed to $\lesssim 0.05\%$ by the *Planck* data (PCP18). Since the parameter combination $\Omega_b h^2$ is well determined by the relative heights of the CMB acoustic peaks, the parameter combination $\Omega_m h^3$ [75] offers a simpler proxy to the acoustic scale θ_* , accurate to typically 0.3%.

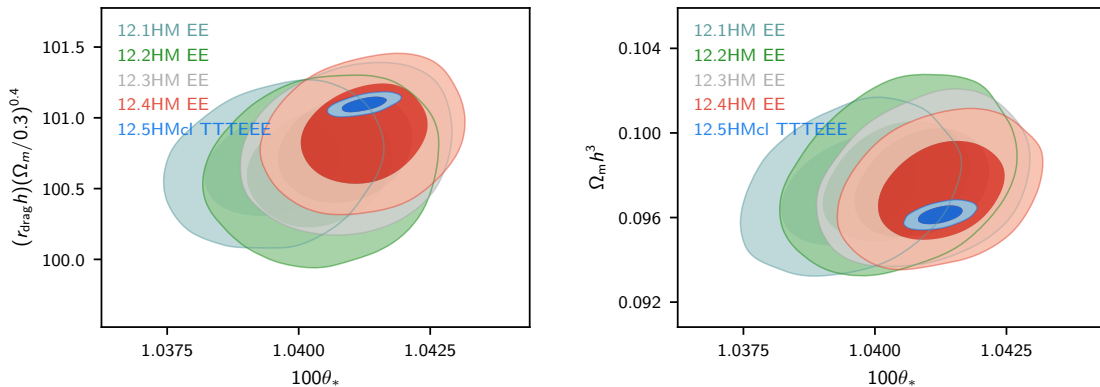


Figure 13.1. Variation of the acoustic scale location parameters determined from the EE likelihoods. The sky area used in polarization increases from 12.1HM through to 12.4HM. (The EE block of the 12.5HMcl likelihood is identical to that of the 12.4HM likelihood). We also show results for the 12.5HMcl TTTEEE likelihood.

Table 16 gives values for the acoustic scale parameters determined from various likelihoods. Note that the TT, TE and EE estimates determined from any given likelihood are almost independent of each other. The agreement between these estimates is excellent. The EE spectra show an interesting feature, however. Since the EE spectra are noisy, the acoustic scale parameters from the EE half mission spectra are less accurate than those determined from the TT and TE spectra. As the sky area is increased from the 12.1HM through to 12.4HM, the EE acoustic scale parameters drift towards closer agreement with those determined from the TT and TE spectra. This is illustrated in Fig. 13.1. The acoustic scale parameters determined from the TT, TE and TTTEEE likelihoods are remarkably stable and show no trend with increasing sky area.

The final seven rows in Table 16 give the acoustic scale results for the TTTEEE likelihoods. The acoustic scale parameters determined from the 12.1HM and 12.5HMcl TTTEEE likelihoods are consistent to better than 0.03%, even though these likelihoods use different sky areas in both temperature and polarization and very different foreground treatments in temperature.

13.3 Consistency between temperature and polarization

Figure 13.2 plots constraints on several key cosmological parameters illustrating the consistency between the TT, TE and the TTTEEE likelihoods. The 12.1HM and 12.1HMcl likelihoods are quite similar to the CamSpec likelihoods used in PCP18. The parameter constraints from these likelihoods are in extremely close agreement with those reported in PCP18 (see e.g. Fig. A.1 of PCP18).

The TT, TE and TTTEEE parameter constraints are consistent with each other in all of the CamSpec likelihoods. The main trend apparent in Fig. 13.2 is for the TE measurement of n_s to drift to lower values as the sky area is increased, though for all likelihoods, the TE measurements of n_s are consistent with those determined from TT and TTTEEE. The most striking result from Fig. 13.2 is the stability of the TTTEEE parameter constraints as we scan through the likelihoods. Comparing the TTTEEE results from 12.1HM and 12.5HMcl, the results for most parameters are consistent to better than 0.2σ . The largest deviation is found

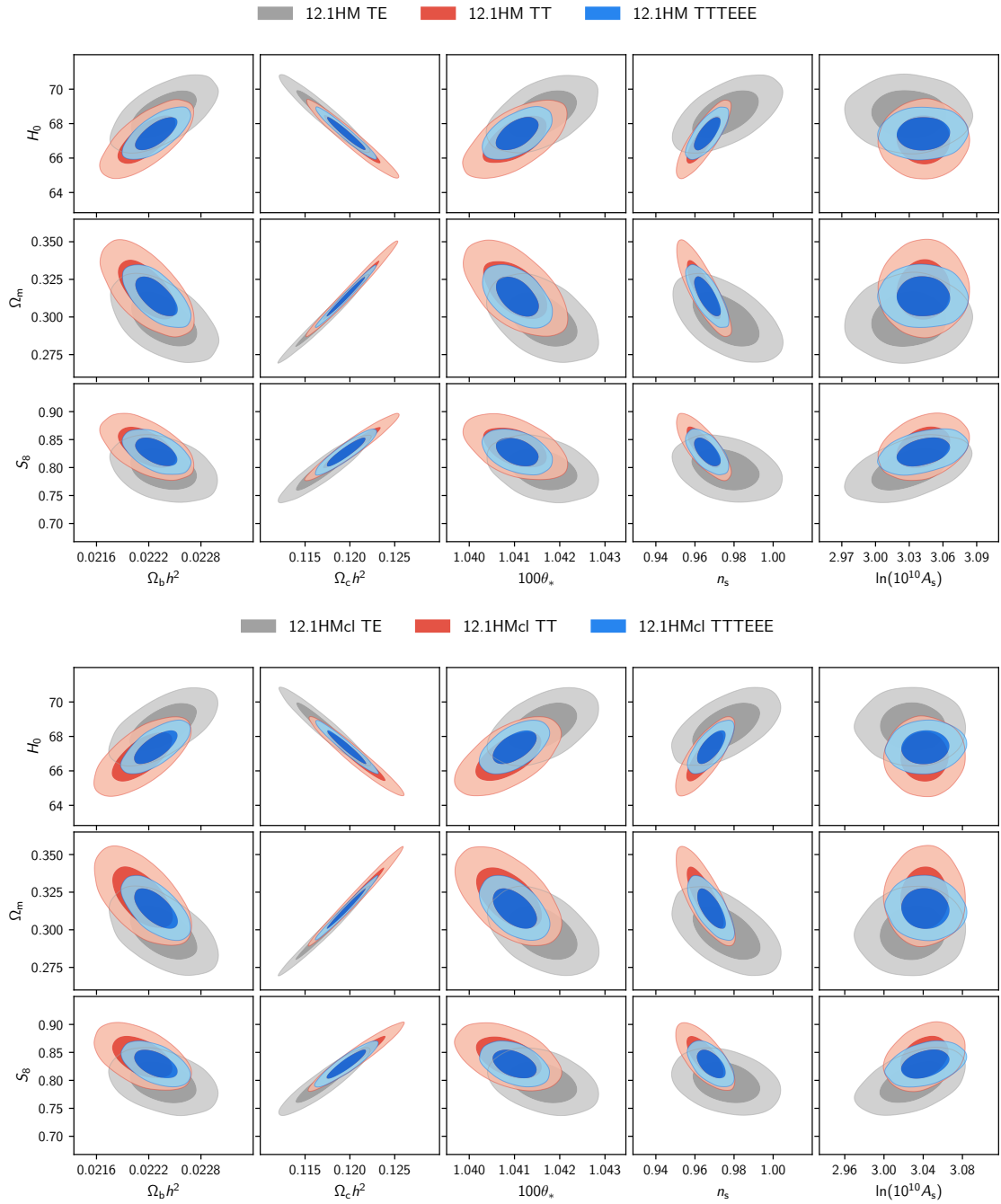


Figure 13.2. 68% and 95% confidence contours for base Λ CDM cosmological parameters determined from the TT, TE and TTTEEE likelihoods. The upper figure shows results for the 12.1HM likelihood, which is similar to the *CamSpec* likelihood discussed in PCP18. The lower figure shows results for the 545 GHz temperature cleaned 12.1HMcl likelihood.

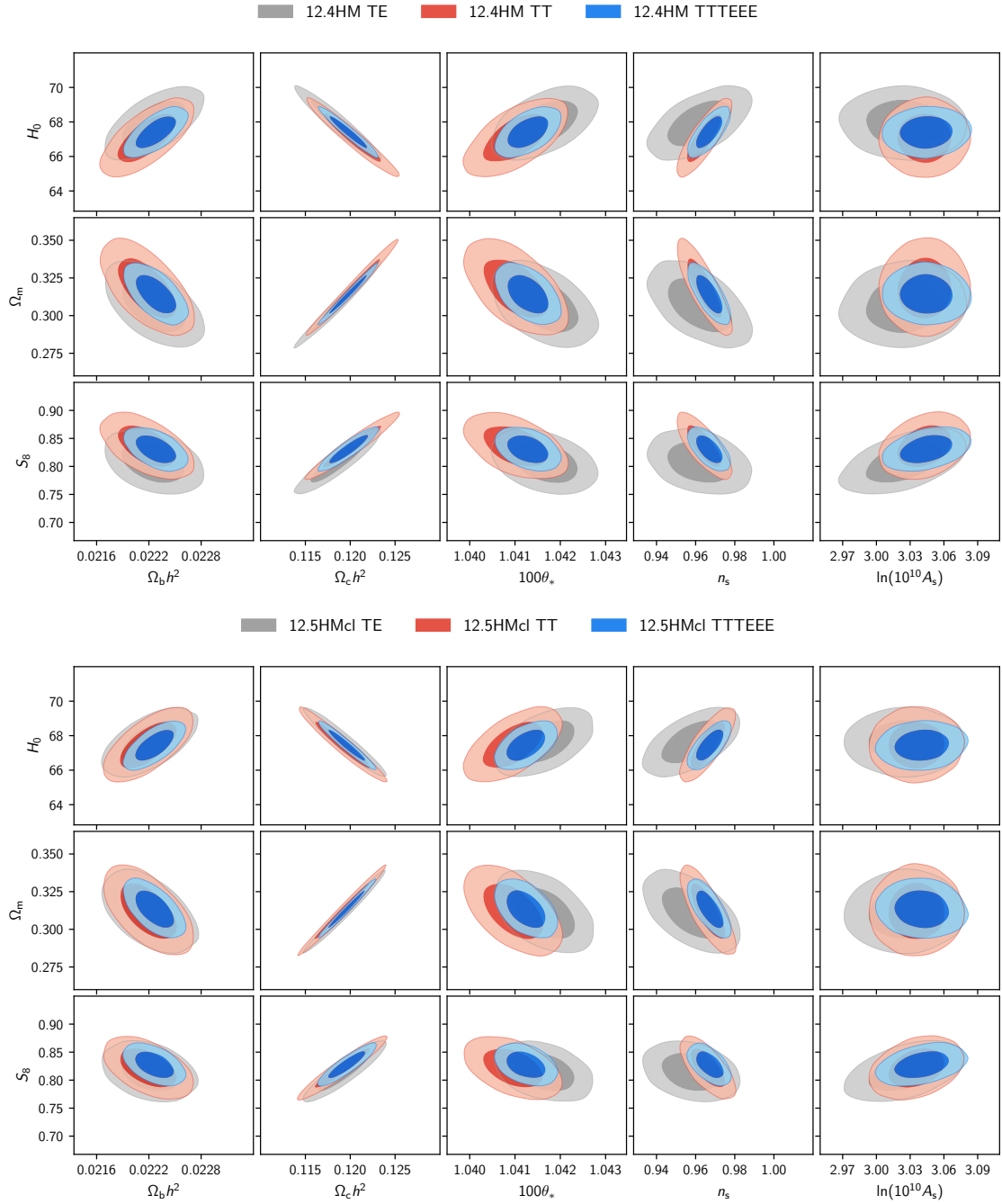


Figure 13.2. (Continued). The upper figure shows results for the 12.4HM likelihood, increasing the sky area in polarization compared to 12.1HM. The lower figure shows results for the 12.5HMcl likelihood which uses more sky area than 12.1HMcl in both temperature and polarization.

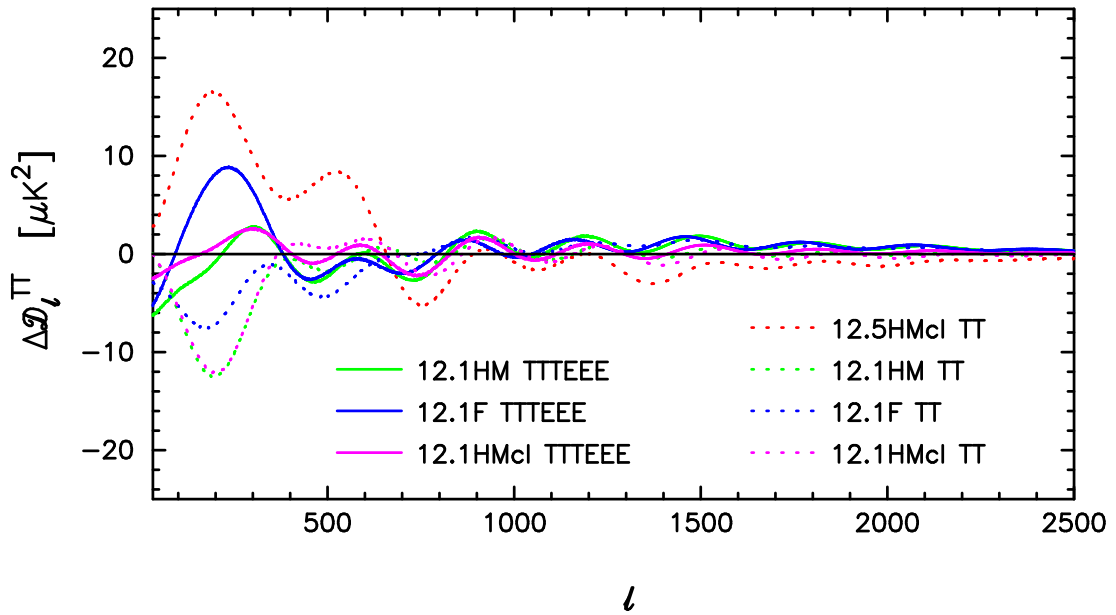


Figure 13.3. Residuals of the best-fit base Λ CDM TT theory spectra determined from various likelihoods. The 12.5HMcl TTTEEE best-fit base Λ CDM temperature spectrum is used as the reference.

for θ_* , which differs by 0.57σ . This is quite a large shift, but one must bear in mind that the formal errors on θ_* from the TTTEEE likelihoods are very small (see Table 16). The values of θ_* determined from these two likelihoods are actually consistent to better than 0.02%.

13.4 Best-fit models

We can get an intuitive feel of the behaviour of these likelihoods by looking at the best-fit base Λ CDM temperature power spectra. We choose the 12.5HMcl TTTEEE best-fit model as a reference and plot the residuals of the best-fit TT theory spectra for various likelihoods in Fig. 13.3. Since this type of plot is extremely sensitive to small absolute calibration differences we have rescaled the temperature spectra by minimising the rms scatter of the spectral differences over the multipole range $500 \leq \ell \leq 1500$. This rescaling largely removes multiplicative differences so that one can see differences in the shapes of the best-fit models.

The residuals are well below $\sim 10 (\mu\text{K})^2$ for all likelihoods at $\ell \gtrsim 800$. At lower multipoles, we see higher residuals of up to $\sim 16 (\mu\text{K})^2$ at $\ell \sim 200$ (corresponding to the first acoustic peak). The largest differences are for the 12.5HMcl TT likelihood, for which we increased sky area to 80% for the 143 and 217 GHz maps. The inter-frequency residuals for the TT spectra used in the 12.5HMcl TT likelihood (see Fig. 13.11) are, however, significantly smaller than the differences seen in Fig. 13.3 which we believe reflect differences in the response of the likelihood to cosmic variance rather than inaccuracies in dust subtraction. The differences between the 545 GHz cleaned and uncleaned likelihoods may, however, be caused by errors in dust subtraction. (For the uncleaned spectra, the foreground model is sufficiently flexible that dust subtraction errors of $\sim 20 (\mu\text{K})^2$ at the first peak can be absorbed by the foreground model and hence not show up in inter-frequency comparisons; see Figs. 11.1 and 11.3.) As expected from Fig. 13.2, the best-fit models for the TTTEEE likelihoods agree extremely well over the entire multipole range.

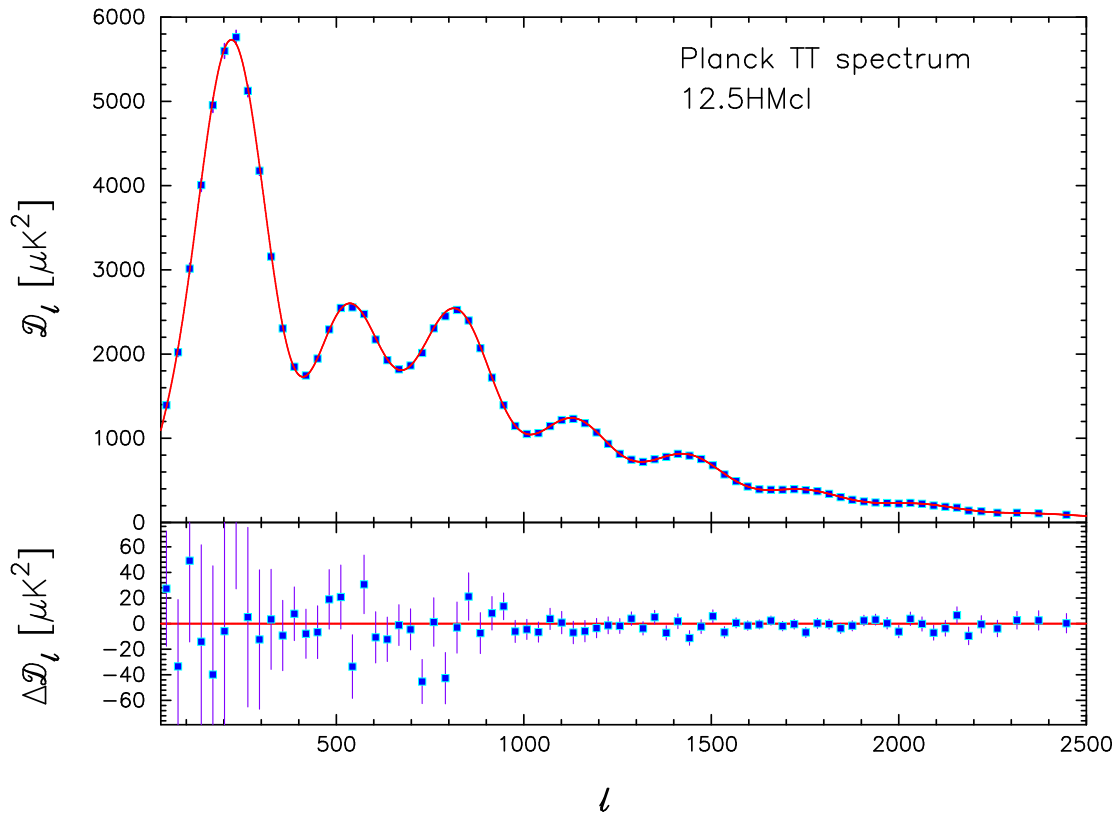


Figure 13.4. The maximum likelihood frequency averaged temperature power spectrum for the 12.5HMcl likelihood. This can be compared with the corresponding plot for the 12.1HM likelihood plotted in Fig. 10.1. The best-fit base Λ CDM cosmology fitted to the 12.5HMcl TTTEEE likelihood is plotted in the upper panel and the residuals with respect to this theoretical model are plotted in the lower panel.

The coadded 12.5HMcl TT, TE and EE spectra are plotted in Figs. 13.4 and 13.5. These plots can be compared with the corresponding plots for the 12.1HM likelihood in Figs. 10.1 and 10.2. The polarization spectra of Fig. 13.5 are compared with the polarization spectra measured by ACTpol and SPTpol in Appendix B. The 12.5HMcl likelihood is statistically more powerful than the 12.1HM and 12.1HMcl likelihoods because of the larger sky area in both temperature and polarization. For each of TT, TE and EE, the residuals plotted in the lower panels of Figs. 13.4 and 13.5 show less scatter than seen in the 12.1HM spectra. In other words, the increase in sky area leads to quieter spectra. This is important evidence in favour of the base Λ CDM cosmological model.

13.5 Comparison with Baryon Acoustic Oscillations and *Planck* lensing

Fig. 13.6 shows the BOSS DR12 constraints on the comoving angular diameter distance $D_M(z)$ and $H(z)$ from the ‘consensus’ results of [6] compared to the *Planck* constraints from the 12.5HMcl likelihood. Section 13.2 shows that the acoustic scale parameters θ_* , Σ and $\Omega_m h^3$ are accurately determined by *Planck* and are extremely stable. In base Λ CDM, fixing the acoustic scale forces the CMB constraints to lie on a degeneracy line in the $D_M(z)$ - $H(z)$ plane depending on the value of $\omega_m = \Omega_m h^2$ (or, equivalently H_0). In fact, to an accuracy of

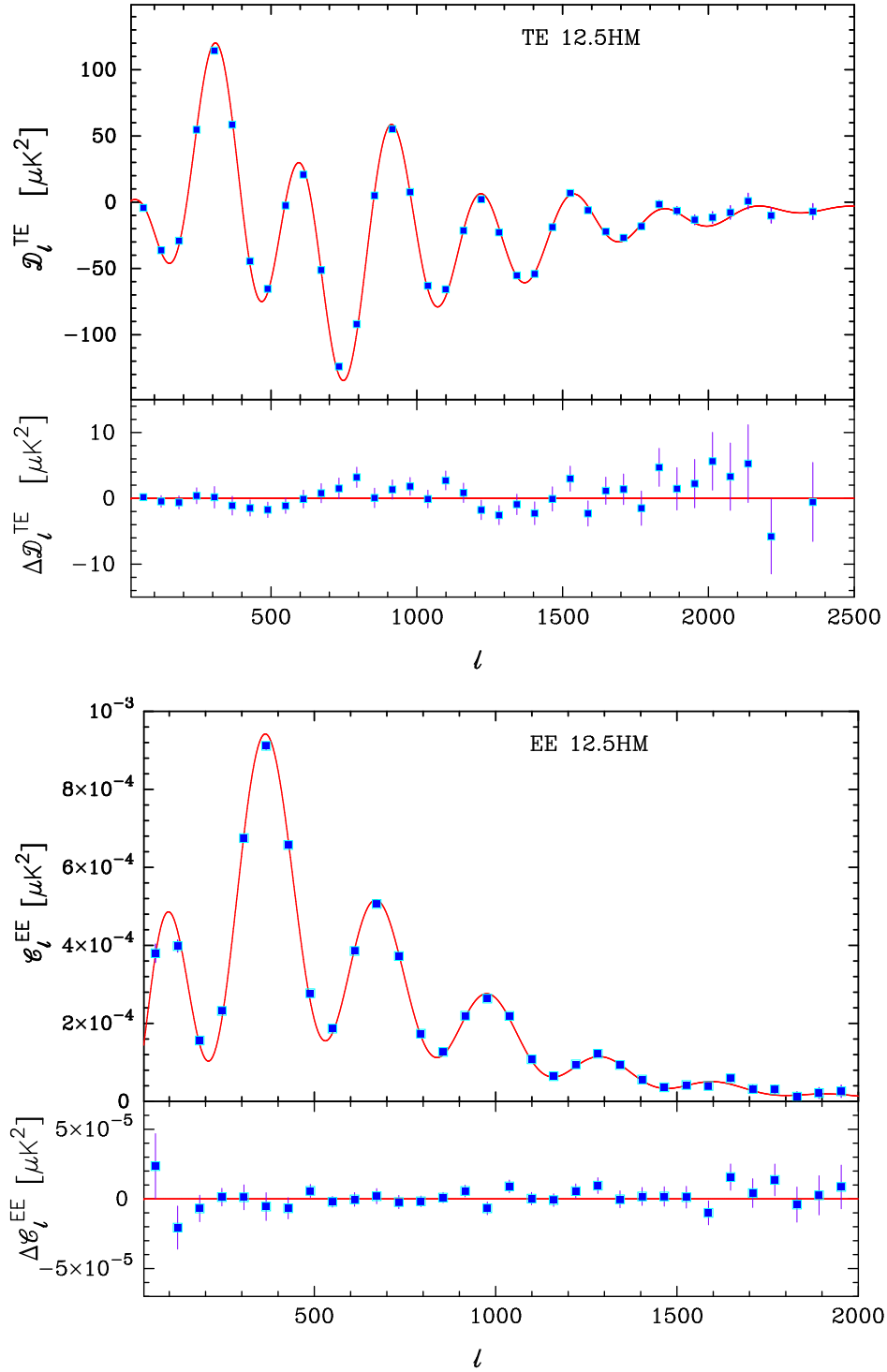


Figure 13.5. The coadded TE and EE power spectra for the 12.5HM likelihood. The best-fit base Λ CDM cosmology fitted to 12.5HM likelihood is plotted in the upper panels. Residuals with respect to this theoretical model are shown in the lower panels.

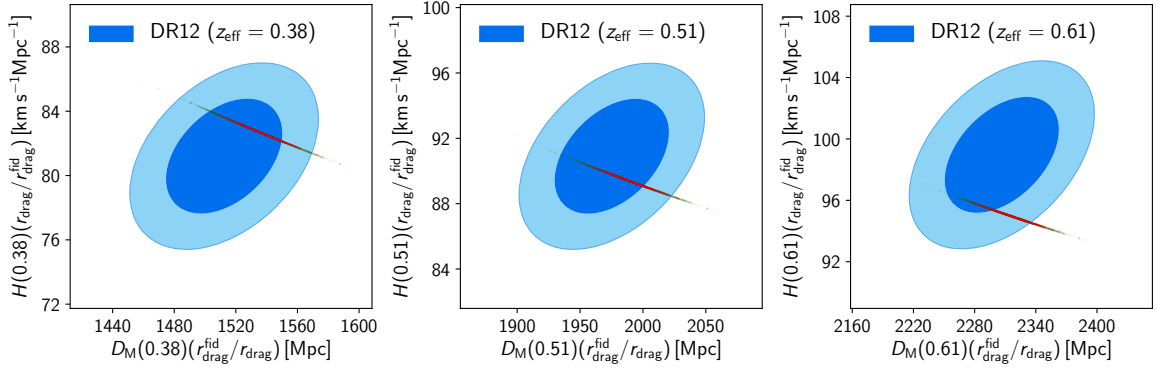


Figure 13.6. The contours show 68% and 95% constraints on D_M and $H(z)$ from the BOSS DR12 BAO analysis of [6] (which adopts a fiducial value of the sound horizon of $r_{\text{drag}}^{\text{fid}} = 147.78$ Mpc). The green and red points show samples from the 12.5HMcl TT and 12.5HMcl TTTEEE chains respectively. For base Λ CDM, the CMB constraints lie accurately on degeneracy lines by $\Omega_m h^2$ (see Eqs. 13.2a - 13.2c). Adding the TE and EE blocks to the 12.5HMcl TT likelihood narrows the range of allowed values of $\Omega_m h^2$, excluding high values which are disfavoured by the BAO data.

about 0.4%, the *Planck* results in Fig. 13.6 lie on the degeneracy lines:

$$\begin{cases} H(z = 0.38)(r_d/r_d^F) &= 57.07 (\omega_m/0.1)^{-0.055} (1 + (\omega_m/0.1)^{-2.046}) \text{ km s}^{-1} \text{ Mpc}^{-1}, \\ D_M(z = 0.38)(r_d^F/r_d) &= 2090 (\omega_m/0.1)^{0.445} / (1 + (\omega_m/0.1)^{-1.451}) \text{ Mpc}, \end{cases} \quad (13.2a)$$

$$\begin{cases} H(z = 0.51)(r_d/r_d^F) &= 59.14 (\omega_m/0.1)^{0.097} (1 + (\omega_m/0.1)^{-2.149}) \text{ km s}^{-1} \text{ Mpc}^{-1}, \\ D_M(z = 0.51)(r_d^F/r_d) &= 2762 (\omega_m/0.1)^{0.338} / (1 + (\omega_m/0.1)^{-1.586}) \text{ Mpc}, \end{cases} \quad (13.2b)$$

$$\begin{cases} H(z = 0.61)(r_d/r_d^F) &= 60.93 (\omega_m/0.1)^{0.189} (1 + (\omega_m/0.1)^{-2.163}) \text{ km s}^{-1} \text{ Mpc}^{-1}, \\ D_M(z = 0.61)(r_d^F/r_d) &= 3261 (\omega_m/0.1)^{0.274} / (1 + (\omega_m/0.1)^{-1.649}) \text{ Mpc}. \end{cases} \quad (13.2c)$$

The green points in Fig. 13.6 show samples from the 12.5HMcl TT chains, while the red points show samples from the 12.5HMcl TTTEEE chains. Adding the polarization data tightens the constraints on $\Omega_m h^2$ (see Fig. 13.2) bringing the *Planck* data into better agreement with the BOSS constraints (which disfavour the high values of $\Omega_m h^2$ allowed by the 12.5HMcl TT chains). Adding *Planck* lensing to the *Planck* temperature likelihoods produces a similar effect (see Fig. 12 of PCP18); *Planck* lensing combined with *Planck* temperature data disfavors high values of $\Omega_m h^2$ leading to better consistency with the BAO results.

The addition of BAO and/or lensing data to the 12.5HMcl TTTEEE likelihood has relatively little effect on the cosmological parameters of the base Λ CDM model. This is illustrated in Fig. 13.7 and Table 17. The *Planck* lensing likelihood is overwhelmed by the TTTEEE likelihood and so adding *Planck* lensing causes negligible shifts in cosmological parameters. As noted in [98] and PCP18, the *Planck* lensing likelihood constrains the parameter combination

$$\sigma_8 \Omega_m^{0.25} = 0.589 \pm 0.020, \quad \text{Planck lensing}, \quad (13.3a)$$

which is compatible with the constraint from the 12.5HMcl TTTEEE likelihood,

$$\sigma_8 \Omega_m^{0.25} = 0.6057 \pm 0.0081, \quad \text{12.5HMcl TTTEEE}. \quad (13.3b)$$

Table 17. Marginalized base Λ CDM parameters with 68% confidence intervals determined from the 12.5HMcl TT, TE and TTTEEE likelihoods. The last column combines 12.5HMcl TTTEEE with the *Planck* lensing and BAO likelihoods.

Parameter	TT	TE	TTTEEE	TTTEEE+BAO+lensing
$\Omega_b h^2$	0.02219 ± 0.00021	0.02221 ± 0.00022	0.02226 ± 0.0014	0.02231 ± 0.00013
$\Omega_c h^2$	0.1191 ± 0.0020	0.1193 ± 0.0019	0.1196 ± 0.0014	0.11914 ± 0.00094
$100 \theta_{MC}$	1.04075 ± 0.00044	1.04145 ± 0.00046	1.04105 ± 0.00029	1.04112 ± 0.00028
τ	0.0521 ± 0.0080	$0.0486^{+0.0087}_{-0.0073}$	0.0533 ± 0.0077	0.0554 ± 0.0073
$\ln(10^{10} A_s)$	3.058 ± 0.016	3.025 ± 0.021	3.040 ± 0.016	3.044 ± 0.014
n_s	0.9661 ± 0.0058	0.958 ± 0.010	0.9671 ± 0.0046	0.9683 ± 0.0040
H_0 [km s ⁻¹ Mpc ⁻¹]	67.47 ± 0.88	67.64 ± 0.82	67.44 ± 0.58	67.68 ± 0.42
Ω_Λ	0.688 ± 0.012	0.689 ± 0.011	0.6865 ± 0.0081	0.6897 ± 0.0056
Ω_m	0.312 ± 0.012	0.311 ± 0.011	0.3135 ± 0.0081	0.3103 ± 0.0056
$\Omega_m h^2$	0.1420 ± 0.0019	0.1422 ± 0.0018	0.1425 ± 0.0013	0.14209 ± 0.00089
$\Omega_m h^3$	0.09576 ± 0.00043	0.09616 ± 0.00046	0.09612 ± 0.00029	0.09616 ± 0.00029
σ_8	0.8057 ± 0.0091	0.800 ± 0.011	0.8095 ± 0.0074	0.8097 ± 0.0060
$\sigma_8(\Omega_m/0.3)^{0.5}$	0.822 ± 0.023	0.815 ± 0.022	0.828 ± 0.016	0.823 ± 0.010
$\sigma_8 \Omega_m^{0.25}$	0.602 ± 0.011	0.598 ± 0.012	0.6057 ± 0.0081	0.6043 ± 0.0056
z_{re}	$7.45^{+0.81}_{-0.79}$	$7.08^{+0.96}_{-0.72}$	$7.58^{+0.81}_{-0.74}$	$7.78^{+0.71}_{-0.70}$
$10^9 A_s$	2.082 ± 0.034	2.060 ± 0.044	2.091 ± 0.033	2.100 ± 0.030
$10^9 A_s e^{-2\tau}$	1.876 ± 0.013	1.869 ± 0.027	1.880 ± 0.012	1.879 ± 0.010
Age [Gyr]	13.817 ± 0.035	13.795 ± 0.034	13.803 ± 0.023	13.794 ± 0.020
z_*	1090.07 ± 0.38	1090.07 ± 0.38	1090.02 ± 0.26	1089.92 ± 0.21
r_* [Mpc]	144.80 ± 0.46	144.73 ± 0.45	144.61 ± 0.30	144.70 ± 0.22
$100 \theta_*$	1.04095 ± 0.00043	1.04165 ± 0.00045	1.04124 ± 0.00028	1.04131 ± 0.00027
z_{drag}	1059.46 ± 0.44	1059.51 ± 0.46	1059.66 ± 0.30	1059.73 ± 0.29
r_{drag} [Mpc]	147.53 ± 0.47	147.45 ± 0.46	147.31 ± 0.31	147.39 ± 0.24
k_D [Mpc ⁻¹]	0.14027 ± 0.00051	0.14036 ± 0.00053	0.14056 ± 0.00034	0.14050 ± 0.00029
z_{eq}	3377 ± 46	3382 ± 43	3391 ± 30	3380 ± 21
k_{eq} [Mpc ⁻¹]	0.01031 ± 0.00014	0.01032 ± 0.00013	0.010349 ± 0.000092	0.010316 ± 0.000065
$100 \theta_{s,eq}$	0.4516 ± 0.0044	0.4514 ± 0.0042	0.4505 ± 0.0030	0.4515 ± 0.0020

Fig. 13.7 shows that BAO measurements have a relatively little effect on the cosmological parameters of the base Λ CDM model. The addition of the BAO data to the 12.5HMcl TTTEEE likelihood causes a small shift towards lower values of $\Omega_c h^2$, lowering Ω_m and σ_8 and raising H_0 .

Cosmological parameters derived from the 12.5HMcl likelihood are summarized in Table 17. We consider the 12.5HMcl TTTEEE results to be the most reliable set of cosmological parameters derived from *Planck* power spectra, based on the consistency of the TT, TE and EE likelihoods and the small residuals in Figs. 13.4 and 13.5.

13.6 Dependence on multipole range

Over the multipole range probed by *WMAP* (which we assume to be approximately 2 – 800), there is excellent agreement between *WMAP* and *Planck* temperature data at both the power spectrum and map level²⁹ (see e.g. Appendix A of PCP13 and [50, 95]). As a consequence, if we restrict the *Planck* temperature likelihood to a maximum multipole $\ell_{max} = 800$, the base Λ CDM cosmological parameters are very close to those determined from *WMAP* [11]. The

²⁹After correcting for a 1.3% calibration error in the 2013 *Planck* HFI maps.

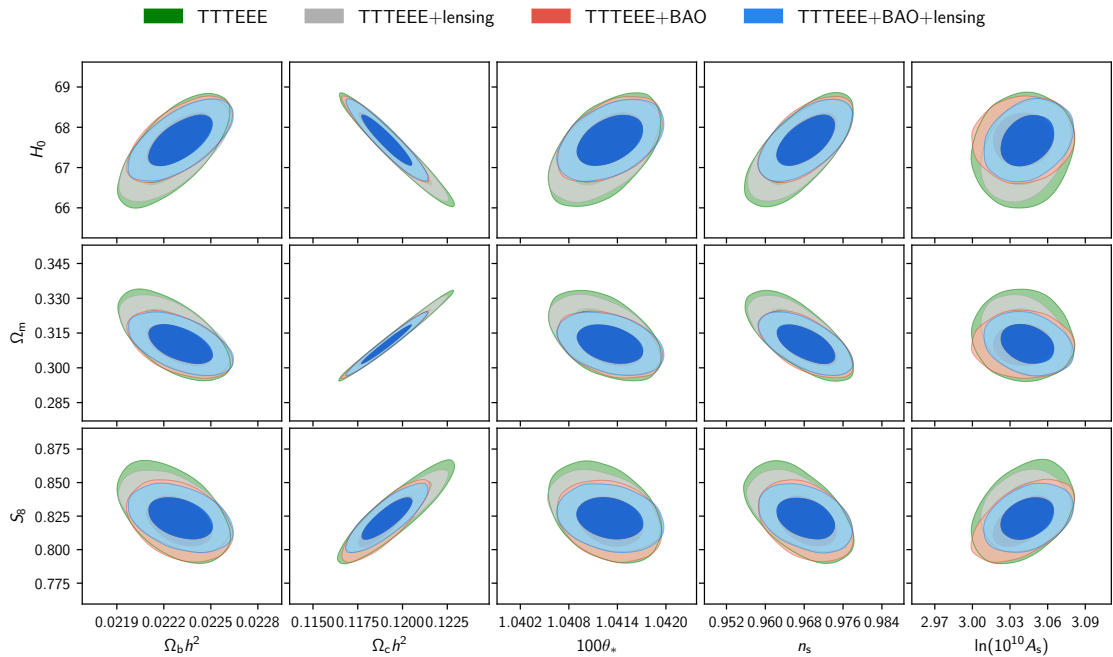


Figure 13.7. 68% and 95% confidence contours for base Λ CDM cosmological parameters determined from the 12.5HMcl TTTEEE likelihood combined with *Planck* lensing and/or BAO data.

question then arises as to whether the shifts in cosmological parameters measured by *Planck* are statistically consistent with the expectations of the base Λ CDM cosmology as ℓ_{\max} is increased to higher multipoles. This issue has been addressed in PCP13, PPL15, [100] and PCP18. In particular, the analysis presented in [100] concluded that the parameter shifts seen in the *Planck* temperature data were broadly consistent with those expected in base Λ CDM, with no compelling evidence for any anomalies.

However, this conclusion has been questioned by [3] who raised the possibility that systematic errors in the *Planck* data at high multipoles may be driving cosmological parameter shifts. We revisit this issue in this section using the statistically more powerful 12.5HMcl likelihood. Addison et al. [3] applied a multipole cut of $1000 \leq \ell \leq 2500$ to the 2015 *Planck* likelihood. With this choice of multipole range, the spectral index n_s is extremely poorly constrained leading to large degeneracies with cosmological parameters of interest. In addition, the standard template-based foreground model contains a large number of parameters. Foreground model parameters, in particular the Galactic dust amplitudes, also become poorly constrained if low multipoles are excluded. Any inconsistency between the foreground model and reality can then affect the cosmological parameters. While we agree with [3] that the general trends of cosmological parameter shifts are insensitive to the foreground model, quantifying their statistical significance to sub- σ accuracy (which is necessary to interpret this exercise) *does* depend on the foreground model. In PCP18, parameter shifts were analyzed using the `plik_lite` *Planck* likelihood (described in PPL18) which marginalizes over foreground and nuisance parameters. With this approach, the foreground parameters are therefore constrained by the full *Planck* multipole range.

We adopt a different approach in this paper by using the 12.5HMcl likelihood. Cleaning the temperature maps with 545 GHz lowers the foreground levels and it is then possible to

constrain the residual foreground levels accurately using either low or high multipole cuts. Likelihood analyses using disjoint multipole ranges are then strictly independent.

Results are shown in Fig. 13.8 for multipole ranges $2 \leq \ell \leq 800$, $50 \leq \ell \leq 800$, $801 \leq \ell \leq 2500$ and for the full multipole range $2 \leq \ell \leq 2500$. To simplify the subsequent discussion, we will refer to the multipole splits as follows LOW ($2 \leq \ell \leq 800$), HIGH ($801 \leq \ell \leq 2500$) and FULL ($2 \leq \ell \leq 2500$). We have included the multipole split $50 \leq \ell \leq 800$ in Fig. 13.8 so that it is possible to assess the impact of the temperature power spectrum in the low multipole range $2 \leq \ell \leq 50$, which has a slightly lower amplitude than expected from the best-fit *Planck* base Λ CDM model (see PCP13, [100]).

Table 18 gives numerical values for selected parameters and quantifies the shifts assuming the low and high multipole cuts are independent. The LOW TT parameters shown in Fig. 13.8 are close to those measured by *WMAP*, whereas the HIGH TT parameters prefer higher values of $\Omega_c h^2$ (qualitatively similar to the results found by [3]). Since the acoustic peak scale is insensitive to multipole range, this shift to higher values of $\Omega_c h^2$ leads to lower values of H_0 for the HIGH likelihood (cf. Eqs. 13.2a-13.2c). The HIGH likelihood also favours higher values of the amplitude parameters, as measured by σ_8 , S_8 and the CMB lensing combination $\sigma_8(\Omega_m)^{0.25}$. The parameter shifts are not particularly anomalous and both the LOW and HIGH multipole contours overlap with the FULL TT contours. We note that the very low TT multipoles, $2 \leq \ell \leq 50$, have a relatively small effect on the parameter shifts. The lower panels in Fig. 13.8 show the equivalent results for the TTTEEE likelihoods. Interestingly, the addition of the TE and EE likelihoods over the multipole range $2 \leq \ell \leq 800$ reduces the parameter errors substantially, driving the cosmological parameters close to those of the FULL TTTEEE likelihood. In contrast, since TE and EE from *Planck* are noisy at $\ell \gtrsim 800$, the addition of the polarization data has a relatively small effect on the HIGH TTTEEE likelihood. The LOW and HIGH TTTEEE parameters listed in Table 18 are consistent to better than 2.2σ .

From these results, we conclude that the base Λ CDM cosmological parameters from the *Planck* high multipoles are displaced towards higher values of $\Omega_c h^2$, S_8 and lower values of H_0 compared to the FULL TTTEEE solution. The LOW TT likelihood is displaced towards lower values of $\Omega_c h^2$, S_8 and higher values of H_0 . Both of these results are consistent with statistical fluctuations. As shown in Fig. 13.8, adding TE and EE to TT over the multipole range $2 \leq \ell \leq 800$ drives the parameters close to those of the full TTTEEE solution. Adding BAO to $\ell \leq 800$ TT also excludes low $\Omega_m h^2$, as does *Planck* TE+BAO (see Fig. 13.9). We therefore strongly disagree with the conclusions of [3]. The parameter shifts seen in *Planck* do not suggest systematics in the *Planck* data at high multipoles, instead there is considerable evidence that the $\ell = 2 - 800$ and $\ell = 801 - 2500$ TT parameters both differ from the truth as a result of modest statistical fluctuations.

The cause of these parameter shifts is apparent in Fig. 13.10. The blue points in this figure show the residuals of the coadded TT spectrum with respect to the $2 \leq \ell \leq 2500$ 12.5HMcl TTTEEE best fit cosmology. The green points show the residuals of the coadded spectrum at $\ell > 800$ using the foreground solution determined from the $800 \leq \ell \leq 2500$ TTTEEE likelihood. The differences between the blue and green points show the impact of the different foreground solution, which is small but non-negligible. The purple line shows the best-fit base Λ CDM TTTEEE cosmology fitted to $800 \leq \ell \leq 2500$ (which is disfavoured by the points at $\ell \leq 800$). The purple line responds to the oscillatory features in the multipole range $800 \lesssim \ell \lesssim 1500$ (which is also apparent in Figs. 11.2 and 11.5) and is reproducible to high precision across frequencies (see Fig. 13.11).

In summary, our analysis is consistent with the conclusions of [100] and PCP18, namely

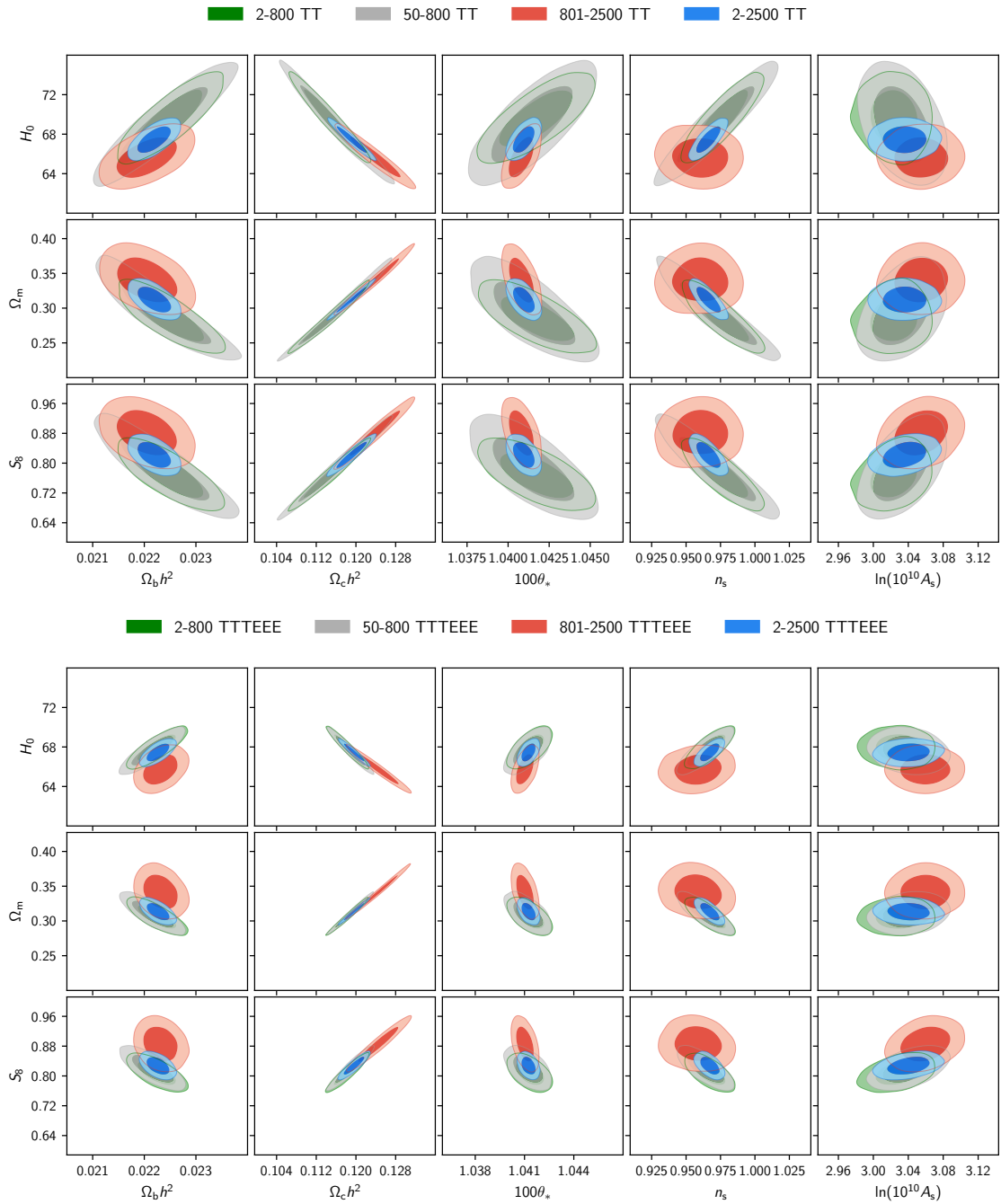


Figure 13.8. Base Λ CDM parameter constraints determined from the 12.5HMcl likelihood for various multipole ranges. The upper panels show results from the TT likelihood and lower panels show results from the TTTEEE likelihood.

■ 2-800 TT
 ■ TE+BAO
 ■ 2-800 TTTEEE
 ■ 2-2500 TTTEEE

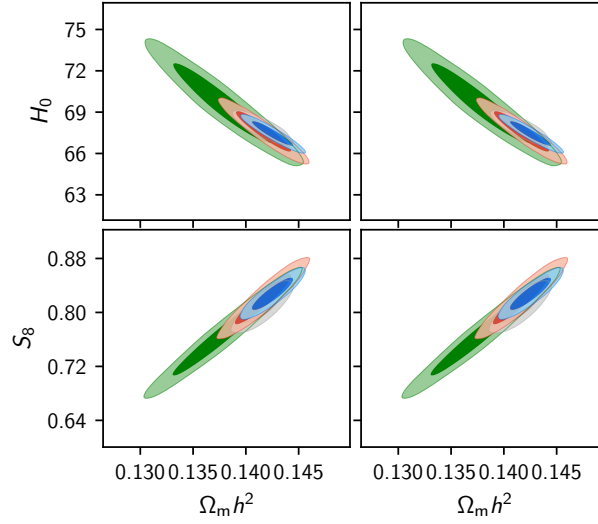


Figure 13.9. Parameter shifts showing the progression to high $\Omega_m h^2$, low H_0 and high S_8 for the 12.5HMcl TE+BAO likelihood, for the 12.5HMcl TTTEEE likelihood limited to $2 \leq \ell \leq 800$ and for the full 12.5HMcl TTTEEE covering $2 \leq \ell \leq 2500$.

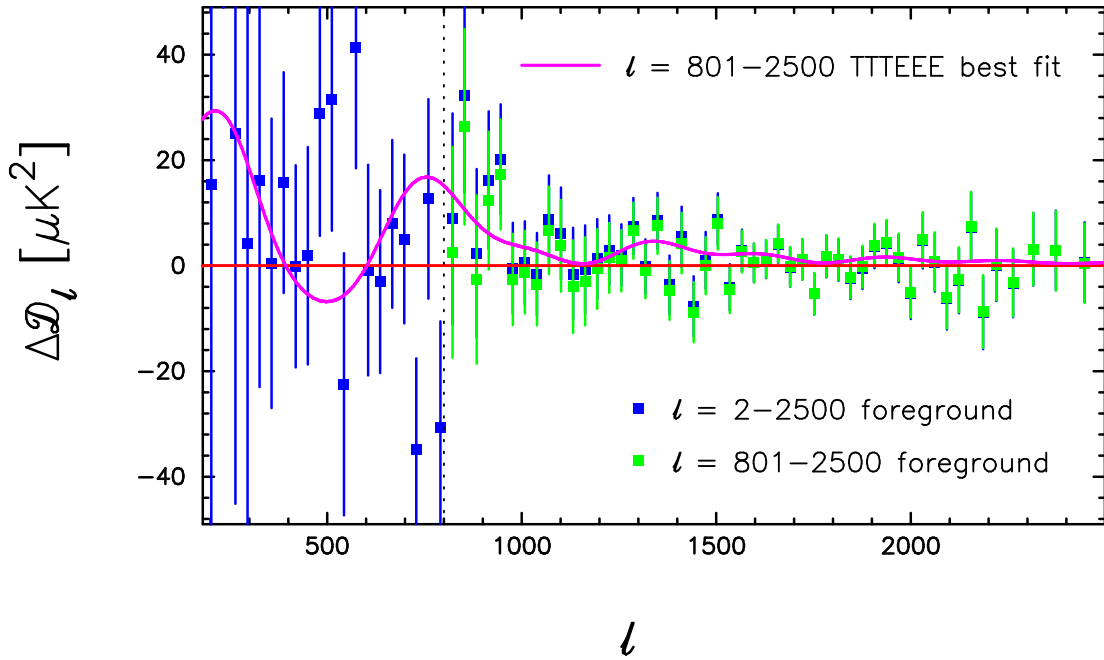


Figure 13.10. The blue points show the residuals of the coadded 12.5HMcl TT spectrum with respect to the best fit base Λ CDM model fitted to the 12.5HMcl full TTTEEE likelihood. The green points show the residuals of the coadded 12.5HMcl TT spectrum at $\ell > 800$ using the foreground solution of the 12.5HMcl TTTEEE likelihood fitted over the multipole range $801 \leq \ell \leq 2500$. The best fit base Λ CDM cosmology fitted to the $801 \leq \ell \leq 2500$ 12.5HMcl TTTEEE likelihood is shown as the purple line.

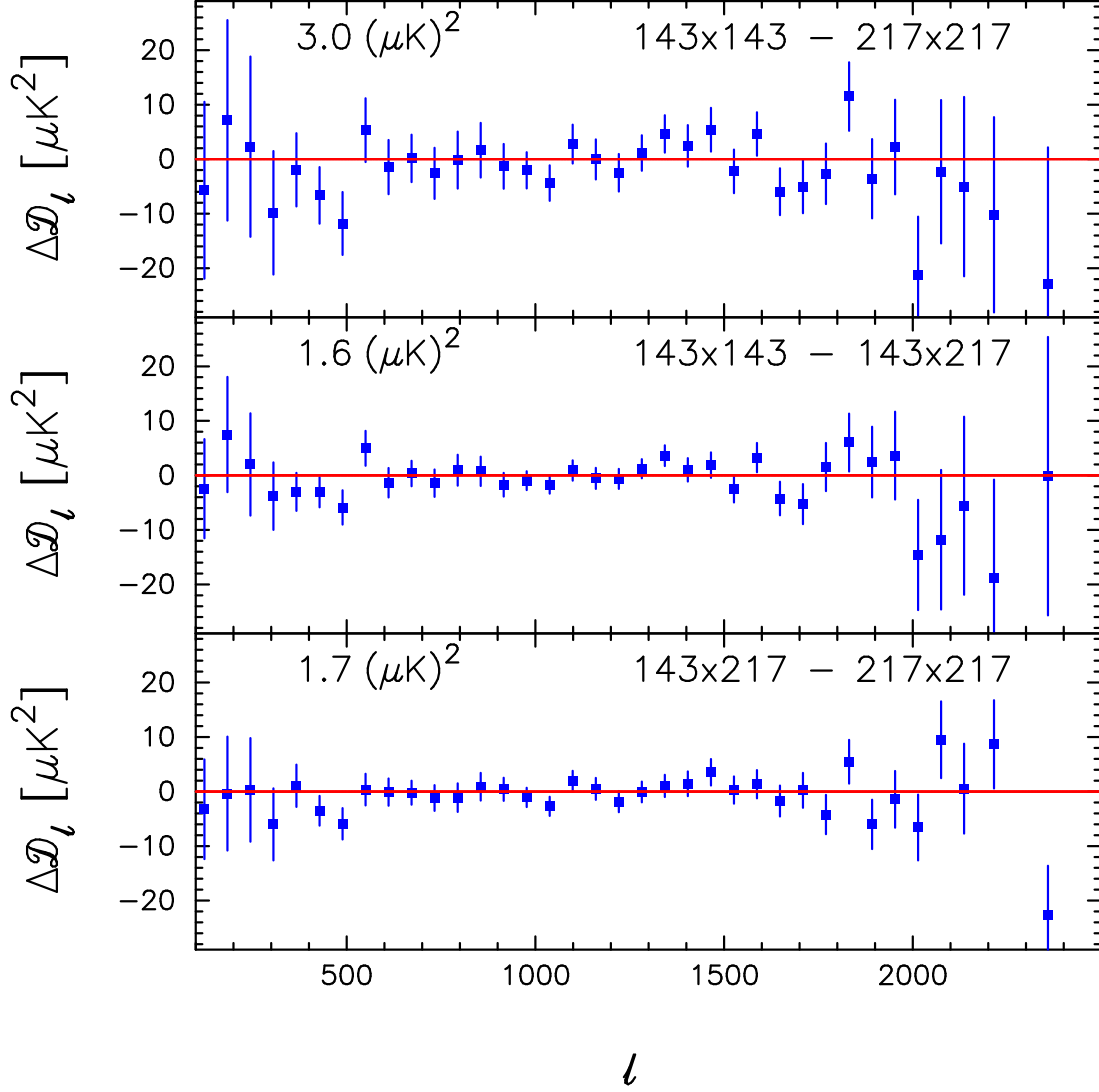


Figure 13.11. Inter-frequency differences for the 12.5HMcl TT spectra (as in Fig. 11.3). This figure uses the 12.5HMcl TTTEEE foreground solution. The error bars for the power spectrum differences are computed from appropriate linear combinations of the `CamSpec` covariance matrices. The numbers in each panel give the rms residuals of the bandpower differences over the multipole range $800 \leq \ell \leq 1500$.

Table 18. Base Λ CDM cosmological parameters for different multipole ranges determined from the 12.5HMcl likelihood. The numbers in the fourth and seventh columns list the parameter shifts in standard deviations assuming that the low and high multipole parameters are independent. H_0 is given in units of $\text{km s}^{-1}\text{Mpc}^{-1}$.

Param.	[1] 2-800 TT	[2] 801-2500 TT	[1]-[2]	[3] 2-800 TTTEEE	[4] 801-2500 TTTEEE	[3]-[4]
$\Omega_b h^2$	0.02249 ± 0.00041	0.02205 ± 0.00038	1.16σ	0.02243 ± 0.00024	0.02232 ± 0.00022	0.30σ
$\Omega_c h^2$	0.1147 ± 0.0032	0.1238 ± 0.0033	-1.86σ	0.1183 ± 0.0018	0.1246 ± 0.0027	-1.96σ
$100\theta_*$	1.0417 ± 0.0014	1.04081 ± 0.00050	0.09σ	1.04133 ± 0.00057	1.04102 ± 0.00035	0.46σ
n_s	0.976 ± 0.012	0.960 ± 0.013	0.90σ	0.9672 ± 0.0074	0.958 ± 0.011	0.66σ
H_0	69.58 ± 1.80	65.67 ± 1.30	1.76σ	67.93 ± 0.89	65.72 ± 1.00	1.65σ
Ω_m	0.286 ± 0.021	0.340 ± 0.021	-1.82σ	0.306 ± 0.0011	0.342 ± 0.016	-1.85σ
σ_8	0.790 ± 0.0040	0.827 ± 0.014	-1.92σ	0.8002 ± 0.0091	0.830 ± 0.011	-1.94σ
S_8	0.771 ± 0.040	0.881 ± 0.039	-1.98σ	0.808 ± 0.021	0.886 ± 0.031	-2.09σ
$\sigma_8 \Omega_m^{0.25}$	0.577 ± 0.020	0.631 ± 0.019	-1.98σ	0.595 ± 0.011	0.635 ± 0.015	-2.15σ

that parameter shifts between low and high multipoles are consistent with statistical fluctuations. The features which drive the parameters from the 801 – 2500 TT likelihood are mainly located in the multipole range 801 – 1500 and are reproducible to high accuracy in the 143×143 , 143×217 and 217×217 spectra. The base Λ CDM parameters derived from the LOW TTTEEE likelihood are very close to those derived from the FULL TT and TTTEEE likelihoods. This is a very important consistency check of the *Planck* data. Most of the *Planck* TT results for base Λ CDM can be recovered to comparable accuracy from $\ell \leq 800$ if one includes the polarization spectra.

13.7 Tensions with other astrophysical data

We will not make an extensive comparison of these results with other astrophysical data in this paper, since this topic has been reviewed in detail in PCP18. However we make the following observations:

H_0 tension: As noted in PCP13, the best-fit *Planck* value of H_0 differs from direct measurements based on the Cepheid-Type Ia supernova distance ladder [108–110]. The latest value from the SH0ES³⁰ collaboration [111] is $H_0 = 74.03 \pm 1.42 \text{ km s}^{-1}\text{Mpc}^{-1}$, differing by $6.59 \text{ km s}^{-1}\text{Mpc}^{-1}$ from the 12.5HMcl TTTEEE value of H_0 listed in Table 17. Interestingly, the statistical significance of the discrepancy between *Planck* and SH0ES has grown from 2.5σ in PCP13 to 4.3σ today. There are also hints, for example, from strong gravitational lensing time delays [18] that the late time value of H_0 may differ from the *Planck* value. The H_0 discrepancy is perhaps the most intriguing tension with the base Λ CDM model at this time. There is a general consensus, from application of the inverse distance ladder to BAO and Type Ia supernovae data, that this discrepancy, if real, requires physics that reduces the value of the sound horizon r_{drag} irrespective of the nature of dark energy [8, 12, 24, 62, 66]. For a review of possible theoretical explanations of this tension see [55].

Weak Gravitational Lensing: Recently, three large cosmic shear surveys have reported constraints on the parameter combination $S_8 = \sigma_8(\Omega_m/0.3)^{0.5}$. The Dark Energy Survey (DES) Year 1 data [121] gives

$$S_8 = 0.792 \pm 0.024, \quad \text{DES}, \quad (13.4a)$$

³⁰Supernovae, H_0 , for the Equation of State of Dark Energy.

(where we quote the result from PCP18 which imposes the $\sum m_\nu = 0.06$ eV neutrino mass constraint used in the *Planck* analysis). The Kilo-Degree Survey (KiDS)+Vista Kilo-Degree Infrared Galaxy Survey (VIKING) gives [45]

$$S_8 = 0.737_{-0.036}^{+0.040}, \quad \text{KV450}, \quad (13.4b)$$

(updating the earlier results from the KiDS-450 survey [46]). The Subaru Hyper Suprime-Cam (HSC) first year data give [44]

$$S_8 = 0.780_{-0.033}^{+0.030}, \quad \text{HSC}. \quad (13.4c)$$

These estimates are all lower than the value $S_8 = 0.828 \pm 0.016$ from the 12.5HMcl TTTEEE likelihood. If we crudely combine these estimates assuming that they are statistically independent, we find $S_8 = 0.778 \pm 0.017$ which is only about 2.1σ away from the *Planck* result. In our view, there is no compelling evidence of a discrepancy between *Planck* and constraints from cosmic shear surveys at this stage³¹.

There are, of course, a number of potential sources of systematic error in both the forward distance scale and weak lensing measurements, which we will not discuss here. The key point that we wish to make is that the *Planck* results are remarkably robust between frequencies, between temperature and polarization and between sky fractions. The *Planck* results are therefore unlikely to be affected by systematic errors to any significant degree. If the tensions with the distance scale and weak lensing measurements persist and can be shown to be free of systematic errors, then this will indicate new physics beyond the base Λ CDM model.

14 Extensions to Λ CDM

PCP18 reported two unusual results related to extensions to the base Λ CDM cosmology involving the phenomenological A_L parameter and spatial curvature Ω_K . For both parameters, the TTTEEE **CamSpec** and **Plik** likelihoods behaved differently. As noted in PCP18, the primary reason for these differences is that **Plik** used polarization efficiency corrections derived from the EE spectra. As discussed in Sect. 6 in **CamSpec** we use polarization efficiency corrections derived from TE and EE spectra, which are clearly more accurate for the TE spectra. In this section, we investigate how these parameters vary using the statistically more powerful 12.5HMcl likelihood. For completeness, we also investigate constraints on the neutrino mass $\sum m_\nu$, on the number of relativistic species N_{eff} and on tensor modes.

14.1 The A_L parameter

It has been noted since PCP13 that the *Planck* temperature data favour values of $A_L > 1$. In PCP18, the **Plik** likelihood gave $A_L = 1.243 \pm 0.096$ (TT+lowE) and 1.180 ± 0.065 (TTTEEE+lowE), favouring $A_L > 1$ at 2.5σ and 2.8σ respectively. The **CamSpec** likelihood used in PCP18 (which is similar to the 12.1HM likelihood produced for this paper) gave $A_L = 1.246_{-0.100}^{+0.092}$ (TT+lowE) and $A_L = 1.149 \pm 0.072$ (TTTEEE+lowE), favouring $A_L > 1$ at 2.5σ and 2.1σ respectively. For the **Plik** likelihood, adding TE and EE made the discrepancy with $A_L = 1$ worse, whereas for **CamSpec** the addition of polarization reduced the discrepancy. (Though, importantly, for both likelihoods the addition of polarization data caused the best fit value of A_L to fall.)

³¹The situation is, however, still quite fluid. For example, recently [7] reported results from a combined analysis of DES and KV450 finding $S_8 = 0.755_{-0.021}^{+0.019}$ for base Λ CDM. This differs by 2.9σ from our estimate based on the 12.5HMcl TTTEEE likelihood.

Table 19. Parameters for extensions to Λ CDM.

12.1HM Likelihood	A_L	Ω_K	N_{eff}	m_ν (eV)	$r_{0.002}$ (+BK15)
TT	$1.267^{+0.095}_{-0.102}$	$-0.061^{+0.027}_{-0.018}$	$2.89^{+0.27}_{-0.30}$	< 0.47	< 0.052
TE	$0.98^{+0.21}_{-0.24}$	$-0.032^{+0.056}_{-0.022}$	$2.82^{+0.43}_{-0.53}$	< 1.47	< 0.070
TE+BAO	0.93 ± 0.19	-0.0008 ± 0.0024	$2.78^{+0.34}_{-0.38}$	< 0.35	< 0.071
TTTEEE	1.156 ± 0.070	$-0.037^{+0.019}_{-0.013}$	2.89 ± 0.21	< 0.36	< 0.061
TTTEEE+lensing	1.061 ± 0.042	$0.0092^{+0.0065}_{-0.0064}$	2.84 ± 0.21	< 0.30	< 0.059
TTTEEE+lensing+BAO	1.058 ± 0.038	0.0004 ± 0.0020	2.95 ± 0.19	< 0.14	< 0.060
12.5HMcl Likelihood	A_L	Ω_K	N_{eff}	m_ν (eV)	$r_{0.002}$ (+BK15)
TT	1.218 ± 0.097	$-0.048^{+0.025}_{-0.018}$	$2.92^{+0.30}_{-0.34}$	< 0.67	< 0.058
TE	0.96 ± 0.19	$-0.020^{+0.044}_{-0.020}$	$2.95^{+0.40}_{-0.47}$	< 1.32	< 0.065
TE+BAO	1.00 ± 0.17	0.0010 ± 0.0023	$3.05^{+0.32}_{-0.37}$	< 0.25	< 0.069
TTTEEE	1.149 ± 0.067	$-0.035^{+0.018}_{-0.013}$	$2.96^{+0.21}_{-0.24}$	< 0.34	< 0.056
TTTEEE+lensing	1.064 ± 0.040	$-0.0101^{+0.0066}_{-0.0065}$	$2.91^{+0.20}_{-0.24}$	< 0.26	< 0.057
TTTEEE+lensing+BAO	1.062 ± 0.036	0.0004 ± 0.0019	3.01 ± 0.19	< 0.13	< 0.058

It is important to note that the A_L parameter is very poorly constrained by the power spectra at low multipoles. For example, over the multipole range $2 \leq \ell \leq 800$, the 12.5HMcl TT likelihood gives $A_L = 1.32 \pm 0.48$. The A_L parameter is therefore extremely sensitive to the *Planck* data at high multipoles. Results for A_L for the 12.1HM and 12.5HMcl likelihoods are given in Table 19. Compared to the CamSpec TT likelihood used in PCP18, A_L from the 12.1HM TT likelihood is slightly higher, differing from unity by about 2.6σ . The only significant difference between these likelihoods is that we fix the relative calibrations between frequencies in the 12.1HM likelihood, as described in Sect. 9.1.1, rather than allowing them to vary as nuisance parameters. This illustrates the extreme sensitivity of the A_L parameter to the nuisance parameter/foreground model. The 12.5HMcl TT likelihood covers more sky area at 143 and 217 GHz compared to 12.1HMcl and we see that the amplitude of A_L goes down, differing from unity by 2.2σ . This is what we would have expected to see given that the residuals of the 217×217 and 143×217 spectra with respect to the base Λ CDM best fit (see Fig. 11.5) decrease in amplitude as sky area is increased. We find similar results for the full mission 12.1F likelihood, which improves the signal-to-noise of the temperature spectra. The behaviour of A_L is consistent with a moderate statistical fluctuation, driven by a chance match of the TT power spectrum residuals in the multipole range $\sim 800 - 1500$ which are reproducible over the frequency range 143 – 217 GHz. These residuals decline in amplitude with increasing sky area and also by switching to the full mission spectra. The TE and EE spectra do not provide strong constraints on A_L because they are noisy at high multipoles. As can be seen from Fig. 14.1, which shows constraints in the $A_L - H_0$ plane, the TE spectrum disfavors high values of H_0 , so when the polarization blocks of the likelihood are added to the TT blocks, the value of A_L goes down³². The 12.5HMcl TTTEEE constraints give $A_L = 1.149 \pm 0.067$, i.e. a 2.2σ deviation from unity. Adding *Planck* lensing, the value of A_L goes down further reducing the discrepancy to 1.6σ . The best-fit 12.5HMcl TTTEEE A_L model is plotted against the temperature data in Fig. 14.5.

³²Note that none of our likelihoods reproduce the 2.8σ deviation from $A_L = 1$ reported for the Plik TTTEEE likelihood in PCP18.

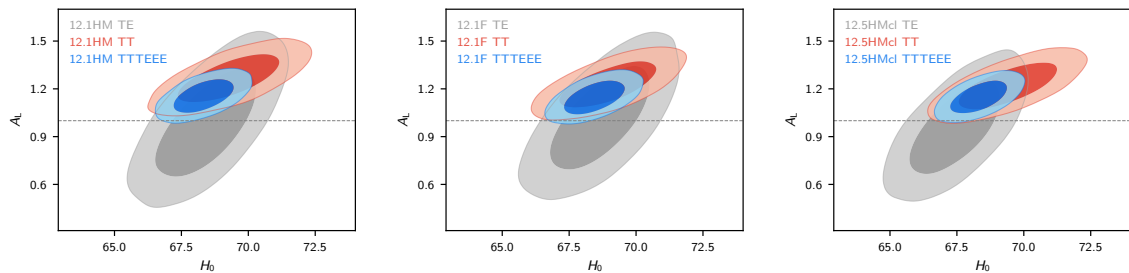


Figure 14.1. 68% and 95% contours on the parameters A_L and H_0 (in units of $\text{km s}^{-1}\text{Mpc}^{-1}$) for various likelihood combinations: 12.1HM likelihood (left), 12.1F (middle) and 12.5HMcl (right). The horizontal dotted line shows $A_L = 1$.

14.2 Spatial Curvature

As discussed in PCP18, the fluctuations in the *Planck* spectra that cause A_L to be higher than unity also couple with spatial curvature, driving the best fit *Planck* cosmology towards closed universes. This tendency has been noted by a number of authors [27, 28, 42, 72].

Constraints on Ω_K for various likelihood combinations³³ are plotted in Fig. 14.2 and listed in Table 19. From TT alone, the pull towards closed Universes is at about the 2σ level. The polarization spectra are relatively neutral towards Ω_K , so for the 12.5HMcl TTTEEE likelihood, the significance level for $\Omega_K < 0$ drops slightly. From the CMB power spectra alone, it is difficult to constrain Ω_K because of the near-exact geometrical degeneracy [19], which is broken only by the lensing of the CMB [119]. As a consequence of the geometrical degeneracy, the parameter Ω_K is highly degenerate with the value of the Hubble constant (see Fig. 14.2) with much of the parameter range allowed by the CMB corresponding to low values of H_0 which are strongly disfavoured by direct measurements. The addition of BAO and/or *Planck* CMB lensing breaks this degeneracy very effectively. This is illustrated in Fig. 14.2. For example, the addition of the BAO data to the TE likelihood constrains the Universe to be nearly spatially flat to an accuracy that is almost as good as the TTTEEE+BAO+lensing likelihood (see also Table 19).

Posteriors for Ω_K are shown in the right hand panel of Fig. 14.2 for various likelihood combinations. As with A_L , the *Planck* results are consistent with a moderate statistical fluctuation in the temperature spectra that favours closed universes at about the 2σ level. With the addition of BAO and/or *Planck* lensing data, we find strong evidence to support a spatially flat Universe. Given the recent interest in models with spatial curvature, we have given a more detailed statistical analysis of the results from the 12.5HMcl likelihood in [34], including the role of assuming a uniform prior in Ω_K .

14.3 Relativistic species and massive neutrinos

For completeness, Table 19 gives results for the number of relativistic species and the sum of neutrino masses for the 12.1HM and 12.5HMcl likelihoods. These results are consistent with those reported in PCP18. Increasing the number of relativistic species above the value $N_{\text{eff}} = 3.046$ of the base ΛCDM model has been proposed as a possible solution of the tension between direct measurements of H_0 and the value inferred from the CMB [12, 110]. However, it is clear from Fig. 14.3 that this solution is quite strongly disfavoured by *Planck*. Allowing

³³Note that these results assume a uniform prior for Ω_K over the range $-0.3 \leq \Omega_K \leq 0.3$.

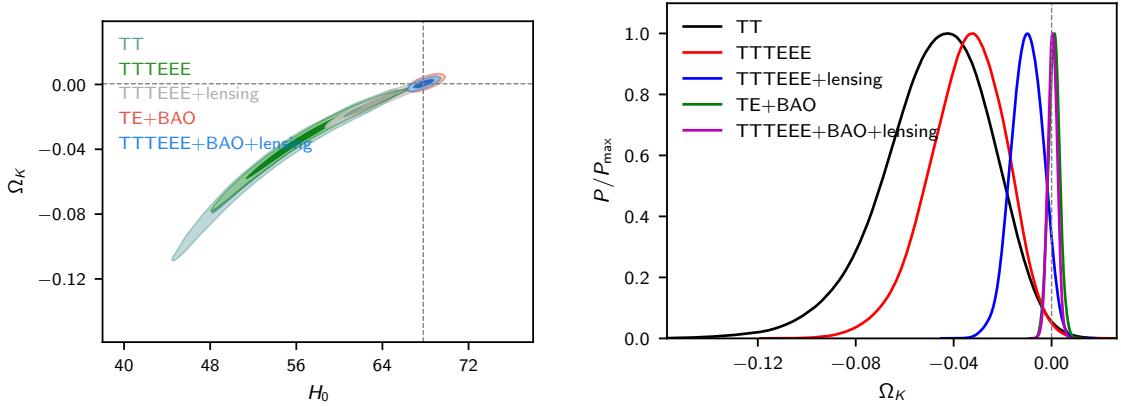


Figure 14.2. The figure to the left shows 68% and 95% contours in the H_0 - Ω_K plane for various likelihood combinations using the 12.5HMcl likelihood. The dashed lines show the best-fit values of Ω_K and H_0 for the TTTEEE 12.5HMcl+BAO+lensing likelihood. The figure to the right shows posteriors for Ω_K illustrating that $\Omega_K = 0$ is consistent with the 12.5HMcl TT and TTTEEE likelihoods to within about 2σ .

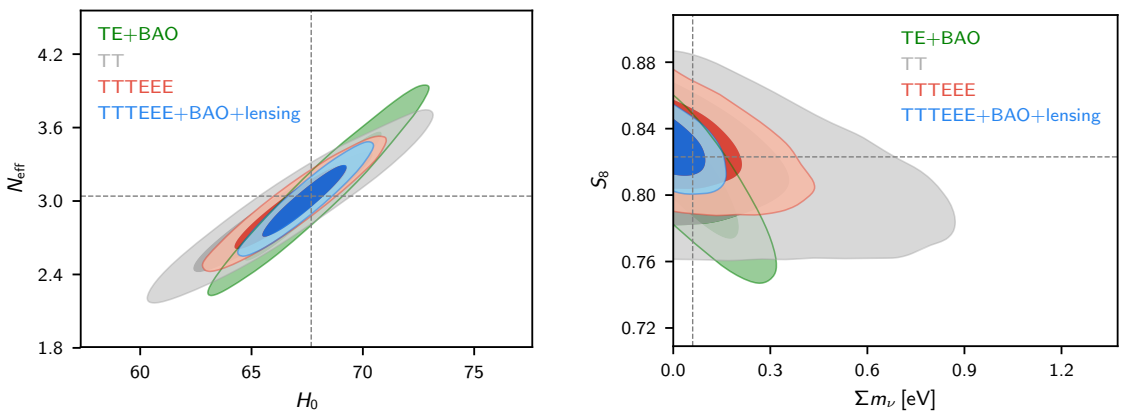


Figure 14.3. 68% and 95% contours derived using the 12.5HMcl likelihood in combination with the BAO and *Planck* lensing likelihoods. The figure to the left shows constraints in the H_0 - N_{eff} plane (with H_0 in units of $\text{km s}^{-1}\text{Mpc}^{-1}$) if N_{eff} is added as an additional parameter to base ΛCDM . The figure to the right shows constraints in the $\sum m_\nu$ - S_8 plane if the sum of neutrino masses is allowed to vary as an additional parameter to the base ΛCDM cosmology. The dashed lines show best fit base ΛCDM parameters of H_0 and S_8 determined from the 12.5HMcl TTTEEE likelihood.

N_{eff} to vary, the 12.5HMcl TTTEEE+BAO+lensing likelihood gives $N_{\text{eff}} = 3.01 \pm 0.19$, $H_0 = 67.42 \pm 1.25 \text{ km s}^{-1}\text{Mpc}^{-1}$, i.e. very close to the best fit parameters of the base ΛCDM model, and discrepant by 3.1σ from the H_0 determination reported in [111].

The plot to the right of Fig. 14.3 shows constraints on the sum of neutrino masses. As explained in PCP18, the *Planck* power spectra constrain neutrino masses through the effects of lensing. The fluctuations in the TT power spectrum that favour $A_L > 1$ could shift the neutrino mass constraints towards lower values. Since the 12.5HMcl likelihood favours lower values of A_L than reported in PCP18, it is interesting to investigate the constraints on neutrino

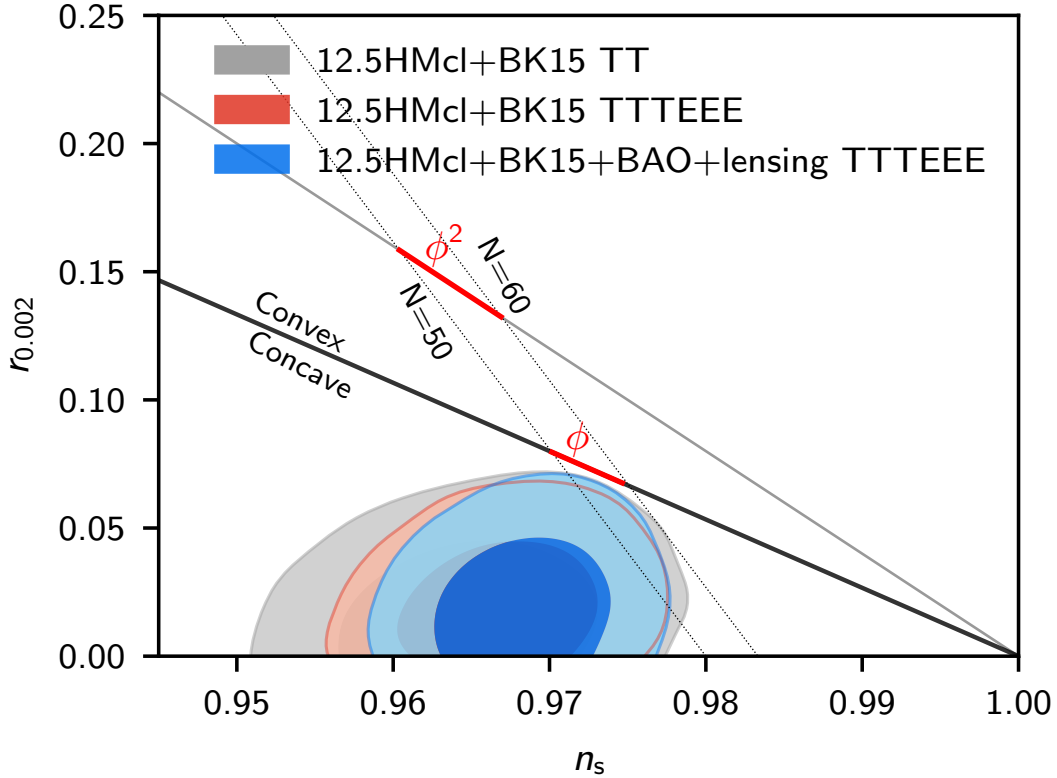


Figure 14.4. 68% and 95% constraints in the n_s - $r_{0.002}$ plane for various likelihood combinations combined with the BK15 B-mode measurements of [15]. The thick black line shows the n_s - r relation for a linear potential, $V(\phi) \propto \phi$, to first order in slow roll parameters. The red portion shows the range of parameters allowed in inflationary models with e-folding numbers in the range 50-60. The thin black line shows the n_s - r relation for a quadratic potential $V(\phi) \propto \phi^2$.

masses derived from the 12.5HMcl likelihood. In fact, we find almost no difference in the 95% upper limits, with $\sum m_\nu < 0.36$ eV from the 12.1HM TTTEEE likelihood and $\sum m_\nu < 0.34$ eV for the 12.5HMcl TTTEEE likelihood. The addition of BAO and *Planck* lensing to the 12.5HMcln TTTEEE likelihood lowers this limit to $\sum m_\nu < 0.13$ eV, almost identical to the constraint reported in PCP18. It has been argued [68] that massive neutrinos with $\sum m_\nu$ in the range 0.2 – 0.4 eV may explain the tension between low redshift measurements of the amplitude of the mass fluctuations (including the weak galaxy lensing measurements summarized in Sect. 13.7) and the base Λ CDM results from *Planck*. However, Fig. 14.3 shows that this solution is quite strongly disfavoured by the *Planck* and BAO data.

14.4 Tensor amplitude

The *Planck* results, combined with BAO measurements, show that our Universe is almost spatially flat with a spectrum of nearly scale invariant adiabatic fluctuations. In addition, the *Planck* data show no evidence for primordial non-Gaussianity [90, 92]. These results are consistent with single field models of inflation (see [89, 93, 104] and references therein). If the Universe did indeed experience an inflationary phase, there should exist a nearly scale-

invariant spectrum of tensor fluctuations [118] with a highly uncertain amplitude that depends on the energy scale of inflation. Allowing tensor modes is therefore one of the best motivated extensions of the base Λ CDM model and their detection would provide an important clue towards understanding the physics of inflation. The *Planck* temperature spectra provide relatively poor constraints on tensor modes because of cosmic variance on large scales [54]. However, tensor modes can be detected via B-mode polarization anisotropies [52, 115]. At present, the strongest constraints on primordial B-mode anisotropies come from the BICEP2-Keck Array collaboration [15–17], developing on earlier work by the BICEP2 collaboration [14]. Joint constraints using our **CamSpec** likelihoods combined with the BICEP2-Keck Array measurements of [15] (denoted BK15) are plotted in Fig. 14.4³⁴. The 95% upper limits on the tensor-scalar ratio given by the 12.5HMcl TTTEEE+BK15+BAO+lensing likelihood are

$$r_{0.002} < 0.058, \quad r_{0.05} < 0.062, \quad (14.1)$$

determined mainly by the BK15 measurements. Excluding the BK15 likelihood, the 95% upper limit is $r_{0.002} < 0.11$, so the main contribution of the *Planck* data to Fig. 14.4 is to constrain the spectral index n_s .

As discussed in detail in PCP18 and [104], the most striking result to emerge from *Planck* and the BICEP2-Keck Array results is the requirement of unusually flat inflationary potentials and therefore a hierarchy in the magnitudes of the inflationary slow-roll parameters. Inflationary model building has therefore shifted towards ideas on how to explain this hierarchy (see e.g. [1, 5, 51] and references therein).

14.5 Summary

This section has investigated some simple one-parameter extensions to the base Λ CDM cosmology. None of these extensions are strongly favoured by *Planck* data. Figure 14.5 shows the best-fit temperature power spectra for extended models fitted to the 12.5HMcl TTTEEE likelihood. These models have nearly identical temperature power spectra as a consequence of degeneracies with other cosmological parameters. Note that for models such as Ω_K , external data is necessary to break the strong internal degeneracies inherent in the CMB data (for example, as shown in Fig. 14.2, the addition of BAO data breaks the geometrical degeneracy leading to tight constraints on Ω_K). Models with strong internal degeneracies are extremely sensitive to systematics in the *Planck* data. However, for the extended models considered here, we find consistency between the *Planck* temperature and polarization spectra and consistency between the *Planck* power spectra, *Planck* lensing and BAO data. There is no evidence of systematics in the *Planck* power spectra, even for strongly degenerate models such as A_L and Ω_K .

15 Conclusions

Our main aim in this paper has been to present a description of **CamSpec** in sufficient detail that an independent researcher should be able to reproduce our results working with *Planck* 2018 data available from the PLA. *Planck* is a complex data set and requires an appreciation

³⁴As in PCP13-PCP18, we report constraints on the tensor-scalar ratio $r_{0.002}$, which is the relative amplitude of the tensor and scalar primordial fluctuation spectra at a pivot scale of $k = 0.002 \text{ Mpc}^{-1}$. The tensor spectral index is set to the value expected in single-field inflation models, $n_t = -r_{0.05}/8$, where $r_{0.05}$ is the tensor-to-scalar ratio at a pivot scale $k = 0.05 \text{ Mpc}^{-1}$. The scalar spectral index n_s is defined at a pivot scale of $k = 0.05 \text{ Mpc}^{-1}$ (see Eq. 2 of PCP18).

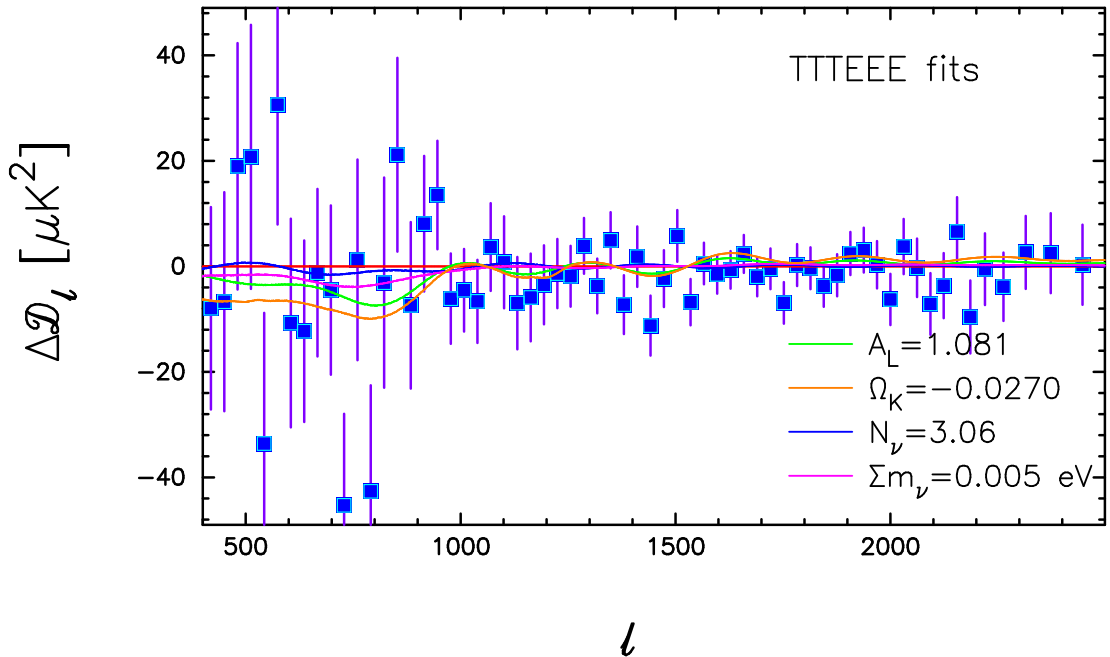


Figure 14.5. The blue points show the residuals of coadded 12.5HMcl TT spectrum relative to the best fit base Λ CDM cosmology fitted to the 12.5HMcl TTTEEE likelihood. The lines show the residuals of the best-fit TT spectra for one-parameter extensions to base Λ CDM fitted to the 12.5HMcl TTTEEE likelihood, with best-fit parameters as listed in the figure.

of the intricacies of the data if one is to build an accurate power spectrum-based likelihood. We hope that this paper will give readers such an appreciation.

A further aim has been to demonstrate the remarkable consistency of the *Planck* power spectra between individual detectors, between frequencies and with varying sky areas, reinforcing the conclusions of PCP18, PPL18 and earlier *Planck* collaboration papers. The main data systematics that we have investigated are as follows:

- correlated noise between detsets;
- small effective calibration differences in the temperature maps;
- effective polarization efficiencies;
- temperature-to-polarization leakage.

Throughout this paper, we have developed internal consistency checks to correct these data systematics or, as in the case of temperature-to-polarization leakage, to check our models for these corrections. With the exception of low multipole polarization, we find no evidence for any further instrumental systematics in the *Planck* power spectra that could impact on the fidelity of our high multipole likelihoods.

We have analysed the properties of Galactic dust emission in temperature and polarization, separating out isotropic extragalactic foregrounds such as the CIB from anisotropic dust emission. We find that over large areas of sky ($\sim 80\%$), Galactic emission is remarkably universal and can be subtracted to high accuracy using high frequency *Planck* maps as templates. We find no evidence, to high accuracy, for any decorrelation of polarized dust emission over the frequency range 100 – 353 GHz.

PCP18 reported a number of ‘unusual’ results, though not at high statistical significance. These included large residuals in the 217×217 spectrum at $\ell \sim 1460$, the tendency for the *Planck* temperature power spectra to favour high values of A_L and to favour $\Omega_k < 0$. PCP18 also showed that the **Plik** and **CamSpec** likelihoods behaved differently for some models if the polarization spectra were added to the temperature spectra. We have investigated these issues further by creating a set of likelihoods using very different models for temperature foregrounds. We have also produced statistically more powerful likelihoods by using full mission dataset spectra and by extending sky coverage in temperature and polarization. For base Λ CDM, the cosmological parameters are extremely stable as we scan through these likelihoods as shown in Fig. 13.2. The main trend that we found is for the TE parameters to come into better agreement with the TT parameters as the sky area is increased. The TTTEEE parameters from these likelihoods are highly consistent and in excellent agreement with the base Λ CDM cosmological parameters reported in PCP18. Given the internal consistency of the *Planck* spectra, the agreement between temperature and polarization spectra, and insensitivity of the likelihoods to sky area and foreground removal, we believe that the *Planck* results, as presented in the *Planck* collaboration papers, are secure.

We disagree strongly with the conclusions of [3] concerning the statistical significance of parameter shifts inferred from *Planck* spectra at low and high multipoles. We find no evidence for any anomalous parameter shifts. It is straightforward to isolate the features in the high multipole region of the temperature spectrum responsible for the cosmological parameters determined from the multipole range $801 \leq \ell \leq 2500$. These features are consistent across the 143×143 , 143×217 and 217×217 spectra. Significantly, if we restrict the combined TTTEEE likelihood to the multipole range $2 \leq \ell \leq 800$, we infer cosmological parameters for base Λ CDM that are in very good agreement, and have comparable accuracy, to the parameters determined from the $2 \leq \ell \leq 2500$ TT likelihoods. Our analysis reveals no evidence that systematics at high multipoles have any significant impact on the parameters of the base Λ CDM model derived from *Planck*.

As we scan through the likelihoods in sequence of increasing statistical power, the internal tensions reported in PCP18 decrease in statistical significance. The temperature and polarization spectra also become quieter and come into closer agreement with the best-fit base Λ CDM cosmology. The results on A_L and Ω_K reported in PCP18 are consistent with modest statistical fluctuations which decline in statistical significance as we increase the statistical power of the likelihoods. For all extensions of base Λ CDM considered here, the addition of the *Planck* polarization spectra to the temperature spectra *always* drives parameters closer to those of base Λ CDM. As far as we can see, the base Λ CDM model is a perfect fit to the *Planck* spectra within the statistical errors.

What does this mean for the future of CMB research? If external data, such as direct determinations of H_0 , or cosmic shear surveys, are shown to be discrepant with *Planck* then it is unlikely that the *Planck* data are at fault. This would require us to search for new physics that mimics, to high accuracy, the primordial CMB and lensing power spectra measured by *Planck*. It may be possible to find extensions to Λ CDM with strong internal parameter degeneracies that achieve this (see for example, [57]). For such models, the *Planck* data will be essentially neutral and the evidence in favour of new physics will rely entirely on the fidelity of external data. The *Planck* data are, however, limited. They have little statistical power at multipoles $\ell \gtrsim 2000$ and so cannot strongly constrain theoretical models that modify the damping tail of the CMB fluctuations. There have been some claims, at low statistical significance, of an inconsistency between base Λ CDM and CMB polarization

power spectra at high multipoles [43]. Fortunately, an ambitious programme of ground based CMB polarization measurements should provide a strong test of Λ CDM via high resolution observations of the CMB damping tail and CMB lensing [4]. The detection of tensor modes would, of course, have profound implications for inflationary cosmology and early Universe physics. The continuing search for primordial B-modes, from ground and space experiments, e.g. [4, 15, 114], is therefore of paramount importance. The next decade will see a new generation of large-scale structure, weak lensing and low frequency radio surveys. We can only hope that we are lucky, and that we will learn more about early Universe physics, dark matter and dark energy – all of which remain mysterious at this time.

Acknowledgments

GPE would like to thank Caltech (and especially Anthony Readhead) for supporting a visiting fellowship where part of this work was done. SG acknowledges financial support from STFC and the award of a Kavli Institute Fellowship at KICC. We are grateful to our Cambridge colleagues, particularly Anthony Challinor, Marina Migliaccio, Mark Ashdown and Anthony Lasenby for many useful comments on (and contributions to) *Planck* power spectrum analysis over the years. We are indebted to Antony Lewis, for his incredible contributions in developing the `CosmoMC` Monte-Carlo Markov Chain software, which we used for all of the MCMC results reported in this paper and for his graphics scripts which we have used for the production of many of the figures showing parameter constraints. We also thank the `Planck` team, Karim Benabed, Francois Bouchet, Silvia Galli, Eric Hivon, Marius Millea, Simon Prunet, and many other members of the *Planck* collaboration, with whom we have had many constructive discussions over the years. We thank Erminia Calabrese for discussions concerning the *Planck*-ACTpol comparison. We are indebted to the *Planck* Collaboration for their enormous efforts in producing such a wonderful set of data and we thank the *Planck* Science team for permission to use the 2018 detset maps in this paper. We are also grateful to the *Planck* Editorial Board, and particularly to Antony Lewis, for comments on a draft of this paper. We wish to make it clear, however, that the conclusions presented here represent the views of the authors.

A Mathematical Details

A.1 Coupling Matrices

Assuming statistical isotropy, the expectation value of (2) is related to the theoretical spectra C^{TT}, C^{TE}, \dots , via a set of coupling matrices:

$$\begin{aligned}
\langle \tilde{C}^{T_i T_j} \rangle &= K^{T_i T_j} C^{TT}, \\
\langle \tilde{C}^{T_i E_j} \rangle &= K^{T_i E_j} C^{TE}, \\
\langle \tilde{C}^{E_i T_j} \rangle &= K^{E_i T_j} C^{TE}, \\
\langle \tilde{C}^{E_i E_j} \rangle &= K^{E_i E_j} C^{EE} + K^{E_i B_j} C^{BB}, \\
\langle \tilde{C}^{B_i B_j} \rangle &= K^{E_i B_j} C^{EE} + K^{E_i E_j} C^{BB}, \\
\langle \tilde{C}^{E_i B_j} \rangle &= [K^{E_i E_j} - K^{E_i B_j}] C^{EB}, \\
\langle \tilde{C}^{B_i E_j} \rangle &= [K^{E_i E_j} - K^{B_i E_j}] C^{EB}, \\
\langle \tilde{C}^{T_i B_j} \rangle &= K^{T_i E_j} C^{TB}, \\
\langle \tilde{C}^{B_i T_j} \rangle &= K^{E_i T_j} C^{TB}.
\end{aligned} \tag{A.1}$$

The various blocks of the coupling matrix appearing in equation (A.1) are given by the following expressions [48, 56]:

$$K_{\ell_1 \ell_2}^{T_i T_j} = \frac{(2\ell_2 + 1)}{4\pi} \sum_{\ell_3} (2\ell_3 + 1) \tilde{W}_{\ell_3}^{T_i T_j} \begin{pmatrix} \ell_1 & \ell_2 & \ell_3 \\ 0 & 0 & 0 \end{pmatrix}^2 \equiv (2\ell_2 + 1) \Xi_{TT}(\ell_1, \ell_2, \tilde{W}^{T_i T_j}), \tag{A.2a}$$

$$\begin{aligned}
K_{\ell_1 \ell_2}^{T_i E_j} &= \frac{(2\ell_2 + 1)}{8\pi} \sum_{\ell_3} (2\ell_3 + 1) \tilde{W}_{\ell_3}^{T_i P_j} (1 + (-1)^L) \begin{pmatrix} \ell_1 & \ell_2 & \ell_3 \\ 0 & 0 & 0 \end{pmatrix} \begin{pmatrix} \ell_1 & \ell_2 & \ell_3 \\ -2 & 2 & 0 \end{pmatrix} \\
&\equiv (2\ell_2 + 1) \Xi_{TE}(\ell_1, \ell_2, \tilde{W}^{T_i P_j}), \quad L = \ell_1 + \ell_2 + \ell_3,
\end{aligned} \tag{A.2b}$$

$$\begin{aligned}
K_{\ell_1 \ell_2}^{E_i E_j} &= \frac{(2\ell_2 + 1)}{16\pi} \sum_{\ell_3} (2\ell_3 + 1) \tilde{W}_{\ell_3}^{P_i P_j} (1 + (-1)^L)^2 \begin{pmatrix} \ell_1 & \ell_2 & \ell_3 \\ -2 & 2 & 0 \end{pmatrix}^2 \\
&\equiv (2\ell_2 + 1) \Xi_{EE}(\ell_1, \ell_2, \tilde{W}^{P_i P_j}), \quad L = \ell_1 + \ell_2 + \ell_3,
\end{aligned} \tag{A.2c}$$

$$\begin{aligned}
K_{\ell_1 \ell_2}^{E_i B_j} &= K_{\ell_1 \ell_2}^{B_i E_j} = \frac{(2\ell_2 + 1)}{16\pi} \sum_{\ell_3} (2\ell_3 + 1) \tilde{W}_{\ell_3}^{P_i P_j} (1 - (-1)^L)^2 \begin{pmatrix} \ell_1 & \ell_2 & \ell_3 \\ -2 & 2 & 0 \end{pmatrix}^2 \\
&\equiv (2\ell_2 + 1) \Xi_{EB}(\ell_1, \ell_2, \tilde{W}^{P_i P_j}), \quad L = \ell_1 + \ell_2 + \ell_3,
\end{aligned} \tag{A.2d}$$

where for the cross spectrum (i, j) , $\tilde{W}_{\ell}^{X_i X_j}$ is the power spectrum of the ‘‘window’’ function defined by the mask and weighting scheme

$$\tilde{W}_{\ell}^{X_i X_j} = \frac{1}{(2\ell + 1)} \sum_m \tilde{w}_{\ell m}^{X_i} \tilde{w}_{\ell m}^{X_j*}, \tag{A.3}$$

and X denotes the mode (either temperature T or polarization P).

A.2 Covariance matrices

CamSpec uses analytic approximations to the covariance matrices of the pseudo-spectra derived under the assumptions of narrow window functions and uncorrelated (but anisotropic) noise pixel noise $((\sigma_i^T)^2, (\sigma_i^Q)^2, (\sigma_i^U)^2)$ [21, 30, 31, 41]. The expressions are quite cumbersome, and so we give the expressions for only those covariance matrices used to form the TTTEEE

likelihoods. The following equations are based on the analytic formulae developed in [31, 41]:

$$\begin{aligned}
\langle \Delta \tilde{C}_\ell^{T_i T_j} \Delta \tilde{C}_{\ell'}^{T_p T_q} \rangle &\approx (\bar{C}_\ell^{T_i T_p} \bar{C}_{\ell'}^{T_i T_p} \bar{C}_\ell^{T_j T_q} \bar{C}_{\ell'}^{T_j T_q})^{1/2} \Xi_{TT}(\ell, \ell', \tilde{W}^{(ip)(jq)}) \\
&+ (\bar{C}_\ell^{T_i T_q} \bar{C}_{\ell'}^{T_i T_q} \bar{C}_\ell^{T_j T_p} \bar{C}_{\ell'}^{T_j T_p})^{1/2} \Xi_{TT}(\ell, \ell', \tilde{W}^{(iq)(jp)}) \\
&+ (\bar{C}_\ell^{T_j T_q} \bar{C}_{\ell'}^{T_j T_q})^{1/2} \Xi_{TT}(\ell, \ell', \tilde{W}^{2T(ip)(jq)}) \delta_{ip} \\
&+ (\bar{C}_\ell^{T_j T_p} \bar{C}_{\ell'}^{T_j T_p})^{1/2} \Xi_{TT}(\ell, \ell', \tilde{W}^{2T(iq)(jp)}) \delta_{iq} \\
&+ (\bar{C}_\ell^{T_i T_p} \bar{C}_{\ell'}^{T_i T_p})^{1/2} \Xi_{TT}(\ell, \ell', \tilde{W}^{2T(jq)(ip)}) \delta_{jq} \\
&+ (\bar{C}_\ell^{T_i T_q} \bar{C}_{\ell'}^{T_i T_q})^{1/2} \Xi_{TT}(\ell, \ell', \tilde{W}^{2T(jp)(iq)}) \delta_{jp} \\
&+ \Xi_{TT}(\ell, \ell', \tilde{W}^{TT(ip)(jq)}) \delta_{ip} \delta_{jq} + \Xi_{TT}(\ell, \ell', \tilde{W}^{TT(iq)(jp)}) \delta_{iq} \delta_{jp}, \quad (\text{A.4a})
\end{aligned}$$

$$\begin{aligned}
\langle \Delta \tilde{C}_\ell^{T_i E_j} \Delta \tilde{C}_{\ell'}^{T_p E_q} \rangle &\approx (\bar{C}_\ell^{T_i T_p} \bar{C}_{\ell'}^{T_i T_p} \bar{C}_\ell^{E_j E_q} \bar{C}_{\ell'}^{E_j E_q})^{1/2} \Xi_{TE}(\ell, \ell', \tilde{W}^{(ip)(jq)}) \\
&+ \bar{C}_\ell^{T_i E_q} \bar{C}_{\ell'}^{T_p E_j} \Xi_{TT}(\ell, \ell', \tilde{W}^{(iq)(jp)}) \\
&+ (\bar{C}_\ell^{T_i T_p} \bar{C}_{\ell'}^{T_i T_p})^{1/2} \Xi_{TE}(\ell, \ell', \tilde{W}^{2P(ip)(jq)}) \delta_{jq} \\
&+ (\bar{C}_\ell^{E_j E_q} \bar{C}_{\ell'}^{E_j E_q})^{1/2} \Xi_{TE}(\ell, \ell', \tilde{W}^{2T(jq)(ip)}) \delta_{ip} \\
&+ \Xi_{TE}(\ell, \ell', \tilde{W}^{TP(ip)(jq)}) \delta_{ip} \delta_{jq}, \quad (\text{A.4b})
\end{aligned}$$

$$\begin{aligned}
\langle \Delta \tilde{C}_\ell^{E_i E_j} \Delta \tilde{C}_{\ell'}^{E_p E_q} \rangle &\approx (\bar{C}_\ell^{E_i E_p} \bar{C}_{\ell'}^{E_i E_p} \bar{C}_\ell^{E_j E_q} \bar{C}_{\ell'}^{E_j E_q})^{1/2} \Xi_{EE}(\ell, \ell', \tilde{W}^{(ip)(jq)}) \\
&+ (\bar{C}_\ell^{E_i E_q} \bar{C}_{\ell'}^{E_i E_q} \bar{C}_\ell^{E_j E_p} \bar{C}_{\ell'}^{E_j E_p})^{1/2} \Xi_{EE}(\ell, \ell', \tilde{W}^{(iq)(jp)}) \\
&+ (\bar{C}_\ell^{E_j E_q} \bar{C}_{\ell'}^{E_j E_q})^{1/2} \Xi_{EE}(\ell, \ell', \tilde{W}^{2P(ip)(jq)}) \delta_{ip} \\
&+ (\bar{C}_\ell^{E_j E_p} \bar{C}_{\ell'}^{E_j E_p})^{1/2} \Xi_{EE}(\ell, \ell', \tilde{W}^{2P(iq)(jp)}) \delta_{iq} \\
&+ (\bar{C}_\ell^{E_i E_p} \bar{C}_{\ell'}^{E_i E_p})^{1/2} \Xi_{EE}(\ell, \ell', \tilde{W}^{2P(jq)(ip)}) \delta_{jq} \\
&+ (\bar{C}_\ell^{E_i E_q} \bar{C}_{\ell'}^{E_i E_q})^{1/2} \Xi_{EE}(\ell, \ell', \tilde{W}^{2P(jp)(ip)}) \delta_{jp} \\
&+ \Xi_{EE}(\ell, \ell', \tilde{W}^{PP(ip)(jq)}) \delta_{ip} \delta_{jq} + \Xi_{EE}(\ell, \ell', \tilde{W}^{PP(iq)(jp)}) \delta_{iq} \delta_{jp}, \quad (\text{A.4c})
\end{aligned}$$

$$\begin{aligned}
\langle \Delta \tilde{C}_\ell^{T_i T_j} \Delta \tilde{C}_{\ell'}^{T_p E_q} \rangle &\approx \frac{1}{2} (\bar{C}_\ell^{T_i T_p} \bar{C}_{\ell'}^{T_i T_p})^{1/2} (\bar{C}_\ell^{T_j E_q} + \bar{C}_{\ell'}^{T_j E_q}) \Xi_{TT}(\ell, \ell', \tilde{W}^{(ip)(jq)}) \\
&+ \frac{1}{2} (\bar{C}_\ell^{T_j T_p} \bar{C}_{\ell'}^{T_j T_p})^{1/2} (\bar{C}_\ell^{T_i E_q} + \bar{C}_{\ell'}^{T_i E_q}) \Xi_{TT}(\ell, \ell', \tilde{W}^{(jp)(iq)}) \\
&+ \frac{1}{2} (\bar{C}_\ell^{T_j E_q} + \bar{C}_{\ell'}^{T_j E_q}) \Xi_{TT}(\ell, \ell', \tilde{W}^{2T(ip)(jq)}) \delta_{ip} \\
&+ \frac{1}{2} (\bar{C}_\ell^{T_i E_q} + \bar{C}_{\ell'}^{T_i E_q}) \Xi_{TE}(\ell, \ell', \tilde{W}^{2T(jp)(iq)}) \delta_{jp}, \quad (\text{A.4d})
\end{aligned}$$

$$\begin{aligned}
\langle \Delta \tilde{C}_\ell^{E_i E_j} \Delta \tilde{C}_{\ell'}^{T_p E_q} \rangle &\approx \frac{1}{2} (\bar{C}_\ell^{E_j E_q} \bar{C}_{\ell'}^{E_j E_q} \ell')^{1/2} (C_\ell^{T_p E_i} + C_{\ell'}^{T_p E_i}) \Xi_{EE}(\ell, \ell', \tilde{W}^{(ip)(jq)}) \\
&+ \frac{1}{2} (\bar{C}_\ell^{E_i E_q} \bar{C}_{\ell'}^{E_i E_q} \ell')^{1/2} (\bar{C}_\ell^{T_p E_j} + \bar{C}_{\ell'}^{T_p E_j}) \Xi_{EE}(\ell, \ell', \tilde{W}^{(iq)(jp)}) \\
&+ \frac{1}{2} (\bar{C}_\ell^{T_p E_i} + \bar{C}_{\ell'}^{T_p E_i}) \Xi_{EE}(\ell, \ell', \tilde{W}^{2P(ip)(jq)}) \delta_{jq} \\
&+ \frac{1}{2} (\bar{C}_\ell^{T_p E_j} + \bar{C}_{\ell'}^{T_p E_j}) \Xi_{EE}(\ell, \ell', \tilde{W}^{2P(jp)(iq)}) \delta_{iq}, \quad (\text{A.4e})
\end{aligned}$$

$$\begin{aligned}
\langle \Delta \tilde{C}_\ell^{T_i T_j} \Delta \tilde{C}_{\ell'}^{E_p E_q} \rangle &\approx (\bar{C}_\ell^{T_i E_p} \bar{C}_{\ell'}^{T_j E_q}) \Xi_{TT}(\ell, \ell', \tilde{W}^{(ip)(jq)}) \\
&+ (\bar{C}_\ell^{T_i E_q} \bar{C}_{\ell'}^{T_j E_p}) \Xi_{TT}(\ell, \ell', \tilde{W}^{(iq)(jp)}), \quad (\text{A.4f})
\end{aligned}$$

where the matrices Ξ are defined in Eqs. (A.2a)-(A.2e), and the window functions are given by

$$\tilde{W}_\ell^{(ij)(pq)} = \frac{1}{(2\ell+1)} \sum_m \tilde{w}_{\ell m}^{(ij)} \tilde{w}_{\ell m}^{(pq)*}, \quad (\text{A.5a})$$

$$\tilde{W}_\ell^{TT(ij)(pq)} = \frac{1}{(2\ell+1)} \sum_m \tilde{w}_{\ell m}^{T(ij)} \tilde{w}_{\ell m}^{T(pq)*}, \quad (\text{A.5b})$$

$$\tilde{W}_\ell^{TP(ij)(pq)} = \frac{1}{(2\ell+1)} \sum_m \frac{1}{2} [\tilde{w}_{\ell m}^{T(ij)} \tilde{w}_{\ell m}^{Q(pq)*} + \tilde{w}_{\ell m}^{T(ij)} \tilde{w}_{\ell m}^{U(pq)*}], \quad (\text{A.5c})$$

$$\tilde{W}_\ell^{2T(ij)(pq)} = \frac{1}{(2\ell+1)} \sum_m \tilde{w}_{\ell m}^{(ij)} \tilde{w}_{\ell m}^{T(pq)*}, \quad (\text{A.5d})$$

$$\tilde{W}_\ell^{2P(ij)(pq)} = \frac{1}{(2\ell+1)} \sum_m \frac{1}{2} [\tilde{w}_{\ell m}^{(ij)} \tilde{w}_{\ell m}^{Q(pq)*} + \tilde{w}_{\ell m}^{(ij)} \tilde{w}_{\ell m}^{U(pq)*}], \quad (\text{A.5e})$$

$$\tilde{W}_\ell^{PP(ij)(pq)} = \frac{1}{(2\ell+1)} \sum_m \frac{1}{2} [\tilde{w}_{\ell m}^{Q(ij)} \tilde{w}_{\ell m}^{Q(pq)*} + \tilde{w}_{\ell m}^{U(ij)} \tilde{w}_{\ell m}^{U(pq)*}], \quad (\text{A.5f})$$

and

$$w_{\ell m}^{(ij)} = \sum_s w_s^i w_s^j \Omega_s Y_{\ell m}^*(\boldsymbol{\theta}_i), \quad (\text{A.6a})$$

$$w_{\ell m}^{T(ij)} = \sum_s (\sigma_s^T)^2 w_s^i w_s^j \Omega_s^2 Y_{\ell m}^*(\boldsymbol{\theta}_i), \quad (\text{A.6b})$$

$$w_{\ell m}^{Q(ij)} = \sum_s (\sigma_s^Q)^2 w_s^i w_s^j \Omega_s^2 Y_{\ell m}^*(\boldsymbol{\theta}_i), \quad (\text{A.6c})$$

$$w_{\ell m}^{U(ij)} = \sum_s (\sigma_s^U)^2 w_s^i w_s^j \Omega_s^2 Y_{\ell m}^*(\boldsymbol{\theta}_i). \quad (\text{A.6d})$$

where the sums in Eqs. refequ:A3a-equ:A3d run over the number of pixels.

As in PPL13, we adopt a heuristic approach to model non-white noise. We compute the noise spectra from odd-even difference maps as described in Sect. 5.1 which we fit to the functional form given in Eq. 5.4. This defines a set of weight factors:

$$\psi_\ell^X = \frac{N^{\text{fit}X}}{\bar{N}^X}, \quad (\text{A.7})$$

where $X = (T, Q, U)$ (each treated as a scalar map) and \bar{N}^X is the white noise spectrum given by a summation over the weighted pixels (Eq. 5.1). The pixel noise estimates $(\sigma^T)_i^2$, $(\sigma^Q)_i^2$ and $(\sigma^U)_i^2$ in Eqs. A.6b- A.6d are then replaced by $\psi_\ell^T (\sigma^T)_i^2$, $\psi_\ell^Q (\sigma^Q)_i^2$ and $\psi_\ell^U (\sigma^U)_i^2$, where $(\sigma^T)_i^2$, $(\sigma^Q)_i^2$ and $(\sigma^U)_i^2$ are the diagonal components of the pixel noise covariance matrix returned by the map making code. To keep data storage to manageable levels, we only store covariance matrix elements for $\Delta\ell = |\ell - \ell'| \leq 200$.

B Comparison with ACTpol and SPTpol

The TE and EE spectra measured by *Planck* are noisy and so have little statistical power at multipoles $\ell \gtrsim 1000$. At higher multipoles, the ground based measurements by ACTpol

[64] and SPTpol [43] have much higher sensitivity. These experiments have measured the TE and EE spectra with high precision up to multipoles of a few thousand, i.e. well into the CMB damping tail. The *Planck* base Λ CDM best-fit model is very well determined and makes accurate predictions of the polarization spectra at high multipoles. It is therefore worth asking whether this model is consistent with the results from ACTpol and SPTpol. Tests of the damping tail provide a particularly important check of extended Λ CDM models, including variants that could lead to a change in the sound horizon (e.g. [57, 58, 73]).

The purpose of this appendix is to show that it is not yet possible to perform such a comparison to high precision. This is illustrated by Fig. B.1 which compares the *Planck*, ACTpol and SPTpol spectra. We make the following observations:

[1] The overall agreement between *Planck*, ACTpol and SPTpol is extremely good, delineating the shapes of the acoustic peaks in both the TE and EE spectra out to multipoles of a few thousand. The fact that three independent investigations agree so well is a remarkable experimental achievement and provides strong support that the primordial fluctuations were dominated by adiabatic modes.

[2] In detail, however, we see that it is difficult to quantitatively test consistency of the spectra to high accuracy. Over the multipole range where *Planck* errors are small, the errors on the ACTpol and SPTpol spectra are large (and vice versa). This means that it is not possible to determine accurate polarization calibrations for ACTpol and SPTpol relative to *Planck* by comparing the power spectra. Without accurate relative calibrations in polarization, one cannot easily stitch together *Planck*, ACTpol and SPTpol polarization spectra to test theoretical predictions well into the CMB damping tail. If one tries to do this for base Λ CDM by allowing relative calibrations to vary as nuisance parameters in, say, a joint *Planck*+SPTpol likelihood analysis, *Planck* overwhelms SPTpol and the recovered cosmology is almost identical to that derived from *Planck* alone [61].

[3] Since the ACTpol and SPTpol TE and EE errors are large compared to those from *Planck* at multipoles $\ell \lesssim 1500$, the base Λ CDM cosmological parameter constraints determined from ACTpol and SPTpol are much weaker than those determined from *Planck*. The ground based experiments do not cover a wide enough range of multipoles to strongly constrain critical parameters such as n_s . The base Λ CDM parameters from both ACTpol and SPTpol are consistent with those determined by *Planck*, though [43] report hints of parameter shifts at high multipoles at low statistical significance. The analysis discussed in PCP18 (based on work reported in [61]) shows that the SPTpol base Λ CDM TEEE parameters converge by $\ell_{\max} = 2500$, so any parameter shifts are driven by the SPTpol spectra in the multipole range $\sim 1000 - 2500$, not by higher multipoles.

[4] ACTpol and SPTpol calibrate temperature at the map level by cross-correlating against *Planck* 143 GHz temperature maps. ACTpol then cross-correlate with the 2015 143 GHz *Planck* Q and U maps³⁵ and infer a polarization efficiency of 0.990 ± 0.025 (which is not corrected for in the ACTpol spectra shown in Fig. B.1). The laboratory study of [113] measured polarization efficiencies for the 143 GHz detectors in the range 84–94%, significantly lower than the efficiencies of detectors at other frequencies. These laboratory values are assumed in the *Planck* HFI map making. However, from the discussion in Sect. 6.3 we infer an effective polarization efficiency for the 143 GHz Q and U maps of 1.015 based on the EE spectra and 1.007 based on the TE spectra. Averaging these estimates gives an effective

³⁵Note that the inferred effective polarization efficiencies of the 2015 *Planck* maps are very close to those of the 2018 maps discussed in Sect. 6.3.

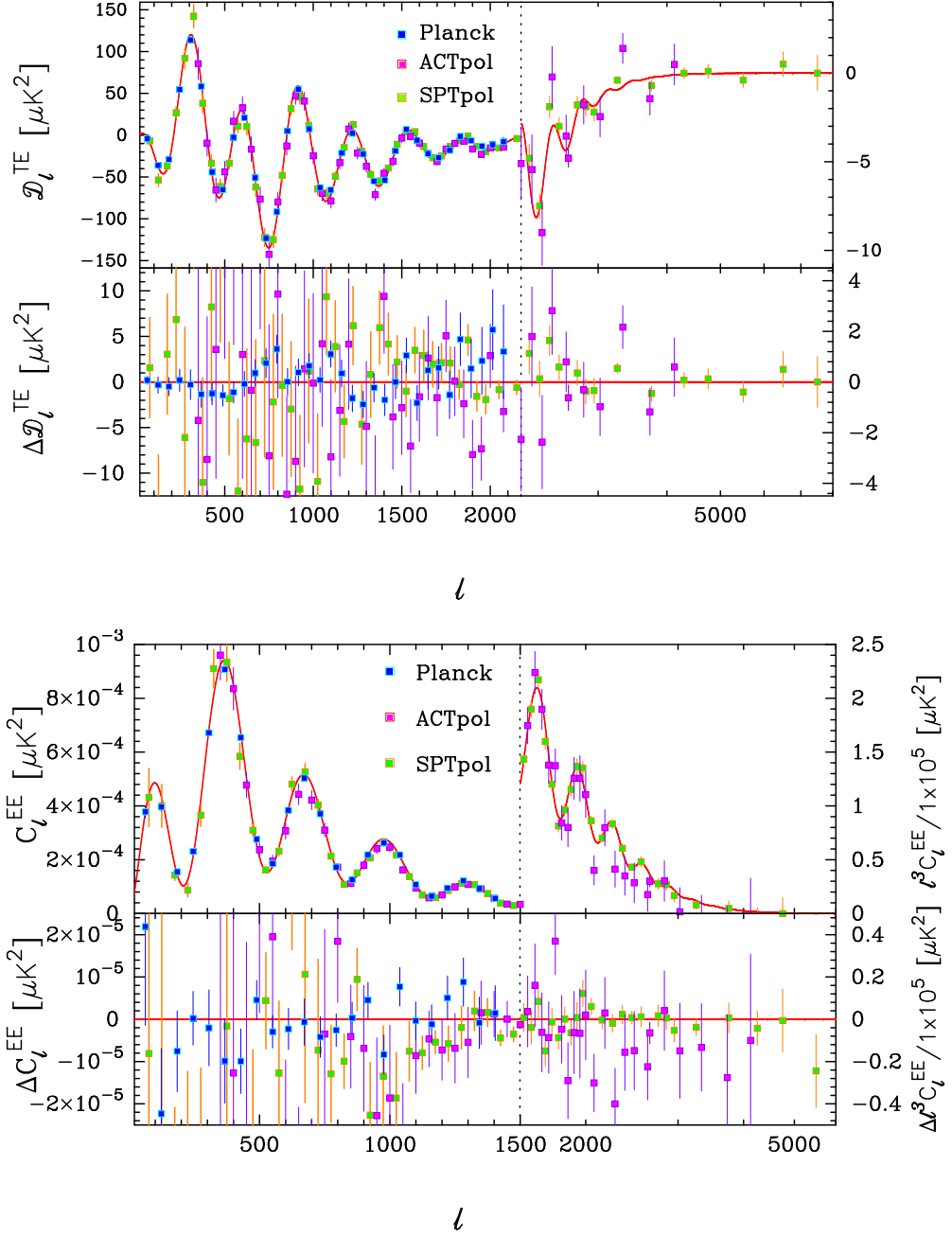


Figure B.1. The 12.5HMcl TE and EE spectra (blue points) compared to the ACTpol and SPTpol spectra. The red line shows the 12.5HMcl TTTEEE best-fit base Λ CDM cosmology. Each plot is split into four panels, with the left-hand panels showing the low multipoles on a linear multipole scale, and the right-hand panels showing the high multipoles on a logarithmic scale. The lower panels in each plot show the residuals relative to the best fit-base Λ CDM model. In the lower figure, showing the EE spectra, we have plotted $\ell^3 C_l^{\text{EE}}$, and its residuals, at high multipoles to emphasise the the shape of the damping tail.

polarization efficiency of *Planck* 143 GHz Q and U maps of 1.011 with an uncertainty of about 0.005. This would bring the ACTpol polarization efficiency closer to unity. Polarization efficiencies 1.011 cannot, however, explain the run of low ACTpol EE points at $\ell \gtrsim 2000$ seen in Fig. B.1 (which may indicate that the contribution from polarized point sources has been over subtracted in the analysis of [64]). SPTpol cross-correlated their polarization maps with the 2015 *Planck* 143 GHz polarization maps and inferred an effective polarization efficiency of 1.06 ± 0.01 . This is higher than expected from their polarization calibration measurements using an external polarized source [23, 53] for reasons that are not yet understood. The polarization efficiency of 1.06 was applied to the published SPTpol TE and EE bandpowers plotted in Fig. B.1. With this factor applied, the SPTpol spectra provide a very good match to the damping tail of our best fit base Λ CDM model.

The key point that we wish to make is that the effective polarization efficiencies of the publically available *Planck* polarization maps differ from unity. This needs to be borne in mind if these maps are used to calibrate other experiments. Uncertainties in polarization efficiencies therefore limit the precision with which the *Planck* polarization power spectra can be ‘stitched’ to ground-based polarization power spectra extending to higher multipoles. The best way of achieving high precision tests of cosmology with ground-based polarization experiments is to make them self-contained by increasing the multipole range, i.e. to improve the accuracy of the polarization spectra at multipoles $\lesssim 2000$ as well as at higher multipoles.

References

- [1] A. Achúcarro, R. Kallosh, A. Linde, D.-G. Wang, and Y. Welling. Universality of multi-field α -attractors. *J. Cosmology Astropart. Phys.*, 4:028, April 2018.
- [2] G. E. Addison, J. Dunkley, and D. N. Spergel. Modelling the correlation between the thermal Sunyaev Zel’dovich effect and the cosmic infrared background. *MNRAS*, 427:1741–1754, December 2012.
- [3] G. E. Addison, Y. Huang, D. J. Watts, C. L. Bennett, M. Halpern, G. Hinshaw, and J. L. Weiland. Quantifying Discordance in the 2015 Planck CMB Spectrum. *ApJ*, 818:132, February 2016.
- [4] P. Ade, J. Aguirre, Z. Ahmed, S. Aiola, A. Ali, D. Alonso, M. A. Alvarez, K. Arnold, P. Ashton, J. Austermann, and et al. The Simons Observatory: science goals and forecasts. *J. Cosmology Astropart. Phys.*, 2:056, February 2019.
- [5] Y. Akrami, R. Kallosh, A. Linde, and V. Vardanyan. Dark energy, α -attractors, and large-scale structure surveys. *J. Cosmology Astropart. Phys.*, 6:041, June 2018.
- [6] S. Alam, M. Ata, S. Bailey, F. Beutler, D. Bizyaev, J. A. Blazek, A. S. Bolton, J. R. Brownstein, A. Burden, C.-H. Chuang, J. Comparat, A. J. Cuesta, K. S. Dawson, D. J. Eisenstein, S. Escoffier, H. Gil-Marín, J. N. Grieb, N. Hand, S. Ho, K. Kinemuchi, D. Kirkby, F. Kitaura, E. Malanushenko, V. Malanushenko, C. Maraston, C. K. McBride, R. C. Nichol, M. D. Olmstead, D. Oravetz, N. Padmanabhan, N. Palanque-Delabrouille, K. Pan, M. Pellejero-Ibanez, W. J. Percival, P. Petitjean, F. Prada, A. M. Price-Whelan, B. A. Reid, S. A. Rodríguez-Torres, N. A. Roe, A. J. Ross, N. P. Ross, G. Rossi, J. A. Rubiño-Martín, S. Saito, S. Salazar-Albornoz, L. Samushia, A. G. Sánchez, S. Satpathy, D. J. Schlegel, D. P. Schneider, C. G. Scóccola, H.-J. Seo, E. S. Sheldon, A. Simmons, A. Slosar, M. A. Strauss, M. E. C. Swanson, D. Thomas, J. L. Tinker, R. Tojeiro, M. V. Magaña, J. A. Vazquez, L. Verde, D. A. Wake, Y. Wang, D. H. Weinberg, M. White, W. M. Wood-Vasey, C. Yèche, I. Zehavi, Z. Zhai, and G.-B. Zhao. The clustering of galaxies in the completed SDSS-III Baryon Oscillation Spectroscopic Survey: cosmological analysis of the DR12 galaxy sample. *MNRAS*, 470:2617–2652, September 2017.

- [7] Marika Asgari, Tilman Tröster, Catherine Heymans, Hendrik Hildebrandt, Jan Luca van den Busch, Angus H. Wright, Ami Choi, Thomas Erben, Benjamin Joachimi, Shahab Joudaki, Arun Kannawadi, Konrad Kuijken, Chieh-An Lin, Peter Schneider, and Joe Zuntz. KiDS+VIKING-450 and DES-Y1 combined: Mitigating baryon feedback uncertainty with COSEBIs. *A&A*, 634:A127, February 2020.
- [8] É. Aubourg, S. Bailey, J. E. Bautista, F. Beutler, V. Bhardwaj, D. Bizyaev, M. Blanton, M. Blomqvist, A. S. Bolton, J. Bovy, H. Brewington, J. Brinkmann, J. R. Brownstein, A. Burden, N. G. Busca, W. Carithers, C.-H. Chuang, J. Comparat, R. A. C. Croft, A. J. Cuesta, K. S. Dawson, T. Delubac, D. J. Eisenstein, A. Font-Ribera, J. Ge, J.-M. Le Goff, S. G. A. Gontcho, J. R. Gott, J. E. Gunn, H. Guo, J. Guy, J.-C. Hamilton, S. Ho, K. Honscheid, C. Howlett, D. Kirkby, F. S. Kitaura, J.-P. Kneib, K.-G. Lee, D. Long, R. H. Lupton, M. V. Magaña, V. Malanushenko, E. Malanushenko, M. Manera, C. Maraston, D. Margala, C. K. McBride, J. Miralda-Escudé, A. D. Myers, R. C. Nichol, P. Noterdaeme, S. E. Nuza, M. D. Olmstead, D. Oravetz, I. Pâris, N. Padmanabhan, N. Palanque-Delabrouille, K. Pan, M. Pellejero-Ibanez, W. J. Percival, P. Petitjean, M. M. Pieri, F. Prada, B. Reid, J. Rich, N. A. Roe, A. J. Ross, N. P. Ross, G. Rossi, J. A. Rubiño-Martín, A. G. Sánchez, L. Samushia, R. T. Génova-Santos, C. G. Scóccola, D. J. Schlegel, D. P. Schneider, H.-J. Seo, E. Sheldon, A. Simmons, R. A. Skibba, A. Slosar, M. A. Strauss, D. Thomas, J. L. Tinker, R. Tojeiro, J. A. Vazquez, M. Viel, D. A. Wake, B. A. Weaver, D. H. Weinberg, W. M. Wood-Vasey, C. Yèche, I. Zehavi, G.-B. Zhao, and BOSS Collaboration. Cosmological implications of baryon acoustic oscillation measurements. *Phys. Rev. D*, 92(12):123516, December 2015.
- [9] N. Battaglia, J. R. Bond, C. Pfrommer, J. L. Sievers, and D. Sijacki. Simulations of the Sunyaev-Zel'dovich Power Spectrum with Active Galactic Nucleus Feedback. *ApJ*, 725:91–99, December 2010.
- [10] C. L. Bennett, M. Halpern, G. Hinshaw, N. Jarosik, A. Kogut, M. Limon, S. S. Meyer, L. Page, D. N. Spergel, G. S. Tucker, E. Wollack, E. L. Wright, C. Barnes, M. R. Greason, R. S. Hill, E. Komatsu, M. R. Nolte, N. Odegard, H. V. Peiris, L. Verde, and J. L. Weiland. First-Year Wilkinson Microwave Anisotropy Probe (WMAP) Observations: Preliminary Maps and Basic Results. *ApJS*, 148:1–27, September 2003.
- [11] C. L. Bennett, D. Larson, J. L. Weiland, N. Jarosik, G. Hinshaw, N. Odegard, K. M. Smith, R. S. Hill, B. Gold, M. Halpern, E. Komatsu, M. R. Nolte, L. Page, D. N. Spergel, E. Wollack, J. Dunkley, A. Kogut, M. Limon, S. S. Meyer, G. S. Tucker, and E. L. Wright. Nine-year Wilkinson Microwave Anisotropy Probe (WMAP) Observations: Final Maps and Results. *ApJS*, 208:20, October 2013.
- [12] J. L. Bernal, L. Verde, and A. G. Riess. The trouble with H_0 . *J. Cosmology Astropart. Phys.*, 10:019, October 2016.
- [13] F. Beutler, C. Blake, M. Colless, D. H. Jones, L. Staveley-Smith, L. Campbell, Q. Parker, W. Saunders, and F. Watson. The 6dF Galaxy Survey: baryon acoustic oscillations and the local Hubble constant. *MNRAS*, 416:3017–3032, October 2011.
- [14] BICEP2 Collaboration, P. A. R. Ade, R. W. Aikin, D. Barkats, S. J. Benton, C. A. Bischoff, J. J. Bock, J. A. Brevik, I. Buder, E. Bullock, C. D. Dowell, L. Duband, J. P. Filippini, S. Fliescher, S. R. Golwala, M. Halpern, M. Hasselfield, S. R. Hildebrandt, G. C. Hilton, V. V. Hristov, K. D. Irwin, K. S. Karkare, J. P. Kaufman, B. G. Keating, S. A. Kernasovskiy, J. M. Kovac, C. L. Kuo, E. M. Leitch, M. Lueker, P. Mason, C. B. Netterfield, H. T. Nguyen, R. O’Brien, R. W. Ogburn, A. Orlando, C. Pryke, C. D. Reintsema, S. Richter, R. Schwarz, C. D. Sheehy, Z. K. Staniszewski, R. V. Sudiwala, G. P. Teply, J. E. Tolan, A. D. Turner, A. G. Vieregg, C. L. Wong, and K. W. Yoon. Detection of B-Mode Polarization at Degree Angular Scales by BICEP2. *Physical Review Letters*, 112(24):241101, June 2014.
- [15] BICEP2 Collaboration, Keck Array Collaboration, P. A. R. Ade, Z. Ahmed, R. W. Aikin,

- K. D. Alexander, D. Barkats, S. J. Benton, C. A. Bischoff, J. J. Bock, R. Bowens-Rubin, J. A. Brevik, I. Buder, E. Bullock, V. Buza, J. Connors, J. Cornelison, B. P. Crill, M. Crumrine, M. Dierickx, L. Duband, C. Dvorkin, J. P. Filippini, S. Fliescher, J. Grayson, G. Hall, M. Halpern, S. Harrison, S. R. Hildebrandt, G. C. Hilton, H. Hui, K. D. Irwin, J. Kang, K. S. Karkare, E. Karpel, J. P. Kaufman, B. G. Keating, S. Kefeli, S. A. Kernasovskiy, J. M. Kovac, C. L. Kuo, N. A. Larsen, K. Lau, E. M. Leitch, M. Lueker, K. G. Megerian, L. Moncelsi, T. Namikawa, C. B. Netterfield, H. T. Nguyen, R. O’Brien, R. W. Ogburn, S. Palladino, C. Pryke, B. Racine, S. Richter, A. Schillaci, R. Schwarz, C. D. Sheehy, A. Soliman, T. St. Germaine, Z. K. Staniszewski, B. Steinbach, R. V. Sudiwala, G. P. Teply, K. L. Thompson, J. E. Tolan, C. Tucker, A. D. Turner, C. Umiltà, A. G. Vieregg, A. Wandui, A. C. Weber, D. V. Wiebe, J. Willmert, C. L. Wong, W. L. K. Wu, H. Yang, K. W. Yoon, and C. Zhang. Constraints on Primordial Gravitational Waves Using Planck, WMAP, and New BICEP2/Keck Observations through the 2015 Season. *Physical Review Letters*, 121(22):221301, November 2018.
- [16] BICEP2 Collaboration, Keck Array Collaboration, P. A. R. Ade, Z. Ahmed, R. W. Aikin, K. D. Alexander, D. Barkats, S. J. Benton, C. A. Bischoff, J. J. Bock, R. Bowens-Rubin, J. A. Brevik, I. Buder, E. Bullock, V. Buza, J. Connors, B. P. Crill, L. Duband, C. Dvorkin, J. P. Filippini, S. Fliescher, J. Grayson, M. Halpern, S. Harrison, G. C. Hilton, H. Hui, K. D. Irwin, K. S. Karkare, E. Karpel, J. P. Kaufman, B. G. Keating, S. Kefeli, S. A. Kernasovskiy, J. M. Kovac, C. L. Kuo, E. M. Leitch, M. Lueker, K. G. Megerian, C. B. Netterfield, H. T. Nguyen, R. O’Brien, R. W. Ogburn, A. Orlando, C. Pryke, S. Richter, R. Schwarz, C. D. Sheehy, Z. K. Staniszewski, B. Steinbach, R. V. Sudiwala, G. P. Teply, K. L. Thompson, J. E. Tolan, C. Tucker, A. D. Turner, A. G. Vieregg, A. C. Weber, D. V. Wiebe, J. Willmert, C. L. Wong, W. L. K. Wu, and K. W. Yoon. Improved Constraints on Cosmology and Foregrounds from BICEP2 and Keck Array Cosmic Microwave Background Data with Inclusion of 95 GHz Band. *Physical Review Letters*, 116(3):031302, January 2016.
- [17] BICEP2/Keck Collaboration, Planck Collaboration, P. A. R. Ade, N. Aghanim, Z. Ahmed, R. W. Aikin, K. D. Alexander, M. Arnaud, J. Aumont, C. Baccigalupi, and et al. Joint Analysis of BICEP2/Keck Array and Planck Data. *Physical Review Letters*, 114(10):101301, March 2015.
- [18] S. Birrer, T. Treu, C. E. Rusu, V. Bonvin, C. D. Fassnacht, J. H. H. Chan, A. Agnello, A. J. Shajib, G. C.-F. Chen, M. Auger, F. Courbin, S. Hilbert, D. Sluse, S. H. Suyu, K. C. Wong, P. Marshall, B. C. Lemaux, and G. Meylan. H0LiCOW - IX. Cosmographic analysis of the doubly imaged quasar SDSS 1206+4332 and a new measurement of the Hubble constant. *MNRAS*, 484:4726–4753, April 2019.
- [19] J. R. Bond, G. Efstathiou, and M. Tegmark. Forecasting cosmic parameter errors from microwave background anisotropy experiments. *MNRAS*, 291:L33–L41, November 1997.
- [20] J.-F. Cardoso, M. Martin, J. Delabrouille, M. Betoule, and G. Patanchon. Component separation with flexible models. Application to the separation of astrophysical emissions. *arXiv e-prints*, March 2008.
- [21] A. Challinor and G. Chon. Error analysis of quadratic power spectrum estimates for cosmic microwave background polarization: sampling covariance. *MNRAS*, 360:509–532, June 2005.
- [22] X. Chen and M. H. Namjoo. Standard Clock in primordial density perturbations and cosmic microwave background. *Physics Letters B*, 739:285–292, December 2014.
- [23] A. T. Crites, J. W. Henning, P. A. R. Ade, K. A. Aird, J. E. Austermann, J. A. Beall, A. N. Bender, B. A. Benson, L. E. Bleem, J. E. Carlstrom, C. L. Chang, H. C. Chiang, H.-M. Cho, R. Citron, T. M. Crawford, T. de Haan, M. A. Dobbs, W. Everett, J. Gallicchio, J. Gao, E. M. George, A. Gilbert, N. W. Halverson, D. Hanson, N. Harrington, G. C. Hilton, G. P. Holder, W. L. Holzapfel, S. Hoover, Z. Hou, J. D. Hrubes, N. Huang, J. Hubmayr, K. D. Irwin, R. Keisler, L. Knox, A. T. Lee, E. M. Leitch, D. Li, C. Liang, D. Luong-Van, J. J.

- McMahon, J. Mehl, S. S. Meyer, L. Mocanu, T. E. Montroy, T. Natoli, J. P. Nibarger, V. Novosad, S. Padin, C. Pryke, C. L. Reichardt, J. E. Ruhl, B. R. Saliwanchik, J. T. Sayre, K. K. Schaffer, G. Smecher, A. A. Stark, K. T. Story, C. Tucker, K. Vanderlinde, J. D. Vieira, G. Wang, N. Whitehorn, V. Yefremenko, and O. Zahn. Measurements of E-Mode Polarization and Temperature-E-Mode Correlation in the Cosmic Microwave Background from 100 Square Degrees of SPTpol Data. *ApJ*, 805:36, May 2015.
- [24] A. J. Cuesta, L. Verde, A. Riess, and R. Jimenez. Calibrating the cosmic distance scale ladder: the role of the sound-horizon scale and the local expansion rate as distance anchors. *MNRAS*, 448:3463–3471, April 2015.
- [25] J. Delabrouille, J.-F. Cardoso, M. Le Jeune, M. Betoule, G. Fay, and F. Guilloux. A full sky, low foreground, high resolution CMB map from WMAP. *A&A*, 493:835–857, January 2009.
- [26] J.-M. Delouis, L. Pagano, S. Mottet, J.-L. Puget, and L. Vibert. SRoll2: an improved mapmaking approach to reduce large-scale systematic effects in the Planck High Frequency Instrument legacy maps. *arXiv e-prints*, January 2019.
- [27] Eleonora Di Valentino, Alessandro Melchiorri, and Joseph Silk. Planck evidence for a closed Universe and a possible crisis for cosmology. *Nature Astronomy*, page 484, Nov 2019.
- [28] Eleonora Di Valentino, Alessandro Melchiorri, and Joseph Silk. Cosmic Discordance: Planck and luminosity distance data exclude LCDM. *arXiv e-prints*, page arXiv:2003.04935, March 2020.
- [29] J. Dunkley, R. Hlozek, J. Sievers, V. Acquaviva, P. A. R. Ade, P. Aguirre, M. Amiri, J. W. Appel, L. F. Barrientos, E. S. Battistelli, J. R. Bond, B. Brown, B. Burger, J. Chervenak, S. Das, M. J. Devlin, S. R. Dicker, W. Bertrand Doriese, R. Dünner, T. Essinger-Hileman, R. P. Fisher, J. W. Fowler, A. Hajian, M. Halpern, M. Hasselfield, C. Hernández-Monteagudo, G. C. Hilton, M. Hilton, A. D. Hincks, K. M. Huffenberger, D. H. Hughes, J. P. Hughes, L. Infante, K. D. Irwin, J. B. Juin, M. Kaul, J. Klein, A. Kosowsky, J. M. Lau, M. Limon, Y.-T. Lin, R. H. Lupton, T. A. Marriage, D. Marsden, P. Mauskopf, F. Menanteau, K. Moodley, H. Moseley, C. B. Netterfield, M. D. Niemack, M. R. Nolta, L. A. Page, L. Parker, B. Partridge, B. Reid, N. Sehgal, B. Sherwin, D. N. Spergel, S. T. Staggs, D. S. Swetz, E. R. Switzer, R. Thornton, H. Trac, C. Tucker, R. Warne, E. Wollack, and Y. Zhao. The Atacama Cosmology Telescope: Cosmological Parameters from the 2008 Power Spectrum. *ApJ*, 739:52, September 2011.
- [30] G. Efstathiou. A maximum likelihood analysis of the low cosmic microwave background multipoles from the Wilkinson Microwave Anisotropy Probe. *MNRAS*, 348:885–896, March 2004.
- [31] G. Efstathiou. Hybrid estimation of cosmic microwave background polarization power spectra. *MNRAS*, 370:343–362, July 2006.
- [32] G. Efstathiou and S. Gratton. Approximate maximum-likelihood cross-spectrum estimates and likelihoods. *Planck Internal Communication*, 2014.
- [33] G. Efstathiou and M. Migliaccio. A simple empirically motivated template for the thermal Sunyaev-Zel’dovich effect. *MNRAS*, 423:2492–2497, July 2012.
- [34] George Efstathiou and Steven Gratton. The evidence for a spatially flat Universe. *arXiv e-prints*, page arXiv:2002.06892, February 2020.
- [35] H. K. Eriksen, C. Dickinson, C. R. Lawrence, C. Baccigalupi, A. J. Banday, K. M. Górski, F. K. Hansen, P. B. Lilje, E. Pierpaoli, M. D. Seiffert, K. M. Smith, and K. Vanderlinde. Cosmic Microwave Background Component Separation by Parameter Estimation. *ApJ*, 641:665–682, April 2006.
- [36] H. K. Eriksen, J. B. Jewell, C. Dickinson, A. J. Banday, K. M. Górski, and C. R. Lawrence.

Joint Bayesian Component Separation and CMB Power Spectrum Estimation. *ApJ*, 676:10–32, March 2008.

- [37] R. Fernández-Cobos, P. Vielva, R. B. Barreiro, and E. Martínez-González. Multiresolution internal template cleaning: an application to the Wilkinson Microwave Anisotropy Probe 7-yr polarization data. *MNRAS*, 420:2162–2169, March 2012.
- [38] D. P. Finkbeiner, M. Davis, and D. J. Schlegel. Extrapolation of Galactic Dust Emission at 100 Microns to Cosmic Microwave Background Radiation Frequencies Using FIRAS. *ApJ*, 524:867–886, October 1999.
- [39] E. M. George, C. L. Reichardt, K. A. Aird, B. A. Benson, L. E. Bleem, J. E. Carlstrom, C. L. Chang, H.-M. Cho, T. M. Crawford, A. T. Crites, T. de Haan, M. A. Dobbs, J. Dudley, N. W. Halverson, N. L. Harrington, G. P. Holder, W. L. Holzapfel, Z. Hou, J. D. Hrubes, R. Keisler, L. Knox, A. T. Lee, E. M. Leitch, M. Lueker, D. Luong-Van, J. J. McMahon, J. Mehl, S. S. Meyer, M. Millea, L. M. Mocanu, J. J. Mohr, T. E. Montroy, S. Padin, T. Plagge, C. Pryke, J. E. Ruhl, K. K. Schaffer, L. Shaw, E. Shirokoff, H. G. Spieler, Z. Staniszewski, A. A. Stark, K. T. Story, A. van Engelen, K. Vanderlinde, J. D. Vieira, R. Williamson, and O. Zahn. A Measurement of Secondary Cosmic Microwave Background Anisotropies from the 2500 Square-degree SPT-SZ Survey. *ApJ*, 799:177, February 2015.
- [40] K. M. Górski, E. Hivon, A. J. Banday, B. D. Wandelt, F. K. Hansen, M. Reinecke, and M. Bartelmann. HEALPix: A Framework for High-Resolution Discretization and Fast Analysis of Data Distributed on the Sphere. *ApJ*, 622:759–771, April 2005.
- [41] S. Hamimeche and A. Lewis. Likelihood analysis of CMB temperature and polarization power spectra. *Phys. Rev. D*, 77(10):103013, May 2008.
- [42] Will Handley. Curvature tension: evidence for a closed universe. *arXiv e-prints*, page arXiv:1908.09139, Aug 2019.
- [43] J. W. Henning, J. T. Sayre, C. L. Reichardt, P. A. R. Ade, A. J. Anderson, J. E. Austermann, J. A. Beall, A. N. Bender, B. A. Benson, L. E. Bleem, J. E. Carlstrom, C. L. Chang, H. C. Chiang, H.-M. Cho, R. Citron, C. Corbett Moran, T. M. Crawford, A. T. Crites, T. de Haan, M. A. Dobbs, W. Everett, J. Gallicchio, E. M. George, A. Gilbert, N. W. Halverson, N. Harrington, G. C. Hilton, G. P. Holder, W. L. Holzapfel, S. Hoover, Z. Hou, J. D. Hrubes, N. Huang, J. Hubmayr, K. D. Irwin, R. Keisler, L. Knox, A. T. Lee, E. M. Leitch, D. Li, A. Lowitz, A. Manzotti, J. J. McMahon, S. S. Meyer, L. Mocanu, J. Montgomery, A. Nadolski, T. Natoli, J. P. Nibarger, V. Novosad, S. Padin, C. Pryke, J. E. Ruhl, B. R. Saliwanchik, K. K. Schaffer, C. Sievers, G. Smecher, A. A. Stark, K. T. Story, C. Tucker, K. Vanderlinde, T. Veach, J. D. Vieira, G. Wang, N. Whitehorn, W. L. K. Wu, and V. Yefremenko. Measurements of the Temperature and E-mode Polarization of the CMB from 500 Square Degrees of SPTpol Data. *ApJ*, 852:97, January 2018.
- [44] C. Hikage, M. Oguri, T. Hamana, S. More, R. Mandelbaum, M. Takada, F. Köhlinger, H. Miyatake, A. J. Nishizawa, H. Aihara, R. Armstrong, J. Bosch, J. Coupon, A. Ducout, P. Ho, B.-C. Hsieh, Y. Komiyama, F. Lanusse, A. Leauthaud, R. H. Lupton, E. Medezinski, S. Mineo, S. Miyama, S. Miyazaki, R. Murata, H. Murayama, M. Shirasaki, C. Sifón, M. Simet, J. Speagle, D. N. Spergel, M. A. Strauss, N. Sugiyama, M. Tanaka, Y. Utsumi, S.-Y. Wang, and Y. Yamada. Cosmology from cosmic shear power spectra with Subaru Hyper Suprime-Cam first-year data. *arXiv e-prints*, September 2018.
- [45] H. Hildebrandt, F. Köhlinger, J. L. van den Busch, B. Joachimi, C. Heymans, A. Kannawadi, A. H. Wright, M. Asgari, C. Blake, H. Hoekstra, S. Joudaki, K. Kuijken, L. Miller, C. B. Morrison, T. Tröster, A. Amon, M. Archidiacono, S. Brieden, A. Choi, J. T. A. de Jong, T. Erben, B. Giblin, A. Mead, J. A. Peacock, M. Radovich, P. Schneider, C. Sifón, and M. Tewes. KiDS+VIKING-450: Cosmic shear tomography with optical+infrared data. *arXiv e-prints*, December 2018.

- [46] H. Hildebrandt, M. Viola, C. Heymans, S. Joudaki, K. Kuijken, C. Blake, T. Erben, B. Joachimi, D. Klaes, L. Miller, C. B. Morrison, R. Nakajima, G. Verdoes Kleijn, A. Amon, A. Choi, G. Covone, J. T. A. de Jong, A. Dvornik, I. Fenech Conti, A. Grado, J. Harnois-Déraps, R. Herbonnet, H. Hoekstra, F. Köhlinger, J. McFarland, A. Mead, J. Merten, N. Napolitano, J. A. Peacock, M. Radovich, P. Schneider, P. Simon, E. A. Valentijn, J. L. van den Busch, E. van Uitert, and L. Van Waerbeke. KiDS-450: cosmological parameter constraints from tomographic weak gravitational lensing. *MNRAS*, 465:1454–1498, February 2017.
- [47] E. Hivon, A. Ducout, S. Mottet, and G. Roudier. QuickPol: beam leakage and polarization. *Planck Internal Communication*, 2015.
- [48] E. Hivon, K. M. Górski, C. B. Netterfield, B. P. Crill, S. Prunet, and F. Hansen. MASTER of the Cosmic Microwave Background Anisotropy Power Spectrum: A Fast Method for Statistical Analysis of Large and Complex Cosmic Microwave Background Data Sets. *ApJ*, 567:2–17, March 2002.
- [49] E. Hivon, S. Mottet, and N. Ponthieu. QuickPol: Fast calculation of effective beam matrices for CMB polarization. *A&A*, 598:A25, February 2017.
- [50] Y. Huang, G. E. Addison, J. L. Weiland, and C. L. Bennett. Assessing Consistency between WMAP 9 Year and Planck 2015 Temperature Power Spectra. *ApJ*, 869:38, December 2018.
- [51] R. Kallosh, A. Linde, D. Roest, A. Westphal, and Y. Yamada. Fibre inflation and α -attractors. *Journal of High Energy Physics*, 2:117, February 2018.
- [52] M. Kamionkowski, A. Kosowsky, and A. Stebbins. Statistics of cosmic microwave background polarization. *Phys. Rev. D*, 55:7368–7388, June 1997.
- [53] R. Keisler, S. Hoover, N. Harrington, J. W. Henning, P. A. R. Ade, K. A. Aird, J. E. Austermann, J. A. Beall, A. N. Bender, B. A. Benson, L. E. Bleem, J. E. Carlstrom, C. L. Chang, H. C. Chiang, H.-M. Cho, R. Citron, T. M. Crawford, A. T. Crites, T. de Haan, M. A. Dobbs, W. Everett, J. Gallicchio, J. Gao, E. M. George, A. Gilbert, N. W. Halverson, D. Hanson, G. C. Hilton, G. P. Holder, W. L. Holzapfel, Z. Hou, J. D. Hrubes, N. Huang, J. Hubmayr, K. D. Irwin, L. Knox, A. T. Lee, E. M. Leitch, D. Li, D. Luong-Van, D. P. Marrone, J. J. McMahon, J. Mehl, S. S. Meyer, L. Mocuano, T. Natoli, J. P. Nibarger, V. Novosad, S. Padin, C. Pryke, C. L. Reichardt, J. E. Ruhl, B. R. Saliwanchik, J. T. Sayre, K. K. Schaffer, E. Shirokoff, G. Smecher, A. A. Stark, K. T. Story, C. Tucker, K. Vanderlinde, J. D. Vieira, G. Wang, N. Whitehorn, V. Yefremenko, and O. Zahn. Measurements of Sub-degree B-mode Polarization in the Cosmic Microwave Background from 100 Square Degrees of SPTpol Data. *ApJ*, 807:151, July 2015.
- [54] L. Knox and M. S. Turner. Detectability of tensor perturbations through anisotropy of the cosmic background radiation. *Physical Review Letters*, 73:3347–3350, December 1994.
- [55] Lloyd Knox and Marius Millea. The Hubble Hunter’s Guide. *arXiv e-prints*, page arXiv:1908.03663, Aug 2019.
- [56] A. Kogut, D. N. Spergel, C. Barnes, C. L. Bennett, M. Halpern, G. Hinshaw, N. Jarosik, M. Limon, S. S. Meyer, L. Page, G. S. Tucker, E. Wollack, and E. L. Wright. First-Year Wilkinson Microwave Anisotropy Probe (WMAP) Observations: Temperature-Polarization Correlation. *ApJS*, 148:161–173, September 2003.
- [57] C. D. Kreisch, F.-Y. Cyr-Racine, and O. Doré. The Neutrino Puzzle: Anomalies, Interactions, and Cosmological Tensions. *arXiv e-prints*, February 2019.
- [58] L. Lancaster, F.-Y. Cyr-Racine, L. Knox, and Z. Pan. A tale of two modes: neutrino free-streaming in the early universe. *J. Cosmology Astropart. Phys.*, 7:033, July 2017.
- [59] P. Larsen, A. Challinor, B. D. Sherwin, and D. Mak. Demonstration of Cosmic Microwave

Background Delensing Using the Cosmic Infrared Background. *Physical Review Letters*, 117(15):151102, October 2016.

- [60] S. M. Leach, J.-F. Cardoso, C. Baccigalupi, R. B. Barreiro, M. Betoule, J. Bobin, A. Bonaldi, J. Delabrouille, G. de Zotti, C. Dickinson, H. K. Eriksen, J. González-Nuevo, F. K. Hansen, D. Herranz, M. Le Jeune, M. López-Caniego, E. Martínez-González, M. Massardi, J.-B. Melin, M.-A. Miville-Deschênes, G. Patanchon, S. Prunet, S. Ricciardi, E. Salerno, J. L. Sanz, J.-L. Starck, F. Stivoli, V. Stolyarov, R. Stompor, and P. Vielva. Component separation methods for the PLANCK mission. *A&A*, 491:597–615, November 2008.
- [61] P. Lemos. Tests of the Planck Cosmology at High and Low Redshifts. *PhD Thesis, University of Cambridge*, 2018.
- [62] P. Lemos, E. Lee, G. Efstathiou, and S. Gratton. Model independent $H(z)$ reconstruction using the cosmic inverse distance ladder. *MNRAS*, November 2018.
- [63] A. Lewis and S. Bridle. Cosmological parameters from CMB and other data: A Monte Carlo approach. *Phys. Rev. D*, 66(10):103511, November 2002.
- [64] T. Louis, E. Grace, M. Hasselfield, M. Lungu, L. Maurin, G. E. Addison, P. A. R. Ade, S. Aiola, R. Allison, M. Amiri, E. Angile, N. Battaglia, J. A. Beall, F. de Bernardis, J. R. Bond, J. Britton, E. Calabrese, H.-m. Cho, S. K. Choi, K. Coughlin, D. Crichton, K. Crowley, R. Datta, M. J. Devlin, S. R. Dicker, J. Dunkley, R. Dünner, S. Ferraro, A. E. Fox, P. Gallardo, M. Gralla, M. Halpern, S. Henderson, J. C. Hill, G. C. Hilton, M. Hilton, A. D. Hincks, R. Hlozek, S. P. P. Ho, Z. Huang, J. Hubmayr, K. M. Huffenberger, J. P. Hughes, L. Infante, K. Irwin, S. Muya Kasanda, J. Klein, B. Koopman, A. Kosowsky, D. Li, M. Madhavacheril, T. A. Marriage, J. McMahon, F. Menanteau, K. Moodley, C. Munson, S. Naess, F. Nati, L. Newburgh, J. Nibarger, M. D. Niemack, M. R. Nolta, C. Nuñez, L. A. Page, C. Pappas, B. Partridge, F. Rojas, E. Schaan, B. L. Schmitt, N. Sehgal, B. D. Sherwin, J. Sievers, S. Simon, D. N. Spergel, S. T. Staggs, E. R. Switzer, R. Thornton, H. Trac, J. Treu, C. Tucker, A. Van Engelen, J. T. Ward, and E. J. Wollack. The Atacama Cosmology Telescope: two-season ACTPol spectra and parameters. *J. Cosmology Astropart. Phys.*, 6:031, June 2017.
- [65] M. Lueker, C. L. Reichardt, K. K. Schaffer, O. Zahn, P. A. R. Ade, K. A. Aird, B. A. Benson, L. E. Bleem, J. E. Carlstrom, C. L. Chang, H.-M. Cho, T. M. Crawford, A. T. Crites, T. de Haan, M. A. Dobbs, E. M. George, N. R. Hall, N. W. Halverson, G. P. Holder, W. L. Holzapfel, J. D. Hrubes, M. Joy, R. Keisler, L. Knox, A. T. Lee, E. M. Leitch, J. J. McMahon, J. Mehl, S. S. Meyer, J. J. Mohr, T. E. Montroy, S. Padin, T. Plagge, C. Pryke, J. E. Ruhl, L. Shaw, E. Shirokoff, H. G. Spieler, B. Stalder, Z. Staniszewski, A. A. Stark, K. Vanderlinde, J. D. Vieira, and R. Williamson. Measurements of Secondary Cosmic Microwave Background Anisotropies with the South Pole Telescope. *ApJ*, 719:1045–1066, August 2010.
- [66] E. Macaulay, R. C. Nichol, D. Bacon, D. Brout, T. M. Davis, B. Zhang, B. A. Bassett, D. Scolnic, A. Möller, C. B. D’Andrea, S. R. Hinton, R. Kessler, A. G. Kim, J. Lasker, C. Lidman, M. Sako, M. Smith, M. Sullivan, T. M. C. Abbott, S. Allam, J. Annis, J. Asorey, S. Avila, K. Bechtol, D. Brooks, P. Brown, D. L. Burke, J. Calcino, A. Carnero Rosell, D. Carollo, M. Carrasco Kind, J. Carretero, F. J. Castander, T. Collett, M. Crocce, C. E. Cunha, L. N. da Costa, C. Davis, J. De Vicente, H. T. Diehl, P. Doel, A. Drlica-Wagner, T. F. Eifler, J. Estrada, A. E. Evrard, D. A. Finley, B. Flaugher, R. J. Foley, P. Fosalba, J. Frieman, L. Galbany, J. García-Bellido, E. Gaztanaga, K. Glazebrook, S. González-Gaitán, D. Gruen, R. A. Gruendl, J. Gschwend, G. Gutierrez, W. G. Hartley, D. L. Hollowood, K. Honscheid, J. K. Hoormann, B. Hoyle, D. Huterer, B. Jain, D. J. James, T. Jeltema, E. Kasai, E. Krause, K. Kuehn, N. Kuropatkin, O. Lahav, G. F. Lewis, T. S. Li, M. Lima, H. Lin, M. A. G. Maia, J. L. Marshall, P. Martini, R. Miquel, P. Nugent, A. Palmese, Y.-C. Pan, A. A. Plazas, A. K. Romer, A. Roodman, E. Sanchez, V. Scarpine, R. Schindler, M. Schubnell, S. Serrano, I. Sevilla-Noarbe, R. Sharp, M. Soares-Santos, F. Sobreira, N. E.

- Sommer, E. Suchyta, E. Swann, M. E. C. Swanson, G. Tarle, D. Thomas, R. C. Thomas, B. E. Tucker, S. A. Uddin, V. Vikram, A. R. Walker, and P. Wiseman. First Cosmological Results using Type Ia Supernovae from the Dark Energy Survey: Measurement of the Hubble Constant. *arXiv e-prints*, November 2018.
- [67] D. S. Y. Mak, A. Challinor, G. Efstathiou, and G. Lagache. Measurement of CIB power spectra over large sky areas from Planck HFI maps. *MNRAS*, 466:286–319, April 2017.
- [68] I. G. McCarthy, S. Bird, J. Schaye, J. Harnois-Deraps, A. S. Font, and L. van Waerbeke. The BAHAMAS project: the CMB-large-scale structure tension and the roles of massive neutrinos and galaxy formation. *MNRAS*, 476:2999–3030, May 2018.
- [69] I. G. McCarthy, A. M. C. Le Brun, J. Schaye, and G. P. Holder. The thermal Sunyaev-Zel’dovich effect power spectrum in light of Planck. *MNRAS*, 440:3645–3657, June 2014.
- [70] A. M. Meisner and D. P. Finkbeiner. Modeling Thermal Dust Emission with Two Components: Application to the Planck High Frequency Instrument Maps. *ApJ*, 798:88, January 2015.
- [71] S. Mitra, G. Rocha, K. M. Górski, K. M. Huffenberger, H. K. Eriksen, M. A. J. Ashdown, and C. R. Lawrence. Fast Pixel Space Convolution for Cosmic Microwave Background Surveys with Asymmetric Beams and Complex Scan Strategies: FEBeCoP. *ApJS*, 193:5, March 2011.
- [72] Chan-Gyung Park and Bharat Ratra. Using the Tilted flat- Λ CDM and the Untilted Non-flat Λ CDM Inflation Models to Measure Cosmological Parameters from a Compilation of Observational Data. *ApJ*, 882(2):158, Sep 2019.
- [73] M. Park, C. D. Kreisch, J. Dunkley, B. Hadzhiyska, and F.-Y. Cyr-Racine. Λ CDM or self-interacting neutrinos? - how CMB data can tell the two models apart. *arXiv e-prints*, April 2019.
- [74] A. A. Penzias and R. W. Wilson. A Measurement of Excess Antenna Temperature at 4080 Mc/s. *ApJ*, 142:419–421, July 1965.
- [75] W. J. Percival, W. Sutherland, J. A. Peacock, C. M. Baugh, J. Bland-Hawthorn, T. Bridges, R. Cannon, S. Cole, M. Colless, C. Collins, W. Couch, G. Dalton, R. De Propris, S. P. Driver, G. Efstathiou, R. S. Ellis, C. S. Frenk, K. Glazebrook, C. Jackson, O. Lahav, I. Lewis, S. Lumsden, S. Maddox, S. Moody, P. Norberg, B. A. Peterson, and K. Taylor. Parameter constraints for flat cosmologies from cosmic microwave background and 2dFGRS power spectra. *MNRAS*, 337:1068–1080, December 2002.
- [76] Planck Collaboration. Planck 2015 results. XIII. Cosmological parameters. *ArXiv e-prints*, February 2015.
- [77] Planck Collaboration, A. Abergel, P. A. R. Ade, N. Aghanim, M. I. R. Alves, G. Aniano, C. Armitage-Caplan, M. Arnaud, M. Ashdown, F. Atrio-Barandela, and et al. Planck 2013 results. XI. All-sky model of thermal dust emission. *A&A*, 571:A11, November 2014.
- [78] Planck Collaboration, R. Adam, P. A. R. Ade, N. Aghanim, Y. Akrami, M. I. R. Alves, M. Arnaud, F. Arroja, J. Aumont, C. Baccigalupi, and et al. Planck 2015 results. I. Overview of products and scientific results. *ArXiv e-prints*, February 2015.
- [79] Planck Collaboration, R. Adam, P. A. R. Ade, N. Aghanim, M. Arnaud, M. Ashdown, J. Aumont, C. Baccigalupi, A. J. Banday, R. B. Barreiro, and et al. Planck 2015 results. IX. Diffuse component separation: CMB maps. *ArXiv e-prints*, February 2015.
- [80] Planck Collaboration, R. Adam, P. A. R. Ade, N. Aghanim, M. Arnaud, M. Ashdown, J. Aumont, C. Baccigalupi, A. J. Banday, R. B. Barreiro, and et al. Planck 2015 results. VIII. High Frequency Instrument data processing: Calibration and maps. *A&A*, 594:A8, September 2016.

- [81] Planck Collaboration, R. Adam, P. A. R. Ade, N. Aghanim, M. Arnaud, J. Aumont, C. Baccigalupi, A. J. Banday, R. B. Barreiro, J. G. Bartlett, and et al. Planck intermediate results. XXX. The angular power spectrum of polarized dust emission at intermediate and high Galactic latitudes. *A&A*, 586:A133, February 2016.
- [82] Planck Collaboration, P. A. R. Ade, N. Aghanim, M. I. R. Alves, C. Armitage-Caplan, M. Arnaud, M. Ashdown, F. Atrio-Barandela, J. Aumont, H. Aussel, and et al. Planck 2013 results. I. Overview of products and scientific results. *A&A*, 571:A1, November 2014.
- [83] Planck Collaboration, P. A. R. Ade, N. Aghanim, M. I. R. Alves, C. Armitage-Caplan, M. Arnaud, M. Ashdown, F. Atrio-Barandela, J. Aumont, C. Baccigalupi, and et al. Planck 2013 results. XIII. Galactic CO emission. *A&A*, 571:A13, November 2014.
- [84] Planck Collaboration, P. A. R. Ade, N. Aghanim, C. Armitage-Caplan, M. Arnaud, M. Ashdown, F. Atrio-Barandela, J. Aumont, C. Baccigalupi, A. J. Banday, and et al. Planck 2013 results. IX. HFI spectral response. *A&A*, 571:A9, November 2014.
- [85] Planck Collaboration, P. A. R. Ade, N. Aghanim, C. Armitage-Caplan, M. Arnaud, M. Ashdown, F. Atrio-Barandela, J. Aumont, C. Baccigalupi, A. J. Banday, and et al. Planck 2013 results. VII. HFI time response and beams. *A&A*, 571:A7, November 2014.
- [86] Planck Collaboration, P. A. R. Ade, N. Aghanim, C. Armitage-Caplan, M. Arnaud, M. Ashdown, F. Atrio-Barandela, J. Aumont, C. Baccigalupi, A. J. Banday, and et al. Planck 2013 results. XII. Diffuse component separation. *A&A*, 571:A12, November 2014.
- [87] Planck Collaboration, P. A. R. Ade, N. Aghanim, C. Armitage-Caplan, M. Arnaud, M. Ashdown, F. Atrio-Barandela, J. Aumont, C. Baccigalupi, A. J. Banday, and et al. Planck 2013 results. XV. CMB power spectra and likelihood. *A&A*, 571:A15, November 2014.
- [88] Planck Collaboration, P. A. R. Ade, N. Aghanim, C. Armitage-Caplan, M. Arnaud, M. Ashdown, F. Atrio-Barandela, J. Aumont, C. Baccigalupi, A. J. Banday, and et al. Planck 2013 results. XVI. Cosmological parameters. *A&A*, 571:A16, November 2014.
- [89] Planck Collaboration, P. A. R. Ade, N. Aghanim, C. Armitage-Caplan, M. Arnaud, M. Ashdown, F. Atrio-Barandela, J. Aumont, C. Baccigalupi, A. J. Banday, and et al. Planck 2013 results. XXII. Constraints on inflation. *A&A*, 571:A22, November 2014.
- [90] Planck Collaboration, P. A. R. Ade, N. Aghanim, C. Armitage-Caplan, M. Arnaud, M. Ashdown, F. Atrio-Barandela, J. Aumont, C. Baccigalupi, A. J. Banday, and et al. Planck 2013 results. XXIV. Constraints on primordial non-Gaussianity. *A&A*, 571:A24, November 2014.
- [91] Planck Collaboration, P. A. R. Ade, N. Aghanim, C. Armitage-Caplan, M. Arnaud, M. Ashdown, F. Atrio-Barandela, J. Aumont, C. Baccigalupi, A. J. Banday, and et al. Planck 2013 results. XXX. Cosmic infrared background measurements and implications for star formation. *A&A*, 571:A30, November 2014.
- [92] Planck Collaboration, P. A. R. Ade, N. Aghanim, M. Arnaud, F. Arroja, M. Ashdown, J. Aumont, C. Baccigalupi, M. Ballardini, A. J. Banday, and et al. Planck 2015 results. XVII. Constraints on primordial non-Gaussianity. *A&A*, 594:A17, September 2016.
- [93] Planck Collaboration, P. A. R. Ade, N. Aghanim, M. Arnaud, F. Arroja, M. Ashdown, J. Aumont, C. Baccigalupi, M. Ballardini, A. J. Banday, and et al. Planck 2015 results. XX. Constraints on inflation. *A&A*, 594:A20, September 2016.
- [94] Planck Collaboration, P. A. R. Ade, M. I. R. Alves, G. Aniano, C. Armitage-Caplan, M. Arnaud, F. Atrio-Barandela, J. Aumont, C. Baccigalupi, A. J. Banday, R. B. Barreiro, E. Battaner, K. Benabed, A. Benoit-Lévy, J.-P. Bernard, M. Bersanelli, P. Bielewicz, J. J. Bock, J. R. Bond, J. Borrill, F. R. Bouchet, F. Boulanger, C. Burigana, J.-F. Cardoso, A. Catalano, A. Chamballu, H. C. Chiang, L. P. L. Colombo, C. Combet, F. Couchot, A. Coulais, B. P. Crill, A. Curto, F. Cuttaia, L. Danese, R. D. Davies, R. J. Davis, P. de

Bernardis, G. de Zotti, J. Delabrouille, F.-X. Désert, C. Dickinson, J. M. Diego, S. Donzelli, O. Doré, M. Douspis, J. Dunkley, X. Dupac, T. A. Enßlin, H. K. Eriksen, E. Falgarone, F. Finelli, O. Forni, M. Frailis, A. A. Fraisse, E. Franceschi, S. Galeotta, K. Ganga, T. Ghosh, M. Giard, J. González-Nuevo, K. M. Górski, A. Gregorio, A. Gruppuso, V. Guillet, F. K. Hansen, D. L. Harrison, G. Helou, C. Hernández-Monteagudo, S. R. Hildebrandt, E. Hivon, M. Hobson, W. A. Holmes, A. Hornstrup, A. H. Jaffe, T. R. Jaffe, W. C. Jones, E. Keihänen, R. Keskitalo, T. S. Kisner, R. Kneissl, J. Knoche, M. Kunz, H. Kurki-Suonio, G. Lagache, J.-M. Lamarre, A. Lasenby, C. R. Lawrence, J. P. Leahy, R. Leonardi, F. Levrier, M. Liguori, P. B. Lilje, M. Linden-Vørnle, M. López-Caniego, P. M. Lubin, J. F. Macías-Pérez, B. Maffei, A. M. Magalhães, D. Maino, N. Mandolesi, M. Maris, D. J. Marshall, P. G. Martin, E. Martínez-González, S. Masi, S. Matarrese, P. Mazzotta, A. Melchiorri, L. Mendes, A. Mennella, M. Migliaccio, M.-A. Miville-Deschênes, A. Moneti, L. Montier, G. Morgante, D. Mortlock, D. Munshi, J. A. Murphy, P. Naselsky, F. Nati, P. Natoli, C. B. Netterfield, F. Noviello, D. Novikov, I. Novikov, N. Oppermann, C. A. Oxborrow, L. Pagano, F. Pajot, D. Paoletti, F. Pasian, O. Perdereau, L. Perotto, F. Perrotta, F. Piacentini, D. Pietrobon, S. Plaszczyński, E. Pointecouteau, G. Polenta, L. Popa, G. W. Pratt, J. P. Rachen, W. T. Reach, M. Reinecke, M. Remazeilles, C. Renault, S. Ricciardi, T. Riller, I. Ristorcelli, G. Rocha, C. Rosset, G. Roudier, J. A. Rubiño-Martín, B. Rusholme, E. Salerno, M. Sandri, G. Savini, D. Scott, L. D. Spencer, V. Stolyarov, R. Stompor, R. Sudiwala, D. Sutton, A.-S. Suur-Uski, J.-F. Sygnet, J. A. Tauber, L. Terenzi, L. Toffolatti, M. Tomasi, M. Tristram, M. Tucci, L. Valenziano, J. Valiviita, B. Van Tent, P. Vielva, F. Villa, B. D. Wandelt, A. Zacchei, and A. Zonca. Planck intermediate results. XXII. Frequency dependence of thermal emission from Galactic dust in intensity and polarization. *A&A*, 576:A107, April 2015.

- [95] Planck Collaboration, P. A. R. Ade, M. Arnaud, M. Ashdown, J. Aumont, C. Baccigalupi, A. J. Banday, R. B. Barreiro, E. Battaner, K. Benabed, A. Benoit-Lévy, J.-P. Bernard, M. Bersanelli, P. Bielewicz, J. R. Bond, J. Borrill, F. R. Bouchet, C. Burigana, J.-F. Cardoso, A. Catalano, A. Challinor, A. Chamballu, H. C. Chiang, P. R. Christensen, D. L. Clements, S. Colombi, L. P. L. Colombo, F. Couchot, A. Coulais, B. P. Crill, A. Curto, F. Cuttaia, L. Danese, R. D. Davies, R. J. Davis, P. de Bernardis, A. de Rosa, G. de Zotti, J. Delabrouille, F.-X. Désert, C. Dickinson, J. M. Diego, H. Dole, S. Donzelli, O. Doré, M. Douspis, X. Dupac, T. A. Enßlin, H. K. Eriksen, F. Finelli, O. Forni, M. Frailis, A. A. Fraisse, E. Franceschi, S. Galeotta, K. Ganga, M. Giard, J. González-Nuevo, K. M. Górski, S. Gratton, A. Gregorio, A. Gruppuso, J. E. Gudmundsson, F. K. Hansen, D. Hanson, D. L. Harrison, S. Henrot-Versillé, D. Herranz, S. R. Hildebrandt, E. Hivon, M. Hobson, W. A. Holmes, A. Hornstrup, W. Hovest, K. M. Huffenberger, A. H. Jaffe, T. R. Jaffe, W. C. Jones, E. Keihänen, R. Keskitalo, J. Knoche, M. Kunz, H. Kurki-Suonio, G. Lagache, A. Lähteenmäki, J.-M. Lamarre, A. Lasenby, C. R. Lawrence, R. Leonardi, J. León-Tavares, J. Lesgourgues, M. Liguori, P. B. Lilje, M. Linden-Vørnle, M. López-Caniego, P. M. Lubin, J. F. Macías-Pérez, D. Maino, N. Mandolesi, M. Maris, P. G. Martin, E. Martínez-González, S. Masi, S. Matarrese, P. Mazzotta, P. R. Meinhold, A. Melchiorri, L. Mendes, A. Mennella, M. Migliaccio, S. Mitra, M.-A. Miville-Deschênes, A. Moneti, L. Montier, G. Morgante, D. Mortlock, A. Moss, D. Munshi, J. A. Murphy, P. Naselsky, F. Nati, P. Natoli, H. U. Nørgaard-Nielsen, F. Noviello, D. Novikov, I. Novikov, C. A. Oxborrow, L. Pagano, F. Pajot, D. Paoletti, B. Partridge, F. Pasian, G. Patanchon, D. Pearson, T. J. Pearson, O. Perdereau, F. Perrotta, F. Piacentini, M. Piat, E. Pierpaoli, D. Pietrobon, S. Plaszczyński, E. Pointecouteau, G. Polenta, N. Ponthieu, L. Popa, G. W. Pratt, S. Prunet, J.-L. Puget, J. P. Rachen, M. Reinecke, M. Remazeilles, C. Renault, S. Ricciardi, I. Ristorcelli, G. Rocha, G. Roudier, J. A. Rubiño-Martín, B. Rusholme, M. Sandri, D. Scott, V. Stolyarov, R. Sudiwala, D. Sutton, A.-S. Suur-Uski, J.-F. Sygnet, J. A. Tauber, L. Terenzi, L. Toffolatti, M. Tomasi, M. Tristram, M. Tucci, L. Valenziano, J. Valiviita, B. Van Tent, P. Vielva, F. Villa, L. A. Wade, B. D. Wandelt, I. K. Wehus, S. D. M. White, D. Yvon, A. Zacchei, and A. Zonca. Planck 2013 results. XXXI. Consistency of the Planck data. *A&A*, 571:A31,

November 2014.

- [96] Planck Collaboration, N. Aghanim, Y. Akrami, M. Ashdown, J. Aumont, C. Baccigalupi, M. Ballardini, A. J. Banday, R. B. Barreiro, N. Bartolo, S. Basak, R. Battye, K. Benabed, J.-P. Bernard, M. Bersanelli, P. Bielewicz, J. J. Bock, J. R. Bond, J. Borrill, F. R. Bouchet, F. Boulanger, M. Bucher, C. Burigana, R. C. Butler, E. Calabrese, J.-F. Cardoso, J. Carron, A. Challinor, H. C. Chiang, J. Chluba, L. P. L. Colombo, C. Combet, D. Contreras, B. P. Crill, F. Cuttaia, P. de Bernardis, G. de Zotti, J. Delabrouille, J.-M. Delouis, E. Di Valentino, J. M. Diego, O. Doré, M. Douspis, A. Ducout, X. Dupac, S. Dusini, G. Efstathiou, F. Elsner, T. A. Enßlin, H. K. Eriksen, Y. Fantaye, M. Farhang, J. Fergusson, R. Fernandez-Cobos, F. Finelli, F. Forastieri, M. Frailis, E. Franceschi, A. Frolov, S. Galeotta, S. Galli, K. Ganga, R. T. Génova-Santos, M. Gerbino, T. Ghosh, J. González-Nuevo, K. M. Górski, S. Gratton, A. Gruppuso, J. E. Gudmundsson, J. Hamann, W. Handley, D. Herranz, E. Hivon, Z. Huang, A. H. Jaffe, W. C. Jones, A. Karakci, E. Keihänen, R. Keskitalo, K. Kiiveri, J. Kim, T. S. Kisner, L. Knox, N. Krachmalnicoff, M. Kunz, H. Kurki-Suonio, G. Lagache, J.-M. Lamarre, A. Lasenby, M. Lattanzi, C. R. Lawrence, M. Le Jeune, P. Lemos, J. Lesgourgues, F. Levrier, A. Lewis, M. Liguori, P. B. Lilje, M. Lilley, V. Lindholm, M. López-Caniego, P. M. Lubin, Y.-Z. Ma, J. F. Macías-Pérez, G. Maggio, D. Maino, N. Mandolesi, A. Mangilli, A. Marcos-Caballero, M. Maris, P. G. Martin, M. Martinelli, E. Martínez-González, S. Matarrese, N. Mauri, J. D. McEwen, P. R. Meinhold, A. Melchiorri, A. Mennella, M. Migliaccio, M. Millea, S. Mitra, M.-A. Miville-Deschênes, D. Molinari, L. Montier, G. Morgante, A. Moss, P. Natoli, H. U. Nørgaard-Nielsen, L. Pagano, D. Paoletti, B. Partridge, G. Patanchon, H. V. Peiris, F. Perrotta, V. Pettorino, F. Piacentini, L. Polastri, G. Polenta, J.-L. Puget, J. P. Rachen, M. Reinecke, M. Remazeilles, A. Renzi, G. Rocha, C. Rosset, G. Roudier, J. A. Rubiño-Martín, B. Ruiz-Granados, L. Salvati, M. Sandri, M. Savelainen, D. Scott, E. P. S. Shellard, C. Sirignano, G. Sirri, L. D. Spencer, R. Sunyaev, A.-S. Suur-Uski, J. A. Tauber, D. Tavagnacco, M. Tenti, L. Toffolatti, M. Tomasi, T. Trombetti, L. Valenziano, J. Valiviita, B. Van Tent, L. Vibert, P. Vielva, F. Villa, N. Vittorio, B. D. Wandelt, I. K. Wehus, M. White, S. D. M. White, A. Zacchei, and A. Zonca. Planck 2018 results. VI. Cosmological parameters. *arXiv e-prints*, July 2018.
- [97] Planck Collaboration, N. Aghanim, Y. Akrami, M. Ashdown, J. Aumont, C. Baccigalupi, M. Ballardini, A. J. Banday, R. B. Barreiro, N. Bartolo, S. Basak, K. Benabed, J. P. Bernard, M. Bersanelli, P. Bielewicz, J. J. Bock, J. R. Bond, J. Borrill, F. R. Bouchet, F. Boulanger, M. Bucher, C. Burigana, R. C. Butler, E. Calabrese, J. F. Cardoso, J. Carron, B. Casaponsa, A. Challinor, H. C. Chiang, L. P. L. Colombo, C. Combet, B. P. Crill, F. Cuttaia, P. de Bernardis, A. de Rosa, G. de Zotti, J. Delabrouille, J. M. Delouis, E. Di Valentino, J. M. Diego, O. Doré, M. Douspis, A. Ducout, X. Dupac, S. Dusini, G. Efstathiou, F. Elsner, T. A. Enßlin, H. K. Eriksen, Y. Fantaye, R. Fernandez-Cobos, F. Finelli, M. Frailis, A. A. Fraisse, E. Franceschi, A. Frolov, S. Galeotta, S. Galli, K. Ganga, R. T. Génova-Santos, M. Gerbino, T. Ghosh, Y. Giraud-Héraud, J. González-Nuevo, K. M. Górski, S. Gratton, A. Gruppuso, J. E. Gudmundsson, J. Hamann, W. Handley, F. K. Hansen, D. Herranz, E. Hivon, Z. Huang, A. H. Jaffe, W. C. Jones, E. Keihänen, R. Keskitalo, K. Kiiveri, J. Kim, T. S. Kisner, N. Krachmalnicoff, M. Kunz, H. Kurki-Suonio, G. Lagache, J. M. Lamarre, A. Lasenby, M. Lattanzi, C. R. Lawrence, M. Le Jeune, F. Levrier, A. Lewis, M. Liguori, P. B. Lilje, M. Lilley, V. Lindholm, M. López-Caniego, P. M. Lubin, Y. Z. Ma, J. F. Macías-Pérez, G. Maggio, D. Maino, N. Mandolesi, A. Mangilli, A. Marcos-Caballero, M. Maris, P. G. Martin, E. Martínez-González, S. Matarrese, N. Mauri, J. D. McEwen, P. R. Meinhold, A. Melchiorri, A. Mennella, M. Migliaccio, M. Millea, M. A. Miville-Deschênes, D. Molinari, A. Moneti, L. Montier, G. Morgante, A. Moss, P. Natoli, H. U. Nørgaard-Nielsen, L. Pagano, D. Paoletti, B. Partridge, G. Patanchon, H. V. Peiris, F. Perrotta, V. Pettorino, F. Piacentini, G. Polenta, J. L. Puget, J. P. Rachen, M. Reinecke, M. Remazeilles, A. Renzi, G. Rocha, C. Rosset, G. Roudier, J. A. Rubiño-Martín, B. Ruiz-Granados, L. Salvati, M. Sandri, M. Savelainen, D. Scott, E. P. S. Shellard, C. Sirignano, G. Sirri, L. D. Spencer, R. Sunyaev,

A. S. Suur-Uski, J. A. Tauber, D. Tavagnacco, M. Tenti, L. Toffolatti, M. Tomasi, T. Trombetti, J. Valiviita, B. Van Tent, P. Vielva, F. Villa, N. Vittorio, B. D. Wandelt, I. K. Wehus, A. Zacchei, and A. Zonca. Planck 2018 results. V. CMB power spectra and likelihoods. *arXiv e-prints*, page arXiv:1907.12875, Jul 2019.

- [98] Planck Collaboration, N. Aghanim, Y. Akrami, M. Ashdown, J. Aumont, C. Baccigalupi, M. Ballardini, A. J. Banday, R. B. Barreiro, N. Bartolo, S. Basak, K. Benabed, J.-P. Bernard, M. Bersanelli, P. Bielewicz, J. J. Bock, J. R. Bond, J. Borrill, F. R. Bouchet, F. Boulanger, M. Bucher, C. Burigana, E. Calabrese, J.-F. Cardoso, J. Carron, A. Challinor, H. C. Chiang, L. P. L. Colombo, C. Combet, B. P. Crill, F. Cuttaia, P. de Bernardis, G. de Zotti, J. Delabrouille, E. Di Valentino, J. M. Diego, O. Doré, M. Douspis, A. Ducout, X. Dupac, G. Efstathiou, F. Elsner, T. A. Enßlin, H. K. Eriksen, Y. Fantaye, R. Fernandez-Cobos, F. Forastieri, M. Frailis, A. A. Fraisse, E. Franceschi, A. Frolov, S. Galeotta, S. Galli, K. Ganga, R. T. Génova-Santos, M. Gerbino, T. Ghosh, J. González-Nuevo, K. M. Górski, S. Gratton, A. Gruppuso, J. E. Gudmundsson, J. Hamann, W. Handley, F. K. Hansen, D. Herranz, E. Hivon, Z. Huang, A. H. Jaffe, W. C. Jones, A. Karakci, E. Keihänen, R. Keskitalo, K. Kiiveri, J. Kim, L. Knox, N. Krachmalnicoff, M. Kunz, H. Kurki-Suonio, G. Lagache, J.-M. Lamarre, A. Lasenby, M. Lattanzi, C. R. Lawrence, M. Le Jeune, F. Levrier, A. Lewis, M. Liguori, P. B. Lilje, V. Lindholm, M. López-Caniego, P. M. Lubin, Y.-Z. Ma, J. F. Macías-Pérez, G. Maggio, D. Maino, N. Mandolesi, A. Mangilli, A. Marcos-Caballero, M. Maris, P. G. Martin, E. Martínez-González, S. Matarrese, N. Mauri, J. D. McEwen, A. Melchiorri, A. Mennella, M. Migliaccio, M.-A. Miville-Deschênes, D. Molinari, A. Moneti, L. Montier, G. Morgante, A. Moss, P. Natoli, L. Pagano, D. Paoletti, B. Partridge, G. Patanchon, F. Perrotta, V. Pettorino, F. Piacentini, L. Polastri, G. Polenta, J.-L. Puget, J. P. Rachen, M. Reinecke, M. Remazeilles, A. Renzi, G. Rocha, C. Rosset, G. Roudier, J. A. Rubiño-Martín, B. Ruiz-Granados, L. Salvati, M. Sandri, M. Savelainen, D. Scott, C. Sirignano, R. Sunyaev, A.-S. Suur-Uski, J. A. Tauber, D. Tavagnacco, M. Tenti, L. Toffolatti, M. Tomasi, T. Trombetti, J. Valiviita, B. Van Tent, P. Vielva, F. Villa, N. Vittorio, B. D. Wandelt, I. K. Wehus, M. White, S. D. M. White, A. Zacchei, and A. Zonca. Planck 2018 results. VIII. Gravitational lensing. *arXiv e-prints*, July 2018.
- [99] Planck Collaboration, N. Aghanim, Y. Akrami, M. Ashdown, J. Aumont, C. Baccigalupi, M. Ballardini, A. J. Banday, R. B. Barreiro, N. Bartolo, S. Basak, K. Benabed, J.-P. Bernard, M. Bersanelli, P. Bielewicz, J. R. Bond, J. Borrill, F. R. Bouchet, F. Boulanger, M. Bucher, C. Burigana, E. Calabrese, J.-F. Cardoso, J. Carron, A. Challinor, H. C. Chiang, L. P. L. Colombo, C. Combet, F. Couchot, B. P. Crill, F. Cuttaia, P. de Bernardis, A. de Rosa, G. de Zotti, J. Delabrouille, J.-M. Delouis, E. Di Valentino, J. M. Diego, O. Doré, M. Douspis, A. Ducout, X. Dupac, G. Efstathiou, F. Elsner, T. A. Enßlin, H. K. Eriksen, E. Falgarone, Y. Fantaye, F. Finelli, M. Frailis, A. A. Fraisse, E. Franceschi, A. Frolov, S. Galeotta, S. Galli, K. Ganga, R. T. Génova-Santos, M. Gerbino, T. Ghosh, J. González-Nuevo, K. M. Górski, S. Gratton, A. Gruppuso, J. E. Gudmundsson, W. Handley, F. K. Hansen, S. Henrot-Versillé, D. Herranz, E. Hivon, Z. Huang, A. H. Jaffe, W. C. Jones, A. Karakci, E. Keihänen, R. Keskitalo, K. Kiiveri, J. Kim, T. S. Kisner, N. Krachmalnicoff, M. Kunz, H. Kurki-Suonio, G. Lagache, J.-M. Lamarre, A. Lasenby, M. Lattanzi, C. R. Lawrence, F. Levrier, M. Liguori, P. B. Lilje, V. Lindholm, M. López-Caniego, Y.-Z. Ma, J. F. Macías-Pérez, G. Maggio, D. Maino, N. Mandolesi, A. Mangilli, P. G. Martin, E. Martínez-González, S. Matarrese, N. Mauri, J. D. McEwen, A. Melchiorri, A. Mennella, M. Migliaccio, M.-A. Miville-Deschênes, D. Molinari, A. Moneti, L. Montier, G. Morgante, A. Moss, S. Mottet, P. Natoli, L. Pagano, D. Paoletti, B. Partridge, G. Patanchon, L. Patrizii, O. Perdereau, F. Perrotta, V. Pettorino, F. Piacentini, J.-L. Puget, J. P. Rachen, M. Reinecke, M. Remazeilles, A. Renzi, G. Rocha, G. Roudier, L. Salvati, M. Sandri, M. Savelainen, D. Scott, C. Sirignano, G. Sirri, L. D. Spencer, R. Sunyaev, A.-S. Suur-Uski, J. A. Tauber, D. Tavagnacco, M. Tenti, L. Toffolatti, M. Tomasi, M. Tristram, T. Trombetti, J. Valiviita, F. Vansyngel, B. Van Tent, L. Vibert, P. Vielva, F. Villa, N. Vittorio, B. D. Wandelt, I. K. Wehus, and A. Zonca. Planck 2018

results. III. High Frequency Instrument data processing and frequency maps. *ArXiv e-prints*, July 2018.

- [100] Planck Collaboration, N. Aghanim, Y. Akrami, M. Ashdown, J. Aumont, C. Baccigalupi, M. Ballardini, A. J. Banday, R. B. Barreiro, N. Bartolo, S. Basak, K. Benabed, M. Bersanelli, P. Bielewicz, A. Bonaldi, L. Bonavera, J. R. Bond, J. Borrill, F. R. Bouchet, C. Burigana, E. Calabrese, J.-F. Cardoso, A. Challinor, H. C. Chiang, L. P. L. Colombo, C. Combet, B. P. Crill, A. Curto, F. Cuttaia, P. de Bernardis, A. de Rosa, G. de Zotti, J. Delabrouille, E. Di Valentino, C. Dickinson, J. M. Diego, O. Doré, A. Ducout, X. Dupac, S. Dusini, G. Efstathiou, F. Elsner, T. A. Enßlin, H. K. Eriksen, Y. Fantaye, F. Finelli, F. Forastieri, M. Frailis, E. Franceschi, A. Frolov, S. Galeotta, S. Galli, K. Ganga, R. T. Génova-Santos, M. Gerbino, J. González-Nuevo, K. M. Górski, S. Gratton, A. Gruppuso, J. E. Gudmundsson, D. Herranz, E. Hivon, Z. Huang, A. H. Jaffe, W. C. Jones, E. Keihänen, R. Keskitalo, K. Kiiveri, J. Kim, T. S. Kisner, L. Knox, N. Krachmalnicoff, M. Kunz, H. Kurki-Suonio, G. Lagache, J.-M. Lamarre, A. Lasenby, M. Lattanzi, C. R. Lawrence, M. Le Jeune, F. Levrier, A. Lewis, M. Liguori, P. B. Lilje, M. Lilley, V. Lindholm, M. López-Caniego, P. M. Lubin, Y.-Z. Ma, J. F. Macías-Pérez, G. Maggio, D. Maino, N. Mandolesi, A. Mangilli, M. Maris, P. G. Martin, E. Martínez-González, S. Matarrese, N. Mauri, J. D. McEwen, P. R. Meinhold, A. Mennella, M. Migliaccio, M. Millea, M.-A. Miville-Deschênes, D. Molinari, A. Moneti, L. Montier, G. Morgante, A. Moss, A. Narimani, P. Natoli, C. A. Oxborrow, L. Pagano, D. Paoletti, B. Partridge, G. Patanchon, L. Patrizii, V. Pettorino, F. Piacentini, L. Polastri, G. Polenta, J.-L. Puget, J. P. Rachen, B. Racine, M. Reinecke, M. Remazeilles, A. Renzi, G. Rocha, M. Rossetti, G. Roudier, J. A. Rubiño-Martín, B. Ruiz-Granados, L. Salvati, M. Sandri, M. Savelainen, D. Scott, C. Sirignano, G. Sirri, L. Stanco, A.-S. Suur-Uski, J. A. Tauber, D. Tavagnacco, M. Tenti, L. Toffolatti, M. Tomasi, M. Tristram, T. Trombetti, J. Valiviita, F. Van Tent, P. Vielva, F. Villa, N. Vittorio, B. D. Wandelt, I. K. Wehus, M. White, A. Zacchei, and A. Zonca. Planck intermediate results. LI. Features in the cosmic microwave background temperature power spectrum and shifts in cosmological parameters. *A&A*, 607:A95, November 2017.
- [101] Planck Collaboration, N. Aghanim, M. Arnaud, M. Ashdown, J. Aumont, C. Baccigalupi, A. J. Banday, R. B. Barreiro, J. G. Bartlett, N. Bartolo, and et al. Planck 2015 results. XI. CMB power spectra, likelihoods, and robustness of parameters. *A&A*, 594:A11, September 2016.
- [102] Planck Collaboration, N. Aghanim, M. Ashdown, J. Aumont, C. Baccigalupi, M. Ballardini, A. J. Banday, R. B. Barreiro, N. Bartolo, S. Basak, R. Battye, K. Benabed, J.-P. Bernard, M. Bersanelli, P. Bielewicz, J. J. Bock, A. Bonaldi, L. Bonavera, J. R. Bond, J. Borrill, F. R. Bouchet, F. Boulanger, M. Bucher, C. Burigana, R. C. Butler, E. Calabrese, J.-F. Cardoso, J. Carron, A. Challinor, H. C. Chiang, L. P. L. Colombo, C. Combet, B. Comis, A. Coulais, B. P. Crill, A. Curto, F. Cuttaia, R. J. Davis, P. de Bernardis, A. de Rosa, G. de Zotti, J. Delabrouille, J.-M. Delouis, E. Di Valentino, C. Dickinson, J. M. Diego, O. Doré, M. Douspis, A. Ducout, X. Dupac, G. Efstathiou, F. Elsner, T. A. Enßlin, H. K. Eriksen, E. Falgarone, Y. Fantaye, F. Finelli, F. Forastieri, M. Frailis, A. A. Fraisse, E. Franceschi, A. Frolov, S. Galeotta, S. Galli, K. Ganga, R. T. Génova-Santos, M. Gerbino, T. Ghosh, J. González-Nuevo, K. M. Górski, S. Gratton, A. Gruppuso, J. E. Gudmundsson, F. K. Hansen, G. Helou, S. Henrot-Versillé, D. Herranz, E. Hivon, Z. Huang, S. Ilić, A. H. Jaffe, W. C. Jones, E. Keihänen, R. Keskitalo, T. S. Kisner, L. Knox, N. Krachmalnicoff, M. Kunz, H. Kurki-Suonio, G. Lagache, J.-M. Lamarre, M. Langer, A. Lasenby, M. Lattanzi, C. R. Lawrence, M. Le Jeune, J. P. Leahy, F. Levrier, M. Liguori, P. B. Lilje, M. López-Caniego, Y.-Z. Ma, J. F. Macías-Pérez, G. Maggio, A. Mangilli, M. Maris, P. G. Martin, E. Martínez-González, S. Matarrese, N. Mauri, J. D. McEwen, P. R. Meinhold, A. Melchiorri, A. Mennella, M. Migliaccio, M.-A. Miville-Deschênes, D. Molinari, A. Moneti, L. Montier, G. Morgante, A. Moss, S. Mottet, P. Naselsky, P. Natoli, C. A. Oxborrow, L. Pagano, D. Paoletti, B. Partridge, G. Patanchon, L. Patrizii, O. Perdereau, L. Perotto, V. Pettorino,

F. Piacentini, S. Plaszczynski, L. Polastri, G. Polenta, J.-L. Puget, J. P. Rachen, B. Racine, M. Reinecke, M. Remazeilles, A. Renzi, G. Rocha, M. Rossetti, G. Roudier, J. A. Rubiño-Martín, B. Ruiz-Granados, L. Salvati, M. Sandri, M. Savelainen, D. Scott, G. Sirri, R. Sunyaev, A.-S. Suur-Uski, J. A. Tauber, M. Tenti, L. Toffolatti, M. Tomasi, M. Tristram, T. Trombetti, J. Valiviita, F. Van Tent, L. Vibert, P. Vielva, F. Villa, N. Vittorio, B. D. Wandelt, R. Watson, I. K. Wehus, M. White, A. Zacchei, and A. Zonca. Planck intermediate results. XLVI. Reduction of large-scale systematic effects in HFI polarization maps and estimation of the reionization optical depth. *A&A*, 596:A107, December 2016.

- [103] Planck Collaboration, N. Aghanim, M. Ashdown, J. Aumont, C. Baccigalupi, M. Ballardini, A. J. Banday, R. B. Barreiro, N. Bartolo, S. Basak, R. Battye, K. Benabed, J.-P. Bernard, M. Bersanelli, P. Bielewicz, J. J. Bock, A. Bonaldi, L. Bonavera, J. R. Bond, J. Borrill, F. R. Bouchet, F. Boulanger, M. Bucher, C. Burigana, R. C. Butler, E. Calabrese, J.-F. Cardoso, J. Carron, A. Challinor, H. C. Chiang, L. P. L. Colombo, C. Combet, B. Comis, A. Coulais, B. P. Crill, A. Curto, F. Cuttaia, R. J. Davis, P. de Bernardis, A. de Rosa, G. de Zotti, J. Delabrouille, J.-M. Delouis, E. Di Valentino, C. Dickinson, J. M. Diego, O. Doré, M. Douspis, A. Ducout, X. Dupac, G. Efstathiou, F. Elsner, T. A. Enßlin, H. K. Eriksen, E. Falgarone, Y. Fantaye, F. Finelli, F. Forastieri, M. Frailis, A. A. Fraisse, E. Franceschi, A. Frolov, S. Galeotta, S. Galli, K. Ganga, R. T. Génova-Santos, M. Gerbino, T. Ghosh, J. González-Nuevo, K. M. Górski, S. Gratton, A. Gruppuso, J. E. Gudmundsson, F. K. Hansen, G. Helou, S. Henrot-Versillé, D. Herranz, E. Hivon, Z. Huang, S. Ilić, A. H. Jaffe, W. C. Jones, E. Keihänen, R. Keskitalo, T. S. Kisner, L. Knox, N. Krachmalnicoff, M. Kunz, H. Kurki-Suonio, G. Lagache, J.-M. Lamarre, M. Langer, A. Lasenby, M. Lattanzi, C. R. Lawrence, M. Le Jeune, J. P. Leahy, F. Levrier, M. Liguori, P. B. Lilje, M. López-Caniego, Y.-Z. Ma, J. F. Macías-Pérez, G. Maggio, A. Mangilli, M. Maris, P. G. Martin, E. Martínez-González, S. Matarrese, N. Mauri, J. D. McEwen, P. R. Meinhold, A. Melchiorri, A. Mennella, M. Migliaccio, M.-A. Miville-Deschênes, D. Molinari, A. Moneti, L. Montier, G. Morgante, A. Moss, S. Mottet, P. Naselsky, P. Natoli, C. A. Oxborrow, L. Pagano, D. Paoletti, B. Partridge, G. Patanchon, L. Patrizii, O. Perdereau, L. Perotto, V. Pettorino, F. Piacentini, S. Plaszczynski, L. Polastri, G. Polenta, J.-L. Puget, J. P. Rachen, B. Racine, M. Reinecke, M. Remazeilles, A. Renzi, G. Rocha, M. Rossetti, G. Roudier, J. A. Rubiño-Martín, B. Ruiz-Granados, L. Salvati, M. Sandri, M. Savelainen, D. Scott, G. Sirri, R. Sunyaev, A.-S. Suur-Uski, J. A. Tauber, M. Tenti, L. Toffolatti, M. Tomasi, M. Tristram, T. Trombetti, J. Valiviita, F. Van Tent, L. Vibert, P. Vielva, F. Villa, N. Vittorio, B. D. Wandelt, R. Watson, I. K. Wehus, M. White, A. Zacchei, and A. Zonca. Planck intermediate results. XLVI. Reduction of large-scale systematic effects in HFI polarization maps and estimation of the reionization optical depth. *A&A*, 596:A107, December 2016.
- [104] Planck Collaboration, Y. Akrami, F. Arroja, M. Ashdown, J. Aumont, C. Baccigalupi, M. Ballardini, A. J. Banday, R. B. Barreiro, N. Bartolo, S. Basak, K. Benabed, J.-P. Bernard, M. Bersanelli, P. Bielewicz, J. J. Bock, J. R. Bond, J. Borrill, F. R. Bouchet, F. Boulanger, M. Bucher, C. Burigana, R. C. Butler, E. Calabrese, J.-F. Cardoso, J. Carron, A. Challinor, H. C. Chiang, L. P. L. Colombo, C. Combet, D. Contreras, B. P. Crill, F. Cuttaia, P. de Bernardis, G. de Zotti, J. Delabrouille, J.-M. Delouis, E. Di Valentino, J. M. Diego, S. Donzelli, O. Doré, M. Douspis, A. Ducout, X. Dupac, S. Dusini, G. Efstathiou, F. Elsner, T. A. Enßlin, H. K. Eriksen, Y. Fantaye, J. Fergusson, R. Fernandez-Cobos, F. Finelli, F. Forastieri, M. Frailis, E. Franceschi, A. Frolov, S. Galeotta, S. Galli, K. Ganga, C. Gauthier, R. T. Génova-Santos, M. Gerbino, T. Ghosh, J. González-Nuevo, K. M. Górski, S. Gratton, A. Gruppuso, J. E. Gudmundsson, J. Hamann, W. Handley, F. K. Hansen, D. Herranz, E. Hivon, D. C. Hooper, Z. Huang, A. H. Jaffe, W. C. Jones, E. Keihänen, R. Keskitalo, K. Kiiveri, J. Kim, T. S. Kisner, N. Krachmalnicoff, M. Kunz, H. Kurki-Suonio, G. Lagache, J.-M. Lamarre, A. Lasenby, M. Lattanzi, C. R. Lawrence, M. Le Jeune, J. Lesgourgues, F. Levrier, A. Lewis, M. Liguori, P. B. Lilje, V. Lindholm, M. Lpez-Caniego, P. M. Lubin, Y.-Z. Ma, J. F. Macías-Pérez, G. Maggio, D. Maino, N. Mandolesi, A. Mangilli,

A. Marcos-Caballero, M. Maris, P. G. Martin, E. Martínez-González, S. Matarrese, N. Mauri, J. D. McEwen, P. D. Meerburg, P. R. Meinhold, A. Melchiorri, A. Mennella, M. Migliaccio, S. Mitra, M.-A. Miville-Deschênes, D. Molinari, A. Moneti, L. Montier, G. Morgante, A. Moss, M. Münchmeyer, P. Natoli, H. U. Nørgaard-Nielsen, L. Pagano, D. Paoletti, B. Partridge, G. Patanchon, H. V. Peiris, F. Perrotta, V. Pettorino, F. Piacentini, L. Polastri, G. Polenta, J.-L. Puget, J. P. Rachen, M. Reinecke, M. Remazeilles, A. Renzi, G. Rocha, C. Rosset, G. Roudier, J. A. Rubiño-Martín, B. Ruiz-Granados, L. Salvati, M. Sandri, M. Savelainen, D. Scott, E. P. S. Shellard, M. Shiraishi, C. Sirignano, G. Sirri, L. D. Spencer, R. Sunyaev, A.-S. Suur-Uski, J. A. Tauber, D. Tavagnacco, M. Tenti, L. Toffolatti, M. Tomasi, T. Trombetti, J. Valiviita, B. Van Tent, P. Vielva, F. Villa, N. Vittorio, B. D. Wandelt, I. K. Wehus, S. D. M. White, A. Zacchei, J. P. Zibin, and A. Zonca. Planck 2018 results. X. Constraints on inflation. *arXiv e-prints*, July 2018.

- [105] Planck Collaboration, Y. Akrami, M. Ashdown, J. Aumont, C. Baccigalupi, M. Ballardini, A. J. Banday, R. B. Barreiro, N. Bartolo, S. Basak, K. Benabed, J.-P. Bernard, M. Bersanelli, P. Bielewicz, J. R. Bond, J. Borrill, F. R. Bouchet, F. Boulanger, A. Bracco, M. Bucher, C. Burigana, E. Calabrese, J.-F. Cardoso, J. Carron, H. C. Chiang, C. Combet, B. P. Crill, P. de Bernardis, G. de Zotti, J. Delabrouille, J.-M. Delouis, E. Di Valentino, C. Dickinson, J. M. Diego, A. Ducout, X. Dupac, G. Efstathiou, F. Elsner, T. A. Enßlin, E. Falgarone, Y. Fantaye, K. Ferrière, F. Finelli, F. Forastieri, M. Frailis, A. A. Fraisse, E. Franceschi, A. Frolov, S. Galeotta, S. Galli, K. Ganga, R. T. Génova-Santos, T. Ghosh, J. González-Nuevo, K. M. Górski, A. Gruppuso, J. E. Gudmundsson, V. Guillet, W. Handley, F. K. Hansen, D. Herranz, Z. Huang, A. H. Jaffe, W. C. Jones, E. Keihänen, R. Keskitalo, K. Kiiveri, J. Kim, N. Krachmalnicoff, M. Kunz, H. Kurki-Suonio, J.-M. Lamarre, A. Lasenby, M. Le Jeune, F. Levrier, M. Liguori, P. B. Lilje, V. Lindholm, M. López-Caniego, P. M. Lubin, Y.-Z. Ma, J. F. Macías-Pérez, G. Maggio, D. Maino, N. Mandolesi, A. Mangilli, P. G. Martin, E. Martínez-González, S. Matarrese, J. D. McEwen, P. R. Meinhold, A. Melchiorri, M. Migliaccio, M.-A. Miville-Deschênes, D. Molinari, A. Moneti, L. Montier, G. Morgante, P. Natoli, L. Pagano, D. Paoletti, V. Pettorino, F. Piacentini, G. Polenta, J.-L. Puget, J. P. Rachen, M. Reinecke, M. Remazeilles, A. Renzi, G. Rocha, C. Rosset, G. Roudier, J. A. Rubiño-Martín, B. Ruiz-Granados, L. Salvati, M. Sandri, M. Savelainen, D. Scott, J. D. Soler, L. D. Spencer, J. A. Tauber, D. Tavagnacco, L. Toffolatti, M. Tomasi, T. Trombetti, J. Valiviita, F. Vansyngel, F. Van Tent, P. Vielva, F. Villa, N. Vittorio, I. K. Wehus, A. Zacchei, and A. Zonca. Planck 2018 results. XI. Polarized dust foregrounds. *ArXiv e-prints*, January 2018.
- [106] Planck Collaboration, Y. Akrami, M. Ashdown, J. Aumont, C. Baccigalupi, M. Ballardini, A. J. Banday, R. B. Barreiro, N. Bartolo, S. Basak, K. Benabed, M. Bersanelli, P. Bielewicz, J. R. Bond, J. Borrill, F. R. Bouchet, F. Boulanger, M. Bucher, C. Burigana, E. Calabrese, J.-F. Cardoso, J. Carron, B. Casaponsa, A. Challinor, L. P. L. Colombo, C. Combet, B. P. Crill, F. Cuttaia, P. de Bernardis, A. de Rosa, G. de Zotti, J. Delabrouille, J.-M. Delouis, E. Di Valentino, C. Dickinson, J. M. Diego, S. Donzelli, O. Doré, A. Ducout, X. Dupac, G. Efstathiou, F. Elsner, T. A. Enßlin, H. K. Eriksen, E. Falgarone, R. Fernandez-Cobos, F. Finelli, F. Forastieri, M. Frailis, A. A. Fraisse, E. Franceschi, A. Frolov, S. Galeotta, S. Galli, K. Ganga, R. T. Génova-Santos, M. Gerbino, T. Ghosh, J. González-Nuevo, K. M. Górski, S. Gratton, A. Gruppuso, J. E. Gudmundsson, W. Handley, F. K. Hansen, G. Helou, D. Herranz, Z. Huang, A. H. Jaffe, A. Karakci, E. Keihänen, R. Keskitalo, K. Kiiveri, J. Kim, T. S. Kisner, N. Krachmalnicoff, M. Kunz, H. Kurki-Suonio, G. Lagache, J.-M. Lamarre, A. Lasenby, M. Lattanzi, C. R. Lawrence, M. Le Jeune, F. Levrier, M. Liguori, P. B. Lilje, V. Lindholm, M. López-Caniego, P. M. Lubin, Y.-Z. Ma, J. F. Macías-Pérez, G. Maggio, D. Maino, N. Mandolesi, A. Mangilli, A. Marcos-Caballero, P. G. Martin, E. Martínez-González, S. Matarrese, N. Mauri, J. D. McEwen, P. R. Meinhold, A. Melchiorri, A. Mennella, M. Migliaccio, M.-A. Miville-Deschênes, D. Molinari, A. Moneti, L. Montier, G. Morgante, P. Natoli, F. Oppizzi, L. Pagano, D. Paoletti, B. Partridge, M. Peel,

- V. Pettorino, F. Piacentini, G. Polenta, J.-L. Puget, J. P. Rachen, M. Reinecke, M. Remazeilles, A. Renzi, G. Rocha, G. Roudier, J. A. Rubiño-Martín, B. Ruiz-Granados, L. Salvati, M. Sandri, M. Savelainen, D. Scott, D. S. Seljebotn, C. Sirignano, L. D. Spencer, A.-S. Suur-Uski, J. A. Tauber, D. Tavagnacco, M. Tenti, H. Thommesen, L. Toffolatti, M. Tomasi, T. Trombetti, J. Valiviita, B. Van Tent, P. Vielva, F. Villa, N. Vittorio, B. D. Wandelt, I. K. Wehus, A. Zacchei, and A. Zonca. Planck 2018 results. IV. Diffuse component separation. *ArXiv e-prints*, July 2018.
- [107] C. L. Reichardt, L. Shaw, O. Zahn, K. A. Aird, B. A. Benson, L. E. Bleem, J. E. Carlstrom, C. L. Chang, H. M. Cho, T. M. Crawford, A. T. Crites, T. de Haan, M. A. Dobbs, J. Dudley, E. M. George, N. W. Halverson, G. P. Holder, W. L. Holzapfel, S. Hoover, Z. Hou, J. D. Hrubes, M. Joy, R. Keisler, L. Knox, A. T. Lee, E. M. Leitch, M. Lueker, D. Luong-Van, J. J. McMahon, J. Mehl, S. S. Meyer, M. Millea, J. J. Mohr, T. E. Montroy, T. Natoli, S. Padin, T. Plagge, C. Pryke, J. E. Ruhl, K. K. Schaffer, E. Shirokoff, H. G. Spieler, Z. Staniszewski, A. A. Stark, K. Story, A. van Engelen, K. Vanderlinde, J. D. Vieira, and R. Williamson. A Measurement of Secondary Cosmic Microwave Background Anisotropies with Two Years of South Pole Telescope Observations. *ApJ*, 755:70, August 2012.
- [108] A. G. Riess, S. Casertano, W. Yuan, L. Macri, B. Bucciarelli, M. G. Lattanzi, J. W. MacKenty, J. B. Bowers, W. Zheng, A. V. Filippenko, C. Huang, and R. I. Anderson. Milky Way Cepheid Standards for Measuring Cosmic Distances and Application to Gaia DR2: Implications for the Hubble Constant. *ApJ*, 861:126, July 2018.
- [109] A. G. Riess, L. Macri, S. Casertano, H. Lampeitl, H. C. Ferguson, A. V. Filippenko, S. W. Jha, W. Li, and R. Chornock. A 3% Solution: Determination of the Hubble Constant with the Hubble Space Telescope and Wide Field Camera 3. *ApJ*, 730:119, April 2011.
- [110] A. G. Riess, L. M. Macri, S. L. Hoffmann, D. Scolnic, S. Casertano, A. V. Filippenko, B. E. Tucker, M. J. Reid, D. O. Jones, J. M. Silverman, R. Chornock, P. Challis, W. Yuan, P. J. Brown, and R. J. Foley. A 2.4% Determination of the Local Value of the Hubble Constant. *ApJ*, 826:56, July 2016.
- [111] A.G. Riess, S. Casertano, W. Yuan, L.M. Macri, and D. Scolnic. Large Magellanic Cloud Cepheid Standards Provide a 1% Foundation for Determination of the Hubble Constant and Stronger Evidence for Physics Beyond Λ CDM. *arXiv:1903.07603*, 2019.
- [112] A. J. Ross, L. Samushia, C. Howlett, W. J. Percival, A. Burden, and M. Manera. The clustering of the SDSS DR7 main Galaxy sample - I. A 4 per cent distance measure at $z = 0.15$. *MNRAS*, 449:835–847, May 2015.
- [113] C. Rosset, M. Tristram, N. Ponthieu, P. Ade, J. Aumont, A. Catalano, L. Conversi, F. Couchot, B. P. Crill, F.-X. Désert, K. Ganga, M. Giard, Y. Giraud-Héraud, J. Haïssinski, S. Henrot-Versillé, W. Holmes, W. C. Jones, J.-M. Lamarre, A. Lange, C. Leroy, J. Macías-Pérez, B. Maffei, P. de Marcillac, M.-A. Miville-Deschênes, L. Montier, F. Noviello, F. Pajot, O. Perdereau, F. Piacentini, M. Piat, S. Plaszczynski, E. Pointecouteau, J.-L. Puget, I. Ristorcelli, G. Savini, R. Sudiwala, M. Veneziani, and D. Yvon. Planck pre-launch status: High Frequency Instrument polarization calibration. *A&A*, 520:A13, September 2010.
- [114] Y. Sekimoto, P. Ade, K. Arnold, J. Aumont, J. Austermann, C. Baccigalupi, A. Banday, R. Banerji, S. Basak, S. Beckman, M. Bersanelli, J. Borrill, F. Boulanger, M. L. Brown, M. Bucher, E. Calabrese, A. Challinor, Y. Chinone, F. Columbro, A. Cukierman, D. Curtis, P. de Bernardis, M. de Petris, M. Dobbs, T. Dotani, L. Duband, A. Ducout, K. Ebisawa, T. Elleflot, H. Eriksen, J. Errard, R. Flauger, C. Franceschet, U. Fuskeland, K. Ganga, J. R. Gao, T. Ghigna, J. Grain, A. Gruppuso, N. Halverson, P. Hargrave, T. Hasebe, M. Hasegawa, M. Hattori, M. Hazumi, S. Henrot-Versille, C. Hill, Y. Hirota, E. Hivon, D. T. Hoang, J. Hubmayr, K. Ichiki, H. Imada, H. Ishino, G. Jaehnig, H. Kanai, S. Kashima, Y. Kataoka, N. Katayama, T. Kawasaki, R. Keskitalo, A. Kibayashi, T. Kikuchi, K. Kimura, T. Kisner, Y. Kobayashi, N. Kogiso, K. Kohri, E. Komatsu, K. Komatsu, K. Konishi, N. Krachmalnicoff,

- C. L. Kuo, N. Kurinsky, A. Kushino, L. Lamagna, A. T. Lee, E. Linder, B. Maffei, M. Maki, A. Mangilli, E. Martinez-Gonzalez, S. Masi, T. Matsumura, A. Mennella, Y. Minami, K. Mistuda, D. Molinari, L. Montier, G. Morgante, B. Mot, Y. Murata, A. Murphy, M. Nagai, R. Nagata, S. Nakamura, T. Namikawa, P. Natoli, T. Nishibori, H. Nishino, F. Noviello, C. O’Sullivan, H. Ochi, H. Ogawa, H. Ogawa, H. Ohsaki, I. Ohta, N. Okada, G. Patanchon, F. Piacentini, G. Pisano, G. Polenta, D. Poletti, G. Puglisi, C. Raum, S. Realini, M. Remazeilles, H. Sakurai, Y. Sakurai, G. Savini, B. Sherwin, K. Shinozaki, M. Shiraishi, G. Signorelli, G. Smecher, R. Stompor, H. Sugai, S. Sugiyama, A. Suzuki, J. Suzuki, R. Takaku, H. Takakura, S. Takakura, E. Taylor, Y. Terao, K. L. Thompson, B. Thorne, M. Tomasi, H. Tomida, N. Trappe, M. Tristram, M. Tsuji, M. Tsujimoto, S. Uozumi, S. Utsunomiya, N. Vittorio, N. Watanabe, I. Wehus, B. Westbrook, B. Winter, R. Yamamoto, N. Y. Yamasaki, M. Yanagisawa, T. Yoshida, J. Yumoto, M. Zannoni, and A. Zonca. Concept design of the LiteBIRD satellite for CMB B-mode polarization. In *Space Telescopes and Instrumentation 2018: Optical, Infrared, and Millimeter Wave*, volume 10698 of *Society of Photo-Optical Instrumentation Engineers (SPIE) Conference Series*, page 106981Y, August 2018.
- [115] U. Seljak and M. Zaldarriaga. Signature of Gravity Waves in the Polarization of the Microwave Background. *Physical Review Letters*, 78:2054–2057, March 1997.
- [116] G. F. Smoot, C. L. Bennett, A. Kogut, E. L. Wright, J. Aymon, N. W. Boggess, E. S. Cheng, G. de Amici, S. Gulkis, M. G. Hauser, G. Hinshaw, P. D. Jackson, M. Janssen, E. Kaita, T. Kelsall, P. Keegstra, C. Lineweaver, K. Loewenstein, P. Lubin, J. Mather, S. S. Meyer, S. H. Moseley, T. Murdock, L. Rokke, R. F. Silverberg, L. Tenorio, R. Weiss, and D. T. Wilkinson. Structure in the COBE differential microwave radiometer first-year maps. *ApJ*, 396:L1–L5, September 1992.
- [117] D. N. Spergel, R. Flauger, and R. Hložek. Planck data reconsidered. *Phys. Rev. D*, 91(2):023518, January 2015.
- [118] A. A. Starobinskij. Spectrum of gravitational background radiation and initial state of the universe. *Pisma v Zhurnal Eksperimentalnoi i Teoreticheskoi Fiziki*, 30:719–723, 1979.
- [119] R. Stompor and G. Efstathiou. Gravitational lensing of cosmic microwave background anisotropies and cosmological parameter estimation. *MNRAS*, 302:735–747, February 1999.
- [120] H. Trac, P. Bode, and J. P. Ostriker. Templates for the Sunyaev-Zel’dovich Angular Power Spectrum. *ApJ*, 727:94, February 2011.
- [121] M. A. Troxel, N. MacCrann, J. Zuntz, T. F. Eifler, E. Krause, S. Dodelson, D. Gruen, J. Blazek, O. Friedrich, S. Samuroff, J. Prat, L. F. Secco, C. Davis, A. Ferté, J. DeRose, A. Alarcon, A. Amara, E. Baxter, M. R. Becker, G. M. Bernstein, S. L. Bridle, R. Cawthon, C. Chang, A. Choi, J. De Vicente, A. Drlica-Wagner, J. Elvin-Poole, J. Frieman, M. Gatti, W. G. Hartley, K. Honscheid, B. Hoyle, E. M. Huff, D. Huterer, B. Jain, M. Jarvis, T. Kacprzak, D. Kirk, N. Kokron, C. Krawiec, O. Lahav, A. R. Liddle, J. Peacock, M. M. Rau, A. Refregier, R. P. Rollins, E. Roza, E. S. Rykoff, C. Sánchez, I. Sevilla-Noarbe, E. Sheldon, A. Stebbins, T. N. Varga, P. Vielzeuf, M. Wang, R. H. Wechsler, B. Yanny, T. M. C. Abbott, F. B. Abdalla, S. Allam, J. Annis, K. Bechtol, A. Benoit-Lévy, E. Bertin, D. Brooks, E. Buckley-Geer, D. L. Burke, A. Carnero Rosell, M. Carrasco Kind, J. Carretero, F. J. Castander, M. Crocce, C. E. Cunha, C. B. D’Andrea, L. N. da Costa, D. L. DePoy, S. Desai, H. T. Diehl, J. P. Dietrich, P. Doel, E. Fernandez, B. Flaugher, P. Fosalba, J. García-Bellido, E. Gaztanaga, D. W. Gerdes, T. Giannantonio, D. A. Goldstein, R. A. Gruendl, J. Gschwend, G. Gutierrez, D. J. James, T. Jeltema, M. W. G. Johnson, M. D. Johnson, S. Kent, K. Kuehn, S. Kuhlmann, N. Kuropatkin, T. S. Li, M. Lima, H. Lin, M. A. G. Maia, M. March, J. L. Marshall, P. Martini, P. Melchior, F. Menanteau, R. Miquel, J. J. Mohr, E. Neilsen, R. C. Nichol, B. Nord, D. Petravick, A. A. Plazas, A. K. Romer, A. Roodman, M. Sako, E. Sanchez, V. Scarpine, R. Schindler, M. Schubnell, M. Smith, R. C.

Smith, M. Soares-Santos, F. Sobreira, E. Suchyta, M. E. C. Swanson, G. Tarle, D. Thomas, D. L. Tucker, V. Vikram, A. R. Walker, J. Weller, Y. Zhang, and DES Collaboration. Dark Energy Survey Year 1 results: Cosmological constraints from cosmic shear. *Phys. Rev. D*, 98(4):043528, August 2018.

- [122] M. P. Viero, L. Wang, M. Zemcov, G. Addison, A. Amblard, V. Arumugam, H. Aussel, M. Béthermin, J. Bock, A. Boselli, V. Buat, D. Burgarella, C. M. Casey, D. L. Clements, A. Conley, L. Conversi, A. Cooray, G. De Zotti, C. D. Dowell, D. Farrah, A. Franceschini, J. Glenn, M. Griffin, E. Hatziminaoglou, S. Heinis, E. Ibar, R. J. Ivison, G. Lagache, L. Levenson, L. Marchetti, G. Marsden, H. T. Nguyen, B. O’Halloran, S. J. Oliver, A. Omont, M. J. Page, A. Papageorgiou, C. P. Pearson, I. Pérez-Fournon, M. Pohlen, D. Rigopoulou, I. G. Roseboom, M. Rowan-Robinson, B. Schulz, D. Scott, N. Seymour, D. L. Shupe, A. J. Smith, M. Symeonidis, M. Vaccari, I. Valtchanov, J. D. Vieira, J. Wardlow, and C. K. Xu. HerMES: Cosmic Infrared Background Anisotropies and the Clustering of Dusty Star-forming Galaxies. *ApJ*, 772:77, July 2013.